

# Soils and Rocks

An International Journal of Geotechnical  
and Geoenvironmental Engineering



Volume 43, N. 2  
April-June 2020

# ***SOILS and ROCKS***

An International Journal of Geotechnical and Geoenvironmental Engineering

**Editor** Renato Pinto da Cunha - University of Brasília, Brazil

**Co-editor** José Couto Marques - University of Porto, Portugal

## **Executive Board**

Paulo J. R. Albuquerque  
*Campinas State University, Brazil*

Nuno Cristelo  
*University of Trás-dos-Montes and Alto Douro, Portugal*

Leandro Neves Duarte  
*Federal University of São João Del-Rei, Brazil*

Teresa M. Bodas Freitas  
*Technical University of Lisbon, Portugal*

Gilson de F. N. Gitirana Jr. (*Secretary*)  
*Federal University of Goiás, Brazil*

Sara Rios  
*University of Porto, Portugal*

Paulo Scarano Hemsí  
*Aeronautics Institute of Technology, Brazil*

José A. Schiavon  
*Aeronautics Institute of Technology, Brazil*

Ana Vieira  
*National Laboratory for Civil Engineering, Portugal*

## **Advisory Panel**

H. Einstein  
*MIT, USA*

Roger Frank  
*ENPC-Cermes, France*

John A. Hudson  
*Imperial College, UK*

Kenji Ishihara  
*University of Tokyo, Japan*

Michele Jamiolkowski  
*Studio Geotecnico Italiano, Italy*

Willy A. Lacerda  
*COPPE-UFRJ, Brazil*

E. Maranhã das Neves  
*Lisbon Technical University, Portugal*

Paul Marinos  
*NTUA, Greece*

Nielen van der Merve  
*University of Pretoria, South Africa*

James K. Mitchell  
*Virginia Tech., USA*

Lars Persson  
*SGU, Sweden*

Harry G. Poulos  
*University of Sidney, Australia*

Nick Rengers  
*ITC, The Netherlands*

Fumio Tatsuoka  
*Tokyo University of Science, Japan*

Luiz Gonzalles de Vallejo  
*UCM, Spain*

*Soils and Rocks* publishes papers in English in the broad fields of Geotechnical Engineering, Engineering Geology and Geoenvironmental Engineering. The Journal is published in March, June, September and December. Subscription price is US\$ 90.00 per year. The journal, with the name “Solos e Rochas”, was first published in 1978 by the Graduate School of Engineering, Federal University of Rio de Janeiro (COPPE-UFRJ). In 1980 it became the official magazine of the Brazilian Association for Soil Mechanics and Geotechnical Engineering (ABMS), acquiring the national character that had been the intention of its founders. In 1986 it also became the official Journal of the Brazilian Association for Engineering Geology and the Environment (ABGE) and in 1999 became the Latin American Geotechnical Journal, following the support of Latin-American representatives gathered for the Pan-American Conference of Guadalajara (1996). In 2007 the journal acquired the status of an international journal under the name of Soils and Rocks, published by the Brazilian Association for Soil Mechanics and Geotechnical Engineering (ABMS), Brazilian Association for Engineering Geology and the Environment (ABGE) and Portuguese Geotechnical Society (SPG). In 2010, ABGE decided to publish its own journal and left the partnership.

***Soils and Rocks***

|              |                       |
|--------------|-----------------------|
| 1978,        | 1 (1, 2)              |
| 1979,        | 1 (3), 2 (1,2)        |
| 1980-1983,   | 3-6 (1, 2, 3)         |
| 1984,        | 7 (single number)     |
| 1985-1987,   | 8-10 (1, 2, 3)        |
| 1988-1990,   | 11-13 (single number) |
| 1991-1992,   | 14-15 (1, 2)          |
| 1993,        | 16 (1, 2, 3, 4)       |
| 1994-2010,   | 17-33 (1, 2, 3)       |
| 2011,        | 34 (1, 2, 3, 4)       |
| 2012-2019,   | 35-42 (1, 2, 3)       |
| <b>2020,</b> | <b>43 (1, 2,</b>      |

ISSN 1980-9743

CDU 624.131.1

**SOILS and ROCKS**

An International Journal of Geotechnical and Geoenvironmental Engineering

**Publication of****ABMS - Brazilian Association for Soil Mechanics and Geotechnical Engineering****SPG - Portuguese Geotechnical Society****Volume 43, N. 2, April-June 2020****Table of Contents****ARTICLES**

|   |     |
|---|-----|
| <i>Application of Grouting Intensity Number in Spillway Foundation at Jirau HPP/RO</i><br>M.B. Lopes, A.P. Assis  | 171 |
| <i>A Laboratory Study of the Collapse Behaviour of a Compacted Sabkha Soil</i><br>O.Y. Debbab, B. Moussai, A. Messad  | 181 |
| <i>Hydromechanical Behavior of Soil with Tire Fibers</i><br>A.C. Silva, S. Fucale, S.R.M. Ferreira  | 191 |
| <i>Bottom Reinforcement in Braced Excavations: Coupled Analysis and New Method for Basal-Heave Stability Study</i><br>J.L. Borges, R.M. Santos  | 199 |
| <i>Relationship Between Shear Wave Velocity and Piezocone Penetration Tests on the Brazilian Continental Margin</i><br>R.G. Borges, L.O. Souza Junior, M.C.F. Almeida, M.S.S. Almeida | 219 |
| <i>Geogrid Mechanical Damage Caused by Recycled Construction and Demolition Waste (RCDW): Influence of Grain Size Distribution</i><br>M.L. Domiciano, E.C.G. Santos, J. Lins da Silva | 231 |
| <i>Numerical Investigations on Seismic Bearing Capacity of Interfering Strip Footings</i><br>R. Boufarh, D. Saadi, M.S. Laouar  | 247 |

**TECHNICAL NOTES**

|  |     |
|--|-----|
| <i>Drained and Undrained Behavior of an Aeolian Sand from Natal, Brazil</i><br>P.L. Souza Junior, O.F. Santos Junior, T.B. Fontoura, O. Freitas Neto   | 263 |
| <i>Effects of Hydraulic Gradient Variation on the Structure and Strength of a Compacted Tropical Soil</i><br>W.G. Silva, H.N. Pitanga, T.O. Silva, S.L.S. Dias Neto, D.C. Lima, T.P. Trindade              | 271 |
| <i>Physicochemical Modifications in Geomaterials and Their Leachates Extracted from Acidic Attack</i><br>S.T. Ferrazzo, R.S. Tímola, L. Bragagnolo, E. Prestes, E.P. Korf, P.D.M. Prietto, G.D.L.P. Vargas | 279 |
| <i>Sample Quality Assessment: Comparison Between Brass Shelby Tubes and Reinforced PVC Tube Samplers</i><br>A.V. Abreu, M.S.S. Almeida   | 287 |

**CASE STUDY**

|   |     |
|---|-----|
| <i>Influence of Weathering and Correlations Between Wave Propagation Velocity and Durability with Physical and Mechanical Parameters in Phyllites</i><br>T.R.R. Carvalho, M.F. Leão, E.A.G. Marques | 287 |
|---|-----|



## ***Articles***

***Soils and Rocks***  
**v. 43, n. 2**



# Application of Grouting Intensity Number in Spillway Foundation at Jirau HPP/RO

M.B. Lopes, A.P. Assis

**Abstract.** Brazil has one of the largest hydroelectric parks in the world and important ventures for the world ranking have been executed in the country - to cite the most recent, Jirau and Belo Monte Hydraulic Power Plants (HPP). This emphasizes the importance in the continuous study of techniques and theories commonly used, in order to improve the quality of the projects. This work proposed to implement the Grouting Intensity Number (*GIN*) methodology for the grouting of waterproofing curtains, through back analysis and estimation of the results of the Jirau HPP foundation treatment. The *GIN* was chosen from an analysis of curves plotted on a scatter plot as points representing the ratio between the grouting volume (grouting for further analysis) and water (water loss test for estimation) vs. the injection pressure. The maximum grouting intensity selected for the Jirau spillway was  $50 \text{ MPa} \times \text{L/ m}$ , which according to the method authors, Lombardi and Deere represents low fracture of the rock mass. Other authors also applied this methodology, finding values higher than in this paper. Therefore, continuity in studies of the application of *GIN* in projects in Brazil is important to validate its efficiency and to promote progress in this area of dam engineering.

**Keywords:** dams, foundation treatment, *GIN* methodology, grout curtain.

## 1. Introduction

Implementation of dams in Brazil is part of its history and economic development, having as initial incentive for this construction the Northeast drought and its active participation in the world economic (CBDB, 2011). The country stands out in the implementation of large hydroelectric constructions, known in the whole world by their importance and extension, and the generation capacity of energy in Brazil is open to comparison with the oil production in Saudi Arabia.

In September 2013, the Jirau Hydroelectric Power Plant started its commercial operation, located at the Madeira River, in Rondonia, with installed capacity 3,750 MW. According to Chiossi (2013), Jirau HPP is the fifth in national ranking of capacity and one of the 140 hydroelectric powerplants currently in operation, which represents 77.1 % of Brazil's energy supply (Governo do Brasil, 2018).

The Jirau HPP spillway is a reinforced concrete structure, divided into ten blocks and with a flow rate of  $82,600 \text{ m}^3/\text{s}$ . The safety of concrete dams can be achieved by controlling the uplift forces and the displacements provided by induced loads that are transferred to the foundation, and Oliveira (2002) states that the major stability issue is the uplift effect. To reduce the influence of this effect in the concrete dam base, foundation treatments can be used, including grout curtain and drain holes. In 1961, Arthur Casagrande presented the "First Rankine Lecture" at the Institution of Civil Engineers, relating the prejudices and

opinions about the efficiency of grouting under uplift effects (Oliveira, 2002), which since then has generated conflicts among designers.

The first works with grout curtain were carried out in France, in 1802, by the engineer Charles Bérigny, who indicated this alternative for foundation consolidation of Dieppe lock. In Brazil, the first use of the methodology was promoted by IPT - *Institute for Technological Research* - in Barra Bonita dam, in Tiete River, in the 1950s (Levis, 2006). The most utilized criteria of execution in the country was created by Hously in 1976 and updated in 1990, that considers the injectability of the cement grout in rock mass vs. pressure, using the "Split-Spacing" for drilling the grouting holes. This opening system was proposed by Nonveiller in 1979 and prescribes that the initial space of the holes must be chosen considering that the grouting regions do not overlap initially, following the drilling of primary, secondary and tertiary holes (Gama, 2012). For Hously (1990), the grouting pressure must be maintained for fifteen minutes until setting is reached, when the grout is stabilized and gains resistance. Brandão (2014) emphasizes that the setting concept was idealized for unstable grouts, wherein the rheology is susceptible and variable, and can have segregation and sedimentation. For Warner (2004), the use of unstable grouts is outdated and the set should be any point when there is no more absorption of cement grout. These discussions about the grouting pressures to be adopted and its flow encouraged Lombardi & Deere (1993) to develop a methodology that aims to systematize the execution of grout curtains, named as Grouting Intensity Number (*GIN*).

Marieli Biondo Lopes, M.Sc., Professor, Universidade Comunitária da Região de Chapecó, Chapecó, SC, Brazil. e-mail: marybiondo@hotmail.com.

André Pacheco Assis, Ph.D., Professor, Universidade de Brasília, Brasília, DF, Brazil. e-mail: aassis@unb.br.

Submitted on March 22, 2019; Final Acceptance on February 24, 2020; Discussion open until September 30, 2020.

DOI: 10.28927/SR.432171

The *GIN* purpose is to standardize, define the dosage for grout injection, using a unique mix that considers the limited penetration due to the size of the cement particles and, thus the finer the cement particle, the larger the effectiveness of grout injection (Cruz *et al.*, 2009). According to Carvalho *et al.* (2003), Mascarenhas de Moraes HPP was the first development in Brazil to use *GIN* as a grouting treatment procedure and there are technical advantages of this approach when compared to the conventional one, so its use in other projects would increase quality and reliability efficiency. Therefore, this research aims to describe implementation of this procedure at Jirau HPP, to compare the results with the literature, and to point out the benefits that the application of the method can bring to other future dam projects.

## 2. *GIN* Method - Grouting Intensity Number

According to Gama (2012), the grouting behavior is divided in function of two types of fluids: Newtonian and Binghamian. Newtonian fluids are characterized by a force needed to move the liquid, which is related with the dynamic viscosity. In Binghamian fluids, the cohesion or thixotropy exists in addition to the dynamic-plastic viscosity, as shown in Fig. 1, where  $C$  = cohesion;  $\eta$  = viscosity for Binghamian fluids;  $\eta'$  = viscosity for Newtonian fluids;  $\tau$  = shear stress;  $\frac{dv}{dx}$  = shear rate.

Lombardi & Deere (1993) state that the difference between them is that in Newtonian fluids the viscosity governs the penetration velocity and designates their rheological behavior, and in Binghamian fluids, in addition to the viscosity, the cohesion is a resistance to creep and governs the maximum distance of penetration. Figure 2 presents a graph (Houlsby, 1990) where it is possible to verify the cement grout behavior in relation to the dosage, when analyzed in cohesion and viscosity terms. Thicker grouts ( $w/c$  ratios of 0.6:1 and 0.7:1) have a shear stress intercept (cohesion) greater than fine particles ( $w/c$  ratios of 1:1 and 3:1), but the viscosity or percolation distance are less than the

finer particles. For closed discontinuities, higher  $w/c$  ratios are indicated due to their viscosity. In wider-aperture discontinuities, thicker grouts are used, with a lower  $w/c$  ratio.

The grouting pressure is also an important factor, where Levis (2006) cites two trends: American and European. The American System defends the use of low pressures, calculated on the basis of 25 kPa/m (as adopted in the Jirau HPP project). In the European procedure, the pressure factor is 100 kPa/m, which characterizes the adoption of high pressures. The disadvantage of using high pressures is the possibility of causing the elastic opening of the discontinuities and this may be irreversible. The elastic opening is beneficial, but high pressures can open discontinuities that were sealed, becoming harmful (Marques Filho, 1986 *apud* Levis, 2006).

The discussions about the grouting pressures that will be adopted and their fluidity encouraged Lombardi & Deere (1993) to develop the *GIN* methodology - Grouting Intensity Number, with the purpose of defining the grout dosage, using a unique mix and that considers the penetration limited by the size of cement particles. According to the authors, beyond the adoption of a single dosage of grout in all the injection process, the pressure increases gradually in accordance with the grout penetration in the fractures, and it can monitor the pressure, flow velocity and injectability by integrated system with real time data acquisition. So, *GIN* represents the product of grouting volume ( $V$  in L/m) at 1 m and the corresponding grouting pressure ( $p$  in kPa), given by:

$$GIN = p \times V \quad (1)$$

To Lombardi & Deere (1993), the *GIN* main characteristic is the limitation of grouting pressure, preventing excessive pressure and grout volumes that can cause hydraulic fractures or the lifting of foundation mass, as shown in Fig. 3. The *GIN* is supported due to the traditional waterproofing methods of rock foundations having been based

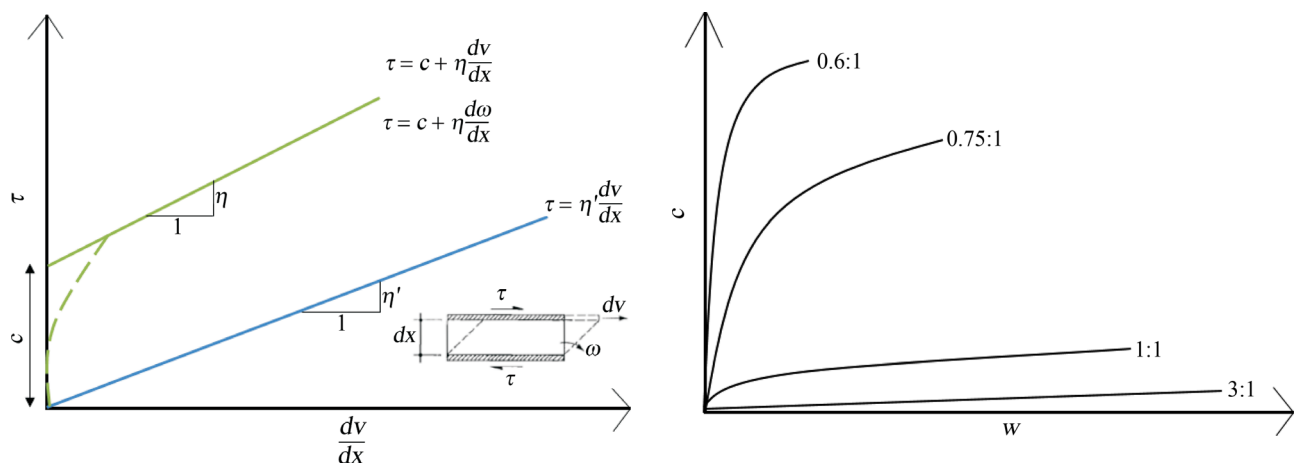


**Figure 1** - Rheological Models: 1) Newtonian; 2) Binghamian.

**Figure 2** - Comparison of cement grout thixotropy for different  $w/c$  ratios by grout weight.

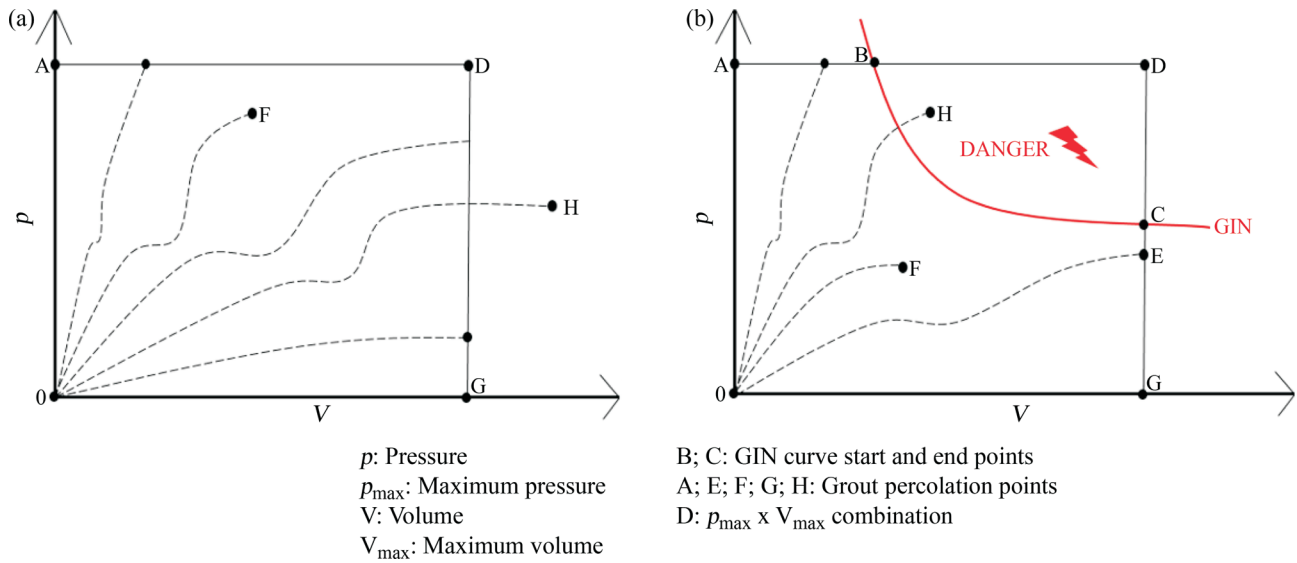


Figure 3 - Limits imposed on the injection process a) Hously Method; b) *GIN* method.

on empirical principles, institutional and professional experiences that conducted to dogmatic beliefs (*op. cit.*).

The *GIN* methodology requires that once selected the intensity level to be grouted, this number is maintained not only for the filling of fractures easily injected (with large volume of absorption and low pressure), but also for the thinner fractures (with lower grout absorption and larger adopted pressure), maintaining the *GIN* constant. Lombardi and Deere (1993) defined guide curves used as reference parameters for the adoption of intensities, in which wider discontinuities require an intensity of 250 MPa × L/m. Finally, in cases characterized by closed and extremely closed cracks, the pressure increases with a small increase in grout volume ( $GIN < 150 \text{ MPa} \times \text{L/m}$ ).

Figure 4 indicates that the maximum limit for volume and pressure needs to be defined, before the elaboration of the *GIN* curve. According to Gama (2012), point *F* is the intersection between curve 2 and curve 1, representing the fi-

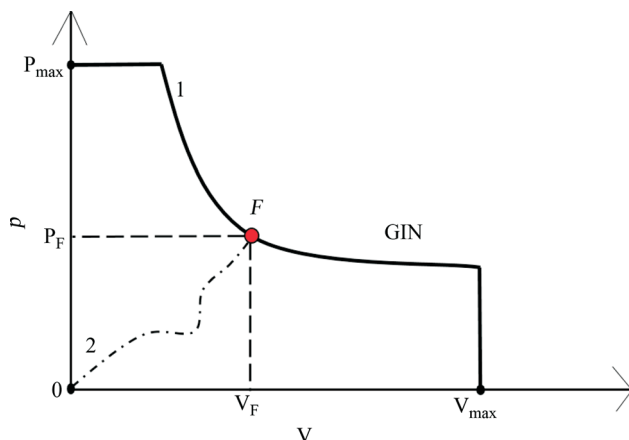


Figure 4 - Representation of the *GIN* curve.

nal values of pressure and absorption, indicated as the *GIN* to be adopted.

Lombardi (1996) defined that the maximum pressure is conditioned by the hydraulic pressure that the rock mass is submitted to, varying between twice or three times this magnitude and the maximum volume by the injectability factors determined in the subsoil survey phase. The author compared the traditional method and the *GIN*, concluding that:

- a) As regards the grouting dosage, using a thicker and more stable grout in the *GIN* method achieves the same objective as the traditional methods;
- b) The mix cohesion, due to the use of lower *w/c* relations, is maintained constant during the entire injection process and, therefore, the setting concept became unnecessary;
- c) The final grouting pressure in the *GIN* methodology remains lower than in the traditional method, reducing the risk of hydraulic fractures in the rock mass.

### 3. Jirau Hydroelectric Powerplant

Jirau HPP was constructed 120 km away from the capital of Rondonia, Porto Velho, near to Jaci Paraná district, in an island of Madeira River, named Ilha do Padre. According to the HPP has generation capacity of 3,750 MW, being capable to supply more than 10 million houses.

The Jirau HPP complex comprises concrete, soil, soil and rockfill, and rockfill with asphalt core structures. Concrete structures encompass two powerhouses, one placed in the right bank of the river with 28 bulb turbines, and the second in the left bank with 22 turbines, summing up 50 generating units with 75 MW. Figure 5 presents the satellite image of the HPP location.



**Figure 5** - Aerial view of the execution of the development (Google Earth, 2014).

In the region, it is possible to find granites of the São Lourenço-Caripunas Intrusive Suite, beyond the conglomerate of soils and rocks of the Palmeiral Formation and sediments of the fluvial terrace in the Quaternary Jaciparana Formation.

In the site investigation carried out along the dam longitudinal axis, the existence of rock masses such as granites, rhyolites and diabase were confirmed, where the granites and rhyolites belong to a batholith with an approximate area of 3,000 km<sup>2</sup>, responsible for the waterfalls of Santo Antônio Teotônio do Inferno (axis of the Ilha do Padre) and Jirau.

The granite of the spillway foundation is very fractured and little weathered on the surface, identifying discontinuities Zx (vertical), Ix (inclined) and Dx (subhorizontal) parallel to the river flow.

The foundation treatment executed in the concrete structures of the Jirau complex was composed of grouting lines and deep drains, following the conventional methodology of Houlsby (1990) and the opening of holes using the split-spacing method proposed by Nonveiller in 1970. For the spillway, three lines for a deep treatment were designed. The upstream line has primary, secondary and tertiary holes, spaced 3 m, with a vertical depth of 20 m and dip of 20°/upstream. The central and downstream lines were formed by possible holes, opened when the required holes exceeded a grout absorption of 30 kg/m, based on design criteria.

The absorption of 30 kg/m or less rates the rock mass as with low permeability, which corresponds to a permeability coefficient  $k$  from  $10^{-5}$  to  $10^{-4}$  cm/s, considered satisfactory for the treatment effectiveness. The design criteria corroborate with the indication of treatment necessity pointed out by Costa (2012), where the author indicates the injection along two or three lines in cases where the hydraulic conductivity of the rock mass is between  $k = 10^{-5}$  to  $5 \times 10^{-4}$  cm/s.

Hole drilling was carried out by a rotary-percussive drilling tool with injection of air and water simultaneously, to prevent drilling debris block the entrance and percolation of cement grout, as mentioned in other cases by Marques and Filho (1986 *apud* Levis, 2006). It is used the ascending form of treatment, where it is drilled the entire hole and then, it is grouted in stretches with double packers, being the fastest process for construction with tight deadlines. The grouts used in the treatment was conventional grouts (cement and water), with initial dosage which  $w/c$  of 0.7:1 and thickened in the end to 0.5:1.

#### 4. Methodological Procedures

The confection of *GIN* curves of the spillway blocks of Jirau HPP was made in two ways to compare the results and selection of the adopted *GIN*: the first by back analysis of the obtained results with the grouting curtain in the original design and, the second, by estimation from the results of Water Loss Tests (in Portuguese - EPA), executed in the primary holes with 24 m spacing (Oliveira *et al.*, 1975).

To determine the *GIN* curve of each spillway block by back analysis, the results of the conventional (Houlsby) method were converted to values of grout pressure x volume for the *GIN* method ( $kP \times L/m$ ), and those values were plotted in a dispersion graph. The pressure is maintained with the same values indicated in grouting bulletins, converting only the unit of measurement to kPa. The cement consumption ( $w/c$  ratios of 0.7:1 and 0.5:1) collected from the bulletins as kg/m was converted into L/m, considering the CP IV-32 cement unit weight of 2,900 kg/m<sup>3</sup>.

After the cement consumption definition for each grout dosage, the final volume of the mix was obtained in L/m. As the *GIN* method adopts a single grout pressure, it is used the criteria of weighted volume, transforming the grout into a homogeneous fluid.

To determine the *GIN* curves by estimation, the results of water absorption in the primary hole, are used the

water volume absorbed by the hole is indicated as cement grout volume to be injected (L/m) and the test pressure as injection pressure (kPa).

The obtained results for the two types were disposed in a dispersion chart (pressure x volume) and hyperbolic curves with random intensities were inserted in those graphs to verify proximity between those points and the predetermined *GIN* curves, choosing for each block the best intensity (kPa x L/m). For the curves, the limits of volume and pressure were also determined in the direction of the volume, adopting an absorption of cement grout or water, and the pressure, the criteria cited by Lombardi (1996), two or three times the rock mass is submitted. For the mandatory (upstream) and possible (downstream) hole lines the theoretical grouting dosage was considered, assessing:

- a) Total consumption of the grout with *w/c* ratio of 0.7:1 in the mandatory holes;
- b) Total consumption of the grout with *w/c* ratio of 0.5:1 in the mandatory holes;
- c) Consumption of water ( $w_{0.7:1}$ ;  $w_{0.5:1}$  - L) and cement ( $c_{0.7:1}$ ;  $c_{0.5:1}$  - kg) for each dosage in the line of mandatory holes;
- d) Theoretical grout dosage given by:

$$\frac{w}{c} = \frac{w_{0.7:1} + w_{0.5:1}}{c_{0.7:1} + c_{0.5:1}} \quad (2)$$

- e) The same was evaluated for the possible grouting lines.

### 5. Results and Discussion

About the grout volume of cement and water, the values found in the grouting bulletins and EPA tests of the curtain in the Jirau HPP ranged from 20 to 800 L/m along the foundation of the spillway blocks. The determination of the maximum pressure magnitude, using the concept cited by Lombardi (1996), adopted:

- a) Water specific weight ( $\gamma_w = 9.81 \text{ kN/m}^3$ ) multiplied by the height of water column ( $H_w$ ), and in this case the normal maximum of the upstream tank of 28 m, obtaining hydraulic pressure ( $\sigma_w$ ) equal to 275 kPa.
- b) The maximum pressure greater than or equal to three times the hydraulic pressure ( $p_{max} = 3 \times \sigma_w$ ) resulted in

825 kPa, which was discarded because all results of the grouting curtain executed in Jirau were below this one. Thus, the adopted pressure was  $2.5 \times \sigma_w$  ( $p_{max} = 700 \text{ kPa}$ ).

From this, the curves confection was divided in those two mentioned groups in grout 4 for each block in the spillway, as detailed in Sections 5.1 and 5.2. Figure 6 shows the spillway scheme and the position of the studied blocks. The results for each group are presented in Table 1.

#### 5.1. *GIN* curves elaborated by back analysis

Figures 7 and 8 present the dispersion graphs and random *GIN* curves for three blocks of the spillway structure that were highlighted in those results in accordance to Table 1.

In Fig. 7, it is possible to observe that the VT-02 Block is in an area of water and cement grout low absorption, with maximum values less than 15 L/m. So, the *GIN* curves plotted in the dispersion graph tend to approach the highest number of points, with intensities varying between 0.8 MPa x L/m (*GIN* 1), 1.5 MPa x L/m (*GIN* 2) and 2.5 MPa x L/m (*GIN* 3).

As the curves were randomly plotted, the chosen curve was the closest one to the plotted points and best represents the situation - for VT-02 (according to Table 1), with *GIN* 2 intensity 1.5 MPa x L/m. However, in block VT-06 (Fig. 7b) there was a higher grout consumption, so there was a greater dispersion of the consumption points, for the same pressure adopted. In addition, the cement grout absorption reached volumes close to 600 L/m, due to its location in a region with greater presence of discontinuities (observed in the EPA results, injection and geological-geotechnical mapping).

However, in the same Fig. 7b it can be verified that three points are distant from the results in other sections of holes in the VT-06 block, and the random *GIN* curves stayed away from those points too. Thus, for VT-06, the highest intensity curve (*GIN* 3, as shown in Table 1) was adopted to consider the high consumption of grout in this region, as a consequence of wider discontinuities.

For the VT-07 block (Fig. 8) the highest injection intensity was adopted, presenting maximum volume

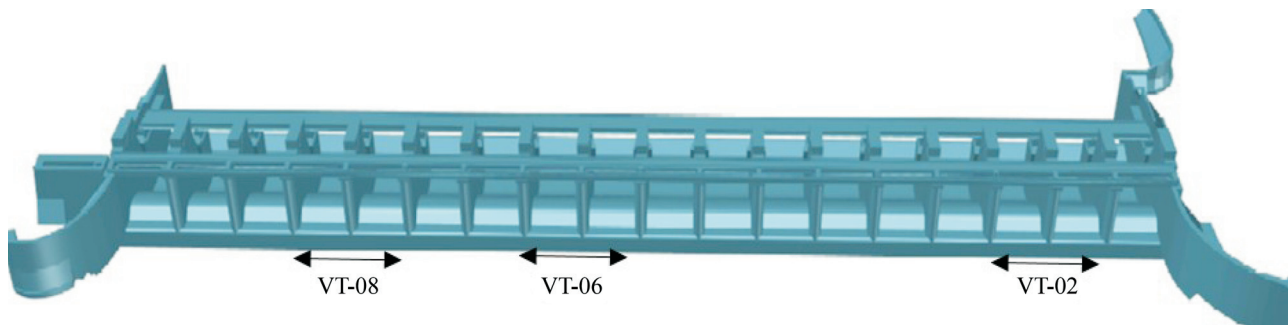


Figure 6 - Spillway structure.

**Table 1** - Results of *GIN* curves adopted for each block and the order of spillway holes.

| Block | <i>GIN</i> curve by back analysis |                  |                               | <i>GIN</i> curve by estimate |                  |                               |
|-------|-----------------------------------|------------------|-------------------------------|------------------------------|------------------|-------------------------------|
|       | $p_{\max}$ (kPa)                  | $v_{\max}$ (L/m) | <i>GIN</i> (MPa $\times$ L/m) | $p_{\max}$ (kPa)             | $v_{\max}$ (L/m) | <i>GIN</i> (MPa $\times$ L/m) |
| VT-01 | 700                               | 20               | 2                             | 700                          | 200              | 12                            |
| VT-02 | 700                               | 20               | 1.5                           | 700                          | 150              | 18                            |
| VT-03 | 700                               | 40               | 1.5                           | 700                          | 30               | 1                             |
| VT-04 | 700                               | 50               | 1.5                           | 700                          | 40               | 3                             |
| VT-05 | 700                               | 350              | 2                             | 700                          | 600              | 30                            |
| VT-06 | 700                               | 600              | 3                             | 700                          | 100              | 7                             |
| VT-07 | 700                               | 750              | 7                             | 700                          | 500              | 30                            |
| VT-08 | 700                               | 450              | 3                             | 700                          | 600              | 50                            |
| VT-09 | 700                               | 250              | 2.5                           | 700                          | 800              | 20                            |
| VT-10 | 700                               | 160              | 2                             | 700                          | 380              | 8                             |

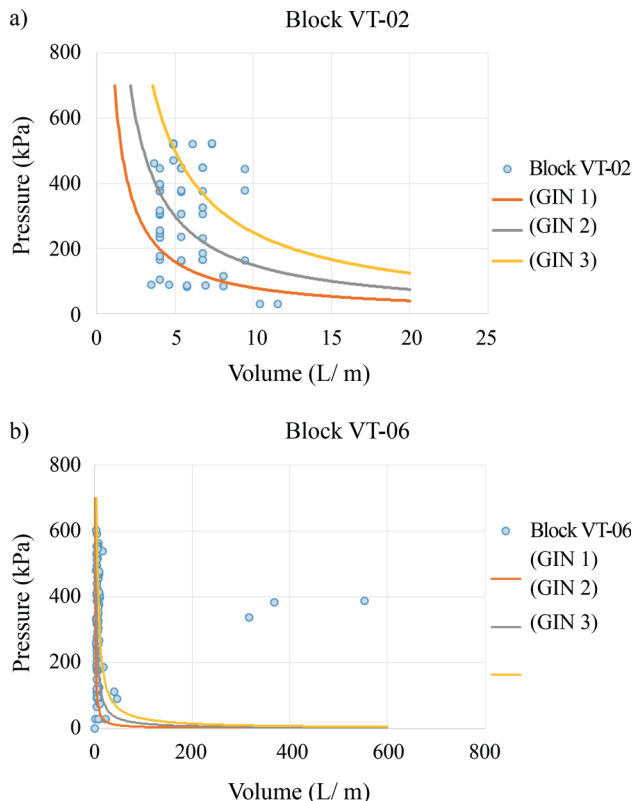
higher than 700 L/m. Unlike VT-06 (Fig. 7b), in the current block, the points were dispersed more uniformly until achieving the maximum volume. Consequently, the adopted *GIN* curves considered higher magnitudes, varying between 0.5 MPa  $\times$  L/m (*GIN* 1), 7 MPa  $\times$  L/m (*GIN* 2) and 15 MPa  $\times$  L/m (*GIN* 3), and thus, adopting the average number. The most significant discontinuities were found between blocks VT-06 and VT-09,

forming the main treatment region in the foundation structure.

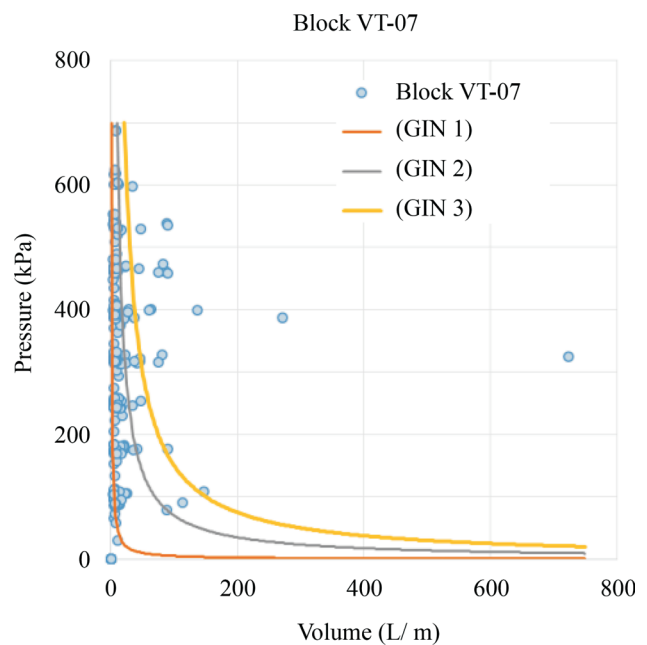
## 5.2. *GIN* curves elaborated by estimation

Figure 9 presents the *GIN* curves determined by estimation for the VT-02 and VT-08 blocks. In Fig. 9a, it is possible to verify that the maximum volumes reach 150 L/m, 7.5 times higher than the volumes obtained by back analysis (Fig. 7a).

For block VT-02, the *GIN* curves plotted in the dispersion graph have magnitudes of 2 MPa  $\times$  L/m (*GIN* 1), 18 MPa  $\times$  L/m (*GIN* 2) and 35 MPa  $\times$  L/m (*GIN* 3), pointing out that the higher intensity of grouting for VT-02 by back



**Figure 7** - *GIN* curves determined by back analysis: a) VT-02 Block; b) VT-06 Block.



**Figure 8** - *GIN* curves determined by back analysis for VT-07 Block.

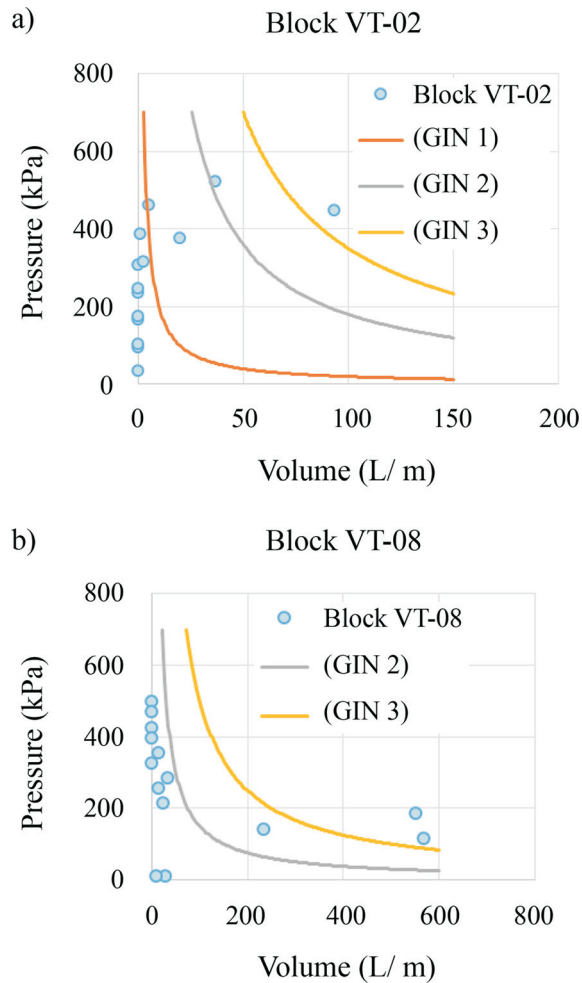


**Figure 9** - *GIN* curves determined by estimation: a) Block VT-02; b) Block VT-08.

analysis was  $2.5 \text{ MPa} \times \text{L/m}$ . In the case of the estimated results, this difference is due to the fact that discontinuities are not filled with grout and facilitate water seepage.

Figure 9b presents the curves of the VT-08 block, with maximum volumes up to  $600 \text{ L/m}$  like the VT-06 block (Fig. 7b). In this graph, one of the *GIN* curves was rejected due to the small dispersion of the plotted points, being very close to the axis. Two curves were then chosen, one with  $15 \text{ MPa} \times \text{L/m}$  (*GIN* 2) and the other with  $50 \text{ MPa} \times \text{L/m}$  (*GIN* 3). The intensities adopted for blocks VT-02 and VT-08 are expressed in Table 1, as well as for the other blocks of the spillway.

In Table 1, for the curves obtained by estimation, the highest intensity adopted in the foundation was in block VT-08 ( $50 \text{ MPa} \times \text{L/m}$ ), unlike the curves made by back analysis, where the largest *GIN* was applied in VT-07 ( $7 \text{ MPa} \times \text{L/m}$ ). VT-08 was the block that presented the largest number of discontinuities during the geological-geotechnical investigation and EPA tests, being these fractures identified by the highest water consumption. During the cement grouting activity, possible holes (LC and LJ)

were opened in greater quantity than in VT-07, which generated points in the dispersion graphs with smaller volumes, shifting the hyperbolic curves closer to the axes, and consequently reducing the product of the pressure with the volume.

### 5.3. Choice of *GIN* curve

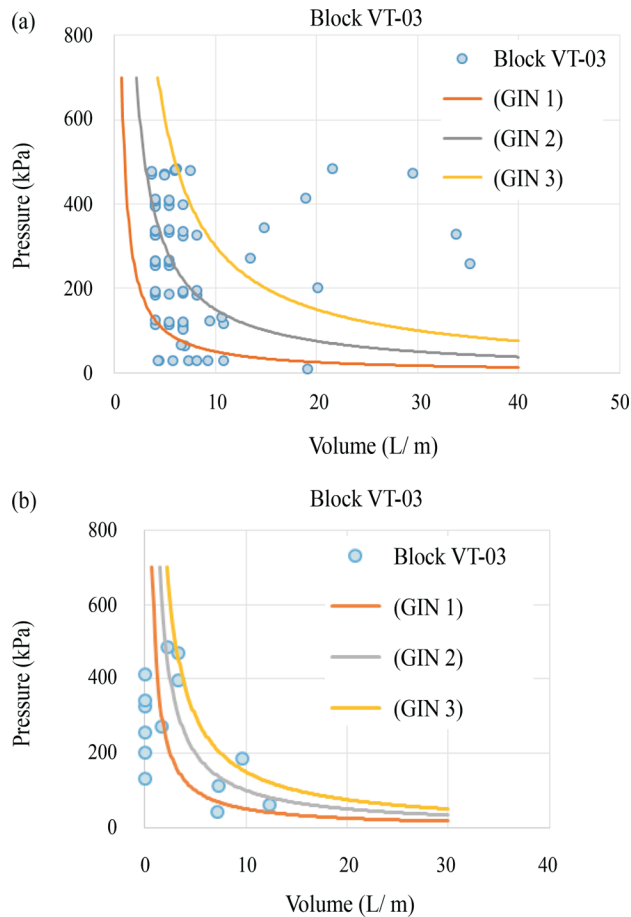
In each block studied, from the three plotted curves, the one that most closely approximated the graph scatter points was chosen. Comparing the *GIN* for the cases obtained by back analysis and estimation (Table 1), a great difference is observed in the results, motivated by what was explained in Section 5.2. However, for both analyses, the maximum pressure is the same and the maximum volumes are similar, but the pressure-volume *GIN* result reaches a difference of up to 16 times. The result of the *GIN* for this work is related not only to the limit numbers of the curves (pressure and volume), but also to the location of the hyperbolic curves adopted, so that they could interconnect the points of dispersion.

Figure 10 compares the curves generated by back analysis and estimation for the VT-03 block. It shows that the *GIN* curves by back analysis and estimation have the same magnitude, being the curve determined by retro analysis (Fig. 10a), the one with the highest intensity ( $1.5 \text{ MPa} \times \text{L/m}$ ) when compared to that by estimation (Fig. 10b), which resulted in an intensity of  $1 \text{ MPa} \times \text{L/m}$ .

As already mentioned, the curves are adequate for the dispersion points and therefore the intensity varies for each block, which can be seen in Fig. 10a where there are more pressure  $\times$  volume points based on grouting hole results. On the other hand, in Fig. 10b, since the number of primary holes with EPA tests in the block is lower, the points are more adjusted and located in the same region. Again, it is proved that for this research, the intensity of the curves depends on the dispersions and not only on the limits of pressure and volume.

According to the guide curves proposed by Lombardi & Deere (1993), for wider-aperture discontinuities, an intensity of more than  $250 \text{ MPa} \times \text{L/m}$  (or  $2,500 \text{ bar} \times \text{L/m}$ ) is used, while for the most tight discontinuities, intensities below  $50 \text{ MPa} \times \text{L/m}$  (or  $500 \text{ bar} \times \text{L/m}$ ) are employed. Comparing the curves that guide the results of this research (Table 1), it can be concluded that the intensities determined by the estimation method are close to those mentioned by Lombardi & Deere (1993), and it can be stated that the foundations of the Jirau Spillway have tight discontinuities (closed) and, therefore, the default would be the adoption of low *GIN* values.

However, it is worth mentioning that the method proposed by Lombardi & Deere (1993) was used in countries such as Argentina, Austria, Ecuador, Mexico, Turkey and Portugal, with different grouting processes from those adopted in Brazil, including aspects of permeability tests of



**Figure 10** - *GIN* curves determined for block VT-03: a) Back analysis; b) Estimation.

the rock mass, in which the EPA test is used in Brazil, and in other countries, Lugeon tests.

The impregnation and determination relationship of the standard curves are based on the results of Lugeon, where 1 Lu (Lugeon unit) is equivalent to a permeability coefficient of  $10^{-5}$  cm/s. The pressures adopted in Europe consider values greater than the American practices, and this is directly related to the local rock mass. Lombardi & Deere (1993) emphasize in their work that the *GIN* improves with the execution of the activity, whereby the intensity can be increased or decreased as the need arises. This makes the study of the application of the method in other countries renew the theoretical parameters, and each work performed provides a database for the following, giving greater reliability to the method.

At the Mascarenhas HPP, Oliveira *et al.* (2001) report that the intensity adopted in the project was  $100 \text{ MPa} \times \text{L/m}$ , with a maximum pressure of 2.2 MPa and a maximum volume of 150 L/m. The *GIN* number of this project corroborates those presented by Lombardi & Deere (1993), and distance themselves from those found in this research. In the case of Mascarenhas HPP, the pressure used is three times greater than the maximum pressure used in

the Jirau HPP, and in this case it is not possible to compare the two cases, where the quality of the rock mass is fundamental for this decision making.

Gama (2012) studied the application of the *GIN* in the Apartadura Dam, located near the city of Portalegre (Portugal). The author has established *GIN* curves by back-analyzing the grouting curtain cement consumption in the original design, which found intensity numbers between  $20.5 \text{ MPa} \times \text{L/m}$  and  $35.5 \text{ MPa} \times \text{L/m}$ , with maximum volume of  $350 \times \text{Lm}$  and maximum pressure of 600 kPa. The limits of the curves adopted by the author are similar to those found in this paper, but the final product distances itself from the results obtained through back analysis, due to the interpolation of the dispersion points.

Finally, the choice of the *GIN* curves was performed for the sake of safety, adopting the method of determination that presented smaller results, that is, the curves obtained by back analysis. As the *GIN* is adapted during the execution process, it is understood that at the beginning of the activity, the intensity is higher and as the grout fills the discontinuities, the need for larger numbers is considerably reduced. This decision was also based on the results of the analysis of the deep treatment performed in the Jirau HPP spillway and explained by Lopes & Assis (2016), which affirmed that the rock mass, even without grouting treatment, has fair hydraulic characteristics, with a permeability coefficient of  $10^{-4}$  cm/s in the region of higher water absorption (VT-06 to VT-09). Thus, since the foundation does not have discontinuities with large apertures and low hydraulic conductivity, there is no need to induce a high injection volume, or to add high pressure, which would result in plastic opening of the existing cracks or hydraulic fracturing.

#### 5.4. Dosage determination of theoretical grout

Tables 2, 3 and 4 present the water (*w*) and cement (*c*) consumption, also the volume of homogeneous grout (*w/c*), determined by Eq. 2.

Tables 2 and 3 show the water and cement requirements during the grouting of mandatory (LM) and occasional LC and LJ holes, and Table 4 is the unification of

**Table 2** - Results of grout cement quantities for each dosage original project.

| Holes      | $c_{0.7}$ (kg) | $c_{0.5}$ (kg) | $c_{\text{Total}}$ (kg) |
|------------|----------------|----------------|-------------------------|
| Mandatory  | 32,849.84      | 6,323.46       | 39,173.30               |
| Occasional | 28,704.34      | 3,105.54       | 31,809.88               |

**Table 3** - Results of the water volume for each dosage.

| Holes      | $w_{0.7}$ (L) | $w_{0.5}$ (L) | $w_{\text{Total}}$ (L) |
|------------|---------------|---------------|------------------------|
| Mandatory  | 32,849.84     | 6,323.46      | 39,173.30              |
| Occasional | 28,704.34     | 3,105.54      | 31,809.88              |

**Table 4** - Results of  $w/c$  relations of theoretical grout.

| Holes      | $w_{0.7} + w_{0.5}$ (L) | $c_{0.7} + c_{0.5}$ (kg) | $w/c$ |
|------------|-------------------------|--------------------------|-------|
| Mandatory  | 26,157                  | 39,173                   | 0.67  |
| Occasional | 21,646                  | 31,810                   | 0.68  |

consumption to determine a single and homogeneous grout as one of the main objectives of the *GIN* methodology. After homogenization, the dosages were similar for both hole types, considering in this case,  $w/c$  ratio of 0.68:1.

The main dosage used in the curtain of the original project of Jirau HPP was a  $w/c$  ratio of 0.7:1, (that represents 80 % of the cement consumption compared with the  $w/c$  ratio of 0.5:1), and the results found by homogenization corroborates this adoption. The prerogative of *GIN* is that, instead of thickening the grout, the process continues with the same water / cement ratio, changing only the magnitude of the pressure and the volume of grout injected. According to Brandão (2014), for the application of the *GIN* in projects, these should adopt stable grouts with higher cohesion values or thicker mixtures that approach the Binghamian behavior, as explained in Fig. 2. Therefore, the dosage used in the original design and that homogenized by Eq. 2 and detailed in Table 4 can be used in the application of the *GIN* method of injection.

## 6. Conclusions

The objective of this work was to evaluate the application of the *GIN* methodology in the Jirau HPP spillway foundation, through the data and results obtained during the construction of the project. The original foundation treatment project was executed according to the conventional methodology proposed by Houlsby (1990), with drilling of split-spacing holes and low pressures according to the American school. The choice of injection intensity numbers (*GIN*) was taken from the study of two situations: the first, by back analysis of the consumption of cement in the grouting holes (primary, secondary, tertiary and occasional); the second situation was the prediction of the intensity based on the results of EPA tests on interleaved primary holes (spacing of 24 m).

The evaluation of the two case studies showed that the *GIN* curves generated by estimation were closer to the literature results cited by Gama (2012), Oliveira *et al.* (2001), and the authors of the *GIN* methodology, Lombardi & Deere (1993). However, Lopes & Assis (2016) evaluated the foundation rock mass of Jirau HPP spillway and affirmed that it had good hydraulic characteristics, even before grouting treatment, indicating that the region does not present wide-aperture discontinuities and does not require high consumption of cement grout and pressures, and thus the curves generated by back analysis are more coherent for adoption.

Another important factor in the choice of *GIN* curves is that the differences in intensities when compared (back analysis *vs.* estimation) are very high, besides the amount of dispersion points adopted for the estimation method is small and does not represent an effective foundation. For this reason, conservatism was chosen, with intensities determined by retroactive analysis and below the standards proposed by Lombardi & Deere (1993).

In choosing the ideal dosage for the injection project, the cement mixtures used at Jirau HPP are within the stability criteria cited by Brandão (2014). Considering that 80 % of the holes were injected with  $w/c$  ratio of 0.7:1, in the application of the *GIN* methodology, it would not be necessary to thicken and change to the  $w/c$  ratio of 0.5:1, only change in the pressures and curve volumes.

It is further noted that the Lombardi & Deere *GIN* indication was determined for a water absorption ratio by Lu-geon tests, where 1 Lu equals a conductivity of  $10^5$  cm /s. The pressure used in injection in most of the projects cited by the authors adopts the European practice, with values higher than those indicated in Brazilian projects. Thus, the boundaries of the guide curves may not be representative of the Brazilian scenario, and the type of the rock masses may differ.

Therefore, it is suggested that the study of the application of the *GIN* methodology in Brazilian projects continue to advance, aiming to improve and elaborate the guide curves for each base material found, correlating them with the EPA results. And, as mentioned in the work of Carvalho *et al.* (2003), the *GIN* has technical and operational advantages to be implemented in Brazil, and its studies must be continued.

## Acknowledgments

To Energia Sustentável do Brasil (ESBR) and to Construções e Comércio Camargo Corrêa (CCCC) for the release of the project and execution data to this research.

## References

- Brandão, A.C.M. (2014). Tratamento de Fundações da Barragem do Escalão Principal do Baixo Sabor. Dissertação de Mestrado, Universidade do Porto, Porto, 110 p.
- Carvalho, E.; Filhote, F.P.T.; Leite, L.C.M.; Domingos, J.R.C.; D'Armada, J.C.R.; Freire Júnior, A.; Martorelli, E.A.; Souza, L.L.; Muniz, F.C.; Scarpin, S.E. & Iañes, J.M. (2003). Execução do vertedouro complementar da UHE Marechal Mascarenhas de Moraes. Proc. XXV Seminário Nacional de Grandes Barragens. Salvador, 9 p.
- Chiossi, N. (2013). Geologia de Engenharia. Oficina de Textos, São Paulo, 424 p.
- Comitê Brasileiro de Barragens (2011). A História das Barragens no Brasil - Séculos XIX, XX e XXI: Cinquenta Anos do Comitê Brasileiro de Barragens. Comitê Brasileiro de Barragens, Rio de Janeiro, 553 p.

- Costa, W.D. (2012). *Geologia de Barragens*. Oficina de Textos, São Paulo, 352 p.
- Cruz, P.T.; Manterón, B. & Freitas, M. (2009). *Concrete face rockfill dams*. Oficina de Textos, São Paulo, 360 p.
- Gama, P.S. (2012). *Injeção de Caldas de Cimento em Fundações Rochosas de Barragens: Revisão Crítica de Metodologias*. Dissertação de Mestrado, Universidade Nova de Lisboa, Lisboa, 200 p.
- Google Earth (2014). Disponível em <http://www.googleearth.com> Acesso em 02 de julho de 2014.
- Governo do Brasil (2018). *Matriz Energética*. Disponível em <http://www.brasil.gov.br/noticias/meio-ambiente/2010/11/matriz-energetica>. Acesso em 04/12/2018.
- Houlsby, A.C. (1990). *Construction and Design of Cement Grouting*. John Wiley & Sons, New York, 466 p.
- Levis, S.D. (2006). *Verificação da Eficácia dos Sistemas de Vedação e Drenagem em Fundações de Barragens de Concreto*. Dissertação de Mestrado, Universidade de São Paulo, São Carlos, 195 p.
- Lombardi, G. & Deere, D. (1993). *Diseño y control del inyectado empleando el principio "GIN"*. In: *Water Power and Dams Construction - Traduzido por Ulrich Hungsberg*. México, 35 p.
- Lombardi, G (1996). *Selecting the grouting intensity*. Proc. 4<sup>th</sup> International Water Power & Dam Construction, Carshalton, Hydropower & Dam International Journal, v. 3, pp. 62-66.
- Lopes, M.B. & Assis, A.P. (2016). *Análise da eficiência do sistema de vedação da fundação em granito de uma barragem de concreto*. Proc. Simpósio Brasileiro de Mecânica das Rochas, Belo Horizonte, CBMR, 8 p.
- Oliveira, F.F. (2002). *Análise de Tensões e Estabilidade Global de Barragens de Concreto Gravidade*. Dissertação de Mestrado, Universidade de Brasília, Brasília, 183 p.
- Oliveira, D.V.; Calixto, R.J. & Moraes, R.B. (2001). *Injeção de cimento com monitoramento em tempo real*. Proc. 24<sup>th</sup> Seminário Nacional de Grandes Barragens, Fortaleza, ABMS, pp. 257-270.
- Oliveira, A.M.S.; Silva, R.F. & Júnior, J.F. (1975). *Ensaio de Perda D'água sob Pressão: Diretrizes*. Boletim ABGE 02. ABGE/IPT, São Paulo, 16 p.
- Warner, J. (2004). *Practical Handbook of Grouting: Soil, Rock and Structures*. John Wiley & Sons, New Jersey, 720 p.

# A Laboratory Study of the Collapse Behaviour of a Compacted Sabkha Soil

O.Y. Debbab, B. Moussai, A. Messad

**Abstract.** Sabkha soils are saline sediments, which can withstand high loads in dry conditions, but upon wetting, they exhibit significant deformation and low shear strength and hence pose great challenge to engineers. This paper investigates the collapsibility of a compacted sabkha soil of Chott El-Hodna (Algeria) using a modified oedometer, which allows water to percolate through the soil sample. The collapsibility tests were conducted on samples compacted at a variety of values of fluid contents and relative compactations using sabkha brine. The standard Proctor tests were performed using distilled water and sabkha brine, and the compaction characteristics were determined using conventional water content and fluid content methods. The results indicate that the conventional water content procedure used to plot the compaction curve overestimates the maximum dry unit weight and underestimates the optimum moisture content. The degree of collapsibility varies from moderate to severe depending on the compaction conditions (*i.e.* relative compaction, initial fluid content, degree of saturation). The collapse potential increases with increasing applied load and compaction fluid content and with decreasing relative compaction. Moreover, it has been demonstrated that the use of a conventional oedometer underestimates the collapse potential of saline soils.

**Keywords:** collapse potential, fluid content, Sabkha soil, saline soils, water content.

## 1. Introduction

With recent economic development in Algeria, extensive infrastructure projects (highways, roads, railways, etc.) are planned to be constructed over areas covered with sabkha soils. However, many infrastructures built through sabkha areas are suffering from severe damage caused by the presence of salts in the soil, including cracks and differential settlements. Severe damage to buildings and roads constructed on sabkha soils in Libya and Saudi Arabia were reported by Khan & Hasnain (1981) and Amin (2004). Moayed *et al.* (2010) reported several deteriorations of recently built roads (raveling, cracking, rutting and formation of landslides) in the region of Taleghan (Iran).

Compacted fills of saline soils employed in the construction of roadways, railways, earthen dams, etc. may experience water penetration after inundation and therefore exhibit problematic collapse potential, which can cause considerable damage to the structure. Therefore, predicting the collapse potential of this type of soils is important for the design of engineering structures.

Al-Amoudi & Abduljawad (1995) performed collapse potential tests on surficial undisturbed sabkha soil of Saudi Arabia and concluded that the collapse is mainly related to the dissolution of salts and it does not occur instantaneously as in loessial soils for example, but requires continuous percolation of water to enhance the dissolution of the cementing agent.

Messad & Moussai (2016b) studied the collapse behaviour of a saline marly soil using conventional and modified oedometers, and concluded that the collapse potential of this type of soils can be obtained only by percolation of water through the soil sample.

Moreover, Mansour *et al.* (2008) performed standard Proctor tests on marly soil from the Dead sea area and reported that the optimum water content decreases and the maximum unit weight increases as the water salinity increases. Similar results were found by Alainachi & Alabdai (2010) & Shariatmadari *et al.* (2011). In these studies, the compaction curve was plotted based on the conventional water content definition, which does not take the presence of salts in the soil into consideration.

The objective of this study is to investigate the collapse behaviour of a compacted sabkha soil of Chott El-Hodna (Algeria) using a modified oedometer that allows water to percolate through the soil sample. To achieve this, an extensive experimental program was conducted, which included particle size distribution, specific gravity, compaction and collapsibility tests. The effect of water salinity on the compaction characteristics of sabkha soil was also highlighted.

## 2. Materials and Their Characteristics

The material used in this study is silty sand collected from the sabkha of Chott El Hodna (Fig. 1). Disturbed samples were retrieved from test pits dug in the sabkha area.

---

O.Y. Debbab, Ph.D. Student, University of Science and Technology Houari Boumediene, Algiers, Algeria.  
B. Moussai, Professor, University of Science and Technology Houari Boumediene, Algiers, Algeria. e-mail: bmoussai@yahoo.ca.  
A. Messad, Lecturer, Yahia Fares University, Media, Algeria.  
Submitted on April 4, 2019; Final Acceptance on March 24, 2020; Discussion open until September 30, 2020.  
DOI: 10.28927/SR.432181



Figure 1 - Chott El Hodna area.

The depth of the test pits was about 0.6 m from the ground surface.

The sabkha brine contained approximately 26 % (by weight of brine) dissolved salts, and its specific gravity was 1.22. The chemical analysis of sabkha brine is given in Table 1.

The particle size distribution shown in Fig. 2 indicates that the sabkha soil is composed of 82 % sand and 18 % fines (silt and clay). This soil is classified as SM according to the Unified Soil Classification System (USCS). Its specific gravity is 2.7. The X-ray diffraction analysis indicated that the soil is mainly composed of quartz and calcite (Fig. 3).

Specific gravity and particle size distribution were performed based on the procedures outlined in ASTM D854-05 (2005) and ASTM D422-63 (2007), respectively.

The moisture content of sabkha soil is determined based on the fluid content ( $\omega_f$ ) definition, which is the ratio between the brine weight and the dry weight of soil solids (Messad & Moussai, 2016a). This definition takes into consideration the presence of salt and is given by the following relationship:

$$\omega_f = \frac{W_b}{W_s} = \frac{W - W_d}{W_d - rW} = \frac{\omega_c}{1 - r - r\omega_c} \quad (1)$$

with  $r = \frac{w_{sa}}{w_b}$  = salinity,  $W_b$  the weight of brine,  $W_{sa}$  the weight of salt,  $W$  the wet weight of soil (including salt),  $W_d$  the dry weight of soil (including salt),  $W_w = W - W_d$  the weight of distilled (fresh) water,  $W_s$  the weight of soil solids (excluding salt) =  $W - W_b = \frac{W_d - rW}{1 - r}$  and  $\omega_c$  the conventional water content =  $\frac{W - W_d}{W_d}$ .

### 3. Compaction

Standard Proctor tests were conducted on the sabkha soil to evaluate the effect of water salinity on the compaction characteristics (optimum moisture content and maximum dry unit weight). The Standard Proctor tests were performed based on the procedure outlined in ASTM D698 (2007) on washed soil samples passing No. 4 sieve using distilled water and sabkha brine.

The compaction characteristics were determined using conventional water content and fluid content methods (Table 2 and Fig. 4).

Table 1 - Chemical analysis of sabkha brine (Messad & Moussai, 2016a).

| pH  | K <sup>+</sup> (g/L) | Ca <sup>2+</sup> (g/L) | Mg <sup>2+</sup> (g/L) | Na <sup>+</sup> (g/L) | Cl <sup>-</sup> (g/L) |
|-----|----------------------|------------------------|------------------------|-----------------------|-----------------------|
| 7.2 | 19.05                | 25.92                  | 15.55                  | 94.59                 | 208.49                |

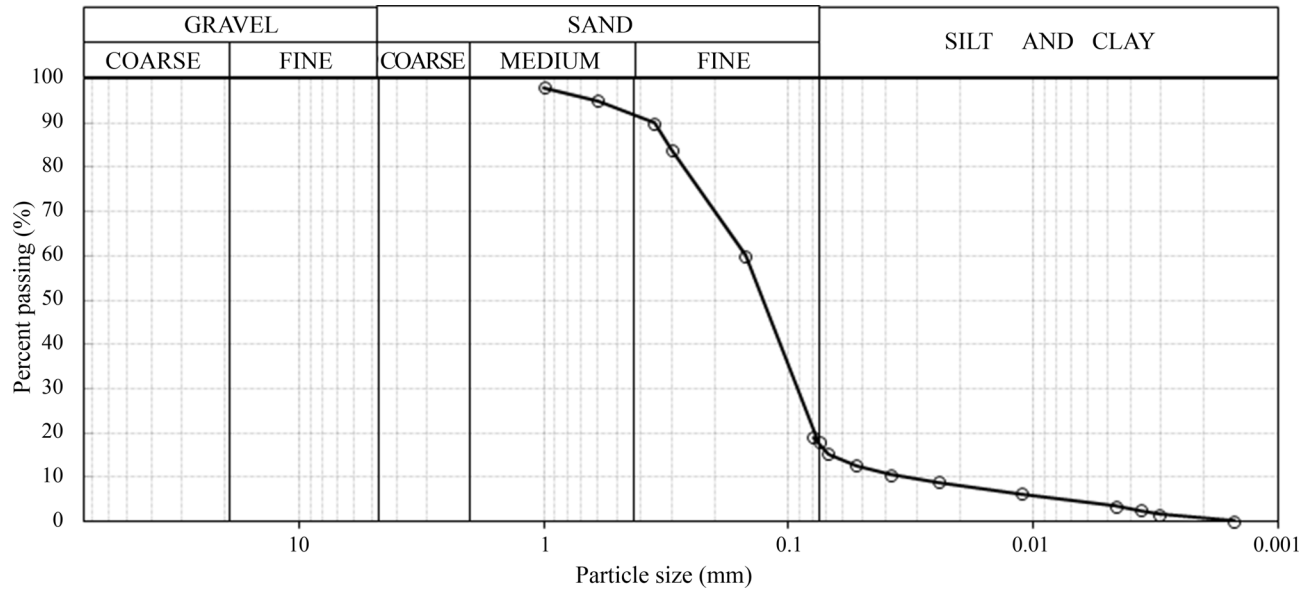


Figure 2 - Particle size distribution of the sabkha soil.

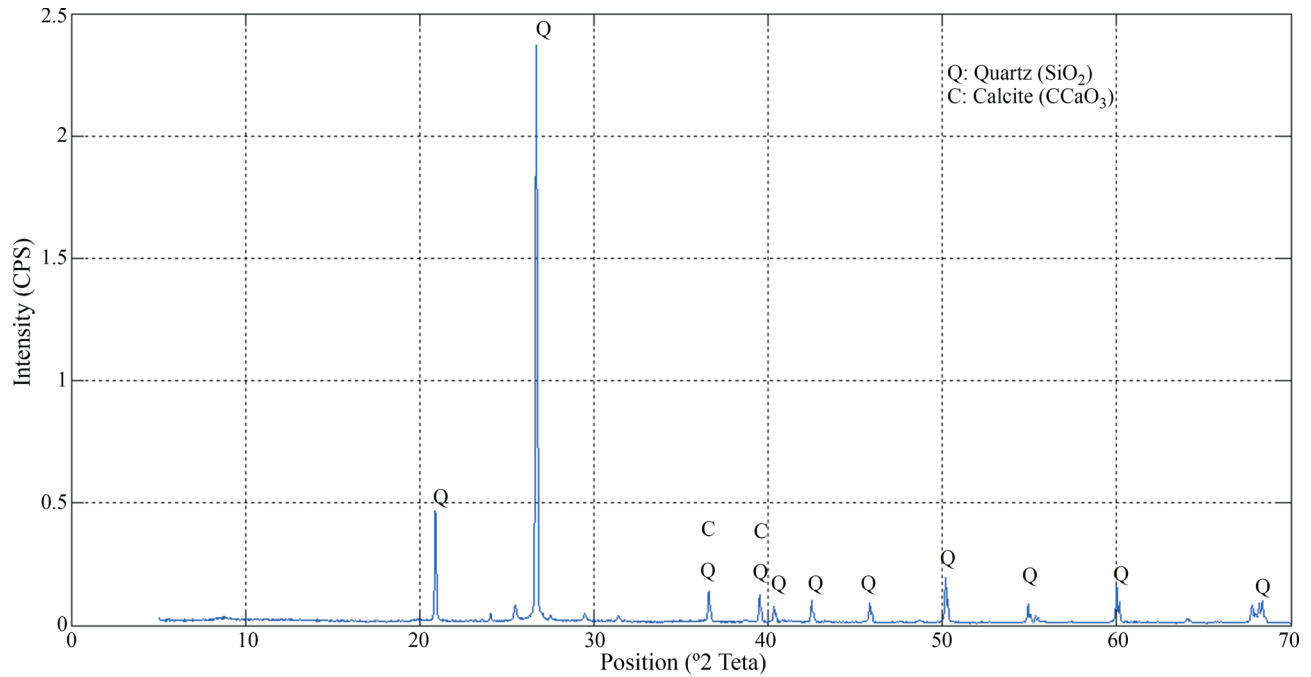


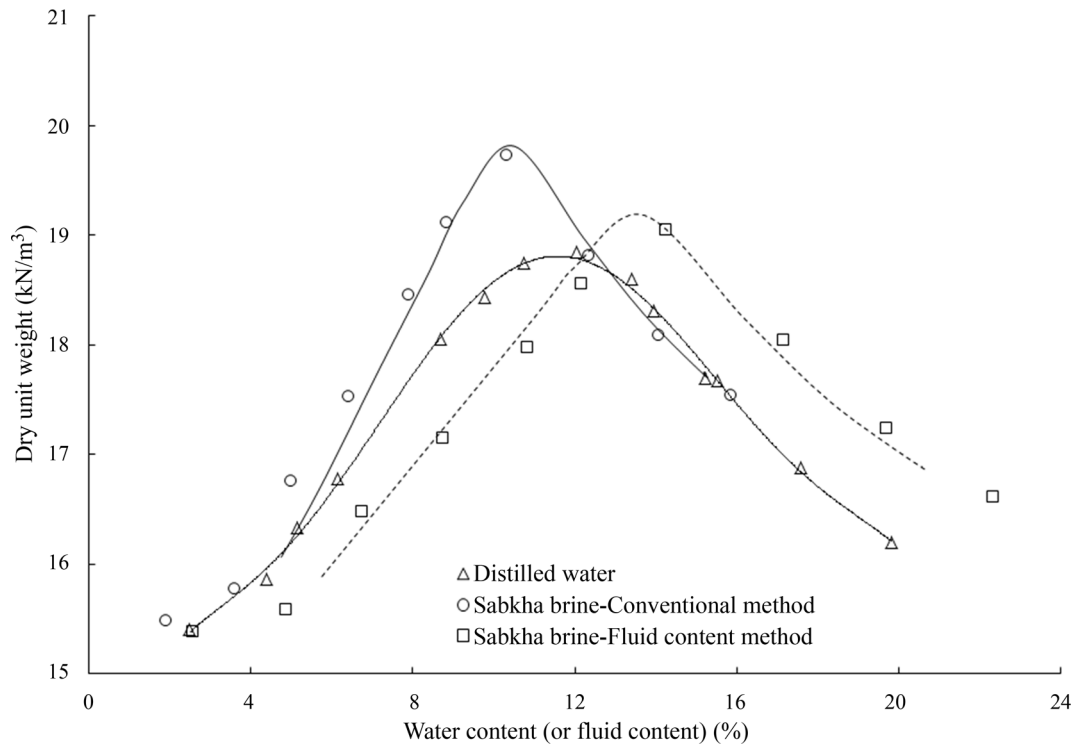
Figure 3 - X-ray diffraction of the sabkha soil.

Table 2 - Compaction test results.

| Type of fluid   | Conventional water content procedure  |                      | Fluid content method                  |                      |
|-----------------|---------------------------------------|----------------------|---------------------------------------|----------------------|
|                 | $\gamma_{d-max}$ (kN/m <sup>3</sup> ) | $\omega_{c-opt}$ (%) | $\gamma_{d-max}$ (kN/m <sup>3</sup> ) | $\omega_{f-opt}$ (%) |
| Distilled water | 18.8                                  | 11.6                 | -                                     | -                    |
| Sabkha brine    | 19.7                                  | 10.3                 | 19.1                                  | 14                   |

It can be seen that for the soil compacted using sabkha water content procedure. However, the optimum moisture content obtained from fluid content procedure is higher than that obtained from conventional water content procedure.

water content procedure. However, the optimum moisture content obtained from fluid content procedure is higher than that obtained from conventional water content procedure.



**Figure 4** - Compaction test curves.

When the conventional water content procedure is used to plot the compaction curve, the maximum dry unit weight increases by about 5 % and the optimum moisture content decreases by about 11 % compared to those obtained using distilled water. These results are in accordance with those reported by Mansour *et al.* (2008).

However, when the fluid content method is used to plot the compaction curve, the maximum dry unit weight decreased by about 3 % and the optimum moisture content increased by about 36 %, compared to those obtained using the conventional water content procedure.

#### 4. Collapse Potential Measurement

The conventional oedometer cannot be used to detect the collapse potential of saline soils, which requires continuous percolation of water to dissolve the salty-cemented matrix. Thus, the fixed-ring oedometer of 70 mm internal diameter and 20 mm height was modified in such a way that it could function as a constant-head permeameter. This is accomplished by making a hole in the side of the metal cylinder to serve as an outlet for the percolating water in order to keep the water head constant as shown in Fig. 5. The existing hole in the bottom of the consolidation cell is used as water inlet. Therefore, the water can flow from the bottom to the top of the sample.

To ensure a constant head, the water level in tank 1 is regulated by a water supply from tank 2 and the excess water in tank 1 is drained as shown in Fig. 5. The volume of water in tank 2 was always kept more than the seeping wa-

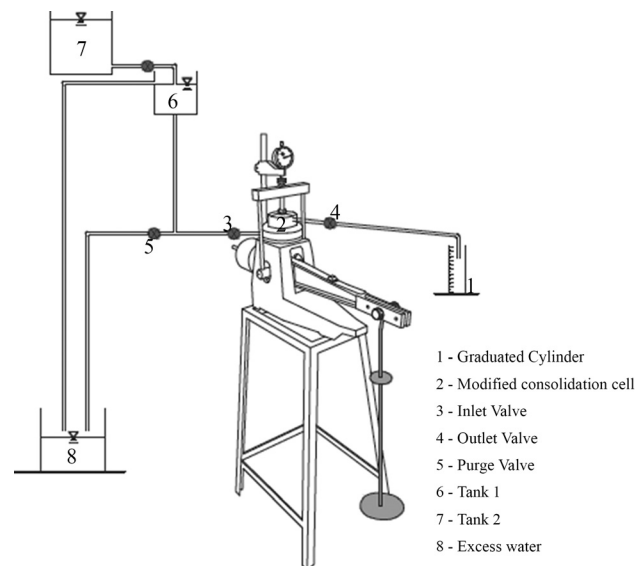


**Figure 5** - Modified oedometer (Messad & Moussai, 2016b).

ter through the sample. The hydraulic gradient used is 20 (Messad & Moussai, 2016b).

The collapsibility tests were conducted using single oedometer method on specimens compacted in the oedometer ring, 70 mm in diameter and 20 mm thick. The specimens were prepared at different values of relative compaction and fluid content using as reference the unit weight and fluid content obtained at the optimum of Standard Proctor test (Fig. 6).

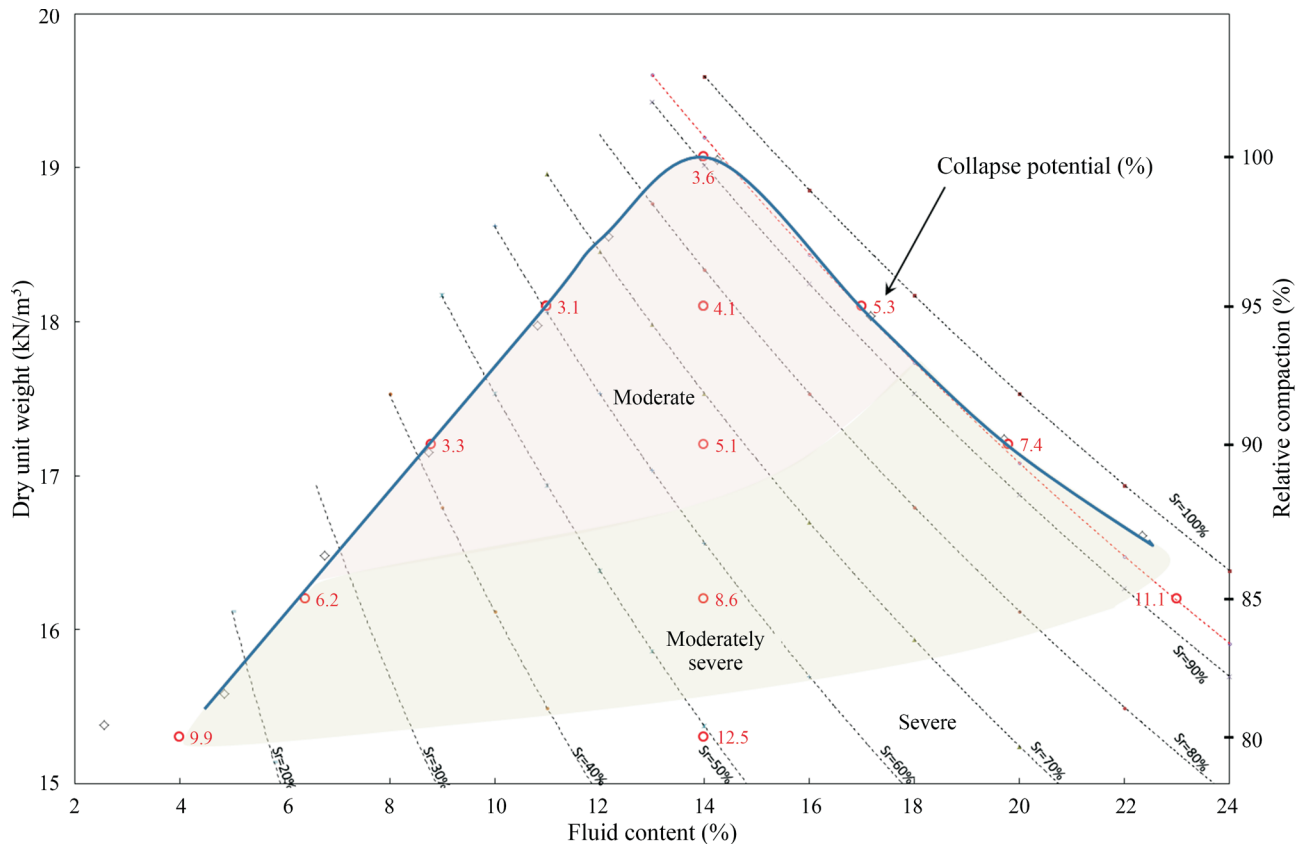


Figure 6 - Contours of equal collapse potential on  $\gamma_d - \omega$  plane measured at 200 kPa.

It should be noted that sabkha soils in the field are subjected to repeated drying and wetting cycles due to climate conditions in the sabkha area, hence the oedometer ring containing the compacted soil specimen was oven dried prior to testing. Then the collapsibility tests were performed using the modified oedometer (Fig. 5). The sample was first subjected to a seating stress of 5 kPa followed by incremental loads up to the desired sustained pressure (e.g. 200 kPa). Then, the oedometer cell containing the soil specimen was filled with distilled water from the bottom up using small hydraulic head (0.2 m) to prevent the trapping of air in the specimen. The inlet valve was closed after oedometer cell filling and the deformation of the specimen was recorded with respect to time until equilibrium. This phase allows measuring the specimen collapse potential before the leaching process.

When the sample ceased to undergo further deformation, the inlet valve was opened and the fluid was allowed to percolate through the specimen until the salinity of the seeping fluid became negligible (0.1 %). This phase allows measuring the specimen collapse potential after leaching under the sustained pressure.

Thereafter, the inlet valve was closed, while keeping the oedometer cell filled with water and the applied load was increased incrementally until the end of the loading process in the same manner as the standard consolidation

test. The load increments used were: 12.5, 25, 50, 100, 200, 400, 800 and 1600 kPa. Each load was maintained until the sample deformation reached equilibrium. The unloading of the sample was proceeded after the completion of the loading process.

Several oedometer tests were conducted on samples compacted over a range of fluid contents ( $\omega_{f-opt} - 10$  to  $\omega_{f-opt} + 9$ ) and relative compactions ( $RC = \gamma_d/\gamma_{d-max} = 80$  to 100 %). The samples were leached with distilled water under an applied pressure of 200 kPa, which is used to define the collapse index ( $I_c$ ) according to ASTM D 5333 (Table 3). Three farther tests were performed on samples compacted at the optimum of Proctor and leached under sustained pressures of 50 kPa, 100 kPa and 200 kPa to investigate the effect of the stress level on the collapse potential of the saline soil.

Table 3 - Classification of Collapse Index,  $I_c$ .

| Degree of collapse | Collapse index (%) |
|--------------------|--------------------|
| None               | 0                  |
| Slight             | 0.1 to 2.0         |
| Moderate           | 2.1 to 6.0         |
| Moderately severe  | 6.1 to 10.0        |
| Severe             | > 10               |

The collapse potential is determined using the relationship given by ASTM D 5333:

$$I_c = \frac{\Delta e}{1 + e_0} \times 100 \quad (2)$$

where:  $\Delta e$  is the reduction in void ratio due to wetting, and  $e_0$  is the initial void ratio. The collapse index ( $I_c$ ) is the collapse potential determined at 200 kPa.

### 4.1. Results and discussion

Figure 6 presents the collapse potential values and contours of equal collapse potential plotted on the  $\omega_f - \gamma_d$  plane for all tested specimens along with the Standard Proctor compaction curve obtained using the fluid content method. The compression curves obtained using the modified oedometer at different fluid contents and dry unit weights are shown in Fig. 7.

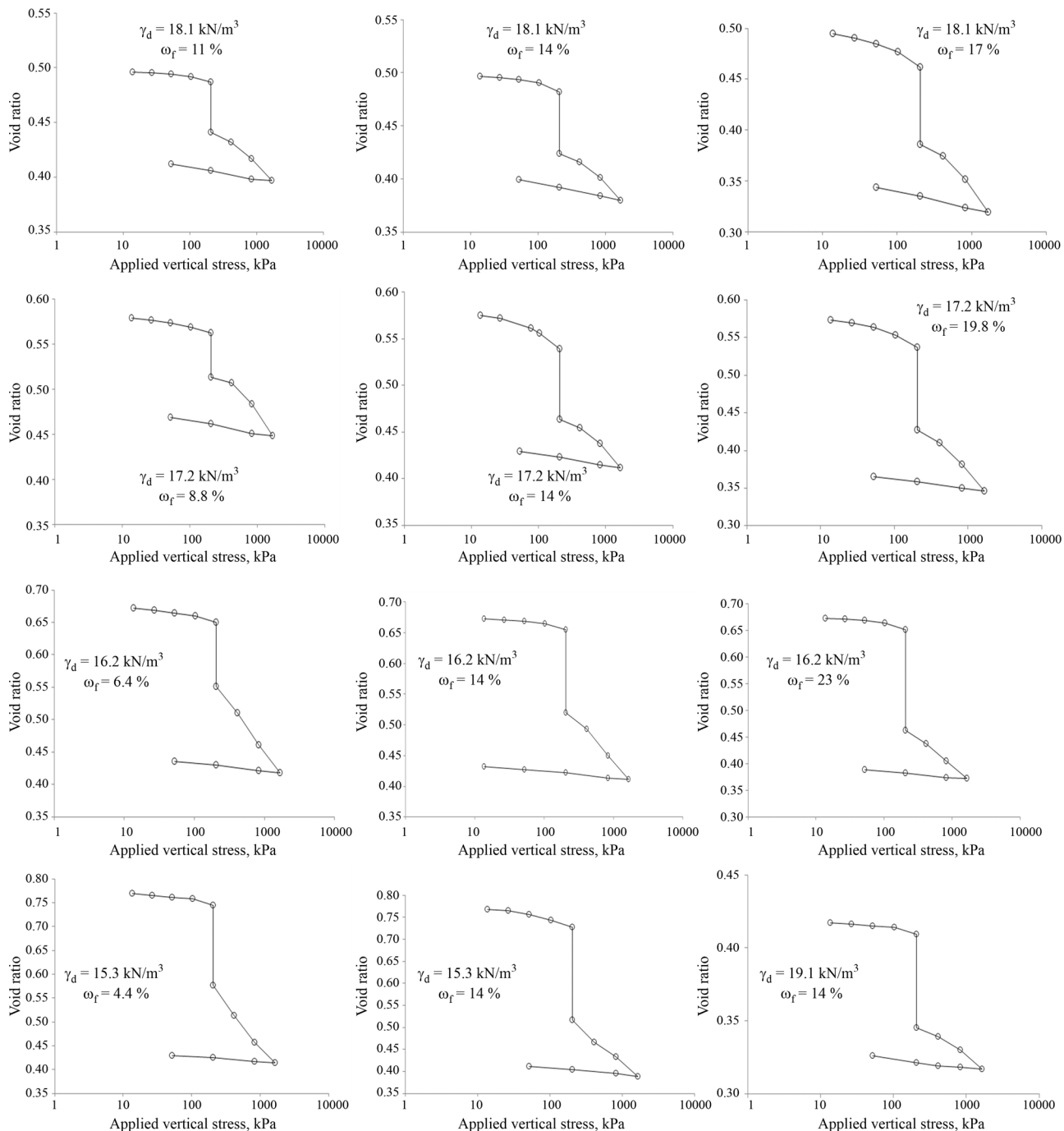


Figure 7 - Void ratio vs. applied stress curves from modified oedometer tests.

Based on these results, the following remarks can be drawn:

- The Proctor compaction curve indicates that the optimum fluid content is 14 % and the maximum dry unit weight is 19.1 kN/m<sup>3</sup>.
- Three regions of collapse potential are identified: moderate, moderately severe and severe according to ASTM (2003) (Table 3).
- The collapse potential values vary from 3.1 % (moderate degree of collapsibility) to 12.5 % (severe degree of collapsibility) depending on the compaction conditions (*i.e.* relative compaction, initial fluid content, degree of saturation).
- The soil is more collapsible on the wet side than on the dry side of optimum. This may be due to the increase of the amount of salt in the pores of soil compacted on the wet side of optimum.
- For specimens having similar initial degree of saturation of about 93 % (*i.e.* along the wet side of the compaction

curve), the collapse potential increases as the relative compaction decreases. Note that the degree of saturation is determined based on the fluid content method.

- For specimens compacted at the Standard Proctor energy, the collapse potential decreases as the relative compaction increases until a minimum value of 3.1 % corresponding to a relative compaction of 95 % and a fluid content of 11.0 % ( $\omega_{f-opt} - 3 \%$ ), beyond which it increases (Fig. 8).
- For specimens having similar fluid content of compaction, the collapse potential increases as the relative compaction decreases (Fig. 9). This result agrees well with that reported by many authors for loessial soils such as Lawton *et al.* (1989) and Lawton *et al.* (1992).
- For specimens compacted at the same relative compaction, the collapse potential increases as the fluid content increases (Fig. 10), which is contrary to the case of loessial soil flooded with distilled water where the collapse potential decreases as the water content of compac-

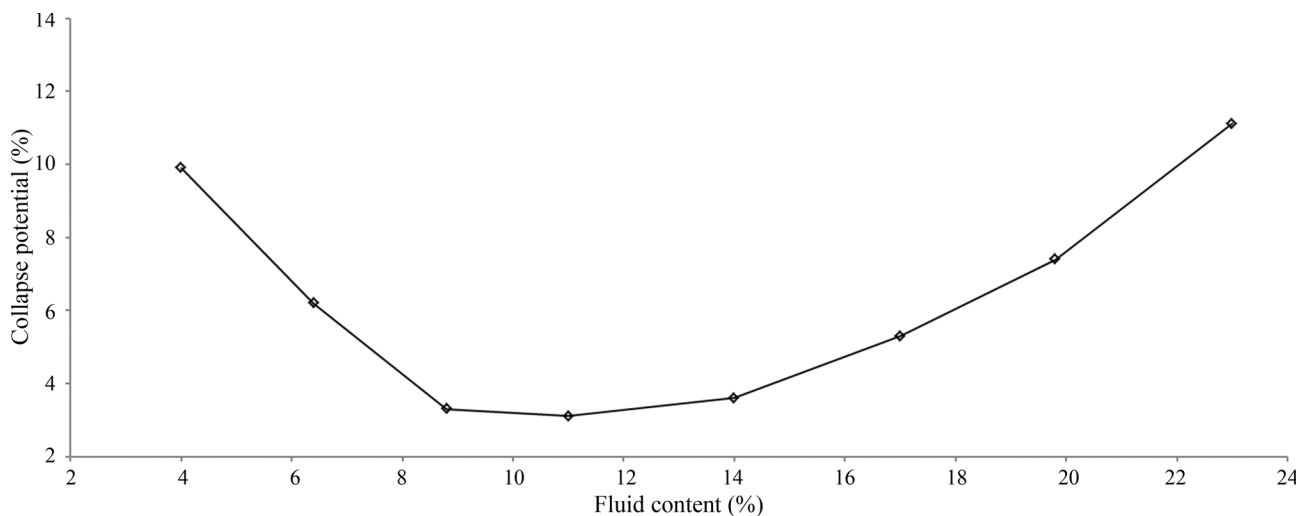


Figure 8 - Collapse potential vs. as compacted fluid content along the compaction curve.

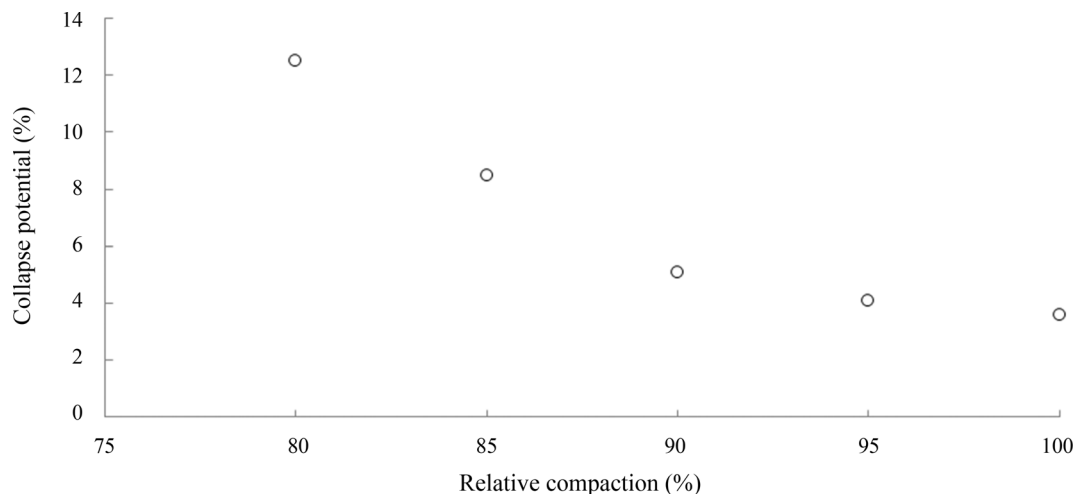
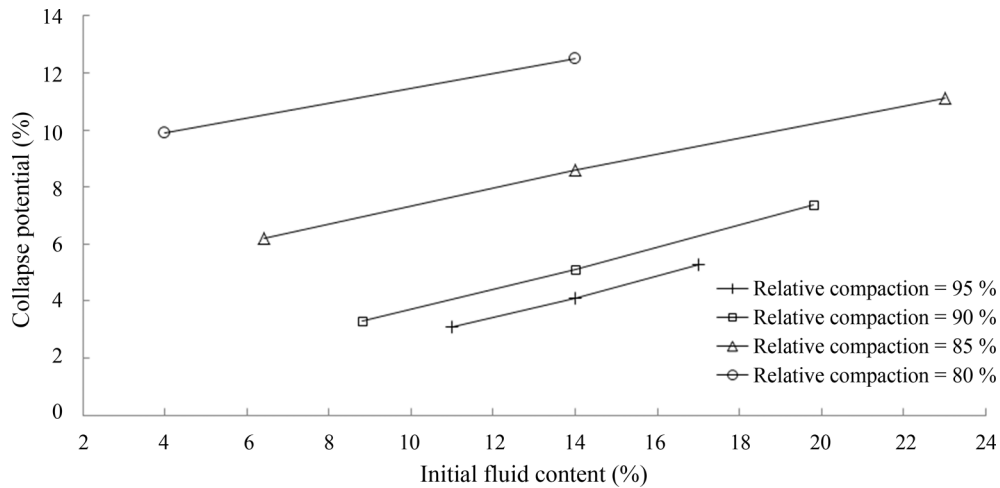


Figure 9 - Collapse potential vs. relative compaction for the fluid content of 14 %.



**Figure 10** - Collapse potential vs. initial fluid content at different relative compactions.

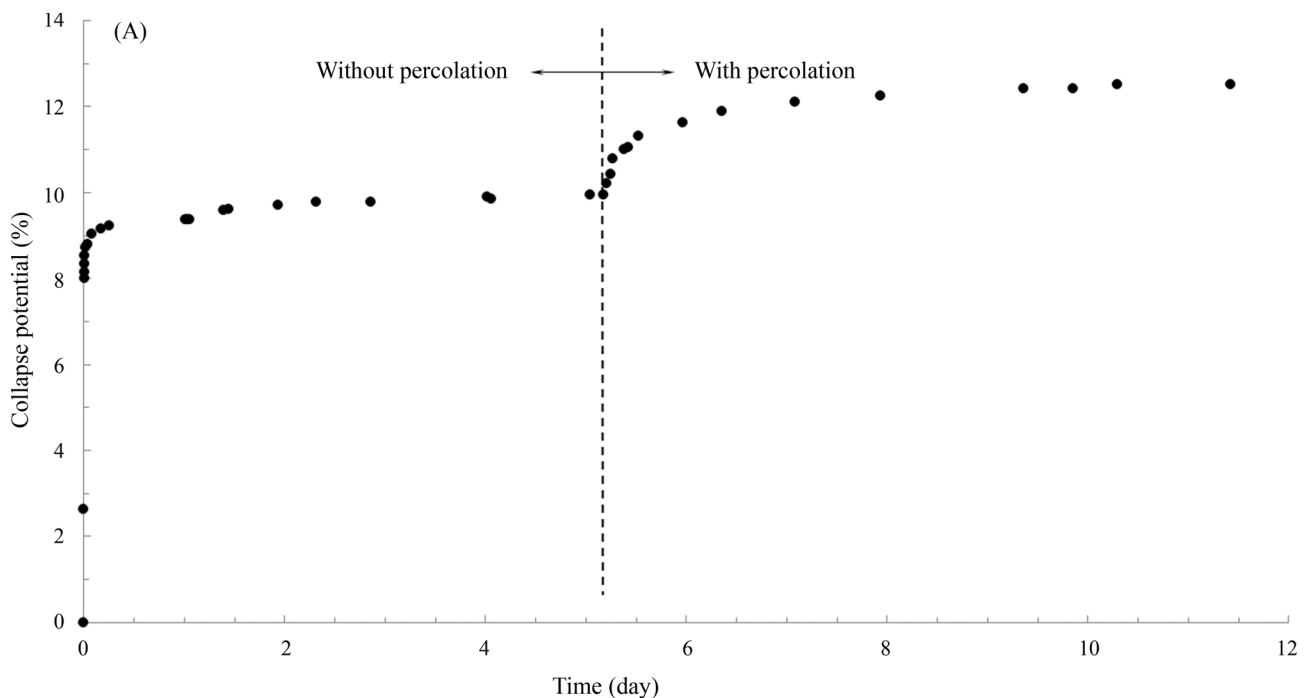
tion increases (Lawton *et al.*, 1989). This can be attributed to the increase of the amount of salt in the specimen with increasing fluid content of compaction, which leads to the increase of collapsibility after wetting and leaching process.

Figure 11a presents an example of the collapse potential vs. the time of flooding indicating the amounts of collapse potential caused by flooding with and without percolation of fluid through the soil specimen, and Fig. 11b presents the collapse potential vs. the time of flooding for all tested specimens.

It can be seen that the collapse potential reaches equilibrium after about 1 to 4 days of flooding without percola-

tion and after about 7 to 18 days of flooding with percolation depending on the compaction conditions (*i.e.* relative compaction, initial fluid content). The results indicate that the flooding without percolation detects only partial collapse potential for saline soils and the total collapse potential can be obtained only by percolation. The amount of collapse potential due to percolation was found to be about 10 to 30 % of the total collapse potential.

In order to evaluate the effect of the sustained pressure on the collapse potential, the soil compacted at optimum fluid content and maximum dry unit weight was tested for three sustained pressures: 50 kPa, 100 kPa and 200 kPa. The results indicate that the collapse potential in-



**Figure 11 - a:** Collapse potential vs. time of flooding for the specimen having:  $\gamma_d = 15.3 \text{ kN/m}^3$  and  $\omega_f = 14 \%$ .

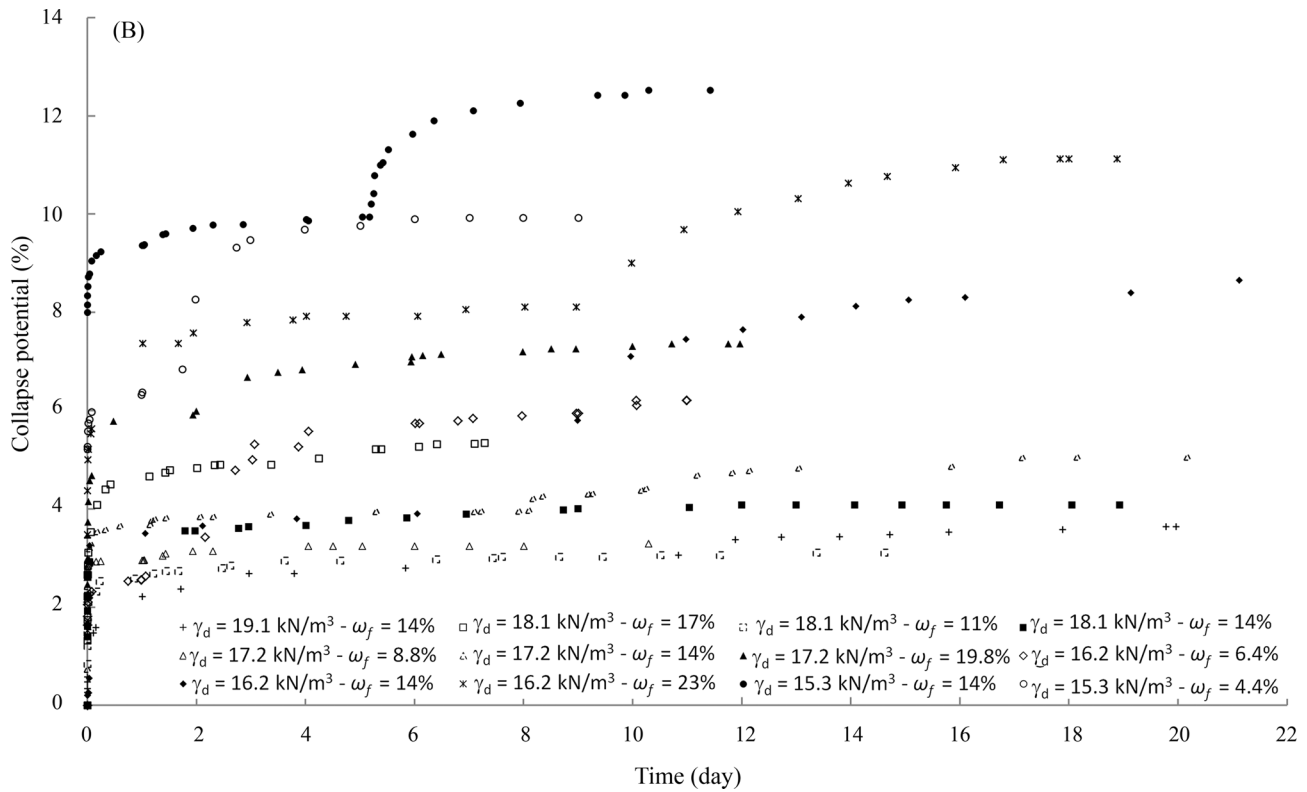


Figure 11 - b: Collapse potential vs. time of flooding for soil specimens of varying unit weight ( $\gamma_d$ ) and fluid content ( $\omega_f$ ).

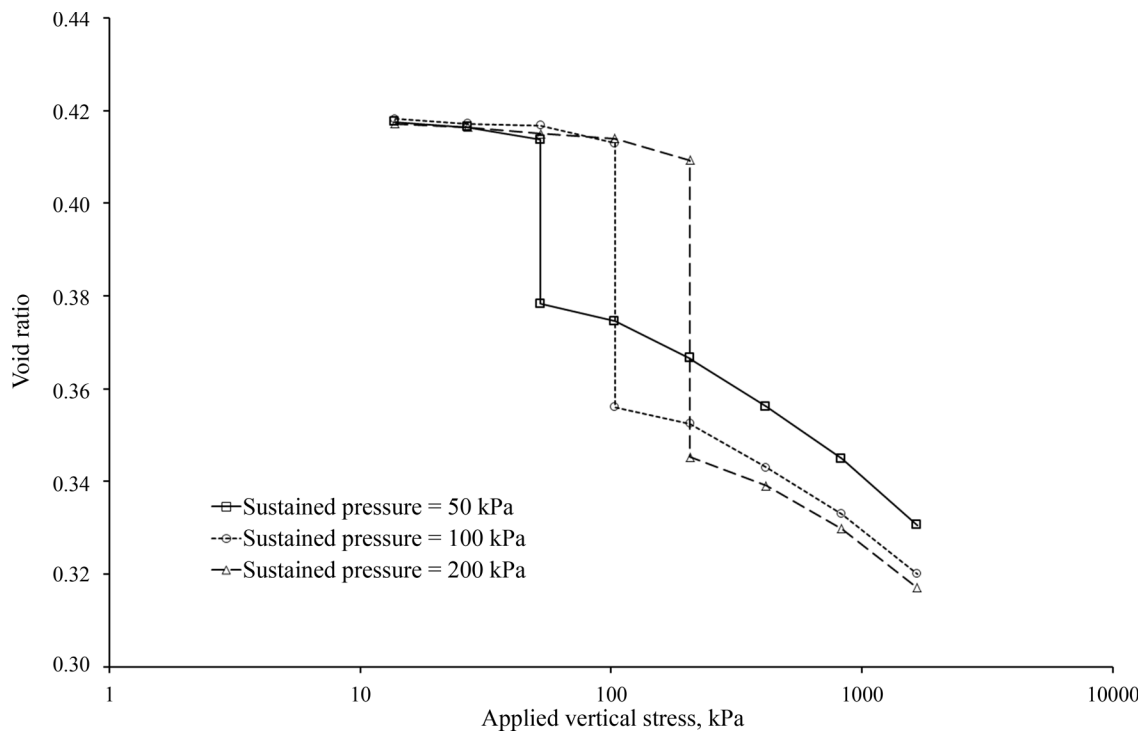


Figure 12 - Void ratio vs. applied stress curves for different sustained pressures.

creases with increasing sustained pressure (Fig. 12), which are consistent with those published in the literature for loessial soils (e.g. Lawton *et al.*, 1989) and for sabkha soils in Saudi Arabia (Al-Amoudi & Abduljawad, 1995).

Moreover, the collapse potential is likely to be significant even for relatively small values of the applied load, which implies that the collapse may be a concern even for lower embankment heights.

## 5. Conclusions

The results of compaction tests indicate the significant effect of water salinity on the compaction characteristics of the sabkha soil. The use of conventional water content procedure to plot the compaction curve overestimates the maximum dry unit weight and underestimates the optimum moisture content. Moreover, the maximum dry unit weight is less affected by the type of fluid and method used to determine the compaction curve compared to the optimum moisture content.

Therefore, for the case of saline soils, it seems more logical to use the fluid content method to determine the compaction characteristics than the conventional water content procedure.

The results of collapsibility tests indicate the ability of the modified oedometer to detect the collapse potential of saline soils. The salt plays the role of cementing agent in dry condition and may dissolve upon wetting and percolation by distilled water causing collapse. This implies that the conventional oedometer cannot be used to assess the collapse potential of saline soils.

The collapsible potential on the wet side is greater than that on the dry side of optimum and the minimum value of collapsibility of the studied soil was found on the dry side of optimum at a relative compaction of about 95 %. Therefore, when a saline soil is intended to be used as a fill or embankment, it is recommended to compact the soil on the dry side of the optimum in order to reduce the risk of collapse after inundation.

The amount of collapse potential seems to depend on relative compaction, fluid content, degree of saturation and applied load. Higher collapse potential is observed in the specimens with higher fluid content and degree of saturation and lower relative compaction. In addition, collapse potential increases with increasing applied load.

The results presented here should be confirmed by further studies on different types of saline soils.

## References

- Al-Amoudi, O.S.B. & Abduljauwad, S.N. (1995). Compressibility and collapse characteristics of arid saline sabkha soils. *Engineering Geology*, 39(3-4):185-202. [https://doi.org/10.1016/0013-7952\(95\)00016-9](https://doi.org/10.1016/0013-7952(95)00016-9)
- Alainachi, I.H. & Alobaidy, G.A. (2010). The effects of Basra gulf salt water on the proctor compaction and CBR test results of soil samples at Baniyas City, Abu Dhabi, UAE. *Electronic Journal of Geotechnical Engineering (EJGE)*, 15(A):1-14. <http://www.ejge.com/2010/Ppr10.001.pdf>
- Amin, A. (2004). Comparative study of the geotechnical properties of the coastal Sabkhas of Saudi Arabia and their hazardous effects. *Bull Eng Geol Env.*, 63:309-314. <https://doi.org/10.1007/s10064-004-0254-5>
- ASTM (2003). Standard Test Methods for Measurement of Collapse Potential of Soils- D-5333. Annual Book of ASTM Standards. <https://doi.org/10.1520/D5333-03>
- ASTM (2005). Standard Test Methods for Specific Gravity of Soil Solids by Water Pycnometer- D854-05. Annual Book of ASTM Standards. <https://doi.org/10.1520/D0854-05>
- ASTM (2007). Standard Test Methods for Particle-Size Analysis of Soils - D422-63. Annual Book of ASTM Standards. <https://doi.org/10.1520/D0422-63R07E02>
- ASTM (2007). Standard Test Methods for Laboratory Compaction Characteristics of Soil Using Standard Effort (12 400 ft-lbf/ft<sup>3</sup> (600 kN-m/m<sup>3</sup>) - D-698. Annual Book of ASTM Standards. <https://doi.org/10.1520/D0698-12E02>
- Khan, M.Y. & Hasnain, S.I. (1981). Engineering properties of sabkha soils in the Bengazi plain and construction problems. *Engineering Geology*, 17:175-183. [https://doi.org/10.1016/0013-7952\(81\)90082-X](https://doi.org/10.1016/0013-7952(81)90082-X)
- Lawton, E.C.; Fragaszy, R.J. & Hardcastle, J.H. (1989). Collapse of compacted clayey sand. *Journal of Geotechnical Engineering*, 9:1252-1267. [https://doi.org/10.1061/\(ASCE\)0733-9410\(1989\)115:9\(1252\)](https://doi.org/10.1061/(ASCE)0733-9410(1989)115:9(1252))
- Lawton, E.C.; Fragaszy, R.J. & Hetherington, M.D. (1992). Review of wetting induced collapse in compacted soils. *Journal of Geotechnical Engineering*, 118(9):1376-1392. [https://doi.org/10.1061/\(ASCE\)0733-9410\(1992\)118:9\(1376\)](https://doi.org/10.1061/(ASCE)0733-9410(1992)118:9(1376))
- Mansour, Z.M.; Taha, M.R. & Chik, Z. (2008). Fresh-brine water effect on the basic engineering properties of Lisan Marl-Dead Sea-Jordan. *Journal of Applied Sciences* 8:3603-3611. <https://doi.org/10.3923/jas.2008.3603.3611>
- Moayed, R.Z.; Izadi, E. & Heidari, S. (2010). Improvement of saline silty sand soil behavior using lime and micro silica. Proc. Fifth Civil Engineering Conference in the Asian Region and Australasian Structural Engineering Conference. Sydney, pp. 466-473.
- Messad, A. & Moussai, B. (2016a). Effect of water salinity on Atterberg limits of El-Hodna sabkha soil. *Bulletin of Engineering Geology and the Environment*, 75:301-309. <https://doi.org/10.1007/s10064-015-0733-x>
- Messad, A. & Moussai, B. (2016b). Evaluation of the collapsibility of El Hodna Sabkha soil - Algeria. Proc. Fourth Geo-China International Conference, Shandong, China 25-27 July, pp. 278-28. <https://doi.org/10.1061/9780784480083.034>
- Shariatmadari, N.; Salami, M. & Karimpour Fard, M. (2011). Effect of inorganic salt solutions on some geotechnical properties of soil-bentonite mixtures as barriers. *International Journal of Civil Engineering*, 9:103-110. <http://ijce.iust.ac.ir/article-1-570-en.html>

# Hydromechanical Behavior of Soil with Tire Fibers

A.C. Silva, S. Fucale, S.R.M. Ferreira

**Abstract.** Products derived from tires have been increasingly used for geotechnical engineering applications because of the economic, environmental, and social benefits they provide. The objective of this paper is to analyze the effect of the addition of rubber fibers from unserviceable tires on the hydromechanical behavior of argillaceous soil from the Barreiras Formation, in the Brazilian northeast. Soil mixtures were prepared containing 10 % and 20 % tire fibers, by weight, at optimum moisture and maximum dry specific weight. Their microstructure, shear strength, and permeability were evaluated. The Scanning Electron Microscopy (SEM) analysis indicates changes in the soil microstructure from the addition of the fibers and there is an intense interaction of fiber with the soil matrix. There is an increase in the shear strength of the blends by up to 47 %, making them more ductile. The saturated hydraulic conductivity of the soil is in the order of  $10^{-10}$  m/s, assuming values between  $10^{-8}$  and  $10^{-6}$  m/s when the tire fibers are inserted into the structure.

**Keywords:** tire fibers, shear strength, permeability, soil-fiber interaction.

## 1. Introduction

The disposal of waste tires is a globally recognized problem. It is estimated that around 1.5 billion used tires are discarded annually worldwide (ETRMA, 2011). In the United States more than 233 million units were discarded in 2013 (RMA, 2014) and in Europe more than 3 million tons are generated annually (ETRA, 2013). In Brazil it is estimated that approximately 450 thousand tons of tires are discarded annually (SEST/SENAT, 2017).

Unserviceable tires are responsible for a number of problems when they are irregularly disposed near public places such as empty lots, water bodies and traffic routes, attracting the disposal of other wastes in these same environments and contributing to the proliferation of disease vectors. The alarming figures for illegal disposal and the problems related to the irregular dumping of tires have driven the development of methods for reusing or recycling both end-of-life tires and waste produced from used tires.

Pneumatic materials, due to their characteristics such as high durability, low density, and low water absorption, can be used in many Civil Engineering applications, such as leachate drainage systems for landfills, drainage layers for roads, reinforcement and improvement of soil support capacity, absorption of vibrations from railway lines, among others (Edinçliler & Ayhan, 2010; Hazarika *et al.*, 2010; Kaushik *et al.*, 2015; Indraratna *et al.*, 2018).

The inclusion of tire-derived materials into the soil has been the focus of several studies, such as reinforcement for road subsoil or as a component of fill material (Bosscher *et al.*, 1997; Edinçliler & Cagatay, 2013), light fill material for containment structures (Reddy & Krishna, 2017; Moghadam *et al.*, 2018), or as an asphalt additive (Xu *et al.*,

2017), due not only to the potential for finding an adequate destination for waste tires, but also because of the characteristics that these materials provide to the soil. Experimental results reported in the literature show that there are improvements to physical properties and to the tension-strain behavior of soils that have been reinforced with pneumatic waste material (Ozkul & Baykal, 2007; Tafreshi *et al.*, 2012; Balunaini *et al.*, 2014; Fu *et al.*, 2014; Anvari *et al.*, 2017).

Fibers added to soils can be either oriented in a preferential direction or randomly distributed. When in a random configuration, there is a reduction of fragile points, resistance isotropy in the soil-fiber mixture and a greater extensibility and ductility in the composite material (Edinçliler & Cagatay, 2013). Another factor that affects the mixtures responses is the fiber content. Several studies have mixed soil with tire fibers in proportions ranging from 10 % to 50 %, obtaining better mechanical response when kept within this range (Edinçliler & Ayhan, 2010; Sellaf *et al.*, 2014; Macedo *et al.*, 2016).

Considering the high generation of non-repairable tires discarded annually in Brazil (SEST/SENAT, 2017) causing an environmental liability, the high resistance to decomposition over time by its constituents (Indraratna *et al.*, 2018) and the possibility of including materials ground tire derivatives as reinforcement for the underground road or as a component of landfill material; this article analyzes the effect of the interaction of rubber tire fibers on the hydromechanical behavior of a soil in the Barreiras Formation, which is widely used as landfill material. The Barreiras Formation extends from Amapá to Rio de Janeiro (Veiga, 2014).

---

Aline Cátia da Silva, M.Sc., D.Sc. student, Departamento de Engenharia Civil, Universidade Federal de Pernambuco, Recife, PE, Brazil. e-mail: alinecatia.catia@gmail.com.  
Stela Fucale, D.Sc., Associate Professor, Programa de Pós-Graduação em Engenharia Civil, Universidade de Pernambuco, Recife, PE, Brazil. e-mail: sfucale@poli.br.  
Silvio Romero de Melo Ferreira, D.Sc., Full Professor, Departamento de Engenharia Civil, Universidade Federal de Pernambuco, Recife, PE, Brazil. e-mail: sr.mf@hotmail.com.

Submitted on May 11, 2019; Final Acceptance on April 22, 2020; Discussion open until September 30, 2020.

DOI: 10.28927/SR.432191

## 2. Materials and Methods

The soil used comes from the Barreiras Formation located in the state of Pernambuco, in Northeastern Brazil. It is poorly graded (Fig. 1), has high plasticity, is classified as clayey sand according to the UCS (Unified Classification System) and is of type (A-7-6) in the TRB (Transportation Research Board) system, as shown in Table 1.

The rubber tire fibers were supplied by a local distributor in Pernambuco, with sizes ranging from 0.1 to 37 mm and average diameter of 1.07 mm (Fig. 2), and are sourced

from the process of retreading unwanted tires. The particle size distribution of the fibers indicates the absence of fine particles ( $\% < 0.075$  mm), Fig. 1, a specific gravity of 1.12 and a water absorption of 6.9 %, Table 1. The addition of fibers to the soil practically does not change the granulometry and plasticity of the mixtures, falling under the UCS classification as clayey sands (SC) and classified as a clayey material (A-7-6) by the TRB, but with lower specific gravities than soil alone, Table 1.

The fibers were added to the soil in two proportions, 10 % and 20 % by dry soil weight, in a random and homo-

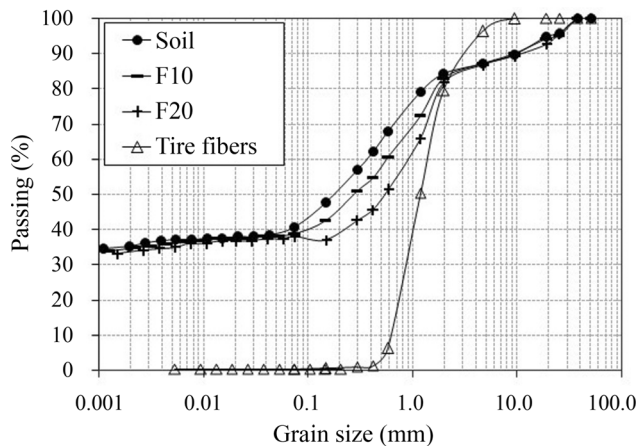


**Figure 1** - Granulometric distribution curves for soil, tire fibers, and soil-fiber mixtures.



**Figure 2** - Tire fibers utilized in the study.

**Table 1** - Geotechnical properties of soil, tire fibers, and soil-fiber mixtures.

| Parameters                                       | Sample                             |       |       |             |    |
|--|------------------------------------|-------|-------|-------------|----|
|  | Soil                               | F10   | F20   | Tire Fibers |    |
| Particle size (%)                                | $\phi > 4.75$ mm*                  | 13    | 13    | 13          | 4  |
|  | $0.075$ mm $> \phi \leq 4.75$ mm*  | 46    | 50    | 51          | 96 |
|  | $0.005$ mm $> \phi \leq 0.075$ mm* | 3     | 1     | 1           | 0  |
|  | $\phi \leq 0.005$ mm*              | 38    | 36    | 35          | 0  |
| Cc   | -                                  | -     | -     | 0.9         |    |
| Cu   | -                                  | -     | -     | 2.2         |    |
| Liquidity limit (%)                              | 44                                 | 47    | 46    | -           |    |
| Plasticity limit (%)                             | 23                                 | 25    | 26    | -           |    |
| Plasticity index (%)                             | 21                                 | 22    | 20    | -           |    |
| Water absorption (%)                             | -                                  | -     | -     | 6.9         |    |
| Specific gravity                                 | 2.66                               | 2.29  | 1.98  | 1.12        |    |
| Optimal moisture (%)                             | 17.5                               | 16.4  | 16.1  | -           |    |
| Maximum dry specific weight (kN/m <sup>3</sup> ) | 17.6                               | 16.1  | 14.8  | -           |    |
| Void ratio                                       | 0.51                               | 0.43  | 0.33  | -           |    |
| UCS classification                               | SC                                 | SC    | SC    | SP          |    |
| TRB classification                               | A-7-6                              | A-7-6 | A-7-6 | A-1-b       |    |

(\*) - description according to D 422-63 (ASTM 2007).

geneous manner. These mixtures are referred to as F10 and F20, respectively. The contents were chosen in light of studies carried out by Macedo *et al.* (2016), who indicated that more satisfactory results were found for values below 30 %.

The soil and fiber-soil mixture test specimens were prepared at optimum moisture, by inserting distilled water corresponding to the optimum content for each material, and compacted to achieve at the maximum dry specific weight previously obtained in the normal Proctor test.

The molding of the test specimens for Scanning Electron Microscopy (SEM) and direct shear tests consisted in dividing the samples into two equal parts, which were statically compacted in a steel mold (Fig. 3) using a press. This procedure was necessary due to the impossibility of compacting the samples directly inside the shear box. The compaction was performed in such a way that the desired size was obtained exactly, with a 15-min wait period following this step for volumetric stabilization of the test specimens, allowing the mixtures to achieve the specific weight required. The test specimens for the permeability test were molded according to the normal Proctor test.

The analysis of the microstructure was performed using the SEM technique on air-dried samples fixed onto a metallic base (with a diameter of 75 mm and an approximate height of 10 mm) with a carbon double-sided tape, and metalized with carbon inside a Cressington Carbon Coater 108 Carbon/Vacuum bell. A JEOL-brand electron scanning microscope was used, operating at 30 kV. From the soil and from each soil-fiber mixture, three samples were metalized, observed and analyzed. The surface of each sample was observed and images representative of the microstructures were selected.

The direct shear tests were carried out using test specimens with dimensions of 100 × 100 mm and a height of 40 mm, consolidated under normal stresses of 50, 100, 150 and 200 kPa, according to standard D 3080 (ASTM, 2011). The shear speed was 0.083 mm/min, the load cell capacity is 5 kN, and the displacements were measured by means of LVDT (Linear Variable Differential Transformer) type transducers, having a sensitivity of 0.001 mm.

The permeability tests of the soil and the mixtures were carried out using permeameters of variable load, ac-

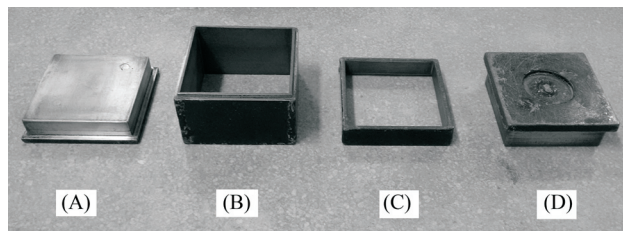


**Figure 3** - Steel mold consisting of: base (a), box (b), collar (c), and lid (d).

ording to the recommendations of standard NBR 14545 (ABNT, 2000), and for specimens with approximately 100 mm diameter and 127 mm height.

### 3. Results and Discussions

The microstructure, shear strength and permeability of soil and mixtures are presented and discussed.

#### 3.1. Analysis of shear strength

The graphs showing shear stress vs. horizontal displacement of the clayey sand exhibit plastic-like behaviors at stress of 50 kPa and plastic with stiffening at higher stresses (100, 150 and 200 kPa), Fig. 4. The mixture F10 presents a slight peak behavior at stresses of 50 and 100 kPa and a plastic response at 150 kPa. The plastic response is also shown by the mixture F20 at 50 and 100 kPa. The soil-fiber mixtures exhibit soil-like behavior at a higher stress (200 kPa).

The graphs for vertical displacement vs. horizontal displacement of the mixtures initially show compression followed by a subsequent dilation at all normal stresses applied, Fig. 4. As the fiber content increases, the onset of dilation and the magnitude of dilation occur for greater horizontal displacements, when compared with the soil.

The analysis of the shear strength for samples that did not show strength peaks was performed based on the criterion of De Campos & Carrillo (1995). The fibers reduced the influence of rotational tension during the test and increased the soil rupture strength at all normal stress levels, indicating the force transfer from the soil matrix to the fibers and increased ductility in the mixtures. The fibers tend to be more mobilized under high tension, requiring greater horizontal displacements for more significant contributions to soil strength.

The friction angle of compacted clayey sand is 29° and it has a cohesion of 10 kPa (Table 2). The shear strength of the soil was increased by up to 47 % when adding 10 % tire fibers, while the addition of 20 % fibers reduced the shear strength of the mixture in relation to the 10 % fiber mixture, though it was still higher than of the soil alone. The interaction between the phases of the mixtures (Fig. 5) shows that the volume of soil interacting with 10 % of fibers is greater than that in the mixture with 20 % fibers. The electromicrography (section 3.3) also shows a lower interaction between soil and fibers in the 20 % mixture, resulting in a lower shear strength.

#### 3.2. Hydraulic conductivity

The average hydraulic conductivity of the saturated clayey sand was  $9.31 \times 10^{-10}$  m/s, indicating low permeability. There are linear relationships between the variation of the fiber content (Fig. 6a), the void ratio of the mixtures (Fig. 6b) and the hydraulic conductivity coefficient. The incorporation of tire fibers into the soil resulted in a significant increase in the permeability of the mixtures, varying

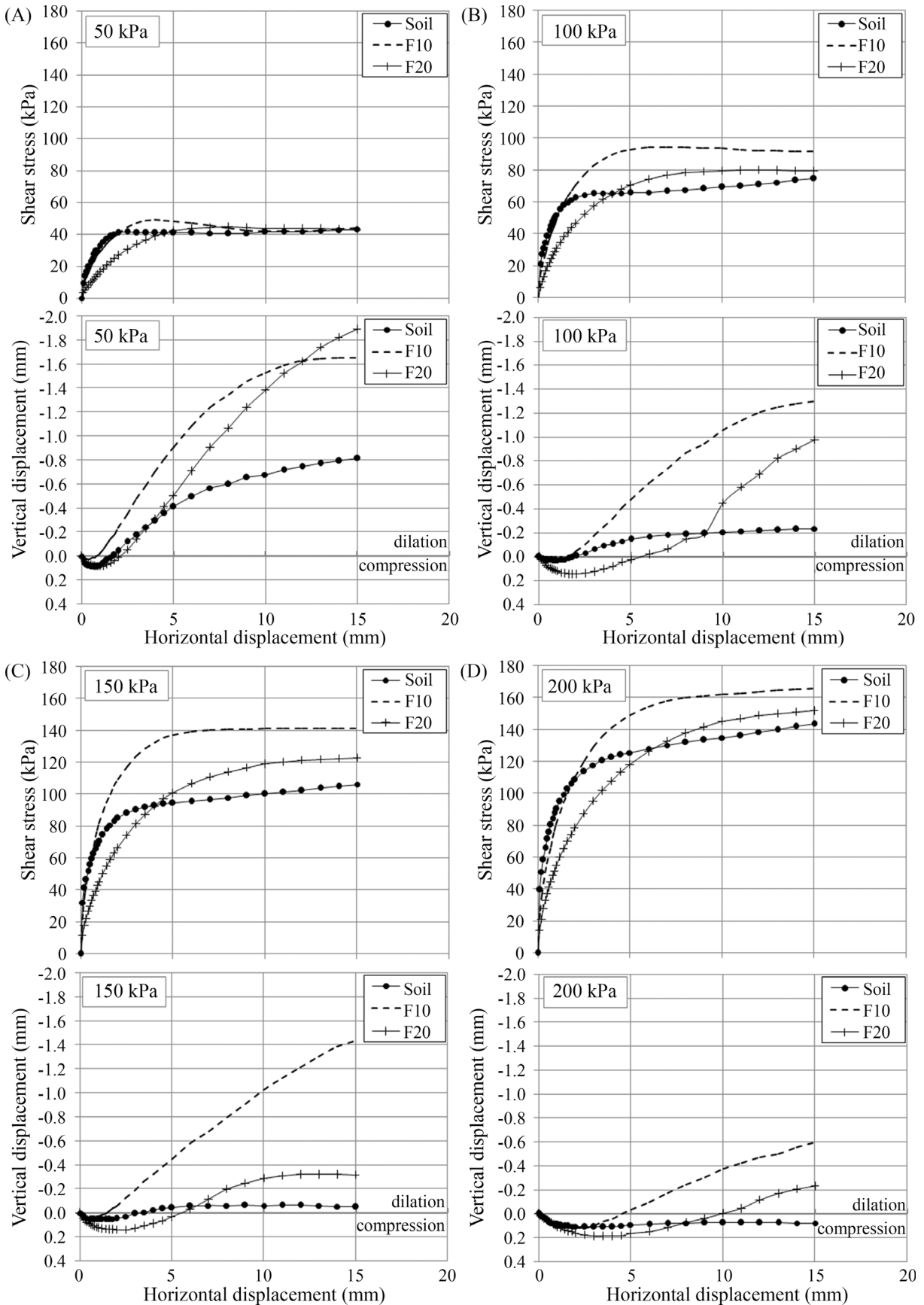
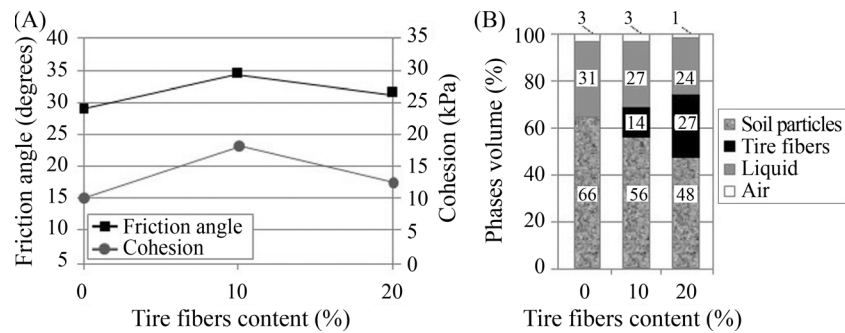


Figure 4 - Results from direct shear tests for: 50 kPa (a), 100 kPa (b), 150 kPa (c), and 200 kPa (d).

**Table 2** - Shear strength parameters.

| Parameters               | Sample                     |        |        |        |
|--------------------------|----------------------------|--------|--------|--------|
|                          | Soil                       | F10    | F20    |        |
| $\sigma_n = 50$ kPa      | $\sigma_n$ corrected (kPa) | 53.14  | 52.05  | 54.27  |
|                          | $\tau_{rup}$ (kPa)         | 40.95  | 49.04  | 44.57  |
|                          | $\epsilon_{rup}$ (mm)      | 7.0    | 4.0    | 8.0    |
| $\sigma_n = 100$ kPa     | $\sigma_n$ corrected (kPa) | 106.28 | 107.40 | 110.92 |
|                          | $\tau_{rup}$ (kPa)         | 66.02  | 94.34  | 79.53  |
|                          | $\epsilon_{rup}$ (mm)      | 6.0    | 7.0    | 10.0   |
| $\sigma_n = 150$ kPa     | $\sigma_n$ corrected (kPa) | 159.41 | 162.82 | 166.38 |
|                          | $\tau_{rup}$ (kPa)         | 95.75  | 140.79 | 119.00 |
|                          | $\epsilon_{rup}$ (mm)      | 6.0    | 8.0    | 10.0   |
| $\sigma_n = 200$ kPa     | $\sigma_n$ corrected (kPa) | 212.55 | 217.09 | 221.83 |
|                          | $\tau_{rup}$ (kPa)         | 128.18 | 159.94 | 145.24 |
|                          | $\epsilon_{rup}$ (mm)      | 6.0    | 8.0    | 10.0   |
| Cohesion intercept (kPa) | 10                         | 18     | 12     |        |
| Friction angle (degrees) | 29                         | 34     | 31     |        |
| R <sup>2</sup>           | 0.99                       | 0.97   | 0.99   |        |



**Figure 5** - Variation of the friction angle and cohesion with fiber content (a) and phase volume for each material (b).

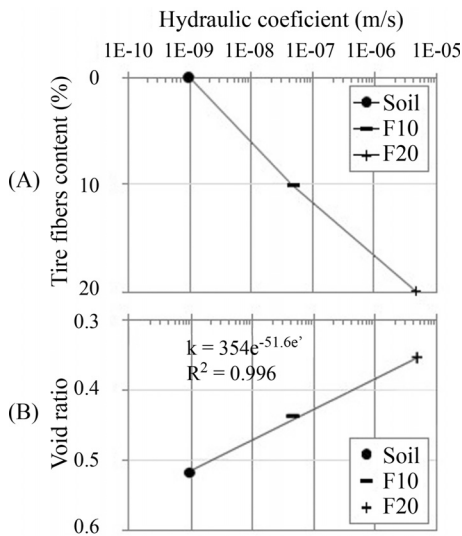


**Figure 6** - Variation of the hydraulic coefficient with tire fiber content (a) and with the void ratio (b).

from  $10^{-10}$  m/s to values on the order of  $10^{-6}$  and  $10^{-8}$  m/s (Fig. 6a), increasing the order of hydraulic conductivity more than 10000 times. It should be noted that there is a reduction in the void ratio for the mixtures due to the insertion of the fibers, different from that occurring for soils (Fig. 6b).

The permeability test results are due to the lower quantity of soil (Fig. 5b) and to the canaliculi existing in the mixtures, caused by the presence of the fibers and larger pores in the soil-fiber contact (macropores). These macropores allow the water to percolate more easily, due to the smaller hydraulic head loss suffered by the water when percolating macrostructure, than among the soil particles (micropores). In this way, the hydraulic conductivity of the macrostructure is of greater importance than that of the microstructure.

### 3.3. Microstructural analysis

The compacted clayey sand is structured into flakes formed by the arrangement of sand grains interconnected by silt and clay particles of dense form (Fig. 7) due to the compaction process, giving the soil a low permeability.

The tire fibers are of different sizes and they are randomly arranged within the soil matrix. On the surface of the soil mixture with 10 % of tire fibers cracks (canaliculi) can be seen (Fig. 8), indicating the presence of the fibers due to its elastic relaxation. The insertion of 10 % fibers altered the surface appearance of the sample, but it can be inferred that there is intense interaction between the tire particles and the clayey sand matrix, explaining the mechanical results obtained.

In the soil mixture with 20 % tire fibers, two different situations are verified (Fig. 9a) in the same electromicrograph: a tire fiber partially adhered to the soil matrix with visible voids (macropores) at the interface (Fig. 9c), and a tire fiber completely enveloped by the soil, without a clear separation zone (Fig. 9b), showing that the presence of the fibers does not completely fragilize the structure, matching up with the results from the mechanical tests, indicating that the adhesion between the two materials is sufficient to improve the strength of the mixture.

### 4. Conclusions

The use of alternative materials as soil reinforcement have been increasingly encouraged in geotechnical engineering. In this article, the influence of tire rubber fibers on the hydromechanical behavior of a soil from Barreiras Formation was investigated. The shear strength, permeability and microstructure of the samples were evaluated. A microstructural analysis was correlated with hydromechanical responses. The following conclusions can be draw:

The tire fibers increased the shear strength of the clayey sand by up to 47 % for the mixture containing 10 % tire fibers and with the applied normal stress increased. The fibers have a high capacity to absorb the energy of deformation applied to the soil. The good mechanical performance found in the soil-fiber mixtures can be attributed to the improved fiber-matrix interaction and the fiber content incorporated into the soil.

The tire residues improved the hydraulic properties of the soil, increasing the hydraulic conductivity by more than 10000 times, this aspect being associated with the effect of the microstructure of the tire fibers on the soil matrix, which provide preferential paths for water percolation and lower head loss, and dependent on the applications of the soil-fibers mixtures.

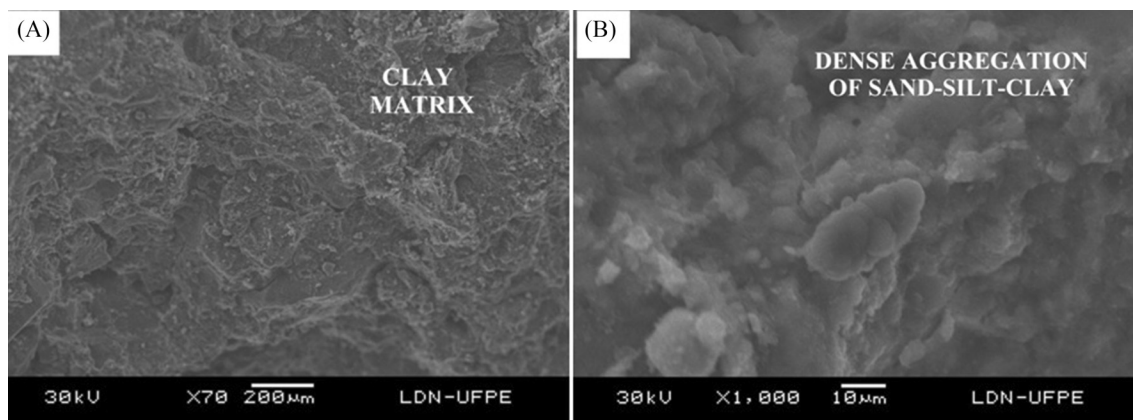


**Figure 7** - Electromicrographs of clayey sand at magnifications of 70× (a) and 1000× (b).

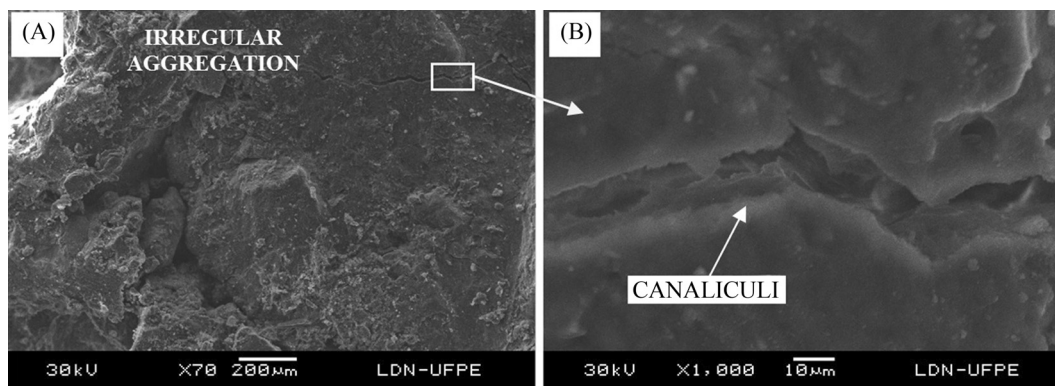


**Figure 8** - Electromicrographs of F10 mixture at magnifications of 70× (a) and 1000× (b).

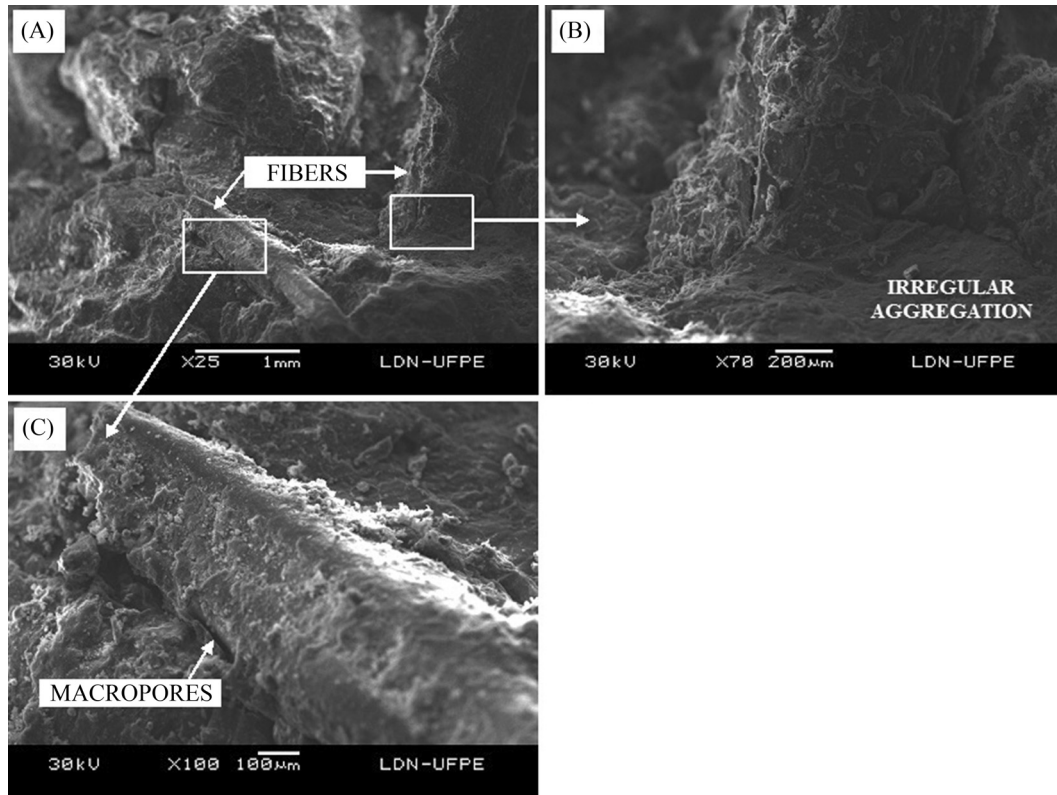


**Figure 9** - Electromicrographs of F20 mixture at magnifications of 25× (a), 70× (b), and 100× (c).

The incorporation of tire fibers, in addition to improvements brought to the soil, also promotes environmental benefits by giving a proper destination for this type of alternative material, reducing what is ordinarily an environmental liability.

### Acknowledgments

The authors would like to acknowledge the program for academic strengthening of University of Pernambuco for the financial support.

### References

- ABNT (2000). Soil - Determination of the Coefficient of Permeability of Clay Soils- NBR 14545. Brazilian Association of Technical Standards, Rio de Janeiro, Brazil, 12 p.
- Anvari, S.M.; Shooshpasha, I. & Kutanaei, S. (2017). Effect of granulated rubber on shear strength of fine-grained sand. *Journal of Rock Mechanics and Geotechnical Engineering*, 9(5):936-944. <https://doi.org/10.1016/j.jrmge.2017.03.008>
- ASTM (2011). Standard Test Method for Direct Shear Test of Soils Under Consolidated Drained Conditions- D 3080. ASTM International, West Conshohocken, Pennsylvania, USA, 9 p.
- ASTM (2007). Standard Test Method for Particle Size Analysis of Soils - D 422-63. ASTM International, West Conshohocken, Pennsylvania, USA, 8 p.
- Balunaini, U.; Mohan, V.K.D.; Prezzi, M. & Salgado, R. (2014). Shear strength of tyre chip-sand and tyre shred-sand mixtures. *Proceedings of the Institution of Civil Engineers - Geotechnical Engineering*, 167(6):585-595. <https://doi.org/10.1680/geng.13.00097>
- Bosscher, J.; Edil, T.B. & Kuraoka, S. (1997). Design of highway embankments using tire chips. *Journal of Geotechnical and Geoenvironmental Engineering, ASCE*, 123(4):295-304. [https://doi.org/10.1061/\(ASCE\)1090-0241\(1997\)123:4\(295\)](https://doi.org/10.1061/(ASCE)1090-0241(1997)123:4(295))
- De Campos, T.M.P. & Carrillo, C.W. (1995). Direct shear testing on an unsaturated soil from Rio de Janeiro. *Proc. Int. Conf. on Unsaturated Soils, UNSAT'95, Balkema, Paris*, pp. 31-38.
- Edinçliler, A. & Ayhan, V. (2010). Influence of tire fiber inclusions on shear strength of sand. *Geosynthetics International*, 17(4):183-192. <https://doi.org/10.1680/gein.2010.17.4.183>
- Edinçliler, A. & Cagatay, A. (2013). Weak subgrade improvement with rubber fibre inclusions. *Geosynthetics*

- International, 20(1):39-46.  
<https://doi.org/10.1680/gein.12.00038>
- ETRA (European Tyre Recycling Association). (2013). Introduction to Tyre Recycling: 2013 (Twenty Years of Tyre Recycling in the EU). Available at <http://www.etra-eu.org/joomla/publicationsand> accessed on July 14th 2017.
- ETRMA (European Tyre & Rubber Manufacturers' Association). (2011). End of Life Tyres - A Valuable Resource with Growing Potential. Available at <http://www.etrma.org/uploads/Modules/Documentsmanager/brochure-elt-2011-final.pdf> and accessed on July 14th 2017.
- Fu, R.; Coop, M.R. & Li, X.Q. (2014). The mechanics of a compressive sand mixed with tyre rubber. *Géotechnique Letters*, 4(3):238-243.  
<https://doi.org/10.1680/geolett.14.00027>
- Hazarika, H.; Yasuhara, K.; Kikuchi, Y.; Karmokar, A.K. & Mitarai, Y. (2010). Multifaceted potentials of tire-derived three-dimensional geosynthetics in geotechnical applications and their evaluation. *Geotextiles and Geomembranes*, 28(3):303-315.  
<https://doi.org/10.1016/j.geotexmem.2009.10.011>
- Indraratna, B.; Sun, Q.; Heitor, A. & Grant, J. (2018). Performance of rubber tire-confined capping layer under cyclic loading for railroad conditions. *Journal of Materials in Civil Engineering*, ASCE, 30(3):06017021.  
[https://doi.org/10.1061/\(ASCE\)MT.1943-5533.0002199](https://doi.org/10.1061/(ASCE)MT.1943-5533.0002199)
- Kaushik, M.K.; Kumar, A. & Bansal, A. (2015). Performance assessment of gravel-Tire chips mixes as drainage layer materials using real active MSW landfill leachate. *Geotechnical and Geological Engineering*, 33(4):1081-1098.  
<https://doi.org/10.1007/s10706-015-9889-1>
- Macedo, M.C.; Fucale, S. & Ferreira, S.R.M. (2016). Geomechanical behavior of soil mixtures with tire residues and construction and demolition waste. *Electronic Journal of Geotechnical Engineering*, 21(19):6393-6410.
- Moghadam, M.J.; Zad, A.; Mehrannia, N. & Dastaran, N. (2018). Experimental evaluation of mechanically stabilized earth walls with recycled crumb rubbers. *Journal of Rock Mechanics and Geotechnical Engineering*, 10(5):947-957.  
<https://doi.org/10.1016/j.jrmge.2018.04.012>
- Özkul, Z.H. & Baykal, G. (2007). Shear behavior of compacted rubber fiber-clay composite in drained and undrained loading. *Journal of Geotechnical and Geoenvironmental Engineering*, ASCE, 133(7):767-781.  
[https://doi.org/10.1061/\(ASCE\)1090-0241\(2007\)133:7\(767\)](https://doi.org/10.1061/(ASCE)1090-0241(2007)133:7(767))
- Reddy, S.B. & Krishna, A.M. (2017). Tyre chips as compressible inclusions in earth-retaining walls. *Proceedings of the Institution of Civil Engineers - Ground Improvement*, 170(3):137-148.  
<https://doi.org/10.1680/jgrim.16.00034>
- RMA (Rubber Manufacturers Association) (2014). 2013 U.S. Scrap Tire Management Summary. Rubber Manufacturers Association, Washington, D.C., pp. 1-18.
- Sellaf, H.; Trouzine, H.; Hamhami, M. & Asroun, A. (2014). Geotechnical properties of rubber tires and sediments mixtures. *Engineering, Technology & Applied Science Research*, 4(2):618-624.
- SEST SENAT (Serviço Social do Transporte/Serviço Nacional de Aprendizagem do Transporte) (2017). Cerca de 450 mil toneladas de pneus são descartados por ano no Brasil. Available <http://www.sestsenat.org.br/imprensa/noticia/cerca-de-450-mil-toneladas-de-pneus-sao-descartados-por-ano-no-brasil> and accessed on July 14th 2017.
- Tafreshi, S.N.M.; Mehrjardi, G.T. & Dawson, A.R. (2012). Buried pipes in rubber-soil backfilled trenches under cyclic loading. *Journal of Geotechnical and Geoenvironmental Engineering*, ASCE, 138(11):1346-1356.  
[https://doi.org/10.1061/\(ASCE\)GT.1943-5606.0000710](https://doi.org/10.1061/(ASCE)GT.1943-5606.0000710)
- Veiga, C.J.V. (2014). Mapeamento da Formação Barreiras na Região Norte Fluminense, entre os Rios Paraíba do Sul e Itabapoana. Trabalho Final de Curso (Geologia), Departamento de Geologia, Instituto de Geociências, Universidade Federal do Rio de Janeiro, Rio de Janeiro, 49 p.
- Xu, O.; Rangaraju, P.R.; Wang, S. & Xiao, F. (2017). Comparison of rheological properties and hot storage characteristics of asphalt binders modified with devulcanized ground tire rubber and other modifiers. *Construction and Building Materials*, 154:841-848.  
<https://doi.org/10.1016/j.conbuildmat.2017.07.221>

## List of Symbols

- $\Phi$ : the particle size  
 $\sigma_n$ : the normal stress  
 $\sigma_{n\ corrected}$ : the corrected normal stress  
 $\tau_{rup}$ : the shear rupture stress  
 $\epsilon_{rup}$ : the rupture deformation  
 $R$ : the coefficient of determination  
 $k$ : the hydraulic coefficient  
 $e'$ : the void ratio  
 F10: mixture having 10 % tire fibers  
 F20: mixture having 20 % tire fibers

# Bottom Reinforcement in Braced Excavations: Coupled Analysis and New Method for Basal-Heave Stability Study

J.L. Borges, R.M. Santos

**Abstract.** Soil-cement bottom reinforcement is commonly used in braced excavations in soft soils, so that ground displacements can be reduced and excavation safety against bottom failure increase. However, there is a lack of studies in the literature regarding such reinforced excavations in which the stability against bottom heave is analysed through mechanical-hydraulic coupled modelling. In the paper, in order to contribute to overcome such deficiency, a braced excavation in soft soil, incorporating a jet-grout base slab, is analysed. A finite element code, which incorporates the above-mentioned features, is used and a new method for basal stability analysis - which utilizes the numerical results obtained by the finite element code - is proposed and applied. Two cases of the same problem, with and without soil-cement bottom slab, are compared.

**Keywords:** basal-heave stability, consolidation, coupled analysis, jet-grout slab, soft soil, strutted excavation.

## 1. Introduction

The construction of deep excavations in soft soil deposits has been one of the major challenges for geotechnical engineers. In such excavations, settlements of the supported ground are usually very large, over 1-2 % of the excavation depth, as reported by Peck (1969) for excavations constructed before the seventies.

However, in the last decades, several new technologies have been considered to improve the control of the induced movements in such excavations. Matos Fernandes *et al.* (2012) summarized several procedures that can be used in practice to control the displacements for deep excavations in soft ground, by considering the use of: (i) stiff (reinforced concrete) walls, to reduce the wall deflection due to bending; (ii) early installation of the first level of supports (struts or pre-stressed anchors, typically), to prevent significant displacements of the upper part of the wall working as a cantilever; (iii) connections between struts and the wall carefully designed and constructed, to ensure that the effective strut stiffness corresponds to a high percentage of its theoretical value; (iv) impermeable walls, to avoid lowering of the water table in permeable layers, which induces consolidation settlements in soft clay strata, as well as to prevent settlements associated with internal erosion of sandy strata; (v) ground treatment before excavation, to support the wall and control displacements under the excavation base at each stage; (vi) walls with tips embedded in the bedrock, to control the displacements under the excavation base; (vii) pre-stressed struts, to increase the effective strut stiffness, closing gaps in the strut-wall connections, as well as to recover part of the displacements induced by previous excavation stages; (viii) staged excavation limited to a min-

imum at each stage, to avoid over-excavation that reduces the support effect provided by the struts or ground anchors.

With regard to the use of ground treatment techniques, one possible solution consists in extending the wall below the excavation base and, before excavation, constructing a soil-cement base slab (using jet grouting or deep soil mixing technologies, for instance) to support the wall below the excavation bottom (Mateus, 2010).

Another important issue that needs to be analysed for braced excavation projects in soft clays is the basal-heave stability, for the lateral earth support system is often controlled by stability requirements. Different methods have been used in practice to perform stability calculations for braced excavations, which basically are based on either limit equilibrium approach (Terzaghi, 1943; Bjerrum & Eide, 1956; Clough & Hansen, 1981; O'Rourke, 1992; Su *et al.*, 1998; Ukritchon *et al.*, 2003) or finite-element analysis (Faheem *et al.*, 2003; Faheem *et al.*, 2004; Cai *et al.*, 2002).

Another pertinent question when excavations are undertaken in saturated clayey soils is the generation of increments of pore pressure during the excavation period and their dissipation after that period (consolidation). After construction, there are pore pressure gradients in the ground that determine a consolidation process. This process is dependent on both the magnitude of pore pressure increments at the end of excavation and the long-term hydraulic conditions. In some cases, settlements of the supported ground increase with time in response to the consolidation, the long term conditions being more unfavourable than those at the end of the excavation period (Borges & Guerra, 2014; Santos, 2014; Monteiro, 2011; Alves, 2012;

José Leitão Borges, Ph.D., Assistant Professor, Departamento de Engenharia Civil, Faculdade de Engenharia, Universidade do Porto, Rua Dr. Roberto Frias, 4200-465 Porto, Portugal. e-mail: leitao@fe.up.pt.

Rita Marialva Santos, M.Sc., Faculdade de Engenharia, Universidade do Porto, Rua Dr. Roberto Frias, 4200-465 Porto, Portugal. e-mail: ritamarialva@gmail.com.

Submitted on August 7, 2019; Final Acceptance on May 26, 2020; Discussion open until September 30, 2020.

DOI: 10.28927/SR.432199

Guerra, 2009). Therefore, realistic analyses that take into account the consolidation effect by performing fully mechanical-hydraulic coupled analyses (Potts *et al.*, 1997; Borges & Guerra, 2014; Costa *et al.*, 2007; Borges & Alves, 2014) are strongly recommended in many cases, despite the practical importance of more simplified studies such as undrained total stress approaches.

In the literature, there is a lack of studies of deep braced excavations in soft soils in which the three above-mentioned issues are simultaneously considered, namely: consolidation effect through mechanical-hydraulic coupled analysis; ground treatment below the excavation base; and basal-heave stability analysis considering the effect of the consolidation.

In the present study, in order to overcome such deficiency, a strutted excavation in soft soil with a jet-grout base slab is analysed. A finite element code is used and a new method for basal stability analysis is proposed, utilizing the numerical results obtained by the finite element program. Comparisons with the classical limit equilibrium methods of Terzaghi (1943) and Bjerrum & Eide (1956) are included. Two cases of the same problem, with and without the soil-cement bottom slab, are compared.

## 2. Finite Element Code

The finite element code utilized in the present study was developed by Borges (1995) and incorporates, among other features, fully mechanical-hydraulic coupled analysis (Biot consolidation theory) (Borges, 1995; Lewis & Schrefler, 1987; Britto & Gunn, 1987) and the  $p$ - $q$ - $\theta$  critical state model for soil constitutive behaviour simulation (Borges, 1995; Lewis & Schrefler, 1987). The initial version of the program was presented in 1995, and several improvements were subsequently developed, including a 3-D coupled analysis version (Borges, 2004).

In the  $p$ - $q$ - $\theta$  model - which is an extension of the Modified Cam-Clay model into the three-dimensional stress space using the Mohr-Coulomb failure criterion - the parameter that defines the slope of the critical state line,  $M$ , is not constant (as happens in the Modified Cam-Clay model), but depends on the angular stress invariant  $\phi$  and the effective friction angle,  $\theta'$ , as follows:

$$M = \frac{3 \sin \phi}{\sqrt{3} \cos \theta + \sin \phi \sin \theta} \quad (1)$$

This defines the Mohr-Coulomb criterion when  $M$  is introduced in the equation of the critical state line

$$q = M \cdot p' \quad (2)$$

where  $p'$  is the effective mean stress and  $q$  the deviatoric stress. In the principal effective stress space, for an arbitrary state  $(\sigma'_1, \sigma'_2, \sigma'_3)$ , where  $\sigma'_1, \sigma'_2$  and  $\sigma'_3$  are the principal effective stresses, the angular stress invariant  $\theta$ , introduced by Nayak and Zienkiewicz (1972), measures the

orientation of the projection of the vector  $(\sigma'_1, \sigma'_2, \sigma'_3)$  on the plane that is normal to the space diagonal  $(\sigma'_1 = \sigma'_2 = \sigma'_3)$  axis).

This is an important feature of the  $p$ - $q$ - $\theta$  model, for the soil critical state depends on  $\theta$ , as shown by triaxial and plane strain tests (Lade & Duncan, 1973; Mita *et al.*, 2004). Drucker-Prager is the failure criterion of the Cam-Clay and Modified Cam-Clay models and does not depend on  $\theta$ . Numerical and laboratorial results presented by several authors (Potts & Zdravkovic, 1999; Mita *et al.*, 2004) showed that strain-stress behaviour of the soil is much better simulated if the slope of the critical state line is defined according to the Mohr-Coulomb criterion, which happens in the  $p$ - $q$ - $\theta$  model. In excavations, where different types of stress-path occur (in different areas of the ground), which correspond to different values of  $\theta$ , the use of the  $p$ - $q$ - $\theta$  model is particularly pertinent.

Figure 1a shows, in the principal effective stress space, the yield and critical state surfaces of the  $p$ - $q$ - $\theta$  model. In the  $p'$ - $q$  plane, the yielding function is an ellipse (Fig. 1b) and, depending on the over-consolidation ratio, the  $p$ - $q$ - $\theta$  model simulates hardening behaviour or softening behaviour. Hardening occurs in normally consolidated or lightly over-consolidated clays while softening occurs in moderately to strongly over-consolidated clays.

The finite element code has been validated against field measurements and used to analyse a wide range of geotechnical structures involving consolidation. With regard to embankments on soft ground, Borges (1995) com-

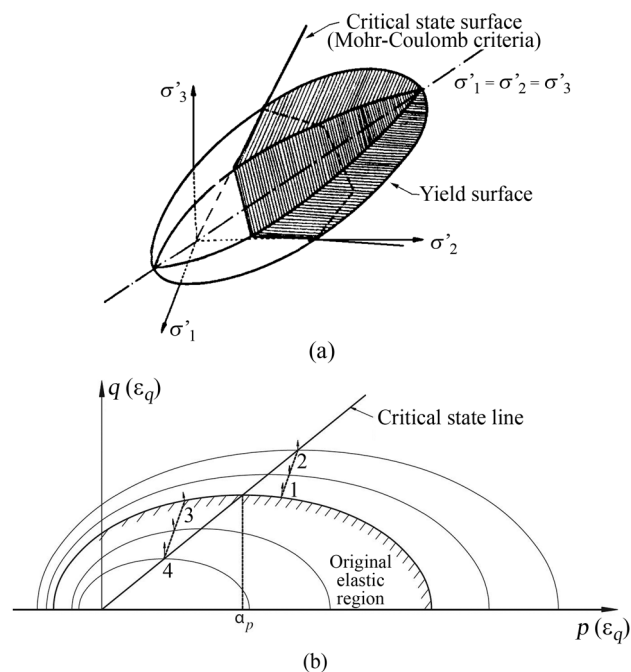


**Figure 1** - Yield and critical state surfaces of the  $p$ - $q$ - $\theta$  critical state model in (a) principal effective stress space and (b)  $p'$ - $q$  space.

pared results of two geosynthetic-reinforced embankments, one constructed up to failure (Quaresma, 1992) and the other observed until the end of consolidation (Yeo, 1986; Basset, 1986a,b). The accuracy was considered adequate in both cases. Very good agreements with field measurements were also observed in an embankment on soft soils incorporating stone columns (Domingues, 2006) and in a braced excavation in very soft ground (Costa *et al.*, 2007; Costa, 2005), an excavation carried out in the City of San Francisco, presented by Clough & Reed (1984), to install a large sewer culvert. Others studies of braced excavations in soft soils were also performed using the same finite element code (Borges & Guerra, 2014; Borges & Alves, 2014; Santos, 2014; Monteiro, 2011; Alves, 2012; Barros, 2015; Pinto, 2011; Azevedo, 2010; Guerra, 2009).

### 3. Stability Analysis Against Bottom Heave

#### 3.1 Preamble

In current practice, two categories of methods have been used to perform stability calculations for braced excavations (Ukritchon *et al.*, 2003): (1) limit equilibrium methods; (2) finite-element methods (FEM). The models proposed by Terzaghi (1943), Bjerrum & Eide (1956), Clough & Hansen (1981), O'Rourke (1992), Su *et al.* (1998) and Ukritchon *et al.* (2003) are of the first category.

Traditionally, the two most quoted methods for analysing bottom heave stability have been the limit equilibrium approaches based on Terzaghi (1943) and Bjerrum & Eide (1956). The latter, which actually stems from Skempton (1951) and was calibrated against observed bottom heave failures, is based on the similarity between the bearing capacity of a deeply embedded footing and a bottom heave failure of an excavation.

Figure 2 shows the assumed failure surfaces for the Terzaghi (1943) and Bjerrum & Eide (1956) methods when the wall is embedded below the excavation base. In this

case, the value of the safety factor  $F$  is given by Eqs. 3 and 4, respectively for Terzaghi (1943) and Bjerrum & Eide (1956) methods:

$$F = \frac{(2 + \pi)s_u + \gamma d + \frac{2ds_a}{B}}{H \left( \gamma - \frac{\sqrt{2}s_{uDE}}{B} \right)} \quad (3)$$

$$F = \frac{N_c s_u + \gamma d + \frac{2ds_a}{B}}{\gamma H} \quad (4)$$

where  $s_u$  is the average strength of the soil along the failure surface below the tip of the wall (lines ACD and ACDE in Figs. 2a and 2b, respectively),  $s_{uDE}$  is the average strength of the soil along line DE for the Terzaghi method (Fig. 2a),  $s_a$  is the average strength of the soil-wall interface on the embedded depth  $d$ ,  $\gamma$  is the unit weight of soil,  $H$  is the vertical length of the wall,  $B$  is the width of the excavation,  $d$  is the embedded depth of the wall below the excavation base and  $N_c$  is the bearing capacity factor, which depends on the values of  $H$ ,  $B$  and  $L$  (horizontal length of the excavation), incorporating the effect of the soil strength above the wall tip and the effect of the finite length ( $L \neq \infty$ ) of the excavation.

Despite their traditional importance, it should be mentioned that the Terzaghi (1943) and Bjerrum & Eide (1956) methods were developed before the introduction of stiffer wall systems (such as reinforced concrete diaphragm walls) and ignore, for example, the effect of ground treatment when a soil-cement slab is constructed below the excavation base. In other words, when different lateral earth support systems are considered, different stress redistributions occur within the soil; such stress redistributions, which can only be captured by more complex methods (such as finite element analysis), influence the overall stability of the structure, and are

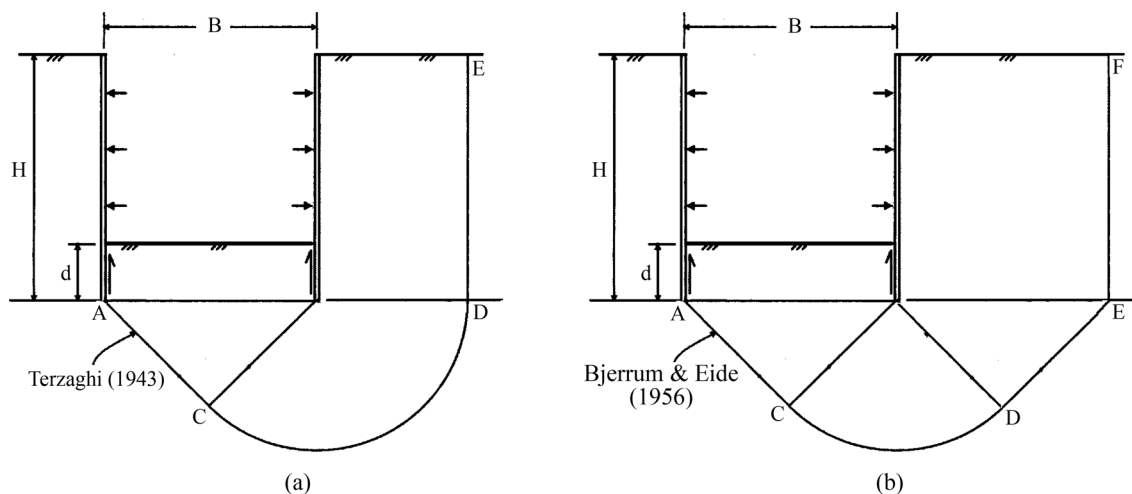


**Figure 2** - Failure surfaces for basal-heave stability analysis of: a) Terzaghi (1943) method; b) Bjerrum & Eide (1956) method.

not taken into account in the two above-mentioned methods, as shown below (Section 5).

A second category of methods for calculating basal-heave stability is based on finite-element analyses (Faheem *et al.*, 2003; Faheem *et al.*, 2004; Cai *et al.*, 2002) with formulations that are similar to those of the finite-element methods for slope stability analysis, widely accepted in the literature for many years.

With regard to slope stability analysis, two types of finite-element methods have been used in practice: (i) the “strength reduction method” (SRM) and (ii) the “enhanced limit slope stability method” (ELSM) (Liu *et al.*, 2015).

In the SRM, the safety factor is evaluated by the gradual reduction of the shear strength parameters (cohesion,  $c$ , and friction angle,  $\phi$ ) of the soil, inducing the divergence (failure) of the nonlinear analysis (Faheem *et al.*, 2003). Reduced shear strength parameters ( $c_f$  and  $\phi_f$ ) will replace the real values of  $c$  and  $\phi$  in the shear strength equation of the Mohr-Coulomb criterion  $\tau_f = c_f + \sigma \tan \phi_f$ , where  $c_f = c/F$ ,  $\phi_f = \tan^{-1}(\tan(\phi)/F)$  and  $F$  is the safety factor.

On the other hand, the ELSM uses the finite-element analysis with the real values of the shear strength parameters of the soil and searches for the critical slip surface with the minimum value of  $F$ . In a 2D-FEM analysis, for an arbitrary slip surface  $L$ , the potential failure line is divided into small line segments, each one located inside of only one element of the 2D-FEM mesh, and the safety factor  $F$  is defined as follows (Borges & Cardoso, 2002; Borges, 2008):

$$F = \frac{\sum_{i=1}^N \tau_{\beta_i} l_i}{\sum_{i=1}^N \tau_i l_i} \quad (5)$$

where  $\tau_i$  - acting shear stress at the  $i$ -segment;  $\tau_{\beta_i}$  - soil shear strength at the  $i$ -segment;  $l_i$  -  $i$ -segment length;  $N$  - number of mesh elements intersected by the failure line.

While the SRM is associated to the Mohr-Coulomb model, more complex constitutive models can be used in the ELSM, such as, for example, critical state models for clays.

In braced excavations, several authors have calculated the basal-heave stability through finite-element analyses, mainly using formulations of the “strength reduction method” (SRM) (Faheem *et al.*, 2003; Faheem *et al.*, 2004; Cai *et al.*, 2002).

A new method for basal-heave stability analysis based on ELSM formulations is proposed in the paper (Section 3.2), which uses the FEM results of the code described in Section 2. This method is applied on the basal stability analysis of the two braced excavations studied below (Section 4-5), as well as compared with the Terzaghi (1943) and Bjerrum & Eide (1956) methods.

### 3.2. New method for basal-heave stability analysis

The proposed method (computer program) for basal-heave stability analysis calculates, at any stage of the problem, the safety factor,  $F$ , along a large number of potential failure surfaces (defined with criterion, as explained below) and searches for the most unfavourable surface, *i.e.* the surface with the lowest value of  $F$ .

Figure 3 illustrates, for a particular stage of a problem, different potential failure surfaces that can be defined and automatically generated by the computer program. A small value for  $b$  (Fig. 3) should be considered, so that a large number of potential failure surfaces is analysed. As depicted in Fig. 3, the automatically generated surfaces basically differ from each other in their slope behind the wall, since, as shown in several studies of braced excavations (Chen *et al.*, 2015; Do *et al.*, 2016), the most unfavourable failure surface might take an inclined direction on that region of the ground. The  $CD$ -segment makes an angle of  $45^\circ$  with the horizontal direction, as well as the  $DT$ -segment. Point  $T$  is the centre of the curve.

For a particular potential failure surface, the proposed method firstly determines the intersection points of the failure line with the edges of the finite elements of the 2D-mesh. Therefore, the failure line is divided into small line segments, each of them located inside of only one of the finite elements of the mesh (Fig. 4).

Thereafter, the average values of the effective stresses ( $\sigma'_x$ ,  $\sigma'_y$ ,  $\sigma'_z$  and  $\tau_{xy}$ , normal and shear stresses in the  $xyz$ -space, where  $xy$  is the plane of the 2D-finite element analysis) at each of those segments are computed by extrapolating from stresses at the Gauss points of the corresponding finite element.

Considering the failure line divided into line segments, the safety factor is computed by Eq. 5.  $\tau_i$  is determined from effective stresses  $\sigma'_x$ ,  $\sigma'_y$  and  $\tau_{xy}$ , known the angle that defines the  $i$ -segment direction.

Since the soil shear strength varies with consolidation and a critical state model is used in the finite element analysis,  $\tau_{\beta_i}$  at each stage is calculated by the following equation of the critical state soil mechanics (Britto & Gunn, 1987):

$$\tau_{\beta_i} = \frac{1}{2} M \exp\left(\frac{\Gamma - v_i}{\lambda}\right) \quad (6)$$

where  $M$  is given by Eq. 1, and  $v_i$ , the specific volume of soil at  $i$ -segment, is determined as follows:

$$v_i = \Gamma - k \ln p_i - (\lambda - k) \ln \alpha_{p_i} \quad (7)$$

At the  $i$ -segment,  $p_i = (\sigma'_{xi} + \sigma'_{yi} + \sigma'_{zi})/3$  is the effective mean stress and  $\alpha_{p_i}$  is the  $p$ -value of the centre of the yield surface in  $p$ - $q$  plane (see Fig. 1b), extrapolated from  $\alpha_p$ -values at Gauss points;  $\lambda$ ,  $k$  and  $\Gamma$  are parameters of the  $p$ - $q$ - $\theta$  model (soil properties), whose meanings are as follows:  $\lambda$ , slope of normal consolidation line and critical state

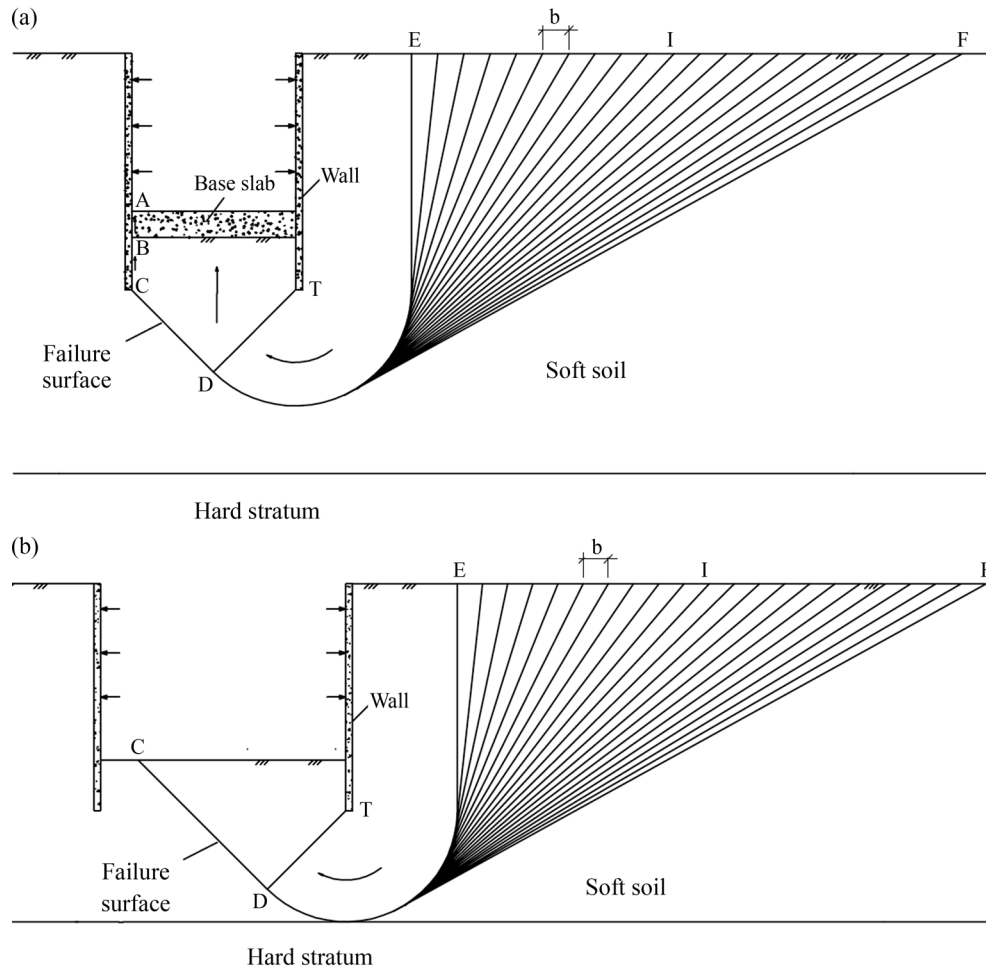


Figure 3 - Potential failure surfaces: a) hard stratum at a large depth; b) hard stratum at a low depth.

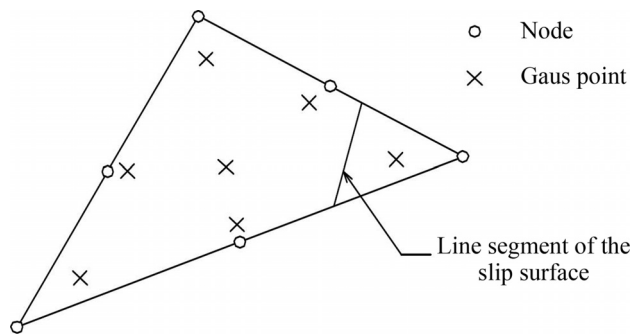


Figure 4 - Six-noded triangular finite element.

line;  $k$ , slope of swelling and recompression line;  $\Gamma$ , specific volume of soil on the critical state line at mean normal stress equal to 1 kPa.

If a part of the failure surface coincides with a soil-wall interface (like the  $BC$ -segment in Fig. 3a) or a jet-grout base slab-wall interface (like the  $AB$ -segment in Fig. 3a),  $\tau_{fi}$  can be calculated with the following equation:

$$\tau_{fi} = a_i + \sigma_{ni} \tan \delta_i \quad (8)$$

where  $a_i$  and  $\delta_i$  are the adhesion and friction angle of the  $i$ -segment of the soil-wall or jet-grout-wall interface (modelled by joint-elements);  $\sigma_{ni}$  is the normal stress on the plane of the  $i$ -segment.

#### 4. Description of the Problem

Two solutions (case A and case B) of a strutted excavation in a soft clay are analysed (Fig. 5), using the above mentioned codes (FEM code and basal-heave stability program). The ground consists of a 35-m-thick soft clay overlying a “hard stratum”. The water table is at the ground surface. A jet-grout base slab is considered for case A (Fig. 5), while none jet-grout slab is modelled for case B. All other characteristics of the problem are kept equal for both cases.

The problem comprises a 12-m-deep excavation with width of 14 m (Fig. 5). The retaining structure is a 1.2 m-thick diaphragm wall of reinforced concrete with length of 19 m (7 m embedded below the excavation base). The excavation is carried out in a total time of 24 days at a uniform rate. A 2.0 m-thick jet-grout slab is considered in case A (constructed with secant columns, before the exca-

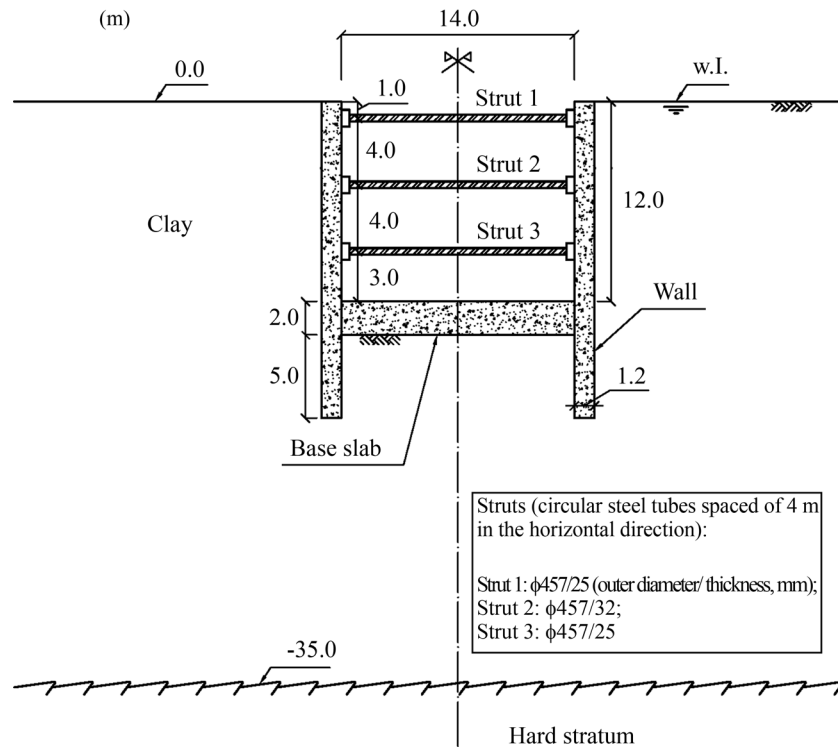


Figure 5 - Cross section of the excavation (case A).

vation) to support the wall below the excavation base. None jet-grout slab is modelled for case B, as said.

In case A, “dissipation holes” in the jet-grout slab (see Fig. 6a) are constructed after the excavation in order to avoid long term overpressures on the lower face of the slab. Therefore, it is assumed that, after the end of excavation, the water flows through the “dissipation holes”, being pumped within the excavated area. This corresponds to defining the boundary condition of pore pressure on the lower face of the slab equal to 20 kPa (considering the unit weight of water equal to 10 kN/m<sup>3</sup> and that the thickness of the slab is 2.0 m).

Circular steel tubes, spaced 4 m in the horizontal direction, are used for the struts, whose sections are indicated in Fig. 5.

Basically, for the present cases, the finite element code uses the following features: a) plane strain conditions; b) fully coupled formulation of the flow and equilibrium equations with soil constitutive relations formulated in effective stresses - Biot consolidation theory (Borges, 1995; Lewis and Schrefler, 1987; Britto and Gunn, 1987); c)  $p$ - $q$ - $\theta$  critical state model to simulate the constitutive behaviour of soil (Borges, 1995; Lewis and Schrefler, 1987);

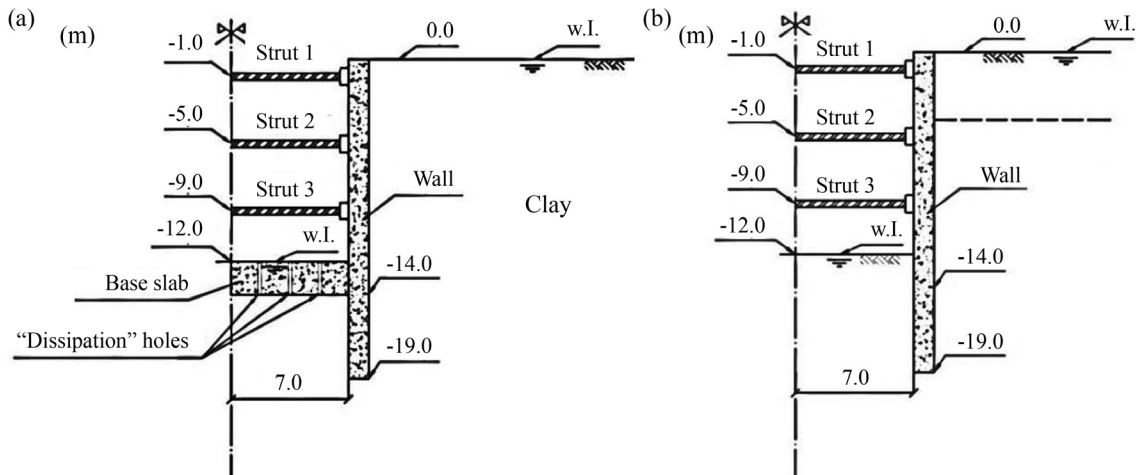


Figure 6 - Hydraulic boundary conditions: a) case A (with base slab); b) case B (without base slab).

d) elastic linear model to simulate the reinforced concrete wall, the jet-grout slab and the steel struts; e) joint elements with elastic-perfectly plastic behaviour to simulate the slab-wall interfaces.

The values of the  $p$ - $q$ - $\theta$  critical state model for the soft clay are indicated in Table 1 ( $\lambda$ , slope of normal consolidation line and critical state line;  $k$ , slope of swelling and recompression line;  $\Gamma$ , specific volume of soil on the critical state line at mean normal stress equal to 1 kPa;  $N$ , specific volume of normally consolidated soil at mean normal stress equal to 1 kPa;  $\phi'$ , angle of shearing resistance defined in effective terms). Table 2 shows other geotechnical properties of the clay:  $\gamma$ , unit weight;  $\nu'$ , Poisson's ratio for drained loading;  $k_h$  and  $k_v$ , coefficients of permeability in horizontal and vertical directions. Table 3 indicates for the clay the variation with depth of the at-rest earth pressure coefficient,  $K_0$ , and undrained shear strength,  $c_u$  ( $\sigma'_{v0}$ , at-rest vertical effective stress). The clay is moderately over-consolidated from the surface to the depth of 4 m and normally consolidated from 4 m to the hard stratum. The values adopted for the clay are similar to those used by Finno *et al.* (1991) regarding an excavation in soft soils constructed in Chicago, USA.

Figure 7 shows the finite element mesh of the problem. Two types of the six-noded triangular element are considered: (i) the coupled element, for the clay elements where consolidation is considered; (ii) the non-coupled element, for the wall and jet-grout slab elements. All six nodes of the coupled element have displacement degrees of freedom while only the three vertex nodes have excess pore pressure degrees of freedom. The six nodes of a non-coupled element have only displacement degrees of freedom.

**Table 1** - Parameters of the  $p$ - $q$ - $\theta$  critical state model.

|           | $\lambda$ | $\kappa$ | $N$  | $\Gamma$ | $\phi'$ ( $^\circ$ ) |
|-----------|-----------|----------|------|----------|----------------------|
| Soft clay | 0.18      | 0.025    | 3.16 | 3.05     | 26                   |

**Table 2** - Geotechnical properties of the clay.

|           | $\gamma$ (kN/m <sup>3</sup> ) | $\nu'$ | $k_x = k_y$ (m/s) |
|-----------|-------------------------------|--------|-------------------|
| Soft clay | 16                            | 0.25   | $10^{-10}$        |

**Table 3** - At-rest earth pressure coefficient and undrained shear strength of the clay.

| Depth (m) | $K_0$   | $c_u$ (kPa)        |
|-----------|---------|--------------------|
| 0-4       | 0.9-0.5 | 13-6.7             |
| $\geq 4$  | 0.5     | $0.28\sigma'_{v0}$ |

The struts are modelled with three-node bar elements with linear elastic behaviour, with a Young's modulus of 206 GPa for the steel. However, due to the difference usually observed in practice between theoretical and effective strut stiffness, the latter was considered equal to half the theoretical stiffness, as suggested by O'Rourke (1992).

Six-node joint elements, with elastic-perfectly plastic behaviour, are used to simulate the interface between the jet-grout base slab and the wall, assuming that a thin portion of soil remains between these two materials. Taking into account the results of laboratorial tests performed by Matos Fernandes (1983), the interface strength was considered equal to the shear strength of the soft soil at the same depth and the elastic tangential stiffness was established as-

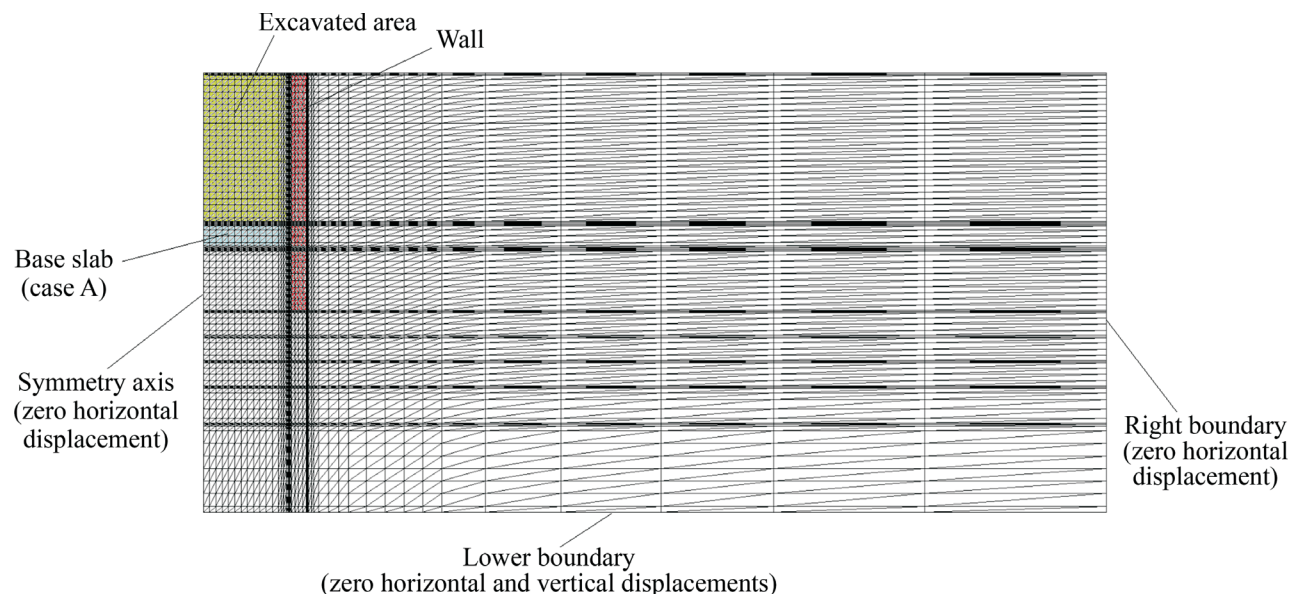


**Figure 7** - Finite element mesh.

suming a tangential displacement of 1 mm required for the shear strength mobilization.

Regarding the boundary conditions, no horizontal displacement is allowed on the vertical boundaries of the mesh, while the bottom boundary (“hard stratum”, at depth of 35 m) is completely fixed in both the vertical and horizontal directions. The left vertical boundary corresponds to the symmetry plan of the problem. In hydraulic terms, it is assumed that, in the unexcavated side, the water level remains at the ground surface (which is a conservative and simplified assumption and presupposes that there is a flow that provides water into the ground). On the excavated side, the water level coincides, at each stage of excavation, with the excavation base (which means that the water, inside the excavated area, is assumed to be pumped). A fully coupled analysis is performed both during and after the excavation period.

The 1.2-m-thick wall is modelled as an isotropic elastic material with a Young’s modulus ( $E$ ) of 18 GPa and a Poisson’s ratio ( $\nu$ ) of 0.2. The isotropic elastic model is also considered for the jet-grout slab with the values of 150 MPa and 0.2 for  $E$  and  $\nu$ , respectively. The value of  $E$  is the same as that mentioned by Jaritngam (2003) for the jet-grout columns constructed in a clayey soil.

The excavation was modelled removing sequentially 1-m-thick layers of finite elements within the area of excavation (see Fig. 7); 2 days of construction, at a uniform rate, was the time considered for each layer.

### 5. Analysis of Results

Theoretically, during the excavation period, because of the very low permeability of the soft soil, the behaviour of the problem can be considered as undrained. Increments of pore pressure and effective stress take place with the excavation process, whose magnitudes depend on both the soil properties and the total stress path, as explained below. Figure 8 illustrates the theoretical stress transfer in an un-

drained triaxial test with an extension stress path (as in an excavation, below its base) (Borges, 1995), where compression and tension stress increments are considered as positive and negative, respectively. Skempton’s  $A$  parameter represents the influence of the soil properties and takes positive values lower than 0.7 in lightly to moderately over-consolidated clays (Lambe & Whitman, 1969). In an extension stress path, as expected, the increment of pore pressure,  $\Delta u$ , is negative. Basically, since total mean stress reduces but the volume of soil does not change (undrained behaviour), negative increments of pore pressure are therefore generated. On the other hand, the equilibrium of stresses also determines that  $\Delta\sigma'_1$  is negative (tension increment) while  $\Delta\sigma'_3$  is positive (compression increment). This is what usually happens during the construction period in an excavation of a saturated clay, below its base (which is corroborated by the numerical results of the present study, as shown below). When the soil behaves elastically (as approximately happens in the early stages of an extension stress path), Skempton’s  $A$  parameter takes the theoretical value of 1/3.

Figure 9 shows colour maps of the pore pressure increments at the end of excavation for cases A and B. Increment of pore pressure is defined herein as the difference between pore pressure at a particular instant and its initial hydrostatic value before excavation.

The results show that negative increments of pore pressures are generated during the excavation, as expected. For both cases, the highest negative value of the increments occurs below the excavation base near the left boundary (symmetry plan), being higher for case B (without base slab). This is explained by the highest decrease of total mean stress associated to the excavation, which occurs on that zone. However, such decrease is smaller for case A due to the slab-wall interaction (shear stresses), which determines that a smaller decrease of total mean stress is trans-

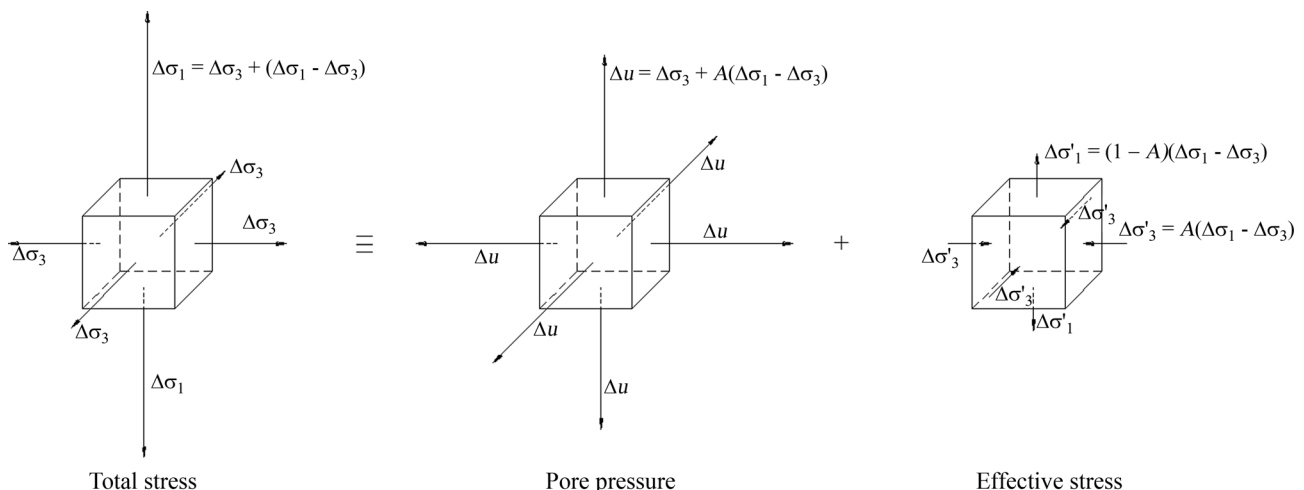
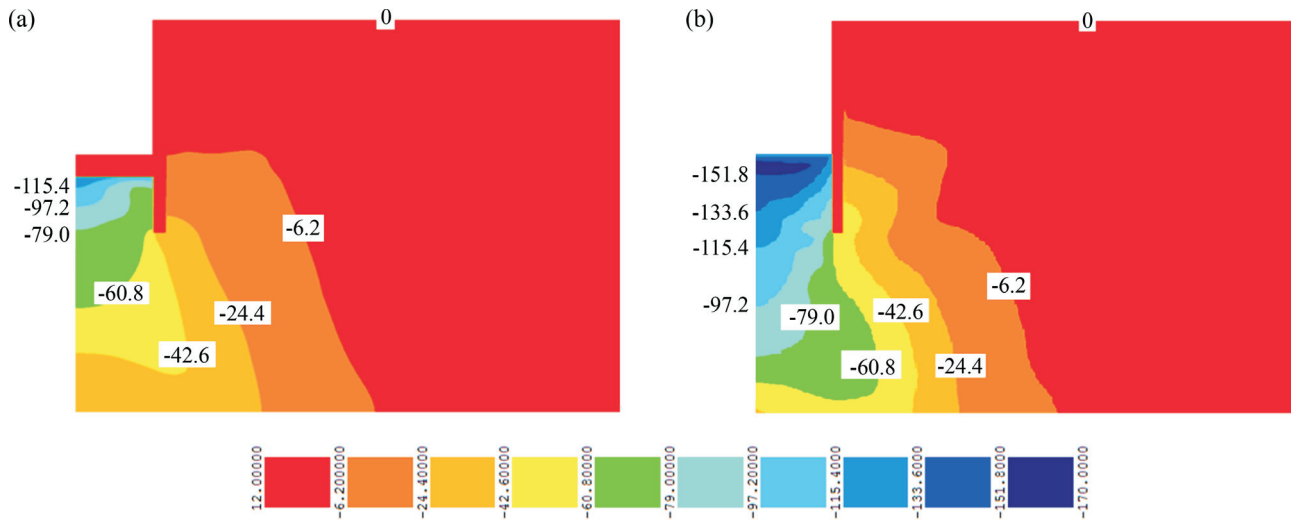


Figure 8 - Theoretical stress increments in an undrained triaxial test with an extension stress path.



**Figure 9** - Increments of pore pressure at the end of excavation (kPa): a) with base slab (case A); b) without base slab (case B).

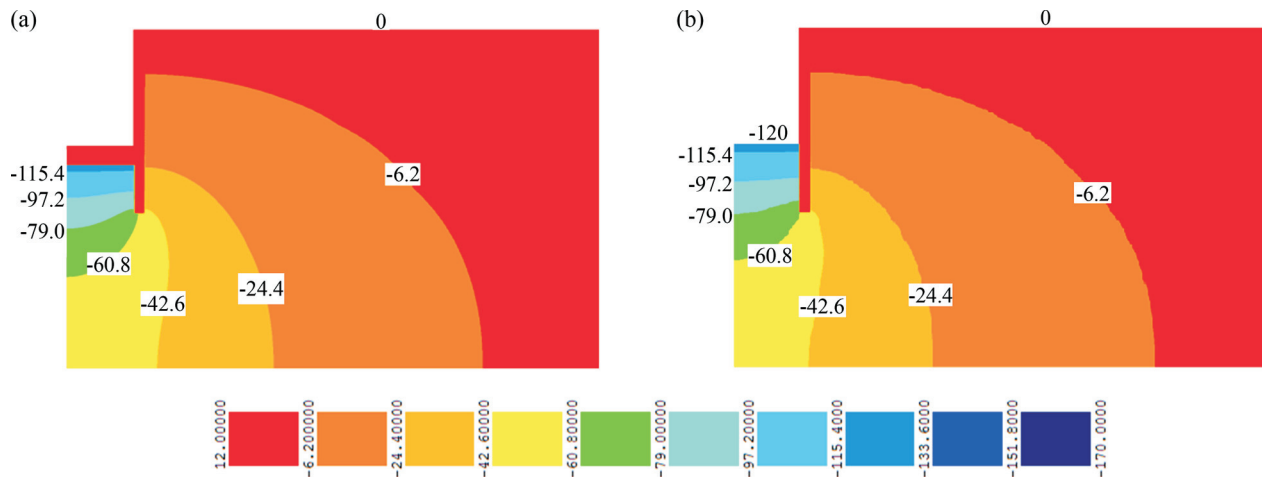
mitted to the soil under the slab and, therefore, smaller negative increments of pore pressures are generated.

On the unexcavated side, a tendency for generating negative increments is also observed, although with lower values than on the excavated side, for a lower decrease of total mean stress occurs on that side. In case A, the jet-grout slab, which supports the wall below the excavation base, contributes to a lower decompression on the unexcavated side and, therefore, lower negative increments of pore pressures are generated on that side.

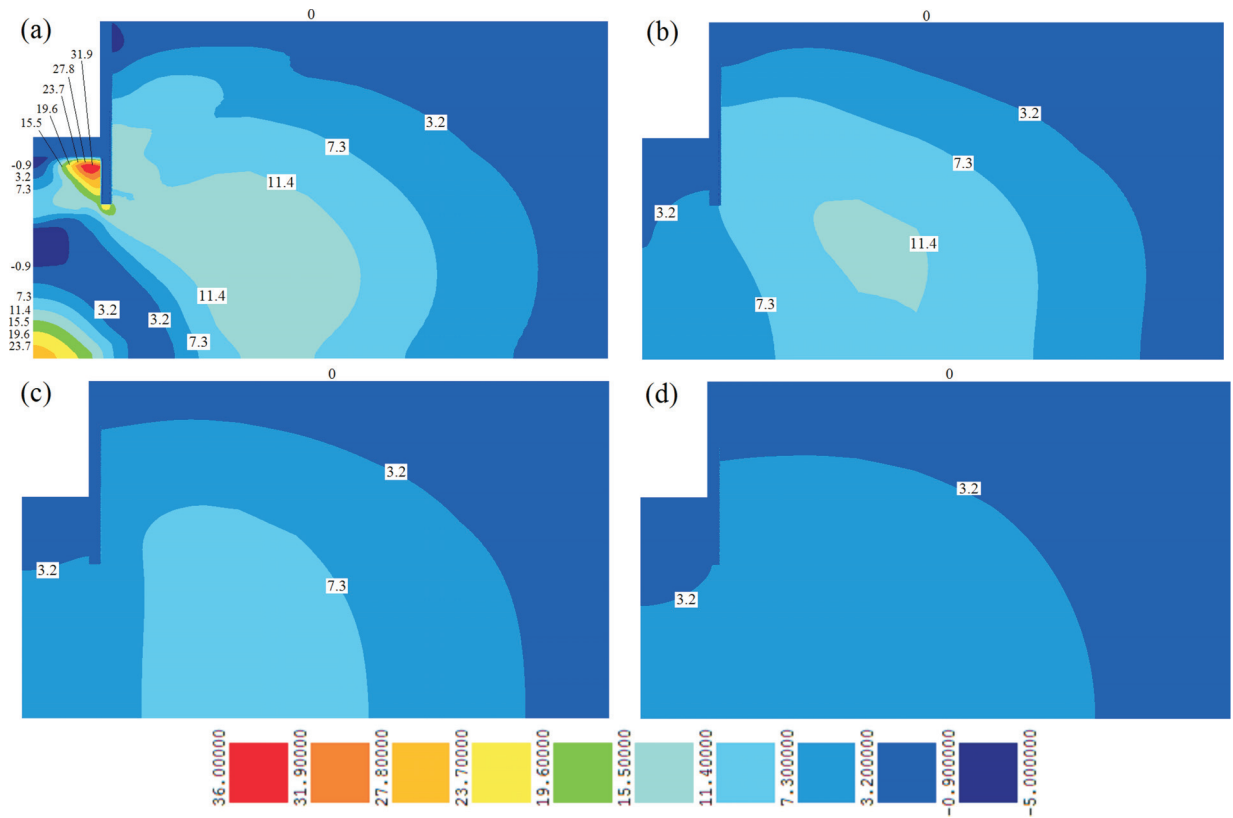
Colour maps of pore pressure increments at the end of consolidation (long term distributions) are shown in Fig. 10. After the excavation period, the geotechnical behaviour of the problem is globally determined by the consolidation process, which is dependent on both the magnitude of the pore pressure increments at the end of excavation and the long term hydraulic conditions. Since the values of pore pressure at the end of consolidation are different from its initial values before excavation (due to the water

table lowering on the excavated side), the consolidation process is only determined by the dissipation of the difference between pore pressure at the end of excavation and pore pressure at the end of consolidation. Comparing Figs. 9 and 10, the most significant variations in response to the consolidation are observed for case B on the excavated side under the excavation base, where water pressure increases (reduction of the negative value of increments of pore pressure). At the end of consolidation, very similar shapes of isovalue curves of increments of pore pressure are observed for both cases. These curves are perpendicular to the flow lines of the steady water flow (from the supported side to the excavated side, passing under the lower wall tip) that is reached at end of consolidation.

In order to complement the understanding of the consolidation process for both cases, Figs. 11 and 12 show colour maps of the differential pore pressure at several stages after the construction period. The differential pore pressure is defined herein as the difference between pore pressure at



**Figure 10** - Increments of pore pressure at the end of consolidation (kPa): a) with base slab (case A); b) without base slab (case B).



**Figure 11** - Differential pore pressure (kPa) for case A (with base slab), at several stages: a) end of construction; b) 6 months after the end of construction; c) 2 years after the end of construction ; d) 5 years after the end of construction.

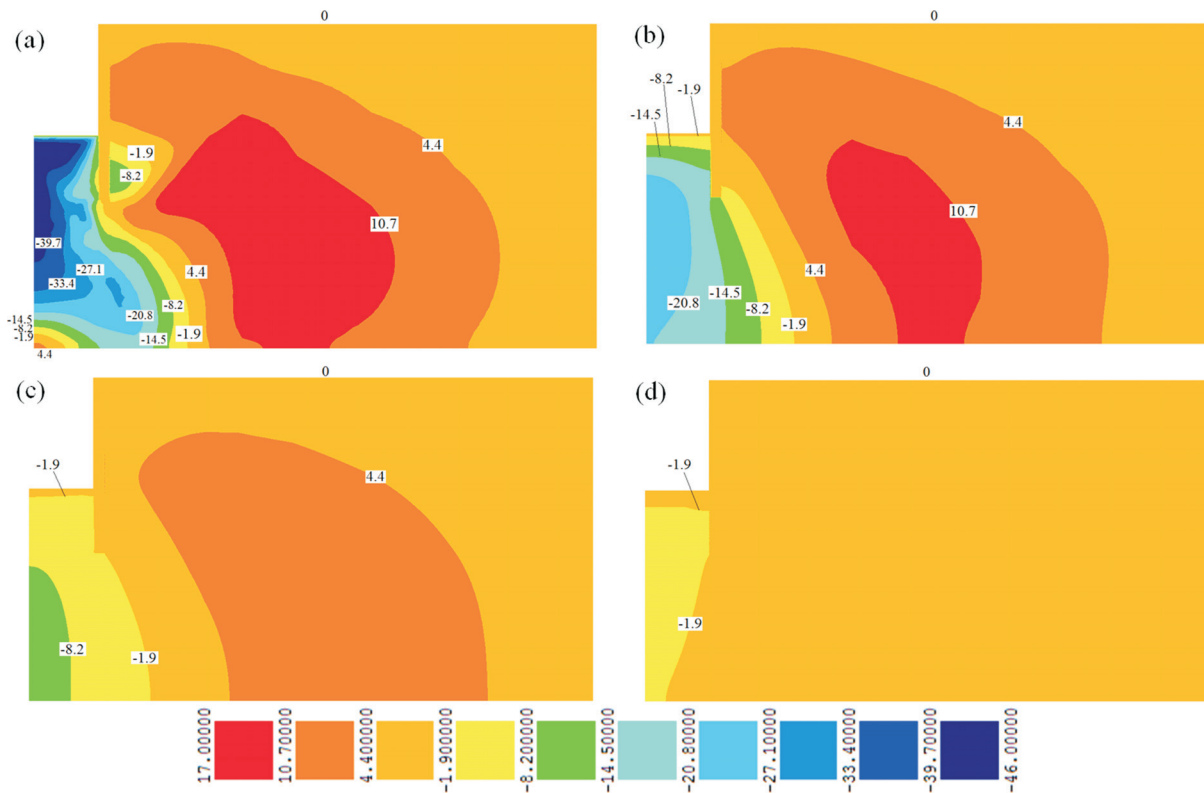


**Figure 12** - Differential pore pressure (kPa) for case B (without base slab), at several stages: a) end of construction; b) 6 months after the end of construction; c) 2 years after the end of construction; d) 5 years after the end of construction.

a particular instant and its long-term value at the end of the consolidation.

From the comparison of the results of Figs. 11 and 12, one can corroborate that, in response to the consolidation, the pore pressure globally decreases for case A, more significantly on the excavated side, while, for case B, it increases on the excavated side and on a region of the supported side near the wall, below the excavation base level.

Principal effective stresses at the end of the excavation are shown in Fig. 13 for both cases. Rotations of the principal stress directions on both sides of the wall, mainly below the excavation base level, are observed in both cases, which means that large shear stress (deviatoric stress) occurs in those regions. However, smaller shear stress (*i.e.*

smaller rotation of the principal stress directions) is observed for case A, which is due to the support effect of the jet-grout slab below the excavation base.

Complementing Fig. 13, Fig. 14 shows colour maps of the stress level,  $SL$ , in the ground for both cases. The stress level,  $SL$ , measures the proximity to the soil critical state and is defined as follows:

$$SL = \frac{q}{p \cdot M} \tag{9}$$

where  $p$  is the effective mean stress,  $q$  the deviatoric stress and  $M$  the parameter which defines the slope of the critical state line in the  $p$ - $q$  plane, as said above (Section 2). In normally consolidated soils,  $SL$  varies from zero to 1, the latter

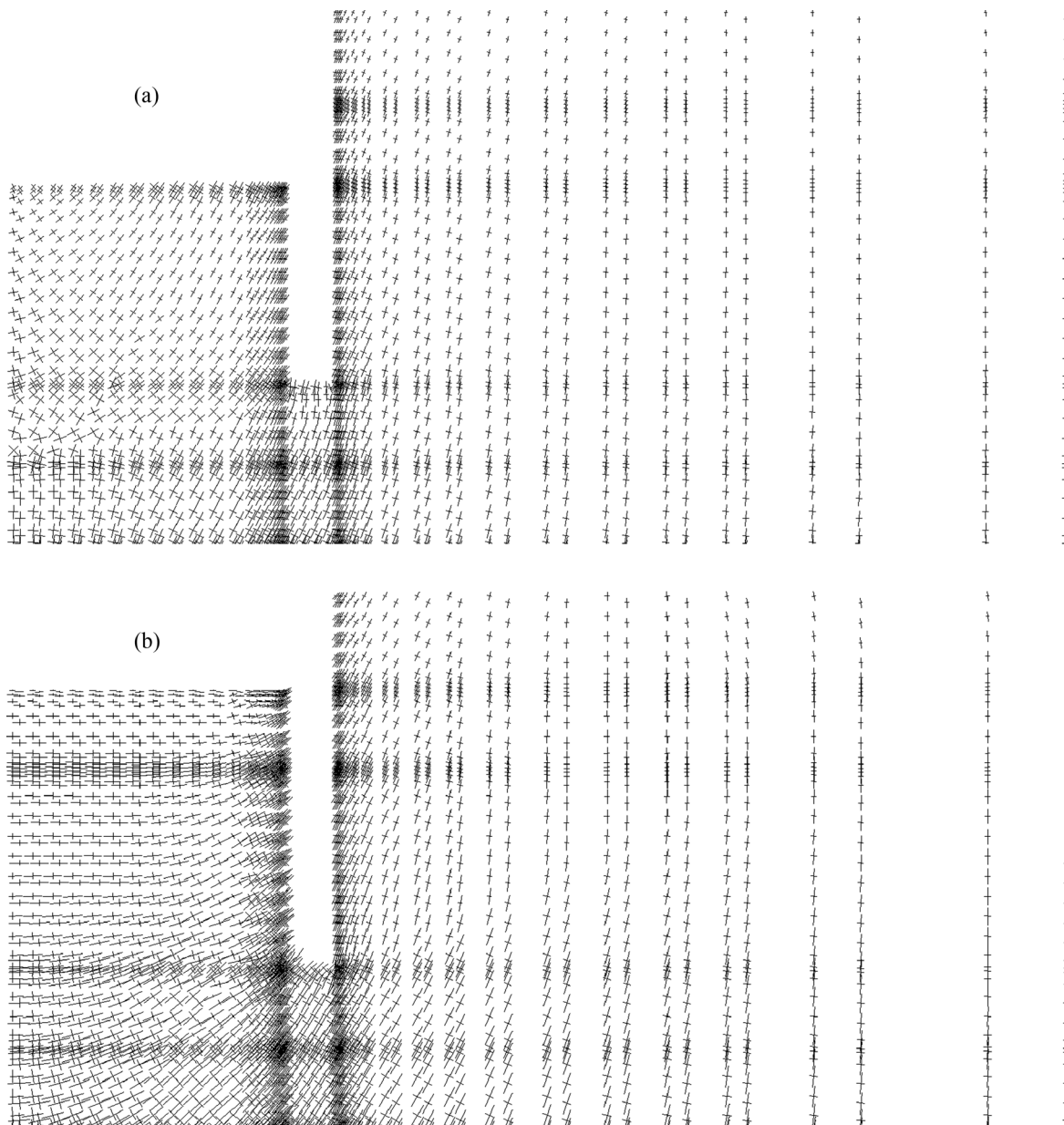


**Figure 13** - Principal effective stresses at the end of excavation: a) with base slab (case A); b) without base slab (case B).

being the critical state level. In over-consolidated soils, because of the peak strength behaviour, the stress level may be higher than 1.

Figure 14 shows that  $SL$  significantly increases during excavation, which is basically related with the increase of the deviatoric stress mentioned above. As expected, at the end of the excavation, higher values of  $SL$  are observed for case B on both sides of the wall below the excavation base level. For this case, in the supported side, the area in critical state extends to larger distances from the wall. However, a contrary effect is observed behind the wall near the ground surface, where  $SL$  is lower for case B. As shown

below, this effect is related to the profile of the wall horizontal displacement for both cases, which takes smaller values near the ground surface for case B, although much higher values for this case are observed for depths larger than 2 m. These differences in the wall displacement profiles determine different stress redistribution within the soil, which induces the mentioned effect in  $SL$ .

Calculated from the finite element (FE) results with the computer program for basal-heave stability analysis described in Section 3.2, Fig. 15 depicts, at several stages of excavation, the values of safety factor ( $F$ ) for both cases A and B, as well as  $F$  obtained by the classical Terzaghi

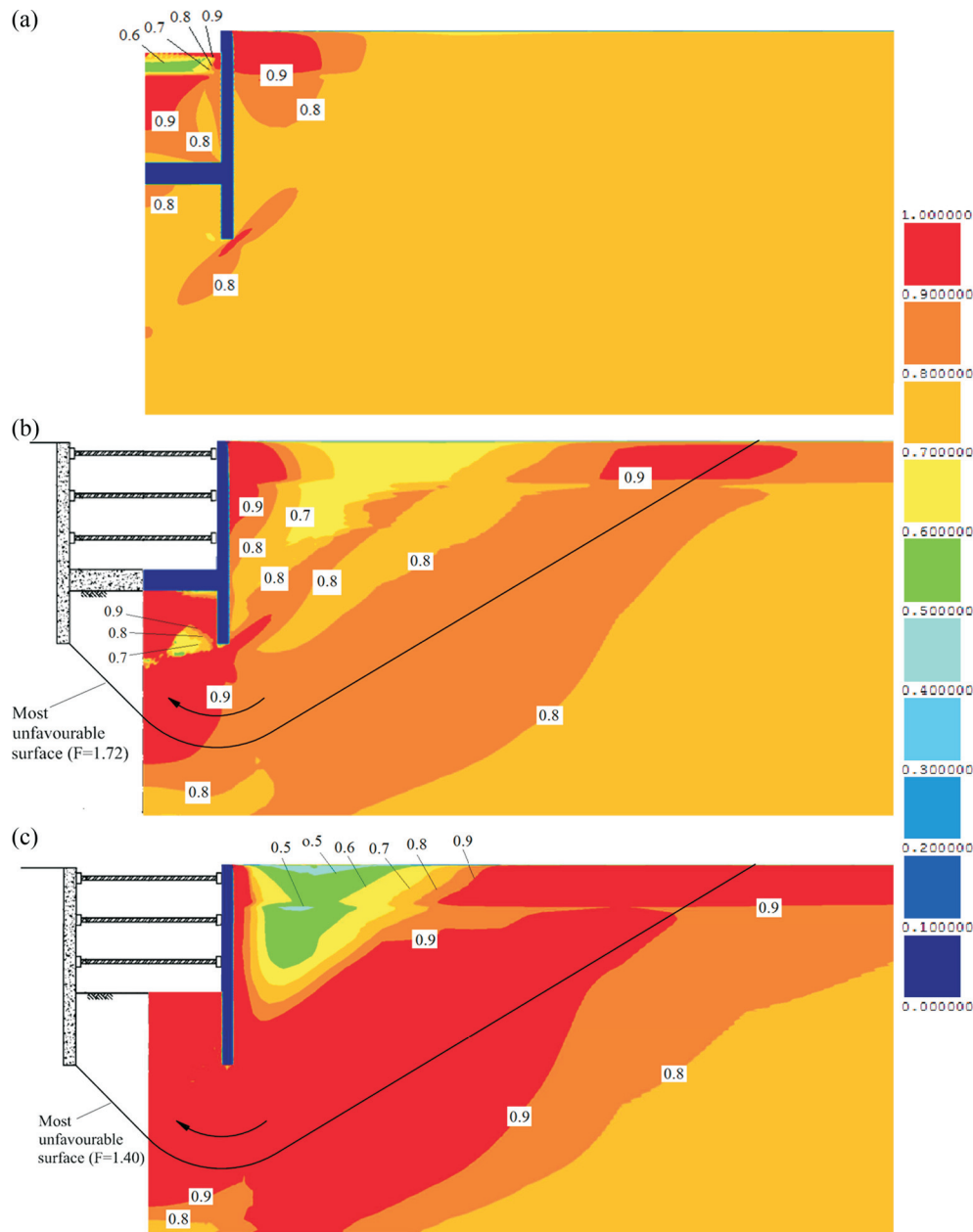


**Figure 14** - Stress level: a) Case A (with base slab) at 2m excavated; b) Case A (with base slab) at the end of excavation; b) Case B (without base slab) at the end of excavation.

(1943) and Bjerrum & Eide (1956) methods. With regard to the FE analysis, Fig. 15 shows the safety factor is significantly increased by the incorporation of the jet-grout base slab ( $F$  takes values of 1.72 and 1.40 for cases A and B respectively, at the end of the excavation; the most unfavourable surface obtained, which is identical for both cases, is also shown in Fig. 14). This clearly corroborates that, by reducing the stress level of the soft soil (as seen above), incorporating a soil-cement slab below the excavation base also implies that a significant increase in stability occurs. As expected, Fig. 15 also shows that such influence on the stability is not captured by the Terzaghi (1943) and Bjerrum & Eide (1956) methods, since their values of  $F$ , similar for both methods, are also very similar to those obtained from the FE analysis for case B (without base slab) but, therefore, significantly different from those of case A (with base slab). As said in Section 3.1, this is a conclusion that reinforces the importance of using more complex methods, like

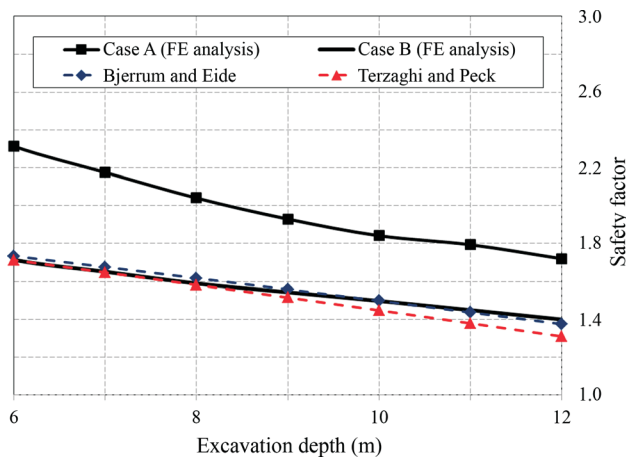
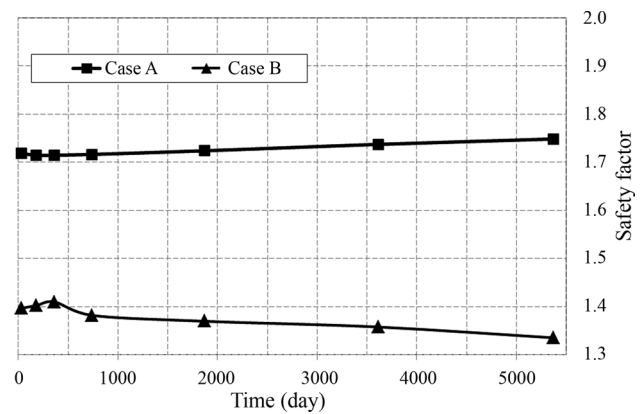


**Figure 15** - Safety factor against bottom heave for cases A (with slab) and B (without slab) obtained from the FE analyses. Comparison with Terzaghi (1943) and Bjerrum & Eide (1956) methods.

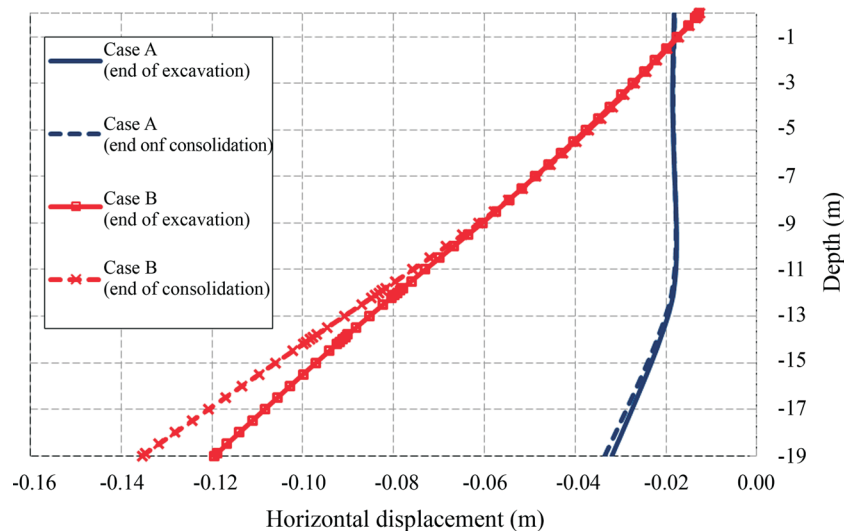
the one presented in this study based on FE analysis and ELSM formulations, whose results incorporate the influence of the retaining system stiffness, so that more accurate results can be reached.

Figure 16 shows the evolution in time of the safety factor in response to the consolidation process after the end of the excavation for both cases A and B, calculated from the FE results. These results show that  $F$  does not change significantly with time for both cases (although it reduces with time in the case without base slab, from a maximum of 1.40 to a minimum of 1.34), which reflects that the ratio of the acting shear stress sum to the shear strength sum along the most unfavourable surface is not significantly influenced by the consolidation process in the present excavation.

Diagrams of the wall horizontal displacement are shown in Fig. 17 for both cases. As expected, these results show that the wall displacement is much larger in the case without the base slab (case B), which corroborates the significant support effect of such structural element. In case B,



**Figure 16** - Safety factor against bottom heave at several stages after the end of excavation for cases A and B (FE analysis).



**Figure 17** - Wall horizontal displacement at the end of excavation and end of consolidation for cases A and B.

in overall terms, the wall rotates with centre at the top of the wall (a typical behaviour when there is no ground treatment below the excavation base), while, for case A, the horizontal displacement is approximately uniform from the top to 12 m depth (level of the base slab). In case A, the embedded depth of the wall takes a typical behaviour of a cantilever, supported on the jet-grout slab. Figure 17 also shows that the wall displacement increases in response to the consolidation, mainly for case B below the excavation base, which is related to the reduction of earth pressure on the excavated side face of the wall, as explained below.

Earth pressure in terms of horizontal stress (*i.e.* pore pressure plus horizontal effective stress) on the wall faces is depicted in Fig. 18, at the end of excavation and at the end of consolidation, for both cases. Earth pressure on the excavated side is depicted as negative while on the supported side it is depicted as positive. In response to the excavation, on the supported side face, there is no significant variation of earth pressure from the top to approximately 10 m depth, while a significant reduction is observed for larger depths (where the wall displacement is larger, as shown in Fig. 17). This reduction is larger for the case without base slab, since the horizontal displacement of the wall is larger. As to the post-excavation period, the earth pressure on the supported side face practically does not change in response to the con-

solidation, which is due to the contrary variations of pore pressure and horizontal effective stress that globally tend to compensate each other.

As to the excavated side, the earth pressure reduces with the excavation for both cases, as expected, because of the soil decompression on that side. Since the horizontal displacement of the wall towards the excavated side is larger for the case without slab (case B), the earth pressure on the excavated side face is larger in this case. Regarding the post-excavation period, a reduction of earth pressure with the consolidation occurs on the excavated side for both cases, although its magnitude is not very high for case A. Similar values of the earth pressure are observed, at the end of consolidation, for both cases.

In order to analyse how the pore pressure and the horizontal effective stress separately act on the wall faces, Fig. 19 depicts their results for both cases at the end of excavation and at the end of consolidation. Values on the excavated side are depicted as negative while on the supported side they are depicted as positive.

On the excavated side face, pore pressure significantly reduces in response to the excavation for both cases, although this reduction is larger for the case without base slab (case B). On this face, pore pressure also decreases in response to the consolidation for case A, while a small con-

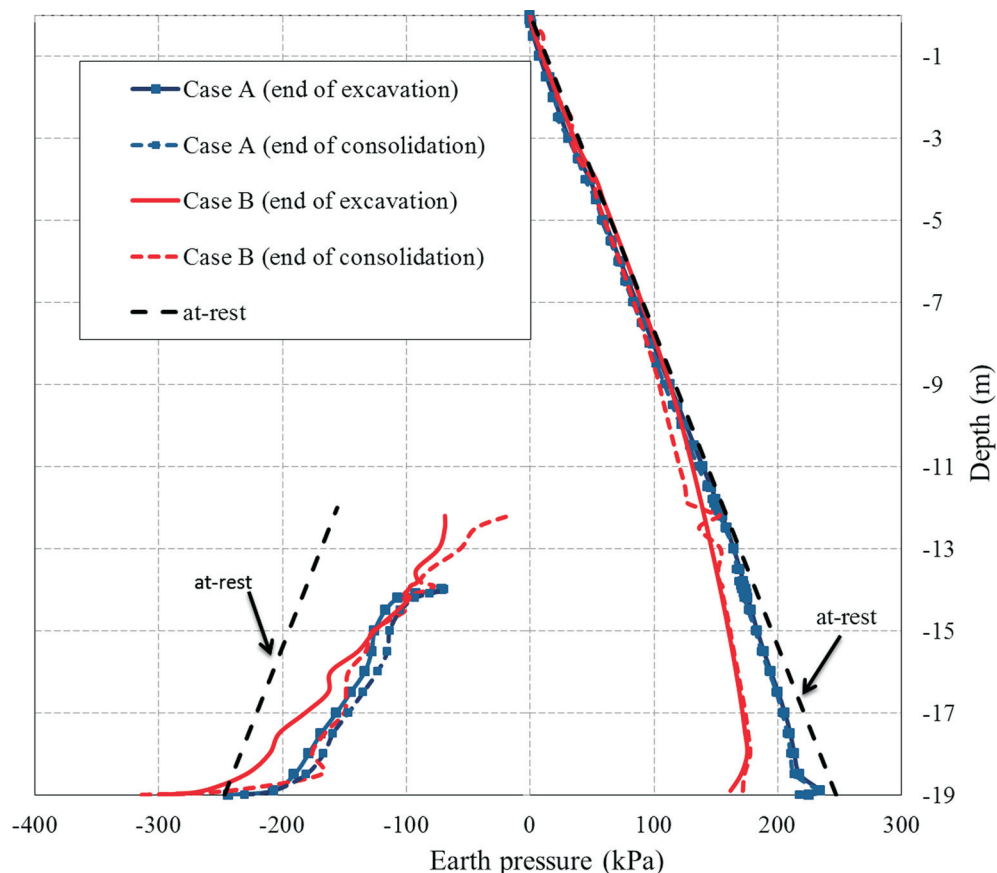


**Figure 18** - Earth pressure on the wall faces at the end of excavation and at the end of consolidation for both cases (with and without base slab).

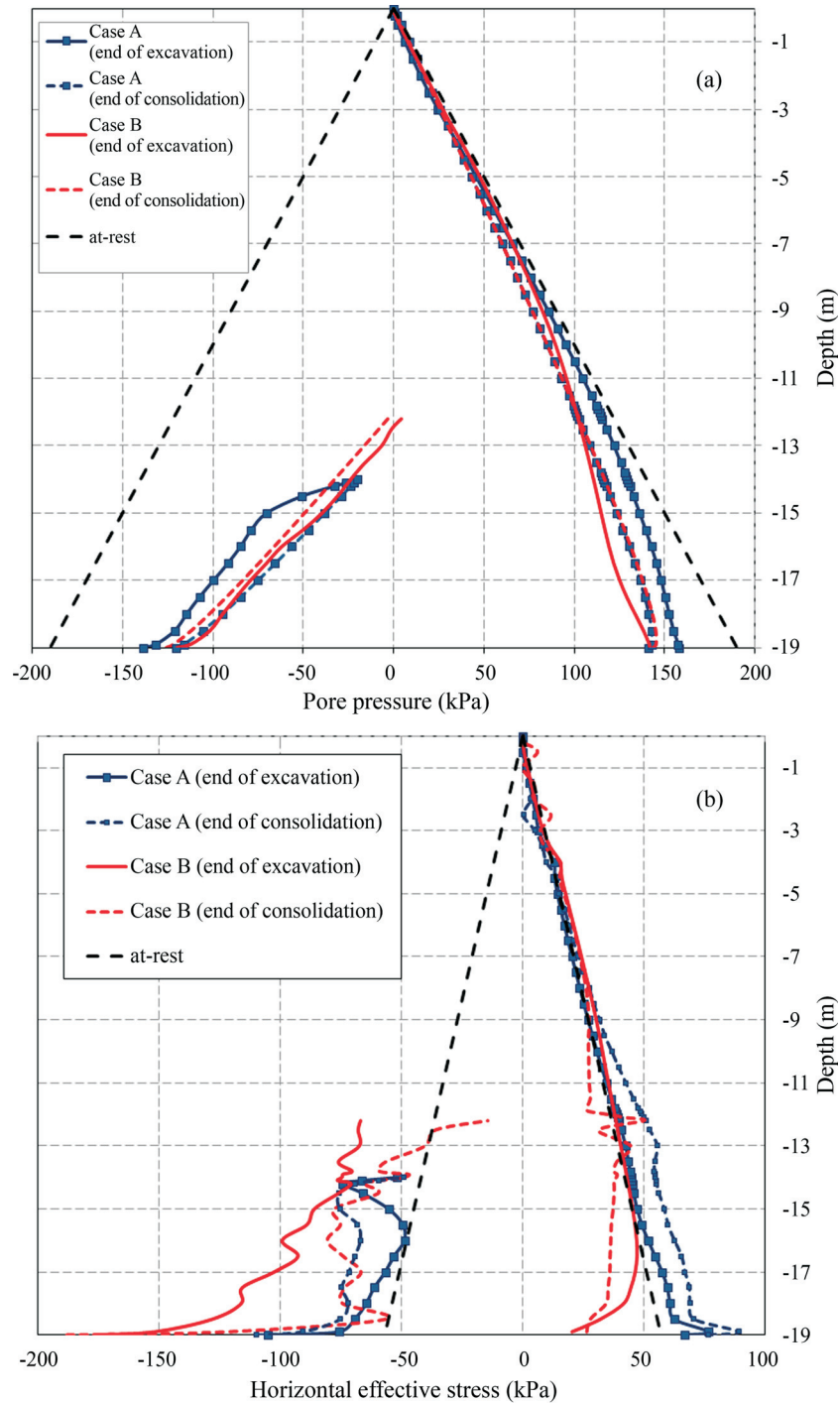


**Figure 19** - Pore pressure (a) and horizontal effective stress (b) on the wall faces at the end of excavation and at the end of consolidation for both cases (with and without base slab).

rary effect is observed for case B. Since long-term values of pore pressure are similar for both cases, this contrary effect is due to the difference of values at the end of excavation.

On the supported side face, a reduction of the pore pressure is also observed in response to the excavation, although with less magnitude than on the excavated side face.

This reduction is also larger for the case without base slab. As to the effects of the consolidation on both cases, they are qualitatively similar to those on the excavated side face, *i.e.* pore pressure also reduces for case A, while a contrary effect is observed for case B (for depths larger than 12 m). At the end of consolidation, pore pressure on the supported side face takes smaller values than its initial hydrostatic

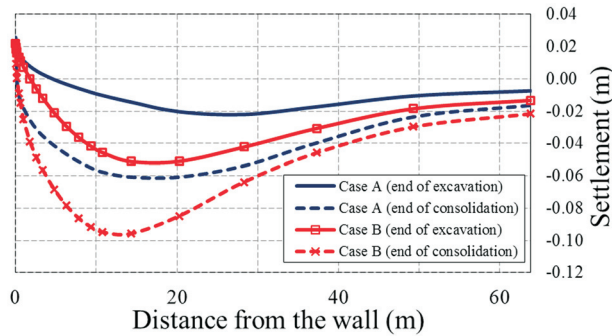


**Figure 20** - Settlements of the ground surface of the unexcavated side at end of excavation and end of consolidation for cases A and B.

values, which is related to the downward water flow that occurs behind the wall, as mentioned above.

As to the horizontal effective stress on the wall faces, Fig. 19b shows that its values significantly increase in response to the excavation on the excavated side face for case B; the same effect also occurs for case A although with less magnitude. As expected, this fact is in consonance with the theoretical scheme of Fig. 8, since, in global terms, extension stress paths take place below the excavation base. In response to the consolidation, the horizontal effective stress on the excavated side face reduces for case B since pore pressure increases, while the contrary effect occurs for case A.

Regarding the horizontal effective stress on the supported side face, its evolution in response to the excavation is different for both cases, mainly for depths larger than 9 m. For case A (with base slab) the evolution is qualitatively similar to that on the excavated side face, *i.e.* the hor-

izontal effective stress increases as pore pressure declines. For case B, both the pore pressure and the horizontal effective stress reduce. This effect is mainly due to the much larger horizontal displacement of the wall towards the excavation side for the case without slab (see Fig. 19). In response to the consolidation, the evolution is qualitatively similar to that on the excavated side face, *i.e.* the horizontal effective stress reduces for case B since pore pressure increases, while the contrary effect occurs for case A.

Figure 20 shows the surface settlements of the unexcavated side. These diagrams have the typical concave shapes and are directly related to the wall horizontal displacements. The settlement is much higher for case B. The maximum value at the end of consolidation increases about 60 % when compared to case A. Figure 20 also shows that, in response to the consolidation, there are significant downward displacements at the surface in both cases, which is determined not only by the increase of the wall displacements with the consolidation (more significant for case B, as shown above), but also by the reduction of soil volume in that side determined by the decrease of pore pressure (more significant for case A).

Figure 21 shows the diagrams of the wall bending moment for cases A and B. As expected, the presence of the jet-grout slab determines that the shape of the diagram is different (since the wall has one extra support). The maximum negative moment occurs near the base slab for case A while it occurs near the strut 2 (at the end of the excavation period) and strut 3 (at the end of consolidation) for case B. In the post-excavation period, the bending moment diagram does not significantly change for case A, while a sig-

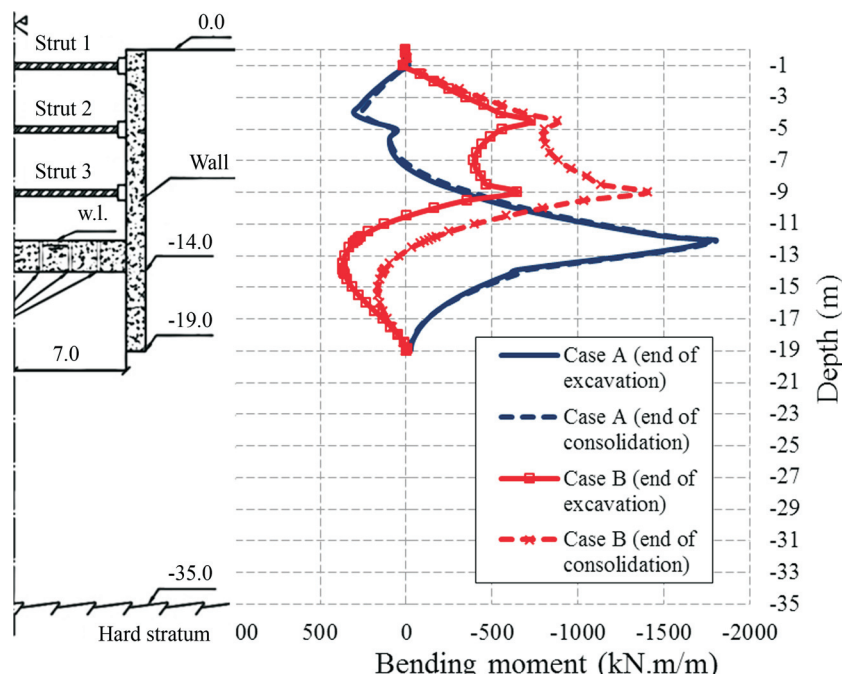


**Figure 21** - Wall bending moment at end of excavation and end of consolidation for cases A and B.

nificant increase of the negative values and reduction of the positive values are observed for case B; this is directly related to the variation of the earth pressure on the wall, where a significant reduction on the excavated side face for case B was observed (Fig. 19), as commented above.

The horizontal compression load in the jet-grout slab for case A is illustrated in Fig. 22. This figure shows that the compression load does not significantly change in response to consolidation, which is also consistent with previous comments on the earth pressure on the wall faces for case A, which also does not significantly change during the post-excitation period (Fig. 18).

## 6. Conclusions

A strutted excavation in soft soil incorporating a jet-grout base slab was analysed through a computer code based on the finite element method and using a new method for basal stability analysis that utilizes the results of the finite element code. Fully mechanical-hydraulic coupled analysis was considered, as well as the  $p$ - $q$ - $\theta$  critical state model for soil constitutive behaviour. Two cases of the same problem, with and without soil-cement bottom slab, were compared. The following conclusions can be highlighted:

- (1) The incorporation of the jet-grout slab improved the excavation stability against bottom failure, as well as it significantly reduced the wall displacements and settlements of the supported ground.
- (2) As expected, the effect of the soil-cement slab on the excavation stability was not captured by the classical limit equilibrium methods of Terzaghi (1943) and Bjerrum & Eide (1956) - their results for safety factor revealed to be similar to those obtained from the FE analysis for the case without slab but significantly different from those of the case with slab. This reinforces the importance of using more complex methods for excavation bottom stability analysis, like the one presented in this study, based on the finite element method and formulations of the “enhanced limit slope stability method”.

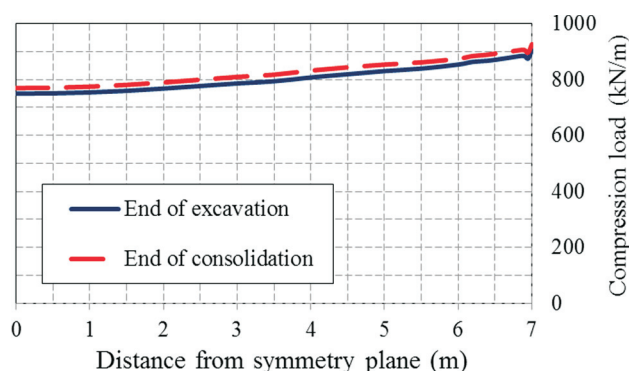


**Figure 22** - Compression load in the jet-grout slab at end of excavation and end of consolidation for case A.

- (3) In response to the consolidation, significant downward displacements on the supported soil surface occurred for both cases (with and without slab), which are basically related with the wall displacements and the reduction of soil volume determined by the decrease of pore pressure on the supported side - associated to the downward flow of the water behind the wall, due to the water table lowering on the excavated side.
- (4) Safety against bottom failure did not significantly change after the end of excavation in response to consolidation, although there was a reduction of safety factor, from of 1.40 to 1.34, during the post-excitation period, for the case without slab.

## References

- Alves, A.N. (2012). Cylindrical Diaphragm Walls in Deep Excavations in Soft Soils. M.Sc. Thesis, University of Porto, Portugal (in Portuguese).
- Azevedo, M.S. (2010). Cylindrical Excavations in Soft Soils Retained by Slurry Walls. M.Sc. Thesis, University of Porto, Portugal (in Portuguese).
- Barros, L. (2015). Berlin-Type Retaining Walls Combined with Jet-Grout or Cutter Soil Mixing Walls: Analysis by the Finite Element Method. M.Sc. Thesis, University of Porto, Portugal (in Portuguese).
- Basset, R.H. (1986a). The instrumentation of the trial embankment and of the Tensar SR2 grid. Proc. Prediction Symposium on a Reinforced Embankment on Soft Ground, King's College, London.
- Basset, R.H. (1986b). Presentation of instrumentation data. Proc. Prediction Symposium on a Reinforced Embankment on Soft Ground, King's College, London.
- Bjerrum, L. & Eide, O. (1956). Stability of strutted excavations in clay. *Géotechnique*, 6(1):32-47. <https://doi.org/10.1680/geot.1956.6.1.32>
- Borges, J.L. (1995). Geosynthetic-Reinforced Embankments on Soft Soils. Analysis and Design. Ph.D. Thesis in Civil Engineering, Faculty of Engineering, University of Porto, Portugal (in Portuguese).
- Borges, J.L. (2004). Three-dimensional analysis of embankments on soft soils incorporating vertical drains by finite element method. *Computers and Geotechnics*, 31(8):665-676. <https://doi.org/10.1016/j.compgeo.2004.11.001>
- Borges, J.L. (2008). Cut slopes in clayey soils: Consolidation and overall stability by finite element method. *Geotechnical and Geological Engineering*, 26(5):479-491. <https://doi.org/10.1007/s10706-008-9182-7>
- Borges, J.L. & Alves, A. (2014). Deep cylindrical excavations in soft soils retained by reinforced concrete diaphragm walls: Analysis considering the consolidation effect. Proc. 8th European Conference on Numerical Methods in Geotechnical Engineering, Delft, The Netherlands, pp. 717-722.

- Borges, J.L. & Cardoso, A.S. (2002). Overall stability of geosynthetic-reinforced embankments on soft soils. *Geotextiles and Geomembranes*, 20(6):395-421. [https://doi.org/10.1016/S0266-1144\(02\)00014-6](https://doi.org/10.1016/S0266-1144(02)00014-6)
- Borges, J.L. & Guerra, G.T. (2014). Cylindrical excavations in clayey soils retained by jet grout walls: Numerical analysis and parametric study considering the influence of consolidation. *Computers and Geotechnics*, 55(1):42-56. <https://doi.org/10.1016/j.compgeo.2013.07.008>
- Britto, A.M. & Gunn, M.J. (1987). *Critical Soil Mechanics Via Finite Elements*. Ellis Horwood Limited, England.
- Cai, F.; Ugai, K. & Hagiwara, T. (2002). Base stability of circular excavations in soft clay. *Journal of Geotechnical and Geoenvironmental Engineering*, 128(8):702-706. [https://doi.org/10.1061/\(ASCE\)1090-0241\(2002\)128:8\(702\)](https://doi.org/10.1061/(ASCE)1090-0241(2002)128:8(702))
- Chen, R.P.; Lee, Z.C.; Chen, Y.M. & Ou, C.Y. (2015). Failure investigation at a collapsed deep excavation in very sensitive organic soft clay. *Journal of Performance of Constructed Facilities*, ASCE, 29(3):04014078. [https://doi.org/10.1061/\(ASCE\)CF.1943-5509.0000557](https://doi.org/10.1061/(ASCE)CF.1943-5509.0000557)
- Clough, G.W. & Hansen, L.A. (1981). Clay anisotropy and braced wall behaviour. *J. Geotech. Engrg. Div.*, 107(7):893-913.
- Clough, G.W. & Reed, M.W. (1984). Measured behaviour of braced wall in very soft clay. *Journal of Geotechnical Engineering Division*, ASCE, 110(1):1-19. [https://doi.org/10.1061/\(ASCE\)0733-9410\(1984\)110:1\(1\)](https://doi.org/10.1061/(ASCE)0733-9410(1984)110:1(1))
- Costa, P.A. (2005). *Braced Excavations in Soft Clayey Soils - Behaviour Analysis Including the Consolidation Effects*. M.Sc. Thesis, Faculty of Engineering, University of Porto, Portugal (in Portuguese).
- Costa, P.A.; Borges, J.L. & Fernandes, M.M. (2007). Analysis of a braced excavation in soft soils considering the consolidation effect. *Geotechnical and Geological Engineering*, 25(6):617-629. <https://doi.org/10.1007/s10706-007-9134-7>
- Do, T.N.; Ou, C.Y. & Chen, R.P. (2016). A study of failure mechanisms of deep excavations in soft clay using the finite element method. *Computers and Geotechnics*, 73(2016):153-163. <https://doi.org/10.1016/j.compgeo.2015.12.009>
- Domingues, T.S. (2006). *Foundation Reinforcement with Stone Columns in Embankments on Soft Soils: Analysis and Design*. M.Sc. Thesis, Faculty of Engineering, University of Porto, Portugal (in Portuguese).
- Faheem, H.; Cai, F.; Ugai, K. & Hagiwarab, T. (2003). Two-dimensional base stability of excavations in soft soils using FEM. *Computers and Geotechnics*, 30:141-163. [https://doi.org/10.1016/S0266-352X\(02\)00061-7](https://doi.org/10.1016/S0266-352X(02)00061-7)
- Faheem, H.; Cai, F. & Ugai, K. (2004). Three-dimensional base stability of rectangular excavations in soft soils using FEM. *Computers and Geotechnics*, 31:67-74. <https://doi.org/10.1016/j.compgeo.2004.02.005>
- Finno, R.J.; Harahap, I.S. & Sabatini, P.J. (1991). Analysis of braced excavations with coupled finite element formulations. *Computers and Geotechnics*, 12(2):91-114. [https://doi.org/10.1016/0266-352X\(91\)90001-V](https://doi.org/10.1016/0266-352X(91)90001-V)
- Guerra, G.T. (2009). *Self-Supported Jet-Grout Walls in Cylindrical Excavations*. M.Sc. Thesis, University of Porto, Portugal (in Portuguese).
- Jaritngam, S. (2003). Design Concept of Soil Improvement for Road construction on soft clay. *Proc. Eastern Asia Society for Transportation Studies*, v. 4, pp. 313-322.
- Lade, P.V. & Duncan, J.M. (1973). Cubical triaxial tests on cohesionless soils. *J. Soil Mech. Found. Div.*, ASCE 99(19): 793-812.
- Lambe, T.W. & Whitman, R.V. (1969). *Soil Mechanics*. John Wiley and Sons, Inc., New York.
- Lewis, R.W. & Schrefler, B.A. (1987). *The Finite Element Method in the Deformation and Consolidation of Porous Media*. John Wiley and Sons, Inc., New York.
- Liu, S.Y.; Shao, L.T. & Li, H.J. (2015). Slope stability analysis using the limit equilibrium method and two finite element methods. *Computers and Geotechnics*, 63:291-298. <https://doi.org/10.1016/j.compgeo.2014.10.008>
- Mateus, R. (2010). *Braced Excavations in Soft Soils Incorporating Jet-Grout Base Slabs and Pre-Stressed Struts*. M.Sc. Thesis, University of Porto, Portugal (in Portuguese).
- Matos Fernandes, M.M. (1983). *Flexible Structures for Earth Retaining: New Design Methods*. Ph.D. Thesis in Civil Engineering, Faculty of Engineering, University of Porto, Portugal (in Portuguese).
- Matos Fernandes, M.; Cardoso, A.S.; Topa Gomes, A.; Borges, J.L.; Guerra, N.C. & Antão, A.N. (2012). Deep excavations in urban areas - Finite element modelling for three geotechnical scenarios and retaining solutions. In: *Innovative Numerical Modelling in Geomechanics*. Taylor & Francis Group, London, pp. 51-76.
- Monteiro, A.S. (2011). *Excavations in Clayey Soils Retained by Jet Grout Walls Reinforced with Steel Beams*. M.Sc. Thesis, University of Porto, Portugal (in Portuguese).
- Mita, K.A.; Dasari, G.R. & Lo, K.W. (2004). Performance of a three-dimensional Hvorslev-Modified Cam Clay model for overconsolidated clay. *International Journal of Geomechanics*, ASCE, 4(4):296-309. [https://doi.org/10.1061/\(ASCE\)1532-3641\(2004\)4:4\(296\)](https://doi.org/10.1061/(ASCE)1532-3641(2004)4:4(296))
- Nayak, G.C. & Zienkiewicz, O.C. (1972). Convenient form of stress invariants for plasticity. *Journal of the Structural Division*, 98(4):949-954.

- O'Rourke, T.D. (1992). Base stability and ground movement prediction for excavations in soft soil. Proc. International Conference on Retaining Structures, Cambridge, pp. 657-686.
- Peck, R.B. (1969). Deep excavations and tunnelling in soft ground. Proc. VIIIth ICSMFE, Mexico City, General Report, State-of-the-Art Volume, pp. 225-290.
- Pinto, M.S. (2011). Excavations Supported by Reinforced Concrete Walls and Slab Bands. M.Sc. Thesis, University of Porto, Portugal (in Portuguese).
- Potts, D.M.; Kovacevic, N. & Vaughan, P.R. (1997). Delayed collapse of cut slopes in stiff clay, *Géotechnique*, 47(5):953-982.  
<https://doi.org/10.1680/geot.1997.47.5.953>
- Potts, D.M. & Zdravkovic, L. (1999). Finite Element Analysis in Geotechnical Engineering - Theory. Thomas Telford, London.
- Quaresma, M.G. (1992). Behaviour and Modelling of an Embankment Over Soft Soils Reinforced by Geotextile. Ph.D. Thesis, Université Joseph Fourier, Grenoble I (in French).
- Santos, R.M. (2014). Basal-Heave Stability of Struttred Excavations in Soft Soils: Safety Analysis by the Finite Element Method. M.Sc. Thesis, University of Porto, Portugal (in Portuguese).
- Skempton, A.W. (1951). The bearing capacity of clays. Proc. Building Research Congress, London, pp. 180-189.
- Su, S.F.; Liao, H.J. & Lin, Y.H. (1998). Base stability of deep excavation in anisotropic soft clay. *J. Geotech. Geoenviron. Eng.*, 124(9):809-819.  
[https://doi.org/10.1061/\(ASCE\)1090-0241\(1998\)124:9\(809\)](https://doi.org/10.1061/(ASCE)1090-0241(1998)124:9(809))
- Terzaghi, K. (1943). *Theoretical Soil Mechanics*. Wiley, New York.
- Ukritchon, B.; Whittle, A.J. & Sloan, S.W. (2003). Undrained stability of braced excavations in clay. *Journal of Geotechnical and Geoenvironmental Engineering*, 129(8):738-755.  
[https://doi.org/10.1061/\(ASCE\)1090-0241\(2003\)129:8\(738\)](https://doi.org/10.1061/(ASCE)1090-0241(2003)129:8(738))
- Yeo, K.C. (1986). Simplified foundation data to predictors. Proc. Prediction Symposium on a Reinforced Embankment on Soft Ground, King's College, London.



# Relationship Between Shear Wave Velocity and Piezocone Penetration Tests on the Brazilian Continental Margin

R.G. Borges, L.O. Souza Junior, M.C.F. Almeida, M.S.S. Almeida

**Abstract.** A detailed characterization of the shear wave velocity profile is an essential tool in the resolution of a variety of seismological and geotechnical engineering problems. The main objective of this study is to present equations capable of providing reliable shear wave velocity profile estimations based on CPTu parameters. The results of a series of pioneering in-situ seismic piezocone penetration tests on the Brazilian continental margin are presented in this paper. A complete geological and geotechnical characterization of multiple sites was performed. Multiparameter and single parameter correlations were proposed between the measured shear wave velocity and the piezocone penetration test parameters. The suitability of the proposed correlations was evaluated by means of a statistical analysis and compared to the performance of previously published correlations using the test data parameters as input. The results show that the study was successful in presenting equations with superior performance for local soil conditions. Furthermore, this study yielded new reliable correlations that will benefit future projects in similar offshore environments.

**Keywords:** correlations, offshore geotechnical investigation, piezocone penetration tests, shear wave velocity.

## 1. Introduction

The shear wave velocity ( $V_s$ ) is a fundamental property of soil, rock, concrete, steel, and other civil engineering materials. For geotechnical problems, the evaluation of the shear wave velocity is especially important in the definition of small-strain soil stiffness and is generally expressed in terms of the maximum shear modulus ( $G_{max}$ ). Shear wave velocity is also useful in site response analysis, evaluation of liquefaction potential (Robertson & Wride, 1998; Youd *et al.*, 2001), soil classification, unit weight estimation, stratigraphy definition, as well as foundation settlement analysis (Andrus & Stokoe II, 2000; Schneider *et al.*, 2001; Andrus *et al.*, 2004; Mayne, 2007; Long & Donohue, 2010; Akin *et al.*, 2011; Chang *et al.*, 2011; Omar *et al.*, 2011). In Brazil, for example, the use of SCPT testing has mostly been limited to the identification of on-shore tropical sites (Giachetti *et al.*, 2006) due to limited availability of equipment (Vitali *et al.*, 2012).

Shear wave velocity measurements in soils can either be obtained in the laboratory, using resonant column tests or bender elements, or in-situ, using geophysical techniques. Compared to laboratory methods, in-situ techniques are advantageous since the soil is tested in its natural environment under anisotropic stress with minimal disturbance effects, which is important in the study of offshore environments. In this context, traditional CPTu combined with seismic measurements makes the Seismic Cone Penetration Test (SCPTu) the most cost-effective way to measure shear wave velocity (Schnaid, 2008).

A substantial number of studies have been conducted since the early 1980s to develop and evaluate empirical correlations between small-strain elastic properties, especially the shear wave velocity or the maximum shear modulus in soils, and the data from cone or piezocone penetration tests (*e.g.*, Rix & Stokoe II, 1991; Hegazy & Mayne, 1995; Mayne & Rix, 1995; Andrus *et al.*, 2007; Long & Donohue, 2010; McGann *et al.*, 2015; Zou *et al.*, 2017; Tong *et al.*, 2018). These studies have shown that cone resistance, sleeve friction, confining stress, depth, and the behavior and geological age of the soil influence the correlations.

Data scatter is a factor to be considered for this type of correlation (Wair *et al.*, 2012), and in order to minimize its influence, correlation studies are usually separated into three categories:

• Correlations for clay - undrained behavior (*e.g.*, Mayne & Rix, 1995; Long & Donohue, 2010; Taboada *et al.*, 2013; Zhang & Tong, 2017);

• Correlations for sands - drained behavior (*e.g.*, Baldi *et al.*, 1989; Hegazy & Mayne, 1995; Taboada *et al.*, 2015);

• Correlations for soils in general (*e.g.*, Hegazy & Mayne, 1995, 2006; Robertson, 2009; McGann *et al.*, 2015).

The use of empirical correlations is an easy and straightforward method for estimating shear wave velocity profiles for numerous applications based on parameters obtained through in-situ tests, or more simply, from vertical

Ricardo Garske Borges, M.Sc., D.Sc. Student, COPPE, Universidade Federal do Rio de Janeiro and CENPES/PETROBRAS, Rio de Janeiro, RJ, Brazil. email: ricardogarskeborges@gmail.com.

Luciano de Oliveira Souza Junior, M.Sc. Student, COPPE, Universidade Federal do Rio de Janeiro, Rio de Janeiro, RJ, Brazil. email: luciano.junior@coc.ufrj.br.

Maria Cascão Ferreira de Almeida, D.Sc., Associate Professor, Escola Politécnica, Universidade Federal do Rio de Janeiro, Rio de Janeiro, RJ, Brazil. email: mariacasciao@poli.ufrj.br.

Márcio de Souza Soares de Almeida, Ph.D., Full Professor, COPPE, Universidade Federal do Rio de Janeiro, Rio de Janeiro, RJ, Brazil. email: almeida@coc.ufrj.br.

Submitted on December 2, 2019; Final Acceptance on May 12, 2020; Discussion open until September 30, 2020.

DOI: 10.28927/SR.432219

effective stresses. Nevertheless, the quality of the correlations is directly linked to the data used, which may not be appropriate for local conditions. Thus, it is important to validate available equations or develop new ones with local data whenever possible. The increasing number of engineering projects in this field, however, makes it vital to properly assess the agreement between measured and predicted values. According to Zhang & Tong (2017), this assessment can be done in terms of simple statistical descriptive parameters (*i.e.*, coefficient of determination, variable coefficient) or with a more complete statistical analysis (*e.g.*, Onyejekwe *et al.*, 2016).

Direct shear wave velocity  $V_s$  measurements are always preferable to estimates based on correlations with cone or piezocone penetration tests. However, such estimates can be particularly useful for projects where it is not possible or economically feasible to obtain local  $V_s$  measurements.

The main objective of this study is to provide new and reliable correlations that relate CPTu parameters with  $V_s$  values for the Brazilian offshore environment. The present research makes use of the first and only dataset from available deep seismic piezocone penetration tests conducted across the Brazilian continental margin between the years 1991 and 1992. Initially, these test results were compared to correlations found in the literature, both for datasets with similar geological conditions as well as general conditions. Statistical correlations were then developed to estimate the shear wave velocity in the soil deposits of these test sites using the parameters from the piezocone penetration tests. Finally, the results for both sets of correlations were evaluated using the statistical approach described by Zhang &

Tong (2017), in order to properly describe the agreement between the measured and predicted shear wave velocities.

## 2. Site Characterization

The piezocone (CPTu) tests were performed in two sedimentary basins, Campos and Santos, on the Brazilian continental margin (Fig. 1). There was a total of 10 study points (4 in the Campos Basin and 6 in the Santos Basin) on the continental slope, each of which is an oil and gas production development field, as shown in Fig. 1.

These tests were performed during the site investigation campaign to characterize gohazards and support the foundation design of fixed and floating oil and gas production platforms to be installed in these areas.

### 2.1. Offshore CPTu testing

A geological and geotechnical site investigation was performed by Fugro-McClelland Marine Geosciences, Inc. for the Brazilian oil company Petrobras from October 1991 to March 1992. The geotechnical boreholes were performed in water depths ranging from -110 m (located in the Tubarão Field) to -502 m (in the Voador-2 Field), and the penetration depths varied between 50 m and 151 m below the seafloor.

The Fugro-McClelland WISON® MkIII cone penetration test system was used, enabling in-situ soil properties to be measured from the base of the borehole (Lange, 1991) and extraction of in-situ samples. The piezocone penetration tests were performed with a standard cone tip (0.001 m<sup>2</sup> cone base area; 60° apex). The probe was pushed into the seabed at a constant rate of about 0.02 m/s, providing a semi-continuous record of the cone tip resistance ( $q_c$ ), slee-

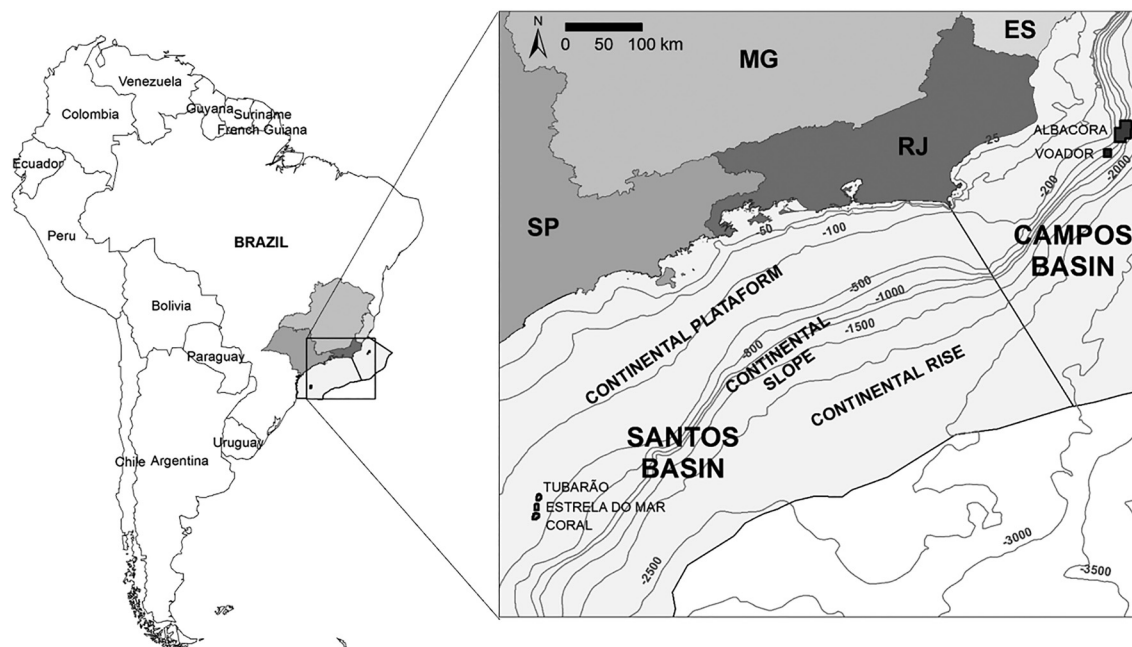


**Figure 1** - Location of Campos and Santos basins with respective investigated fields.

ve friction ( $f_s$ ) and pore pressure generated during the penetration ( $u_2$ ).

The downhole technique was used, which allowed sample collection and in-situ vane tests between successive probe pushes. This technique consisted of performing the CPTu, removing the probe and pushing the sample extractor and vane device for 1 meter, then reinitiating the CPTu. The intervals of sampling varied according to the depth, ranging from 3 m to 10 m. Because of the length of the borehole dedicated to sample extraction, the profiles obtained do not have a continuous shape, as can be seen in Fig. 2.

The shear velocity measurements were made by means of a set of biaxial geophones arranged orthogonally

in the horizontal plane, approximately 0.4 m above the cone tip. A shear wave hammer was used as the seismic source and activated multiple times until a satisfactory signal/noise ratio was obtained. Travel times were computed using the characteristic points approach.

## 2.2. Geological description

The geomorphology of the Campos and Santos basins on the continental margin was largely controlled by the underlying salt tectonics and the depositional geometry of the Upper Miocene. Its current form results from variations in the sea level, contour-current action, sediment remobilization through mass movements, structural geology, imple-

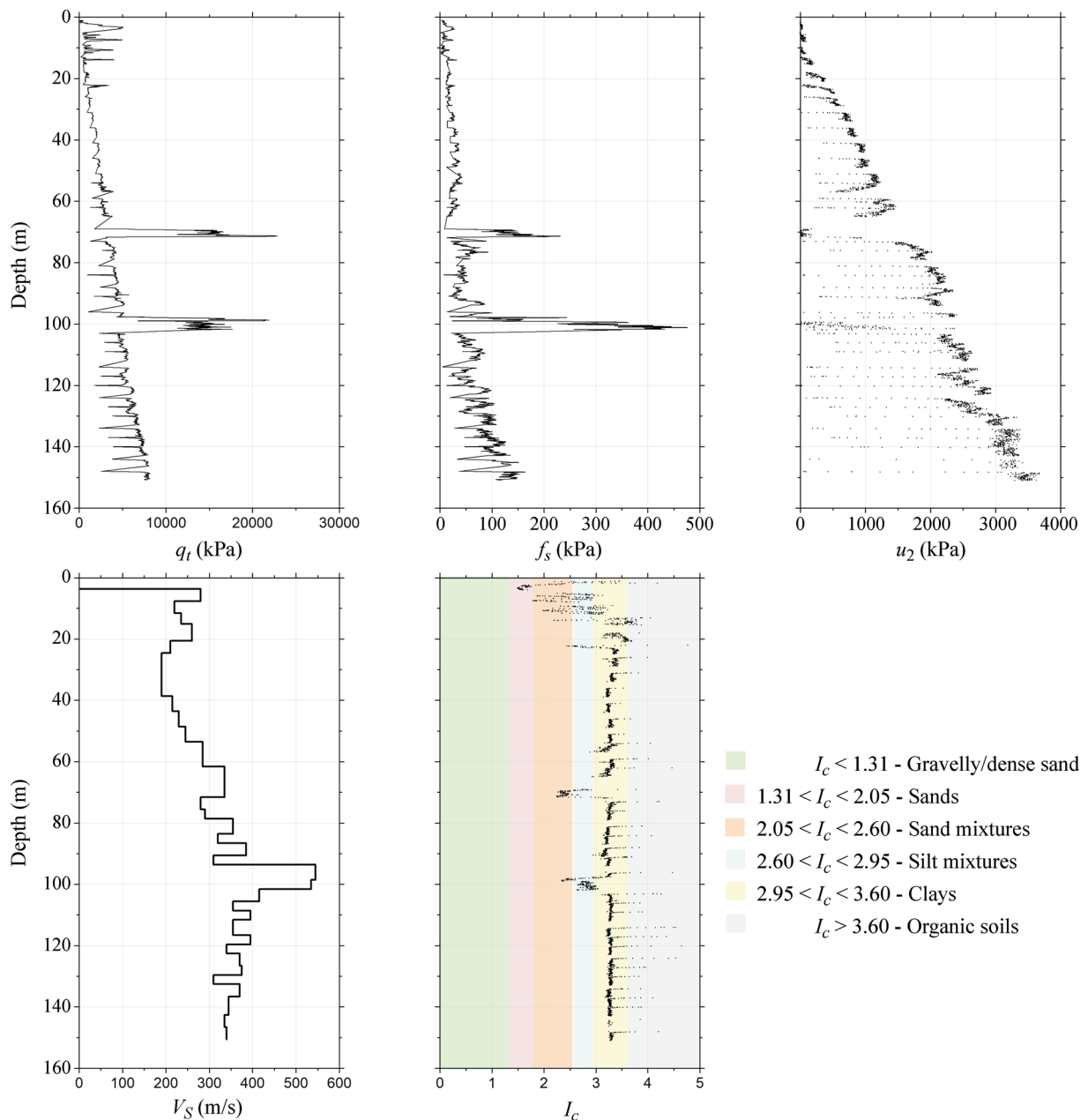


Figure 2 - Albacora Field CPTu profile.

mentation of turbidity systems associated with fluvial systems on the continent, and the control of this drainage by salt tectonics. Systematic sampling and dating of the seabed with piston corers determined that this geomorphology is representative of the end of the Pleistocene and that the subsequent sea level rise during the Holocene interrupted almost all the active processes in the area (Kowsmann *et al.*, 2000; Vicalvi & Kowsmann, 2006).

Some of the piezocone penetration tests in the study area exceeded 100 m in depth below the seafloor, and the paleoclimate curves constructed for the recovered stratigraphic sequences show that they reached a maximum age of 145,000 to 150,000 years B.P., placing them in the Upper Quaternary. The observations made by Vicalvi (1999) regarding the samples recovered from the study area indicate that the Holocene/Pleistocene boundary is always characterized by mud, at variable depths, but relatively close to the seafloor.

### 2.3. Geotechnical description

The laboratory characterization consisted of index tests such as Atterberg limits, particle size distribution, carbonate concentration, as well as oedometer and triaxial tests. Table 1 presents a summary of soil properties for the Campos and Santos basins.

Figure 3 shows the plasticity chart for the fine-grained samples from both basins. As observed, most of the samples retrieved during the campaign can be classified either as CH or CL in the Unified Soil Classification System (USCS). In fact, 86 % of the samples fall into those categories.

For the Campos Basin, the typical geotechnical profile consists of a shallow silty/sandy layer, and layers of silty clay with a few interbedded layers of clayey silts and/or fine sand. Additionally, the presence of organic material, biotite, and bioclasts was detected in all the layers, with an OCR profile varying from normally to slightly overconsolidated clays.

The characteristic profile for the Santos Basin can be described as silty clay with a coarse-grained top layer and interbedded silty/sandy layers. As in the Campos Basin, all the boreholes at this location have a high presence of organic material, biotite, and bioclasts, and the OCR profiles indicate normally to slightly overconsolidated clays.

### 2.4. Data analysis

Due to the large number of boreholes, Fig. 2 shows the deepest CPTu profile (located in the Albacora Field), which is typical in terms of soil characteristics. Note that the parameter profiles do not appear continuous in Fig. 2 due to the necessary interruptions to run sample extraction and in-situ vane tests.

Complementary to the measured parameters ( $q_p$ ,  $f_s$ ,  $u_2$  and  $V_s$ ), the Soil Behavior Type Index ( $I_c$ ) (Robertson & Wride, 1998) was calculated according to Eq. 1.

Table 1 - Summary of the soil properties.

| Basin  | Field          | Code  | Max depth (m) | Number of samples | CL-CH (%) | Unit Weight (kN/m <sup>3</sup> ) | Water content (%) | $I_p$ (%) | $C_c$   | CaCO <sub>3</sub> (%) |
|--------|----------------|-------|---------------|-------------------|-----------|----------------------------------|-------------------|-----------|---------|-----------------------|
| Campos | Albacora       | GS08  | 151           | 24                | 75        | 17.3-19.0                        | 27.1-39.6         | 9-52      | 0.4-0.6 | 5.0-35.0              |
|        |                | GS27  | 120           | 15                | 93        | 14.3-28.3                        | 29.6-34.1         | 26-45     | 0.4-0.8 | 6.4-41.5              |
|        | Voador         | GS28  | 118           | 22                | 95        | 16.1-19.4                        | 28.5-64.7         | 18-44     | -       | 18.0                  |
| Santos | Tubarão        | GS49  | 124           | 20                | 95        | 16.7-18.8                        | 29.3-62.3         | 22-54     | 0.5-0.9 | 5.7-35.3              |
|        |                | GS80  | 51            | 12                | 92        | 16.8-18.0                        | 39.1-55.0         | 18-61     | 0.6-1.3 | 5.0-58.5              |
|        | Estrela do Mar | GS90  | 50            | 11                | 81        | 16.4-18.1                        | 40.4-56.1         | 33-59     | 0.3-1.1 | 8.3-46.0              |
|        |                | GS91  | 117           | 18                | 88        | 16.6-19.0                        | 35.1-52.6         | 20-51     | 0.5-0.9 | 4.6-30.5              |
|        | Coral          | GS92  | 44            | 13                | 70        | 16.7-19.5                        | 28.2-56.2         | 15-51     | 0.2-0.8 | 53.7-68.3             |
|        |                | GS100 | 75            | 14                | 79        | 17.0-19.5                        | 36.6-66.7         | 25-49     | 0.6-1.0 | 4.2-50.2              |
|        |                | GS101 | 117           | 18                | 83        | 17.0-19.8                        | 41.3-56.2         | 31-62     | 0.8-1.0 | 4.0-51.6              |

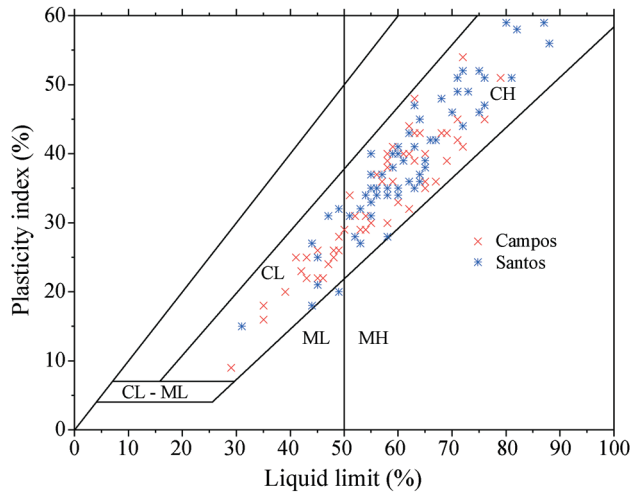


**Figure 3** - Plasticity chart for the fine-grained samples.

$$I_c = [(3.47 - \log Q_{it})^2 + (\log F_r + 1.22)^2]^{0.5} \quad (1)$$

where  $Q_{it}$  is the normalized penetration resistance and  $F_r$  is the normalized friction ratio.

In order to give a more precise overview of the general behavior of the entire CPTu campaign, the density distributions for shear wave velocity and  $I_c$  are presented in Fig. 4. As illustrated in Fig. 4, much of the soil profile can

be classified as clay, according to the Robertson & Wride (1998) classification system. With respect to the shear wave velocity, the density plot in Fig. 4a indicates that most of the points are in the 200-400 m/s interval. Regarding the Soil Behavior Type Index (Fig. 4b), most of the points have  $I_c$  values between 2.95 and 3.6, indicating a prevalence of clayey soil behavior. As shown in Fig. 2, and indicated by the significant density in Fig. 4b, sandy and silty layers are also present in most profiles.

Shear wave velocity values are assumed to be constant along the measurement depths. In the CPTu campaign, the  $V_s$  measurements coincided with the sampling operation, with intervals ranging from 3 m to 10 m, which is greater than the ideal interval of 0.5 m (McGann *et al.*, 2015). However, two factors must be considered regarding these high sampling interval values. The first is related to the fact that the data was collected long before this analysis, precluding any such control. Secondly, with sampling depths of up to 150 m and a uniform Soil Behavior Type Index distribution for most of the profiles, the sampling intervals are likely to have a lower impact on data quality.

The total number of  $V_s$  data points is 258. In order to compare these  $V_s$  measurements with those of the CPTu data, the midpoint depth for each sampling interval is used and the other parameters are averaged, as recommended by Tonni & Simonini (2013) and Andrus *et al.* (2007). This

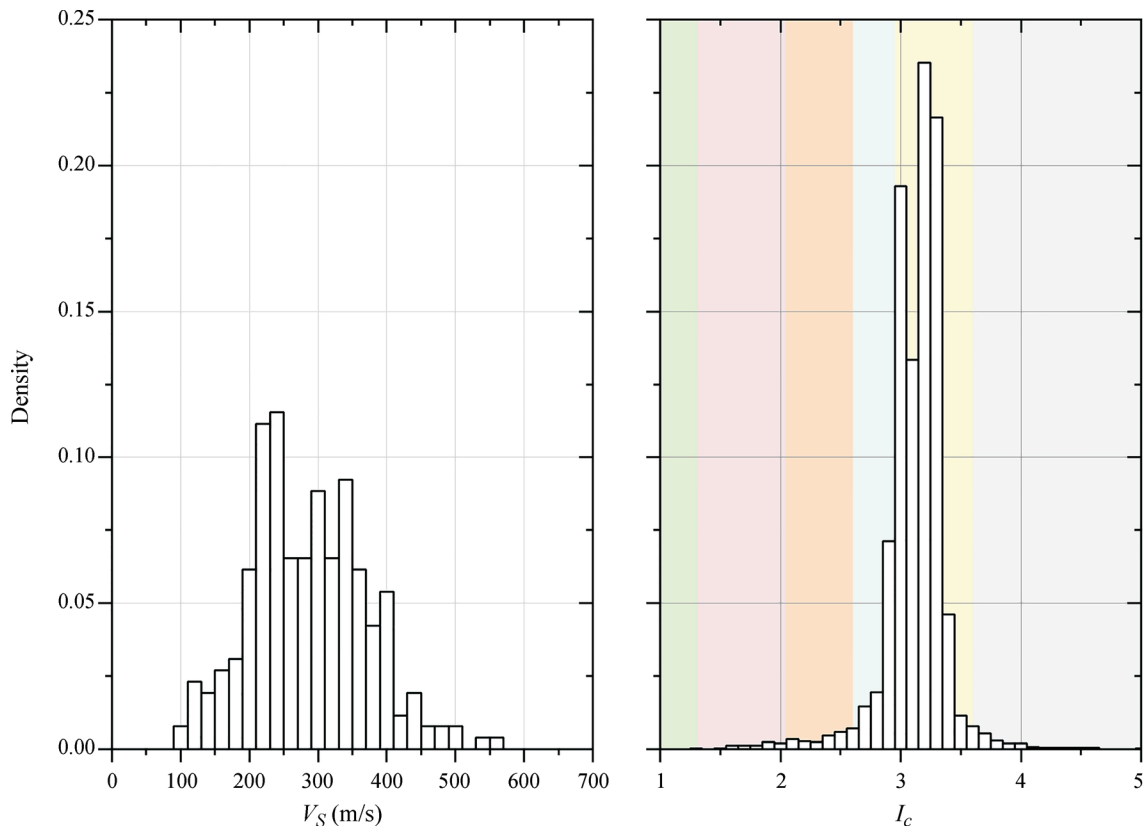


**Figure 4** - Distribution of: (a) shear wave velocity and (b) soil behaviour type index.

procedure attenuates the effects of using long intervals for shear wave velocity measurements and the subsequent comparison with CPTu data. Even though it may be argued that this procedure could associate two layers with very different characteristics, it is still better than considering the midpoint approach for all CPTu parameters. The latter could introduce a localized condition with a respective  $V_s$  value and thereby misrepresent the entire layer (McGann *et al.*, 2015).

### 3. Previous Published CPTu- $V_s$ Correlations

CPTu- $V_s$  correlations have long been an object of study. Different methodologies and equations have been proposed for various site conditions. On the one hand, it is necessary to understand the nature of the database that generated soil-type specific equations, before applying them to site-specific CPTu data. On the other hand, generic correlations (Robertson, 2009; McGann *et al.*, 2015; McGann *et al.*, 2018; Tong *et al.*, 2018) can be applicable for all soil types as they introduce parameters that can account for differences in behavior, such as  $I_c$  and  $B_q$  (McGann *et al.*, 2015).

In this study, four relatively recent published correlations are analyzed using the local CPTu data: two generic correlations (Robertson, 2009; Tong *et al.*, 2018), and two for specific soil types (Long & Donohue, 2010; Taboada *et al.*, 2013). This selection was based on a preliminary fit analysis for the generic correlations and for the correlations with similar offshore conditions for the specific soil type. A brief discussion of the chosen correlations is made before the description of the statistical analysis used to fit the data.

#### 3.1. Generic correlations

Robertson (2009) presented a CPTu- $V_s$  correlation based on a large dataset comprising 1,035 points. The variable  $I_c$  was introduced to account for the soil type variability, and the initial vertical stress ( $\sigma_{v0}$ ) is subtracted from the corrected cone tip resistance ( $q_t$ ) and normalized by the atmospheric pressure ( $p_a$ ). Equation 2 shows the general form of the equation proposed by Robertson (2009).

$$V_s = \left[ 10^{(0.55 I_c + 1.68)} \left( \frac{q_t - \sigma_{v0}}{P_a} \right) \right] \quad (2)$$

Tong *et al.* (2018) developed multiple regression forms based on 14 CPTu tests performed in Holocene floodplain deposits in Nanjing, China, with heterogeneous stratigraphy profiles. The main characteristic of these deposits is related to the presence of silt and sand mixtures, with thinly interbedded layers of various materials. Following the recommendations of Wair *et al.* (2012), Eq. 3 represents the chosen analyzed correlation.

$$V_s = 21.5 q_t^{0.122} f_s^{0.172} \sigma_{v0}^{0.172} \quad (3)$$

#### 3.2. Soil-type specific correlations

Long & Donohue (2010) proposed correlations between  $V_s$  and CPTu data for ten Norwegian marine soft clays based on previous characterization studies. The database included high-quality in-situ measurements and laboratory tests, in order to minimize uncertainties and improve accuracy. Equation 4 shows the relationship from Long & Donohue (2010) based only on the parameter  $q_t$ .

$$V_s = 2.944 q_t^{0.613} \quad (4)$$

Following the general formula proposed by Simonini & Cola (2000), where the normalized pore pressure  $B_q$  defined in Eq. 5 is used to substitute for the use of the initial void ratio  $e_0$ , Long & Donohue (2010) proposed a correlation relating shear wave velocity to the parameters  $q_t$  and  $B_q$ , as shown in Eq. 6.

$$B_q = \frac{u_2 - u_0}{q_t - \sigma_{v0}} = \frac{\Delta u}{q_{net}} \quad (5)$$

$$V_s = 1.96 q_t^{0.579} (1 + B_q)^{1.202} \quad (6)$$

They suggest that both formulas (Eqs. 4 and 6) can be used without any prejudice to the estimated  $V_s$  profile. However, in a preliminary fit quality analysis for the data presented in this work, the second form of regression provided the best set of parameters and, therefore, Eq. 6 was chosen for further analysis.

Taboada *et al.* (2013) analysed P-S logging data for the Bay of Campeche, Mexico, aiming to evaluate the geohazards involved in offshore petroleum exploration. Their study can be directly related to the present work, as it was developed under similar site conditions. The water depths varied from 14 m to 102.3 m with a maximum penetration depth of 121.9 m. The soil profile was composed of soft clay deposits at shallow depths, reaching a maximum of 25 m in the north-eastern portion of the study area. After the top clay layer, a sequence of stiff to hard clays and medium-dense to very-dense sand was found. The correlations that were developed focused on using data from the clay layer, providing soil type-specific correlations. Among the proposed formulae, there are three correlations that included the CPT parameters available in the dataset of the present study, and only one (Eq. 7) with a multiple variable approach which presented the best preliminary agreement between measured and estimated  $V_s$  values.

$$V_s = 14.4 q_{net}^{0.265} \sigma_{v0}^{0.137} \quad (7)$$

where  $q_{net}$  is the net cone resistance obtained from Eq. 8.

$$q_{net} = q_t - \sigma_{v0} \quad (8)$$

#### 3.3. Statistical methods for validation of correlation equations

In order to obtain a good match between predicted and measured shear wave velocity values, many authors

(e.g., Onyejekwe *et al.*, 2016; Zhang & Tong, 2017; Tong *et al.*, 2018) have used a more complete analysis with the evaluation of four indexes: Prediction Bias ( $K$ ), Ranking Index ( $RI$ ); Ranking Distance ( $RD$ ) and Root Mean Square Error ( $RMSE$ ).

The Ranking Index  $K$  is the ratio between the estimated and measured  $V_s$ . According to Onyejekwe *et al.* (2016), the mean of  $K$  usually represents the level of accuracy, whereas its standard deviation indicates the precision of the proposed correlation. The optimum value for the mean value of  $K$  is 1, indicating no underestimation or overestimation. The Ranking Index can be expressed by Eq. 9.

$$K = \frac{V_{Se}}{V_{Sm}} \quad (9)$$

where  $V_{Se}$  is the estimated shear wave velocity and  $V_{Sm}$  is the measured value (Briaud & Tucker, 1988).

The Ranking Index was proposed to provide a better estimate for correlation quality. The Ranking Index  $RI$  is defined by Eq. 10.

$$RI = \left| \mu_{\ln|K|} \right| + \sigma_{\ln|K|} \quad (10)$$

where  $\mu$  and  $\sigma$  are the mean and standard deviation of the data, respectively.

Another parameter to evaluate the fitness of the measured to the estimated data is the Ranking Distance ( $RD$ ), originally proposed by Cherubini & Orr (2000). On a plot with mean ( $\mu$ ) values on the x-axis and standard deviation ( $\sigma$ ) on the y-axis,  $RD$  represents the distance from the optimum condition point, where  $\mu_K = 1$  and  $\sigma_K = 0$ , to the point calculated using the correlation (Tong *et al.*, 2018). Equation 11 expresses the Ranking Distance.

$$RD = \sqrt{(1 + \mu_K)^2 + (\sigma_K)^2} \quad (11)$$

The Root Mean Square Error ( $RMSE$ ) is the square root of the squared difference between the estimated and measured shear wave velocities. Large errors produce large  $RMSE$  values. Therefore, lower  $RMSE$  values indicate better model performance. Equation 12 defines the Root Mean Square Error, where  $n$  is the number of data points.

$$RMSE = \sqrt{\frac{1}{n} \sum_1^n (V_{Se} - V_{Sm})^2} \quad (12)$$

### 3.4. Comparisons

Figure 5 shows the prediction performance of the four aforementioned correlations from the literature using the dataset of the present study. The measured shear wave velocity values ( $V_{sm}$ ) were plotted against the estimated values ( $V_{se}$ ) to show the scatter relative to the 1:1 line. The histogram plots provide an overview of bias distribution showing the mean  $\mu$ , the standard deviation  $\sigma$  and the Coefficient of Variation  $CoV$ . The lower the values of the latter two, the more accurate the estimate.

Among the four correlations selected from the literature, the one proposed by Long & Donohue (2010) was the least applicable, Fig. 5(e, f). The graph shows a large amount of scatter around the 1:1 line, with an  $R^2$  of 0.71 and a mean bias of  $\mu = 1.16$ , indicating overestimation. This correlation did not yield good results when compared to the other three correlations. The most applicable equation of the four was the one presented by Taboada *et al.* (2013), Fig. 5(g, h). It shows the most accurate mean bias of 0.97, indicating a slight tendency for underestimation, and it provided the highest  $R^2$ , with a value of 0.76. The generic correlations from Robertson (2009), Fig. 5(a, b), and Tong *et al.* (2018), Fig. 5(c, d), showed comparable prediction performance, with a tendency for underestimation. The Tong *et al.* (2018) correlation presented the most precise equation, as indicated by the lowest standard deviation for Prediction Bias  $K$  ( $\sigma = 0.13$ ). Table 2 summarizes quantitatively the results of the complete statistical analysis presented in the previous section, thus helping to corroborate the analysis shown in Fig. 5. In summary, the correlation from Taboada *et al.* (2013) was the most accurate and precise equation, with the best prediction performance for the dataset used in this study, and the lowest values of  $RMSE$ ,  $RI$  and  $RD$ . On the other hand, the Long & Donohue (2010) equation was the least applicable correlation, yielding the highest value for all three parameters.

### 4. Proposed CPTu- $V_s$ correlations

The data from the in-situ piezocone penetration tests and the estimated shear wave velocity, based on correlations from previous studies, were used to examine trends for the soils in the present study.

In order to obtain more accurate and precise models for the given site conditions, nonlinear regression analyses were carried out to obtain the shear wave velocity profile, by adjusting power function curves to the data from the ten

**Table 2** - Statistical parameters from the analysis of the literature correlations.

| Correlation | Equation | $R^2$ | $K$   |       |          | $RI$  | $RD$  | $RMSE$ |
|-------------|----------|-------|-------|-------|----------|-------|-------|--------|
|             |          |       | % > 1 | $\mu$ | $\sigma$ |       |       |        |
| Multiple    | 15       | 0.84  | 51.12 | 1.01  | 0.13     | 0.134 | 0.131 | 39.08  |
| Single      | 16       | 0.77  | 58.14 | 1.01  | 0.15     | 0.155 | 0.148 | 45.71  |

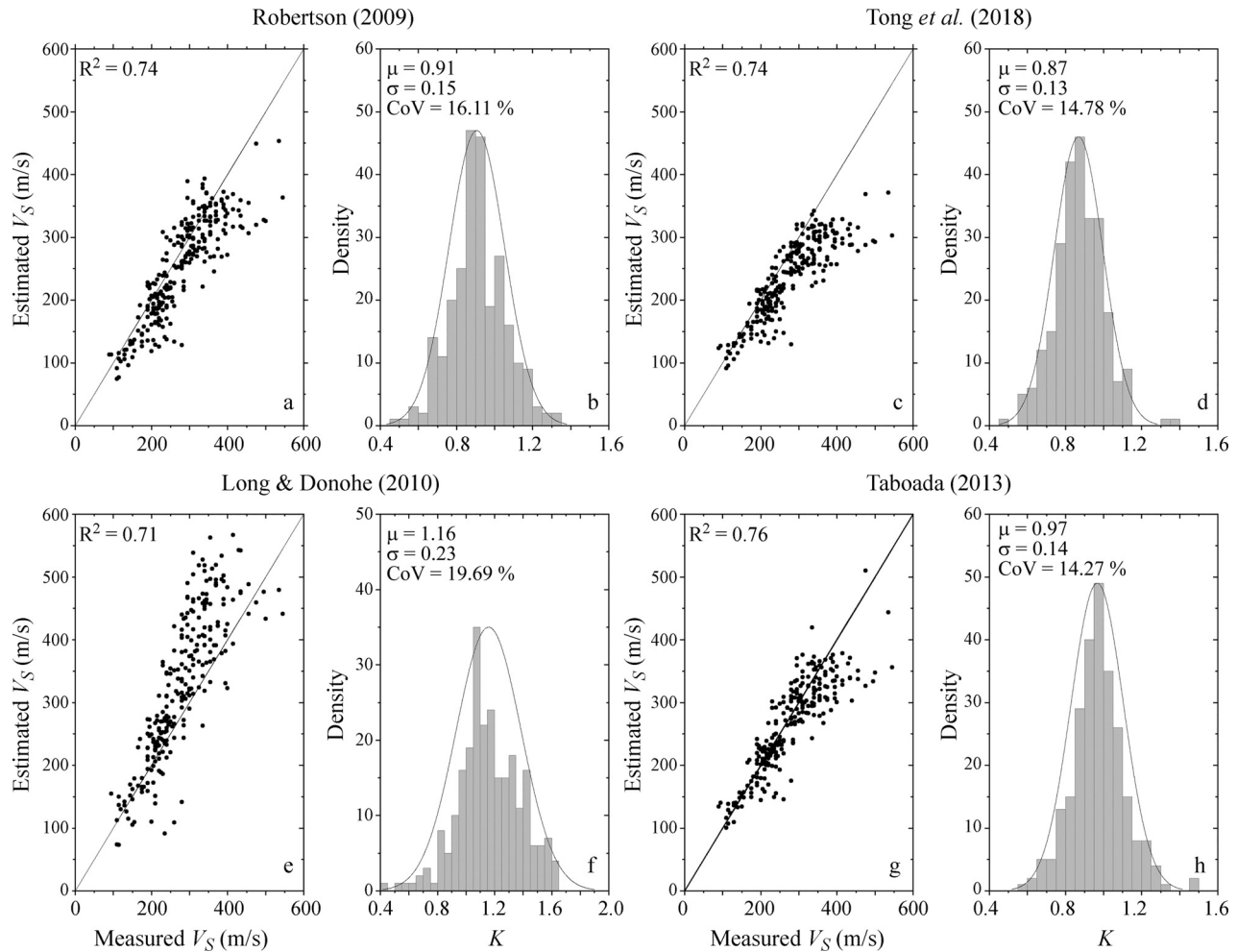


**Figure 5** - Prediction performance of correlations from the literature using the soil conditions from the present study.

boreholes performed in the region. Two model equations were used to generate the proposed correlations. Equation 13 presents the form suggested by Wair *et al.* (2012), using a multiparameter analysis to obtain the shear wave velocity, which is only applicable when CPTu data are available.

$$V_s = a q_t^b f_s^c \sigma'_{v0}{}^d \quad (13)$$

Equation 14 proposes a single variable analysis using only the vertical effective stress  $\sigma'_{v0}$ .

$$V_s = a \sigma'_{v0}{}^b \quad (14)$$

Equations 15 and 16 were then obtained to estimate  $V_s$  in m/s, with  $q_t, f_s$  and  $\sigma'_{v0}$  in kPa (258 data pairs in total were used in these regression analyses).

$$V_s = 9.741 q_t^{0.369} f_s^{-0.1402} \sigma'_{v0}{}^{0.1437} \quad (15)$$

$$V_s = 34.641 \sigma'_{v0}{}^{0.342} \quad (16)$$

## 5. Discussion

Figures 6 and 7 present the prediction performance of the proposed CPTu- $V_s$  correlations, for multiparameter and

single parameter conditions, respectively, with Table 3 summarizing the statistical parameters. As expected, the multiparameter Eqs. 15 (Fig. 6) provided a more applicable correlation, with an  $R^2$  of 0.84 (Fig. 5a), than the single parameter correlation of Eq. 16 (Fig. 7) with an  $R^2$  of 0.77 (Fig. 6a). Equation 15 also had lower values of  $RI$ ,  $RD$  and  $RMSE$  (Table 2), corroborating the Coefficient of Determination,  $R^2$ , cited above.

However, the model proposed by Eq. 16 can be used when data from piezocone penetration tests are not available and it has been shown to provide similar shear wave velocity profiles for use in preliminary investigations. In a comparison between the literature correlations (Table 2) and the proposed correlations (Table 3), the last ones exhibited better performance based on all statistical parameters, as expected. Nevertheless, one must be aware that the proposed equations are only valid for similar geological conditions and should not be applied as general correlations.

Figure 8 presents a direct comparison between the proposed and the literature equations with the measured shear wave velocity profile for the Albacora Field. It may be observed that the proposed equations have a better over-

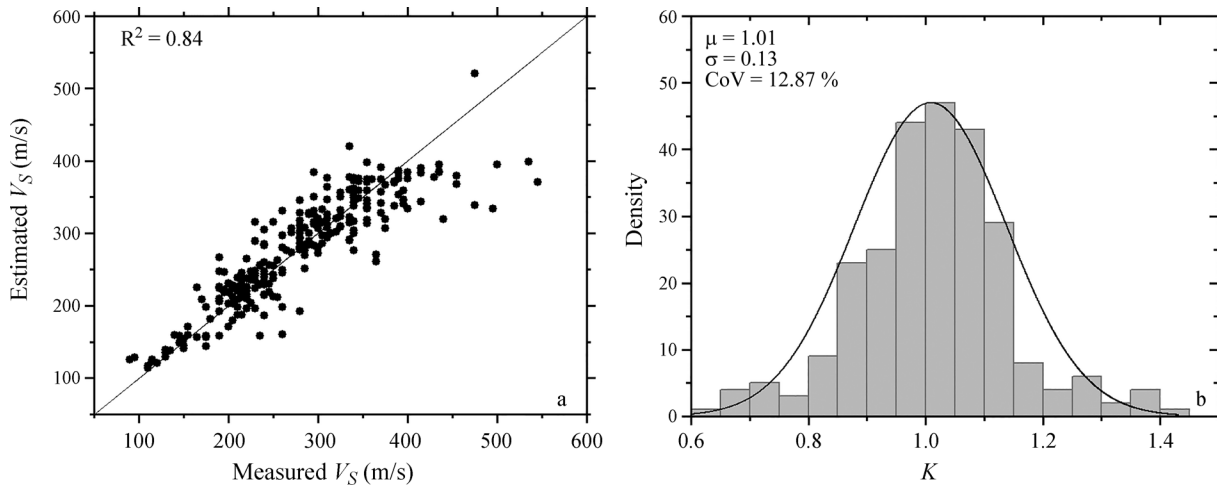


**Figure 6** - Performance of the proposed CPTu- $V_s$  correlations for multiparameter correlation.

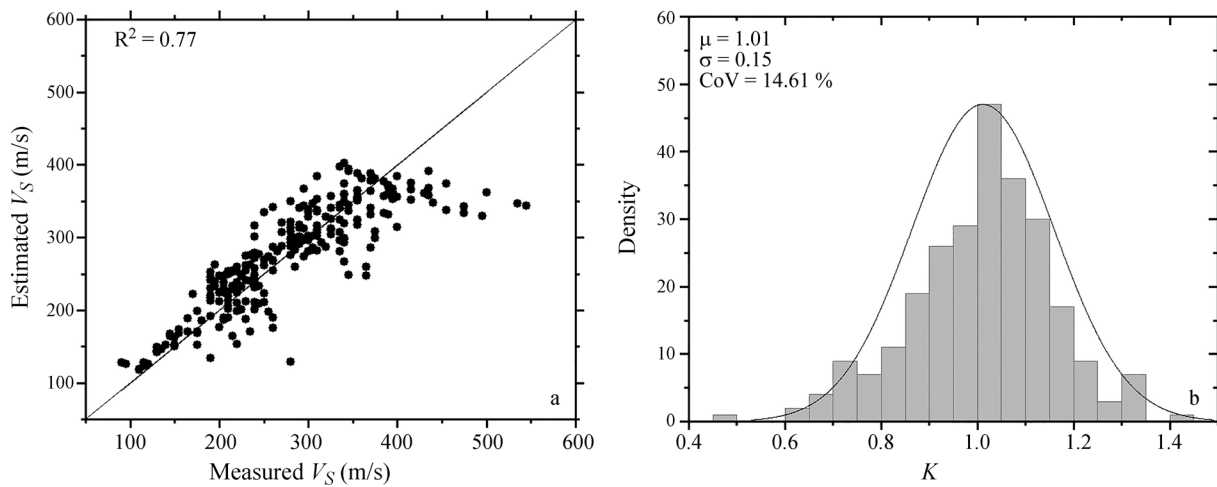


**Figure 7** - Performance of the proposed CPTu- $V_s$  correlations for single parameter correlation.

**Table 3** - Statistical parameters from the proposed correlations.

| Reference                    | Equation | $R^2$ | $K$   |       | $RI$ | $RD$  | $RMSE$ |        |
|------------------------------|----------|-------|-------|-------|------|-------|--------|--------|
|                              |          |       | % > 1 | $\mu$ |      |       |        |        |
| Robertson (2009)             | 2        | 0.74  | 24.42 | 0.91  | 0.15 | 0.277 | 0.173  | 51.614 |
| Tong <i>et al.</i> (2018)    | 3        | 0.74  | 13.18 | 0.87  | 0.13 | 0.304 | 0.184  | 62.085 |
| Long & Donohue (2010)        | 6        | 0.71  | 78.40 | 1.16  | 0.23 | 0.352 | 0.277  | 79.770 |
| Taboada <i>et al.</i> (2013) | 7        | 0.76  | 37.99 | 0.97  | 0.14 | 0.188 | 0.142  | 44.406 |

all fit to the measured  $V_s$  values than the literature equations. It is also seen that among the literature correlations, the one proposed by Taboada *et al.* (2013) had the best fit, and that proposed by Long & Donohue (2010) the worst fit, as pointed out above. The correlations proposed by Tong *et al.* (2018) and Robertson (2009) ranked intermediately between the other two, with a less satisfactory agreement for depths 0-60 m.

## 6. Conclusions

The present study made use of an existing database of in-situ measurements of shear wave velocity and piezocone penetration test parameters conducted on the Brazilian continental margin in order to make reliable correlations between CPTu parameters and  $V_s$  values. The data were collected at ten borehole locations from five areas during a site

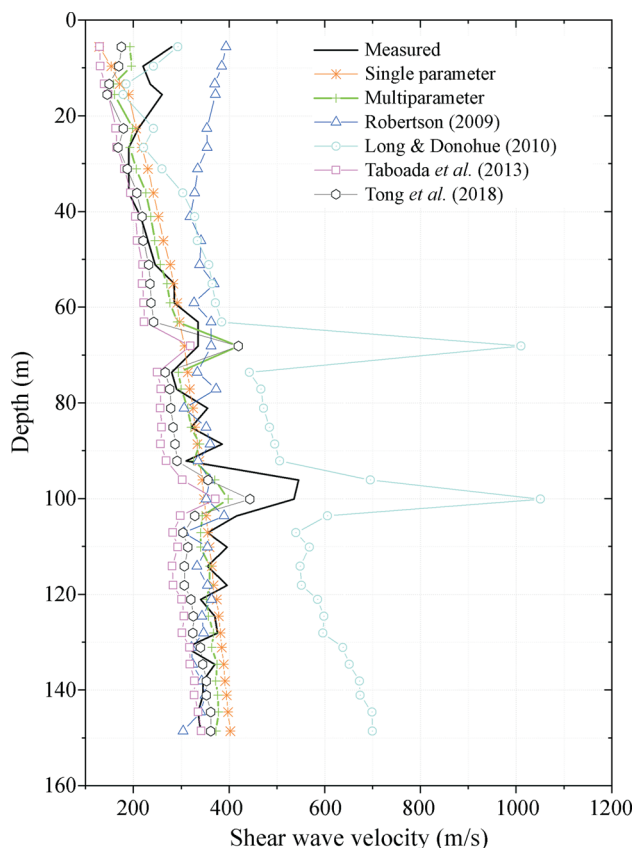


**Figure 8** - Shear wave profile comparison - Albacora Field.

investigation campaign performed for the Brazilian oil company Petrobras, for geohazards assessment and foundation design of oil platforms.

With these available data, four published correlations from the literature were evaluated and two new correlations were proposed. The prediction performance of the correlations was measured in terms of multiple statistical parameters. The main conclusions of this work are as follows:

- The correlation presented by Taboada *et al.* (2013) had the best fit, as expected, considering the similar geological background to the one studied here.
- The correlation proposed by Long & Donohue (2010) yielded the worst fit, primarily because it is the more general database, including data from all types of soil profiles;
- Two new correlations were proposed, using multiparameter analysis and single parameter analysis. The multiparameter correlation yielded the best overall agreement with measured data, as expected. However, since the effective vertical stress is an elemental geotechnical variable, the proposed single parameter correlation can be a powerful tool for preliminary studies;
- Particular attention and engineering judgment should be exercised when applying the proposed CPTu- $V_s$  correlations to sites with soil conditions that differ from those of the database used in this work;

- This study yielded new reliable correlations that will benefit future projects in similar offshore environments.

## Acknowledgments

The authors would like to thank Eng. Cláudio Amaral and Leopoldo Paganelli from Petrobras for providing valuable guidance, discussions and useful comments during the development of the study, as well as Dr. Victor Taboada for his insightful recommendations. The authors are grateful to Petrobras for the technical support and permission to publish the data from the site investigation. This study was financed in part by the Brazilian National Council for Scientific and Technological Development (CNPq), and its support is greatly appreciated.

## References

- Akin, M.K.; Kramer S.L. & Topal, T. (2011). Empirical correlations of shear wave velocity ( $V_s$ ) and penetration resistance (SPT-N) for different soils in an earthquake-prone area (Erbaa-Turkey). *Engineering Geology*, 119(1-2):1-17. <https://doi.org/10.1016/j.enggeo.2011.01.007>.
- Andrus, R.D. & Stokoe II, K.H. (2000). Liquefaction resistance of soils from shear-wave velocity. *Journal of Geotechnical and Geoenvironmental Engineering*, 126(11):1015-1025. [https://doi.org/10.1061/\(ASCE\)1090-0241\(2000\)126:11\(1015\)](https://doi.org/10.1061/(ASCE)1090-0241(2000)126:11(1015)).
- Andrus, R.D.; Piratheepan, P.; Ellis, B.S.; Zhang, J. & Juang, C.H. (2004). Comparing liquefaction evaluation methods using penetration- $V_s$  relationships. *Soil Dynamics and Earthquake Engineering*, 24(9-10):713-721. <https://doi.org/10.1016/j.soildyn.2004.06.001>.
- Baldi, G.; Bellotti, R.; Ghionna, V.N.; Jamiolkowski, M. & Lo Presti, D.C.F. (1989). Modulus of sands from CPT's and DMT's. *Proc. 12th International Conference on Soil Mechanics and Foundation Engineering, ISSMFE, Rio de Janeiro, v. 1, pp. 165-170*.
- Briaud, J.L. & Tucker, L.M. (1988). Measured and predicted axial response of 98 piles. *Journal of Geotechnical Engineering*, 114(9):984-1001. [https://doi.org/10.1061/\(ASCE\)0733-9410\(1988\)114:9\(984\)](https://doi.org/10.1061/(ASCE)0733-9410(1988)114:9(984)).
- Chang, W.J.; Ni, S.H.; Huang, A.B.; Huang, Y.H. & Yang, Y.Z. (2011). Geotechnical reconnaissance and liquefaction analyses of a liquefaction site with silty fine sand in Southern Taiwan. *Engineering Geology*, 123(3):235-245. <https://doi.org/10.1016/j.enggeo.2011.09.003>.
- Cherubini, C. & Orr, T.L.L. (2000). A rational procedure for comparing measured and calculated values in geotechnics. Nakase A. & Tsuchida T (eds), *Coastal Geotechnical Engineering in Practice*, CRC Press, Rotterdam, v. 1, pp. 261-265.

- Giachetti, H.L.; De Mio, G. & Peixoto, A.S.P. (2006). Cross-hole and seismic CPT tests in a tropical soil site. *Proc. GeoCongress 2006*, ASCE, Atlanta, v. 1, pp. 1-6. <https://doi.org/10.1061/40803281872992>.
- Hegazy, Y.A. & Mayne, P.W. (1995). Statistical correlations between  $V_s$  and cone penetration data for different soil types. *Proc. International Symposium on Cone Penetration Testing, CPT' 95*, Linköping, v. 1, pp. 173-178.
- Hegazy, Y.A. & Mayne, P.W. (2006). A global statistical correlation between shear wave velocity and cone penetration data. *Proc. GeoShanghai International Conference 2006, Site and Geomaterial Characterization*, Shanghai, pp. 243-248.
- Kowsmann, R.O.; Borges, H.V. & Vicalvi, M.A. (2000). Piston cores from the SE Brazil continental slope. *Proc. 31st International Geological Congress*, Rio de Janeiro, pp. 1-8.
- Lange, G. (1991). Experience with the seismic cone penetrometer in offshore site investigations. Hovem, J.M.; Richardson M.D. & Stoll R.D. (eds), *Shear Waves in Marine Sediments*, Springer, Dordrecht, pp. 275-282.
- Long, M. & Donohue, S. (2010). Characterization of Norwegian marine clays with combined shear wave velocity and piezocone cone penetration test (CPTU) data. *Canadian Geotechnical Journal*, 47(7):709-718. <https://doi.org/10.1139/T09-133>.
- Mayne, P.W. (2007). In-situ test calibration for evaluating soil parameters. Tan, T.S.; Phoon, K.K.; Hight, D.W. & Leroueil, S. (eds), *Characterization and engineering properties of natural soils*, Taylor & Francis Group, London, v. 3, pp. 1601-1652.
- Mayne, P.W. & Rix, G.J. (1995). Correlations between shear wave velocity and cone tip resistance in natural clays. *Soils and Foundations*, 35(2):107-110. [https://doi.org/10.3208/sandf1972.35.2\\_107](https://doi.org/10.3208/sandf1972.35.2_107).
- McGann, C.R.; Bradley, B.A. & Jeong, S. (2018). Empirical correlation for estimating shear-wave velocity from cone penetration test data for Banks Peninsula loess soils in Canterbury, New Zealand. *Journal of Geotechnical and Geoenvironmental Engineering*, 144(9):04018054. [https://doi.org/10.1061/\(ASCE\)GT.1943-5606.0001926](https://doi.org/10.1061/(ASCE)GT.1943-5606.0001926).
- McGann, C.R.; Bradley, B.A.; Taylor, M.L.; Wotherspoon, L.M. & Cubrinovski, M. (2015). Applicability of existing empirical shear wave velocity correlations to seismic cone penetration test data in Christchurch New Zealand. *Soil Dynamics and Earthquake Engineering*, 75:76-86. <https://doi.org/10.1016/j.soildyn.2015.03.021>.
- Omar, M.N.; Abbis, C.P.; Taha, M.R. & Nayan, K.A.M. (2011). Prediction of long-term settlement on soft clay using shear wave velocity and damping characteristics. *Engineering Geology*, 123(4):259-270. <https://doi.org/10.1016/j.enggeo.2011.06.004>.
- Onyejekwe, S.; Kang, X. & Ge, L. (2016). Evaluation of the scale of fluctuation of geotechnical parameters by autocorrelation function and semivariogram function. *Engineering Geology*, 214:43-49. <https://doi.org/10.1016/j.enggeo.2016.09.014>.
- Rix, G.J. & Stokoe II, K.H. (1991). Correlation of initial tangent modulus and cone penetration resistance. *Proc. 1st International Symposium on Calibration Chamber Testing*, Elsevier Publishing, New York, pp. 351-362.
- Robertson, P.K. (2009). Interpretation of cone penetration tests - A unified approach. *Canadian Geotechnical Journal*, 46(11):1337-1355. <https://doi.org/10.1139/T09-065>.
- Robertson, P.K. & Wride, C.E. (1998). Evaluating cyclic liquefaction potential using the cone penetration test. *Canadian Geotechnical Journal*, 35(3):442-459. <https://doi.org/10.1139/t98-017>.
- Schnaid, F. (2008). *In Situ Testing in Geomechanics*. CRC Press, London, 329 p.
- Schneider, J.A.; Mayne, P.W. & Rix, G.J. (2001). Geotechnical site characterization in the greater Memphis area using cone penetration tests. *Engineering Geology*, 62(1-3):169-184. [https://doi.org/10.1016/S0013-7952\(01\)00060-6](https://doi.org/10.1016/S0013-7952(01)00060-6).
- Simonini, P. & Cola, S. (2000). Use of piezocone to predict maximum stiffness of Venetian soils. *Journal of Geotechnical and Geoenvironmental Engineering*, 126(4):378-382. [https://doi.org/10.1061/\(ASCE\)1090-0241\(2000\)126:4\(378\)](https://doi.org/10.1061/(ASCE)1090-0241(2000)126:4(378)).
- Taboada, V.M.; Cruz, D.; Barrera, P.; Espinosa, E.; Carrasco, D. & Gan, K.C. (2013). Predictive equations of shear wave velocity for Bay of Campeche clay. *Proc. Offshore Technology Conference*, Houston, pp. 1-13.
- Taboada, V.M.; Cruz, D.; Barrera, P.; Renovato Carrion, S.D.; Hernández, J.M. & Gan, K.C. (2015). Predictive equations of shear wave velocity for Bay of Campeche sand. *Proc. 3rd International Symposium of Frontiers in Offshore Geotechnics (ISFOG 2015)*, Oslo, Taylor & Francis Group, London, pp. 1115-1120.
- Tong, L.; Che, H.; Zhang, M. & Li, H. (2018). Review of shear-wave velocity prediction equations based on piezocone penetration test data: example from Yangtze River floodplain deposits at Nanjing, Jiangsu Province, China. *Quarterly Journal of Engineering Geology and Hydrogeology*, 51(2):229-246. <http://dx.doi.org/10.1144/qjegh2016-088>.
- Tonni, L. & Simonini, P. (2013). Shear wave velocity as function of cone penetration test measurements in sand and silt mixtures. *Engineering Geology*, 163:55-67. <https://doi.org/10.1016/j.enggeo.2013.06.005>.
- Vicalvi, M.A. (1999). *Biostratigraphic and paleoclimatic zoning of the upper quaternary of the Campos basin slope and adjacent São Paulo plateau, based on planktonic foraminifera*. D.Sc. Dissertation, Department of

- Geosciences, Federal University of Rio de Janeiro, Rio de Janeiro, 236 p.
- Vicalvi, M.A. & Kowsmann, R.O. (2006). Application of foraminiferal biostratigraphy to the assessment of submarine geohazards. Proc. International Symposium of Foraminifera - Forams 2006, IGEO, Rio de Janeiro, v. 1, pp. 637.
- Vitali, O.P.M.; Pedrini, R.A.A.; Oliveira, L.P.R. & Giachetti, H.L. (2012). Developing a system for down-hole seismic testing together with the CPTU. *Soils and Rocks*, 35(1):75-87.
- Wair, B.R.; Dejong, J.T. & Shantz, T. (2012). Guidelines for estimation of shear wave velocity profiles. Pacific Earthquake Engineering Research Center, California, 95 p.
- Youd, T.L.; Idriss, I.M.; Andrus, R.D.; Arango, I.; Castro, G.; Christian, J.T.; Dobry, R.; Finn, W.D.L.; Harder, L.F.; Hynes, M.E.; Ishihara, K.; Koester, J.P.; Liao, S.S.C.; Marcuson, W.F.; Martin, G.R.; Mitchell, J.K.; Moriwaki, Y.; Power, M.S.; Robertson, P.K.; Seed, R.B. & Stokoe, K.H. (2001). Liquefaction resistance of soils: summary report from the 1996 NCEER and 1998 NCEER/NSF Workshops on evaluation of liquefaction resistance of soils. *Journal of Geotechnical and Geoenvironmental Engineering*, 127(10):817-833. [https://doi.org/10.1061/\(ASCE\)1090-0241\(2001\)127:10\(817\)](https://doi.org/10.1061/(ASCE)1090-0241(2001)127:10(817)).
- Zhang, M. & Tong, L. (2017). New statistical and graphical assessment of CPT-based empirical correlations for the shear wave velocity of soils. *Engineering Geology*, 226:184-191. <https://doi.org/10.1016/j.enggeo.2017.06.007>.
- Zou, H.; Liu, S.; Cai, G.; Puppala, A.J. & Bheemasetti, T.V. (2017). Multivariate correlation analysis of seismic piezocone penetration (SCPTU) parameters and design properties of Jiangsu quaternary cohesive soils. *Engineering Geology*, 228:11-38. <https://doi.org/10.1016/j.enggeo.2017.07.005>.

## List of Symbols

- CaCO<sub>3</sub>: calcium carbonate  
 $R^2$ : coefficient of determination  
 $CoV$ : coefficient of variation  
 $C_c$ : compression index  
 $q_t$ : corrected cone tip resistance  
 $d$ : depth below mudline  
 $\sigma'_{vo}$ : effective vertical stress  
 $\Delta u$ : excess pore pressure  
 $u_0$ : hydrostatic pore pressure  
 $G_{max}$ : maximum shear modulus  
 $\mu$ : mean  
 $q_c$ : measured cone tip resistance  
 $u_2$ : measured pore pressure at the position  $u_2$   
 $q_{net}$ : net cone resistance  
 $Q_m$ : normalized cone resistance  
 $n$ : number of samples  
 $I_p$ : Plasticity Index  
 $B_q$ : pore pressure ratio  
 $K$ : prediction bias  
 $RD$ : ranking distance  
 $RI$ : ranking index  
 $RMSE$ : root mean square error  
 $V_s$ : shear wave velocity  
 $f_s$ : sleeve friction  
 $I_c$ : soil behavior type index  
 $\sigma$ : standard deviation  
 $\gamma$ : total unit weight  
 $\sigma_{vo}$ : total vertical stress  
 $s_u$ : undrained shear strength

# Geogrid Mechanical Damage Caused by Recycled Construction and Demolition Waste (RCDW): Influence of Grain Size Distribution

M.L. Domiciano, E.C.G. Santos, J. Lins da Silva

**Abstract.** Recent studies have shown that recycled construction and demolition waste (RCDW) can be used as backfill material in geosynthetics reinforced soil (GRS) structures. However, besides the environmental and economic benefits of this practice, it is necessary to evaluate the mechanical damages that RCDW could cause to the reinforcement elements. This study aims to investigate the influence of RCDW grain size distribution on short-term geosynthetic mechanical damages. The RCDW used in this investigation was collected at a recycling plant and the geosynthetics consisted of geogrids usually employed in GRS structures. In order to simulate the mechanical damages, a steel box was used and the applied loads within the magnitudes of values normally observed in this type of engineering work. The results showed no significant reduction for tensile strength of geogrids. On the other hand, it was possible to notice the effects of loading process on strain at rupture and stiffness. However, the reduction factors obtained from the damaged geogrids could be applied during GRS design stage. This study concludes that the damages caused by RCDW to geogrids would not prevent the use of this new composite in several engineering works.

**Keywords:** debris, durability, geosynthetics, granulometry, loading process, sustainability.

## 1. Introduction

Due to its need of using a tremendous variety of materials and processes, the construction industry plays a significant role in environmental issues, not just as a domestic industry, but on a global scale. The construction industry stands pointed out as one of the largest producers of solid waste on the planet, being responsible for over 10 billion tons generated worldwide every year (Wu *et al.*, 2019). Therefore, preventing environmental, economic, and social impacts caused by the construction and demolition wastes (CDW) demands attitude changes in order to turn the efficient management and reuse of these wastes into worldwide goals.

In this context, geosynthetics appear as modern and environmentally friendly products derived from researches and development of the polymer industry and geotechnical engineering. These materials have been increasingly used in geotechnical engineering due to their economic and environmental benefits. Over the last decades, geosynthetic reinforced soil (GRS) walls have presented a series of positive ecological parameters when compared to traditional concrete cantilever walls (Jones, 1994), which include 40 % less SO<sub>2</sub> released into the atmosphere during the fabrication of their component parts.

Reinforcement material durability is an important issue related to the design and performance of GRS walls. Therefore, besides promoting good interaction with the geosynthetic, the filling material is expected to be biochemically and mechanically low-aggressive. Bearing in mind these aspects, even though the proposal of using recycled construction and demolition waste (RCDW) as backfill material in GRS structures seems to be an interesting strategy to promote the concept of sustainable development in Civil Engineering, it is crucial to investigate the eventual damages caused by this non-conventional filling material in a field condition.

### 1.1. Characteristics of RCDW grain

The definition of CDW is not a consensus, varying from one country to another. But, apart from some peculiar local construction characteristics, the CDW consist of a mixture of different materials: i) ceramics, ii) concrete blocks, iii) mortar, iv) steel, v) plastic, vi) wood and others. The diversity of materials composing the CDW and the different procedures adopted at recycling plants lead up to products with different properties and grain size distribution (Kartam *et al.*, 2004; Esin & Cosgun, 2007; Angulo *et al.*, 2011; Leite *et al.*, 2011; Ossa *et al.*, 2016).

Marcela L. Domiciano, M.Sc., Assistant Professor, Departamento de Engenharia Civil, Centro Universitário de Goiânia, Av. T-02, 1993, 74215-005, Goiânia, GO, Brazil. E-mail: marcelaleadomiciano@gmail.com.

Eder C.G. Santos, D.Sc., Associate Professor, Escola de Engenharia Civil e Ambiental da Universidade Federal de Goiás, Avenida Universitária, nº 1488, Qd. 86, Setor Universitário, 74.605-220 Goiânia, GO, Brazil. E-mail: edersantos@ufg.br.

Jefferson Lins da Silva, D.Sc., Associate Professor, Escola de Engenharia de São Carlos (EESC) da Universidade de São Paulo, Avenida Trabalhador São-Carlense, 400, Pq Arnold Schmidt, 13.566-590 São Carlos, SP, Brazil. E-mail: jefferson@sc.usp.br.

Submitted on March 16, 2020; Final Acceptance on April 6, 2020; Discussion open until September 30, 2020.

DOI: 10.28927/SR.432231

The granulometric variability of RCDW sampled at recycling plants has been reported in some geotechnical investigations (Santos, 2007; Barbosa, 2017; Santos *et al.*, 2013; Fleury, 2018; Silvestre, 2019) and maximum values (highest coefficient of variation of material percentage passing through a specific mesh aperture) were noted, ranging from 15 % (Barbosa, 2017) to 109 % (Silvestre, 2019). Given that the grain size distribution of RCDW is one of the features that affect the degree of interlocking between its particles, hence affecting the contact area, the evaluation of the granulometric variability can help indicate how standardized it will be.

Another important factor that affects the interlocking characteristic of particulate media is the particle shape. The results reported by Leite *et al.* (2011) revealed that RCDW composition influenced the shapes of the grains - cementitious materials and crushed rocks have a wide predominance of cubic grains - and the particles presented a higher percentage of cubic grains after compaction test. The study concluded that cubic particles could contribute to better densification and higher shear strength. On the other hand, flat and elongated particles would be more susceptible to breaking when compacted. When testing individual RCDW grains, it was possible to verify that particle shapes play a more prominent role in particle breakage phenomena than mineralogy and microstructure (Afshar *et al.*, 2017).

## 1.2. Geosynthetic mechanical damages caused by RCDW

The reduction of geogrid ultimate tensile strength ( $T_{ult}$ ) due to installation damage becomes a problem for determining its allowable tensile strength ( $T_{al}$ ). To deal with the damage caused by installation activities, and others which geosynthetics are exposed to, GRS structure designers consider the application of reduction factors to determine  $T_{al}$ , according to (Allen & Bathurst, 1996):

$$T_{al} = \frac{T_{ult}}{RF} = \frac{T_{ult}}{RF_{ID} \cdot RF_{CR} \cdot RF_D} \quad (1)$$

where  $T_{ult}$  is the ultimate tensile strength;  $RF$ , the global reduction factor;  $RF_{ID}$  is the installation damage reduction factor;  $RF_{CR}$ , the creep reduction factor; and  $RF_D$  is the durability reduction factor. The  $RF_{ID}$  is calculated according to

$$RF_{ID} = \frac{T_{ult_v}}{T_{ult_d}} \quad (2)$$

where  $T_{ult_v}$  and  $T_{ult_d}$  represent the ultimate tensile strength mean value of virgin (undamaged) and damaged specimens, respectively.

This damage can be more severe when geogrids are used together with larger size aggregate particles and compacted with high energy (Huang & Wang, 2007; Pinho-Lopes; Lopes, 2014; Fleury *et al.*, 2019). Mechanical dam-

age to geosynthetics can be evaluated by i) tensile strength, ii) strain at rupture and ii) secant stiffness, from the curves tensile strength against strain obtained in laboratory tensile tests (Allen & Bathurst, 1994).

Some researchers (Paula *et al.*, 2004; Huang, 2006; Huang & Chiou, 2006; Huang & Wang, 2007; Yoo *et al.*, 2009; Rosete *et al.*, 2013; Gonzalez-Torre *et al.*, 2014) carried out the standard laboratory test, according to EN ISO 10722:2007 (BSI, 2007), focused on assessing the mechanical damage to geogrids under repeated loading with granular materials. The values of reduction factors for mechanical damages ( $RF_{MD}$ ), for different repeated loads and granular materials, ranged between 0.93 and 1.54.

Mechanical damages caused by RCDW to geosynthetic reinforcement elements used in an in-field experimental large-scale wall were investigated by Santos *et al.* (2012). The RCDW collected in a construction site located in Brasília, Brazil, consisted of demolition waste submitted to primary crushing in order to reduce its particle size. The geotechnical characterization showed that the RCDW was classified as a sandy gravel. Based on a statistical analysis proposed by Santos (2011), the results revealed that different compaction procedures (lightweight roller or vibratory hammer) caused distinct damages to polyester (PET) geogrid (GG) ( $T_{ult} = 20$  kN/m).

An investigation of the effects of dropping height (0.0 m, 1.0 m and 2.0 m) and compaction procedure (vibratory plate) on the mechanical damages of a polyester (PET) geogrid ( $T_{ult} = 35$  kN/m) revealed that the RCDW, classified as gravely sand, caused damages with low or very low magnitudes, considering all the scenarios investigated (Barbosa & Santos, 2013).

In a recent study, Fleury *et al.* (2019) investigated the occurrence of mechanical damage during the installation of geogrids in an in-field test facility with RCDW backfill material. The results showed that the variation of dropping height (0.0 m, 1.0 m, and 2.0 m) caused a slight reduction in the ultimate tensile strength ( $T_{ult}$ ) ( $RF_{ID} = 0.94$  to 1.21). However, the authors also observed that compaction methods were a relevant factor for geogrid installation damage in most of the investigated scenarios, with  $RF_{ID}$  ranging from 0.98 to 1.22, with the vibratory hammer compaction promoting the highest reduction effect.

Despite the contribution made by laboratory and in-field tests, the investigation of mechanical damage to geosynthetic products caused by non-conventional material brings together the need to evaluate some issues so far not assessed. Bearing in mind the proposal of using RCDW as backfill material, the evaluation of grain size distribution may raise another aspect that could affect the level and way mechanical damages occur to geosynthetic products: particle breakage during the loading process. Therefore, this paper aims to evaluate and quantify the effect of grain size distribution curves on RCDW breakage and its consequence for the mechanical damage caused to geogrids.

## 2. Materials and Methods

### 2.1. Materials

#### 2.1.1. RCDW

The RCDW used in this investigation were produced by a recycling plant in Aparecida de Goiânia-GO, Brazil. The recycling plant uses a jaw crusher, in a single operation, to reduce the particle size of CDW and to produce different materials, such as: i) Aggregate A ( $9.5 \text{ mm} > d > 4.75 \text{ mm}$ ), ii) Aggregate B ( $19 \text{ mm} > d > 9.5 \text{ mm}$ ), iii) Aggregate C ( $d < 19 \text{ mm}$ ), iv) Aggregate D ( $d > 19 \text{ mm}$ ), v) Sand A ( $d < 4.75 \text{ mm}$ , sand composed of crushed CDW), vi) Sand B ( $d < 4.75 \text{ mm}$ , sand composed of crushed concrete) and vii) By-product. Bearing in mind the aims of this study and size limitations of the test box, the RCDW were selected based on their potential to be used as backfill material in GRS structures.

Three types of recycled products were investigated: i) Aggregate A, ii) Aggregate B and iii) Aggregate C (Fig. 1). According to the manufacturer, Aggregate C is composed of equal volumes of Aggregate A, Aggregate B and Sand B. It is important to point out that Aggregate C represents around 44 % of the products sold by the recycling plant nowadays.

#### 2.1.2. Geosynthetics

To investigate the influence of geogrid structure on the strength against mechanical damages, tests were carried out with three types of geogrids, being one composed of polyvinyl alcohol yarns (GGPVA,  $T_{ult} = 35 \text{ kN/m}$ ; mass per unit area,  $M_A = 160 \text{ g/m}^2$ ) and two others of polyester yarns

(GGPET 01,  $T_{ult} = 55 \text{ kN/m}$ ,  $M_A = 280 \text{ g/m}^2$ ; GGPET 02,  $T_{ult} = 35 \text{ kN/m}$ ,  $M_A = 185 \text{ g/m}^2$ ). These geogrids are usually used as reinforcement elements in GRS structures. Figure 2 presents the images of the geogrids.

The dimensions of the geogrid specimen submitted to tensile strength testing consisted of 200 mm (transversal direction) by 1,200 mm (longitudinal direction). The processes of storage, transportation and cutting of the geogrid specimens were carried out carefully to avoid any damages to the virgin samples, as well as any additional damages to the tested specimens.

### 2.2. Experimental program

#### 2.2.1. RCDW characterization

For each kind of RCDW, five samples were collected at one-monthly intervals trying to verify eventual variability of the recycled products, and the sampling procedure was carried out in different parts of the waste pile (bottom, middle and top). The laboratory tests followed the Brazilian standards and consisted in those usually performed for soil characterization: i) specific gravity (NBR 6458, ABNT, 2016a), ii) grain size distribution (NBR 7181, ABNT, 2016b), iii) Atterberg limits (NBR 6459, ABNT, 2016c; NBR 7180, ABNT, 2016d), iv) compaction test (Standard Proctor) (NBR 7182, ABNT, 2016e), and v) gravimetric composition.

Once the RCDW samples were sieved before and after each test of damage reproduction, it was possible to compare grain size distribution curves and particle shapes before and after the loading process. The use of a microscope also aimed to identify the roughness of RCDW particles.

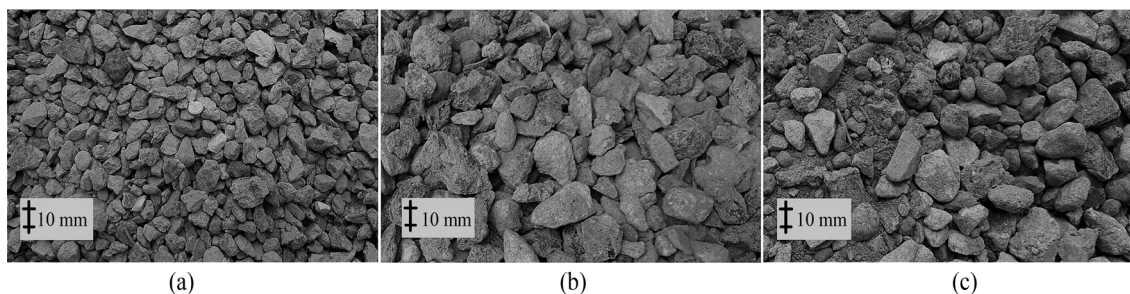


Figure 1 - RCDW: a) Aggregate A, b) Aggregate B and c) Aggregate C.

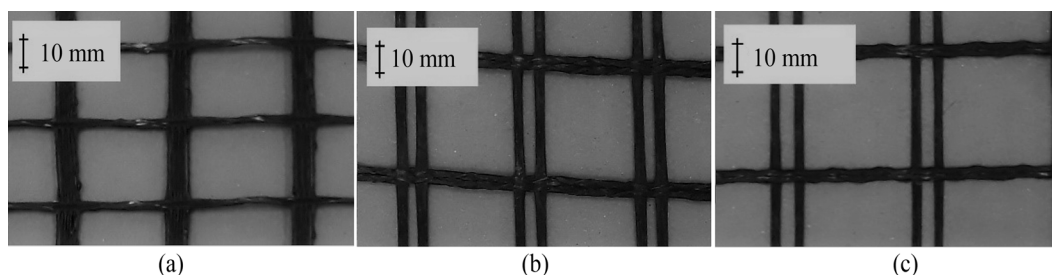


Figure 2 - Geogrids: a) GGPVA, b) GGPET 01 and c) GGPET 02.

The gravimetric composition was carried out according to the procedure presented by Santos (2007). Initially, 10.0 kg of Aggregate C were sieved on a mesh of 4.75 mm under running water; the retained material was left to dry in an oven for at least 12 h; finally, the retained material was sorted by visual analysis (naked eye) according to the different gravimetric compositions. Particles of RCDW smaller than 4.75 mm (including those removed during the washing process) were classified as ‘soil’.

The procedure of evaluating the shape and roughness of RCDW particles, consisting of visual analysis by means of a digital microscope, was used to verify the shape and surface roughness of the RCDW particles. The equipment used has magnification ranging from 5× to 100×. The images of coarse grains (dimensions varying from 2.0 mm to 10.0 mm) were taken using a magnifying glass.

### 2.2.2. Laboratory damage reproduction

The mechanical damage was carried out reproducing the loading process using a steel-made box (440 long × 300 wide × 300 mm high) which is divided into two parts (upper and bottom). At the middle height, the test box has an aperture for geosynthetic installation. Figure 3 shows the equipment dimensions in a perspective view. The mechanical damage tests were performed with the last collected samples of each kind of aggregate (nominated ‘samples #5’).

The test procedure consisted of placing the RCDW (dry condition) in the test box up to its medium height (bottom part completely filled). Then, the RCDW was statically compacted (one-dimensional compression) using a universal testing equipment until the material achieved a compaction degree approximately equal to 85 % (Standard Proctor) - Fleury *et al.* (2019) reported a value of 89 % when compacting recycled materials from the same recycling plant with a vibratory roller. Then, the central part of the geogrid specimen (300 mm long and 200 mm wide) was laid in contact with the RCDW - the extreme portions of the geogrid remained outside the box and not damaged. Finally, the upper part of the test box was positioned, filled up with

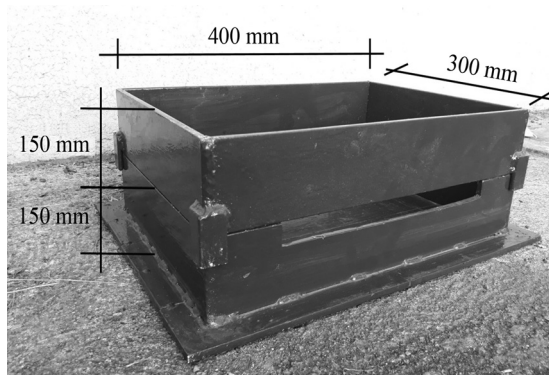


**Figure 3** - Test box perspective view and dimensions.

RCDW and also statically compacted to the same degree of compaction.

Once the test box had been totally assembled, the normal stress was applied (increment of 10.2 kN/min) on a steel plate of 20 × 200 × 340 mm using the universal testing equipment. Considering a GRS higher than 10.0 m and eventual external loads, tests were carried out with 150 kPa, 300 kPa, and 600 kPa. Once achieved the intended load, it was kept for 5 min - enough time to stabilize plate displacement detected by monitoring instruments. Bearing in mind the variability of RCDW, five tests (non-reuse) were performed for each load, which resulted in a total amount of 135 specimens.

Following that, the specimens were carefully exhumed to prevent the occurrence of additional mechanical damages, properly identified and submitted to tensile tests - this last one, at São Carlos School of Engineering (EESC), University of São Paulo (USP). The tensile tests were carried out according to ASTM D-6637-15 - Standard Test Method for Determining Tensile Properties of Geogrids by the Single or Multi-Rib Tensile Method (ASTM, 2015). Figure 4 shows the executive sequence of the damage simulation test.

### 2.2.3. Validation and quantification of damage

To determine valid the occurrence of damage, the method proposed by Santos (2011) was used with the reduction factors (RF) being calculated considering the variability of virgin specimens. According to the method, the confidence interval (nominated  $F_0$ ) of the properties of in-

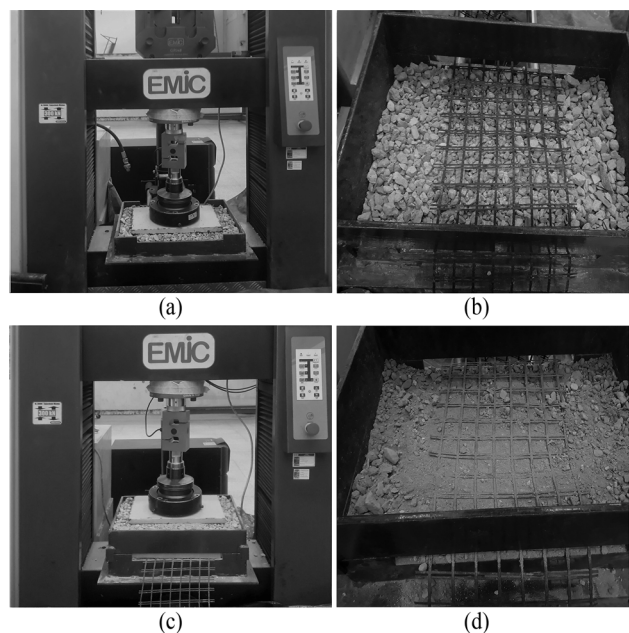


**Figure 4** - Executive sequence: a) static compaction of RCDW in the box bottom part, b) geosynthetic laid in contact with the RCDW, c) application of load during the test, d) exhumation of geogrid specimen.

terest ( $T_{ult}$ ,  $\epsilon_{rup}$ , and  $J_{sec}$ ) was obtained from the tests of virgin specimens using Student's  $t$ -distribution with the sample mean value confidence given by

$$t = \frac{\bar{X} - \mu}{\frac{S}{\sqrt{n}}} \quad (3)$$

where  $t$  is the value of the Student's  $t$ -distribution variable,  $\bar{X}$  is the mean value of the virgin sample;  $\mu$ , the population mean;  $S$ , sample standard deviation; and  $n$  is the sample size.

To calculate the value of  $RF$ , two scenarios were evaluated: i) the damaged sample mean value ( $\bar{X}_d$ ) into the virgin sample confidence level interval raises doubt about the occurrence of damage, hence the reduction factor was assumed as equal to 1.0; ii) in the case of the damaged sample mean value ( $\bar{X}_d$ ) out of the virgin sample confidence level interval, the reduction factor was calculated according to

$$RF_x = \frac{\bar{X}}{\bar{X}_d} \quad (4)$$

where  $RF_x$  is the reduction factor related to the  $X$  parameter,  $\bar{X}$  is the virgin sample mean value of the analyzed parameter and  $\bar{X}_d$  is the damaged sample mean value of analyzed parameter.

### 3. Results and Discussion

#### 3.1. Recycled construction and demolition waste

##### 3.1.1. Granulometric analysis

The grain size distribution curves of RCDW showed a significant variability, which made the samples be better evaluated using a 'grain size distribution range'. These results revealed that the procedures adopted at the recycling plant presented different levels of efficiency, being less efficient (higher variability) when involving processes of mixture of some products for producing a new one. Another factor that must be pointed out is related to the weather conditions during the recycling process, given that samples of Aggregate A (A-A #3 and #4), collected on rainy days, showed higher amount of fine materials. Figures 5 to 7 present the grain size distribution curves of investigated recycled aggregates and show the grain size distribution ranges for each sample of RCDW. Table 1 presents RCDW classification according to the Unified Soil Classification System (USCS) - (ASTM, 2017).

##### 3.1.2. Gravimetric composition

The gravimetric composition analysis revealed that approximately 98 % of the composite materials of Aggregate C #1 can be classified as inert materials (soil, concrete, ceramic materials, and natural gravel), with no more than 2 % composed of metal, wood, paper, plastic and other materials - similar results have been found by Herrador *et al.*

(2012) and Santos *et al.* (2013, 2014). Percentages of soil, Portland cement concrete and ceramics showed significant values of coefficient of variation (COV) equal to 45.19 %, 27.90 % and 70.92 %, respectively. Figure 8 shows the results of the gravimetric composition analysis of the Aggregate C samples.

The variation of soil amount in the RCDW composition can be justified by the fact that buildings in the

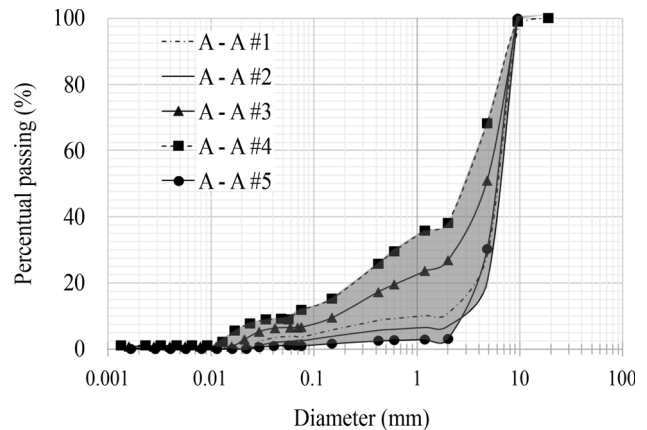


Figure 5 - Aggregate A grain size distribution curves.

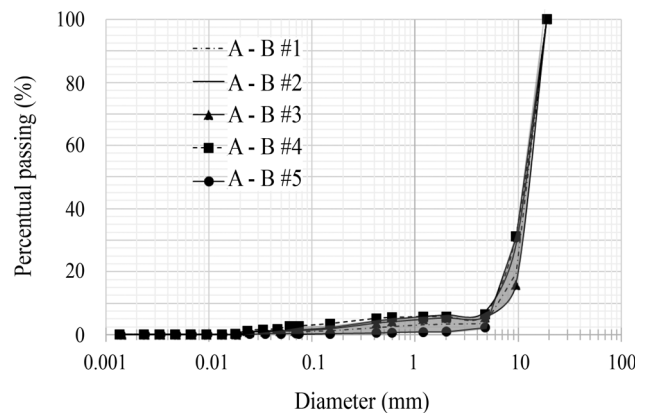


Figure 6 - Aggregate B grain size distribution curves.

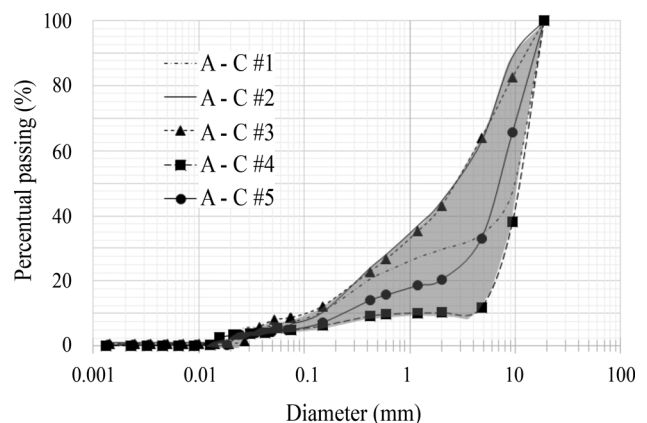


Figure 7 - Aggregate C grain size distribution curves.

**Table 1** - Classification of the RCDW according to the USCS system.

| Sample | Aggregate A       | Aggregate B | Aggregate C       |
|--------|-------------------|-------------|-------------------|
| #1     | GP-GM with sand   | GP          | GW-GM with sand   |
| #2     | GP with sand      | GP          | SW-SM with gravel |
| #3     | SP-SM with gravel | GP          | SW-SM with gravel |
| #4     | SW-SM with gravel | GP          | GP-GM with sand   |
| #5     | GP with sand      | GP          | GP-GM with sand   |

Note: GW = well graded gravel; GP = poorly graded gravel; GM = silty gravel; SW = well-graded sand, fine to coarse sand; SP = poorly graded sand; SM = silty sand.

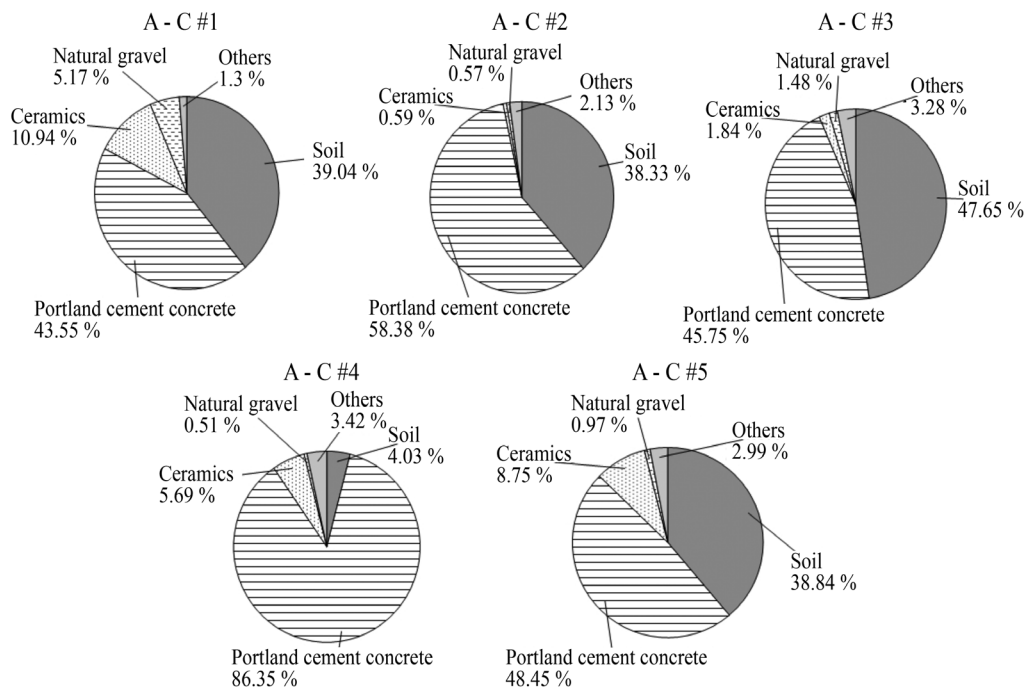
metropolitan area where the recycling plant is located possess underground structures (underground garage, for example), once the deep water table verified at the region allows this type of construction. Therefore, this kind of underground construction is responsible for a significant amount of excavated soil sent to the recycling plant.

The variation of Portland cement concrete and ceramic materials amount reveals, besides the main construction characteristics of the local buildings, the lack of waste management in the construction site. Given that the constructions have several types of materials, such as reinforced concrete, metallic structures, wood, soil, tile, bricks, etc., these materials should be submitted to a process of segregation/separation in the construction site. However, at present, the segregation process is not carried out in most construction sites in Goiânia-GO, Brazil.

### 3.1.3. Specific gravity

Due to the diverse materials found in RCDW, the specific gravity ( $G_s$ ) of i) particles passing in the 4.75-mm sieve and ii) particles passing in the 19-mm sieve and retained by the 4.75-mm sieve were investigated. Results showed that the mean value of  $G_s$  for the particles passing in the 4.75-mm sieve was practically the same for Aggregate B (2.602 g/cm<sup>3</sup>,  $COV = 0.54\%$ ) and Aggregate C (2.603 g/cm<sup>3</sup>,  $COV = 3.28\%$ ); and Aggregate A presented a mean value approximately 20% smaller than the other materials ( $G_s$  equal to 2.166 g/cm<sup>3</sup>).

The  $G_s$  of the grains retained in the 4.75-mm sieve, considering the three materials (A-A, A-B, and A-C) showed mean values ranging from 2.658 g/cm<sup>3</sup> to 2.684 g/cm<sup>3</sup>, similar to the ones reported by Santos & Leite (2018) and approximately 21% higher than those presented by Angulo *et al.* (2011). This fact can be justified by the different focus given to the RCDW studied, since the latter au-

**Figure 8** - Percentage of composite materials.

thors investigated the use of recycled aggregates in non-structural concrete.

The results revealed low variability of  $G_s$  of the RCDW. The variability of the material passing in the 4.75-mm sieve ranged from 0.54 % to 4.21 %, and the variability of the material retained in the 4.75-mm sieve (and passing the 19-mm sieve) ranged from 0.27 % to 1.63 %.

It was observed that Aggregate C presented considerable amount of soil in its composition. Previous studies on the local soil (tropical soil) revealed values of  $G_s$  varying from 2.664 g/cm<sup>3</sup> (Silva *et al.*, 2019) to 2.740 g/cm<sup>3</sup> (Mascarenha *et al.*, 2018). Aggregate A visibly exhibited a greater amount of ceramic material, which is probably responsible for the reduction of its  $G_s$ .

### 3.1.4. Atterberg limits

All the samples presented non-plastic behavior, which can be explained by the fact of having low presence of clay particles (diameter < 0.002 mm). These results also follow those found by Santos *et al.* (2013, 2014) and Ossa *et al.* (2016). It is worth mentioning that these results validate the application of RCDW as backfill material in GRS, according to the recommendation of BSI 8006 (2010).

### 3.1.5. Compaction

Standard Proctor compaction tests were carried out only on four samples of Aggregate C, once the very low amount of fine material did not allow making the test with sample A-C #4. Aggregate A and Aggregate B also were not tested for the same reason. Figure 9 and Table 2 present the results of the compaction test carried out without reuse of material.

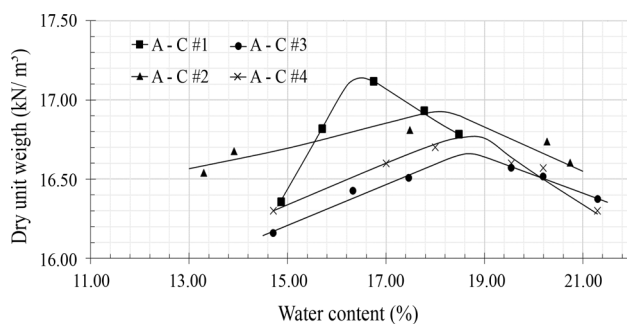


**Figure 9** - Compaction test curves - Aggregate C (except sample A-C #4).

**Table 2** - Maximum dry unit weight and optimum water content - Aggregate C (except sample A-C #4).

| Property   | A-C #1 | A-C #2 | A-C #3 | A-C #5 | Mean   | COV (%) |
|--|--------|--------|--------|--------|--------|---------|
| $\gamma_{d-max}$ (kN/m <sup>3</sup> ) <sup>a</sup> | 17.150 | 16.925 | 16.660 | 16.758 | 16.859 | 1.13    |
| $w_{op}$ (%) <sup>b</sup>                          | 17.10  | 18.00  | 18.70  | 19.00  | 17.60  | 4.70    |

Note: <sup>a</sup>Maximum dry unit weight; <sup>b</sup>Optimum water content.

The results of the compaction test revealed the direct influence of ceramic material content. Higher amount of ceramic material causing higher values of optimum water content was observed. These results follow those presented by Silva *et al.* (2016) and Cardoso *et al.* (2016). However, sample A-C #1, despite having the highest content of ceramic aggregates, showed the lower optimum water content. This discrepancy encourages further investigation into the properties of the ceramic materials present in RCDW.

## 3.2. Influence of loading process on RCDW properties

Considering that the process of applying loads of 150 kPa, 300 kPa and 600 kPa could break the low-resistance particles of RCDW, specific gravity tests carried out and grain size distribution curves were drawn using samples from different loading conditions.

### 3.2.1 Characterization of materials

The results showed that there was no great variation of the values of  $G_s$  of the recycled materials submitted to different loads in comparison to the one presented by the intact material (without loading), even considering both analyzed particle sizes (passing in the 4.75-mm sieve or retained in the 4.75-mm sieve). Table 3 presents the  $G_s$  values of tested materials.

The effects of loading on RCDW characteristics were also investigated with grain size distribution analysis of the tested samples. For this purpose, tests were performed on the materials applying different loads and, to show the percentage difference for different samples and scenarios, curves were drawn in comparison to those not submitted to loading (Fig. 10).

It was noticed that the higher the load applied, the greater the quantity of fine grains in all the tested materials. However, it is possible to point out that specific changes were observed. The highest particle size variations for all samples (A-C, A-B, and A-A) occurred around the grain dimensions of 4.75 mm. In general, the grain breakage showed increase up to the diameter of 4.75 mm and decreased after this diameter.

The Aggregate A appeared as the most sensitive in relation to breakage by increased loading, probably due to its uniform grain size distribution and the presence of some particles of ceramic materials. This statement is strengthened by the results of Aggregate B, which presented smaller breakage value for the different loads. Even though

presenting a uniform grain size distribution, this aggregate was predominantly composed of concrete.

**Table 3** - Effect of loading process on specific gravity of the RCDW aggregates.

| Sample                        | Specific gravity - $G_s$ (g/cm <sup>3</sup> ) |                    |
|-------------------------------|---|--------------------|
|                               | Passing (4.75-mm)                             | Retained (4.75-mm) |
| A-A - No Loading <sup>a</sup> | 2.166   | 2.684              |
| A-A - 150 kPa                 | 2.156   | 2.650              |
| A-A - 300 kPa                 | 2.117   | 2.664              |
| A-A - 600 kPa                 | 2.224   | 2.776              |
| A-B - No Loading <sup>a</sup> | 2.602   | 2.658              |
| A-B - 150 kPa                 | 2.660   | 2.645              |
| A-B - 300 kPa                 | 2.643   | 2.635              |
| A-B - 600 kPa                 | 2.614   | 2.686              |
| A-C - No Loading <sup>a</sup> | 2.603   | 2.674              |
| A-C - 150 kPa                 | 2.600   | 2.658              |
| A-C - 300 kPa                 | 2.586   | 2.678              |
| A-C - 600 kPa                 | 2.609   | 2.678              |

Note: <sup>a</sup>Mean value of five samples.

### 3.2.2. RCDW particle shape and roughness

Images of the studied materials (A-A, A-B, and A-C) - intact and subjected to the loading process - were taken using a microscope to analyze the effect of loading on particle shape and roughness. The materials retained in sieves 9.5-mm, 4.75-mm, and 2.0-mm were analyzed separately, so their characteristics could be verified in relation to the specific applied load.

The images did not allow to verify any difference related to particle shapes. No relationship between loading process and grain roughness changes was observed in grains retained in sieves 2.00-mm and 4.75-mm. This can be justified by the fact that coarser particles are the ones presenting most modification in relation to the shape when subject to loading, as stated by Leite *et al.* (2011). The image of Aggregate C particles retained in the sieve 9.5-mm (Fig. 11) revealed a smooth surface for loading of 600 kPa. Results revealed that the maximum load of 600 kPa, although not enough to break the particle when it consisted of natural aggregate (rock), could remove the mortar around the natural aggregate. This can explain the changes showed when comparing the grain size distribution of materials subject to the loading process.

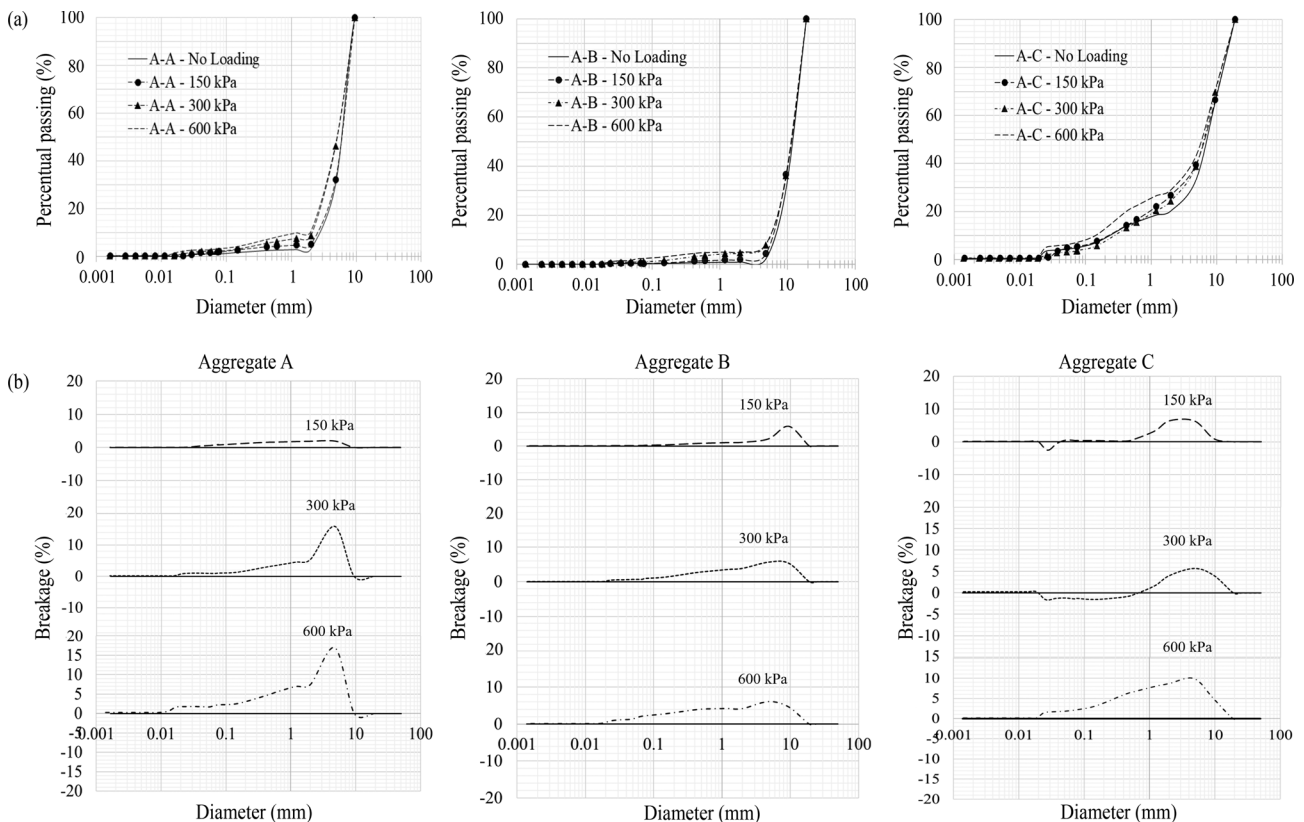


**Figure 10** - Granulometric analysis of aggregates for different loads: a) Grain size distribution curves, b) Percentage difference of particle passing.

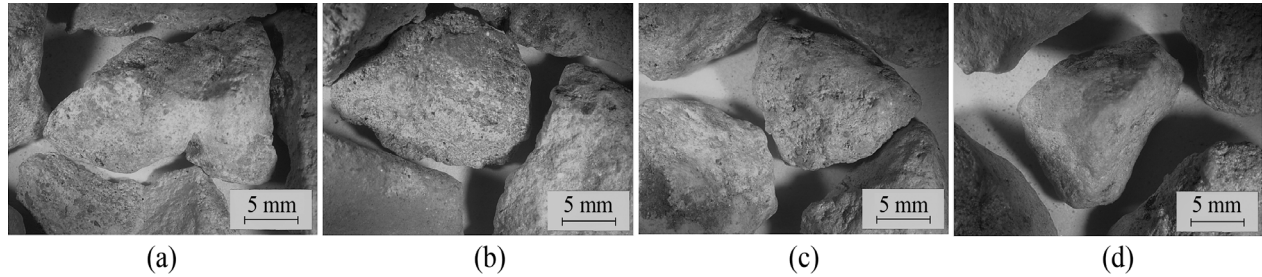


**Figure 11** - Grains of A-C retained sieve 9.5-mm: a) No loading, b) 150 kPa, c) 300 kPa, d) 600 kPa.

### 3.3. Geogrids

#### 3.3.1. Tensile test in virgin samples and determination of confidence interval

The results of tensile tests carried out on five virgin samples of each geogrid type revealed smaller ultimate tensile strength ( $T_{ult}$ ) compared to the manufacturer's information (see section 2.1.2). GGPVA presented a mean value of  $T_{ult}$  equal to 26.3 kN/m and the lowest variability ( $COV = 7.8\%$ ), meanwhile GGPET01 showed a mean value of  $T_{ult}$  equal to 38.7 kN/m and the highest variability ( $COV = 13.2\%$ ). GGPET02 presented a mean value of  $T_{ult}$  equal to 27.4 ( $COV = 12.2\%$ ).

In relation to the tensile stiffness, the GGPVA showed the lowest variability for stiffness at 2% ( $J_{2\%}$ ). This geogrid revealed an average  $J_{2\%}$  equal to 550.00 N/m and value of  $COV$  equal to 6%. Due to the fact that the tensile rupture occurred below the strain of 5%, the stiffness for this scenario ( $J_{5\%}$ ) was not calculated. The results showed that the GGPET 01 presented mean values of  $J_{2\%}$  and  $J_{5\%}$  equal to 694.00 N/m ( $COV = 25\%$ ) and 555.20 N/m

( $COV = 16.2\%$ ), respectively. The GGPET 02 revealed  $J_{2\%}$  equal to 680.00 N/m with the highest variability ( $COV = 33.4\%$ ) and  $J_{5\%}$  equal to 408.80 N/m ( $COV = 16.6\%$ ).

The virgin samples presented values of strains at rupture ( $\epsilon_{rup}$ ) below 5% for the GGPVA, and below 10% for the polyester geogrids (GGPET 01 and GGPET 02). The virgin samples of GGPVA presented the lowest variability of  $\epsilon_{rup}$ , showing value of  $COV$  equal to 5.4% (mean value of  $\epsilon_{rup} = 4.7\%$ ), meanwhile GGPET 01 showed the highest variability, with value of  $COV$  equal to 21.7% (mean value of  $\epsilon_{rup} = 6.6\%$ ). GGPET 02 revealed value of  $COV$  equal to 21.5% (mean value of  $\epsilon_{rup} = 5.8\%$ ) for virgin samples.

Based on the data obtained from the virgin samples, the confidence intervals for each kind of geogrid were determined by means of the Student's  $t$ -distribution. Table 4 presents the confidence limits for each of the parameters of interest and their respective confidence levels. It can be observed that the confidence level values were between 96% and 98%, very similar to the ones found by Barbosa & Santos (2013) and Santos *et al.* (2014).

**Table 4** - Results from tests on virgin samples (5 specimens) associated with the Student's  $t$ -distribution analysis.

| Geogrid  | Tensile strength (kN/m) | Strain at rupture (%)          | $J_{2\%}$ (N/m)              | $J_{5\%}$ (N/m)             |
|----------|-------------------------|--------------------------------|------------------------------|-----------------------------|
| GGPVA    | $\bar{T}_{ult} = 26.3$  | $\bar{\epsilon}_{rup} = 4.7$   | $\bar{J}_{2\%} = 550.0$      | n.a.                        |
|          | $COV = 7.8\%$           | $COV = 5.4\%$                  | $COV = 6\%$                  |                             |
|          | $22.55 < F_0 < 30.05$   | $4.15 < \epsilon_{rup} < 5.26$ | $488.43 < J_{2\%} < 611.57$  |                             |
|          | $CL = 98\%$             | $CL = 98\%$                    | $CL = 98\%$                  |                             |
| GGPET 01 | $\bar{T}_{ult} = 38.7$  | $\bar{\epsilon}_{rup} = 6.6$   | $\bar{J}_{2\%} = 694.0$      | $\bar{J}_{5\%} = 555.2$     |
|          | $COV = 13.2\%$          | $COV = 21.7\%$                 | $COV = 25\%$                 | $COV = 16.2\%$              |
|          | $31.05 < F_0 < 46.35$   | $3.98 < \epsilon_{rup} < 9.22$ | $434.13 < J_{2\%} < 953.87$  | $420.26 < J_{5\%} < 690.14$ |
|          | $CL = 96\%$             | $CL = 98\%$                    | $CL = 96\%$                  | $CL = 96\%$                 |
| GGPET 02 | $\bar{T}_{ult} = 27.4$  | $\bar{\epsilon}_{rup} = 5.8$   | $\bar{J}_{2\%} = 680.0$      | $\bar{J}_{5\%} = 408.8$     |
|          | $COV = 12.2\%$          | $COV = 21.5\%$                 | $COV = 33.4\%$               | $COV = 16.6\%$              |
|          | $22.45 < F_0 < 32.35$   | $3.55 < \epsilon_{rup} < 8.05$ | $254.42 < J_{2\%} < 1105.58$ | $307.07 < J_{5\%} < 510.53$ |
|          | $CL = 96\%$             | $CL = 98\%$                    | $CL = 98\%$                  | $CL = 96\%$                 |

Note:  $T_{ult}$  = ultimate tensile strength;  $\epsilon_{rup}$  = strain at rupture;  $J_{2\%}$  = stiffness at 2% strain;  $J_{5\%}$  = stiffness at 5% strain;  $CL$  = confidence level; n.a. = not available.

3.3.2. Geogrids' tensile strength, strain at rupture and secant tensile stiffness after loading

3.3.2.1. GGPVA

Considering all the scenarios, it was observed that GGPVA did not present the mean value of ultimate tensile strength  $\bar{T}_{ult}$  outside the limits calculated for this parameter. However, the strain at rupture ( $\epsilon_{rup}$ ) appeared as a sensitive parameter to the loading process, which can be verified evaluating the reduction of  $T_{ult}$  values and the increase of *COV*. Figure 12a shows the strength values obtained while testing the GGPVA with each kind of RCDW.

Aggregate C - classified as a poorly graded gravel with silt - caused the higher reduction factor of average  $\epsilon_{rup}$  when the GGPVA was submitted to the load of 150 kPa, which confirms that the responses of this parameter were not affected in a direct relation to loading (Fig. 12b). However, it was possible to see that other load magnitudes caused reductions of this parameter close to the lower limit established by statistical analysis. It is also possible to visualize the increase of *COV* when strain at rupture of virgin and exhumed specimens are compared.

Results revealed that Aggregate B - classified as poorly graded gravel - caused the greatest reduction of  $\epsilon_{rup}$  and the highest variability when tested with a load of 300 kPa if compared to the other loads applied for that same material (Fig. 12b). Evaluating the results from tests with Aggregate A - classified as poorly graded gravel -, it is possible to observe that a load of 600 kPa caused the highest reduction of  $\epsilon_{rup}$ , but this reduction was not directly related to load (Fig. 12b). These results show the need for a better separa-

tion of the materials that compose the RCDW, once the existence of components that could be broken easily (*e.g.* ceramic materials) can cause different damages in the geogrid tested.

In general, the analyses of stiffness at 2 % ( $J_{2\%}$ ) showed that different scenarios (recycled aggregate *vs.* load) have not changed the mean values of this parameter, with most of the values ranging within the limits of virgin specimens - except for scenario Aggregate B submitted to 300 kPa (Fig. 12c). As pointed out during the discussion of the values of  $T_{ult}$ , the results revealed an increase of the *COV* of exhumed samples.

3.3.2.2. GGPET 01

The evaluation of all scenarios revealed that GGPET 01 did not present average ultimate tensile strength ( $\bar{T}_{ult}$ ) outside the limits calculated for this parameter using the virgin specimen data and the Student's *t*-distribution. The mean values of  $\epsilon_{rup}$ ,  $J_{2\%}$ , and  $J_{5\%}$  were also within the limits calculated, however, for these parameters, some specimens presented values beyond the limits. Figures 13a to 13d show the results of each investigated parameter.

GGPET 01 presented the value of strain at rupture, for the sample Aggregate B and load of 300 kPa, with a *COV* value of 13 % (Fig. 13b). The high variation of GGPET 01 samples was beyond the upper limit of the confidence interval, and this performance could be a limitation for its use in some geotechnical works.

3.3.2.3. GGPET 02

Considering the different scenarios analyzed, it was noticed that GGPET 02 did not present average ultimate

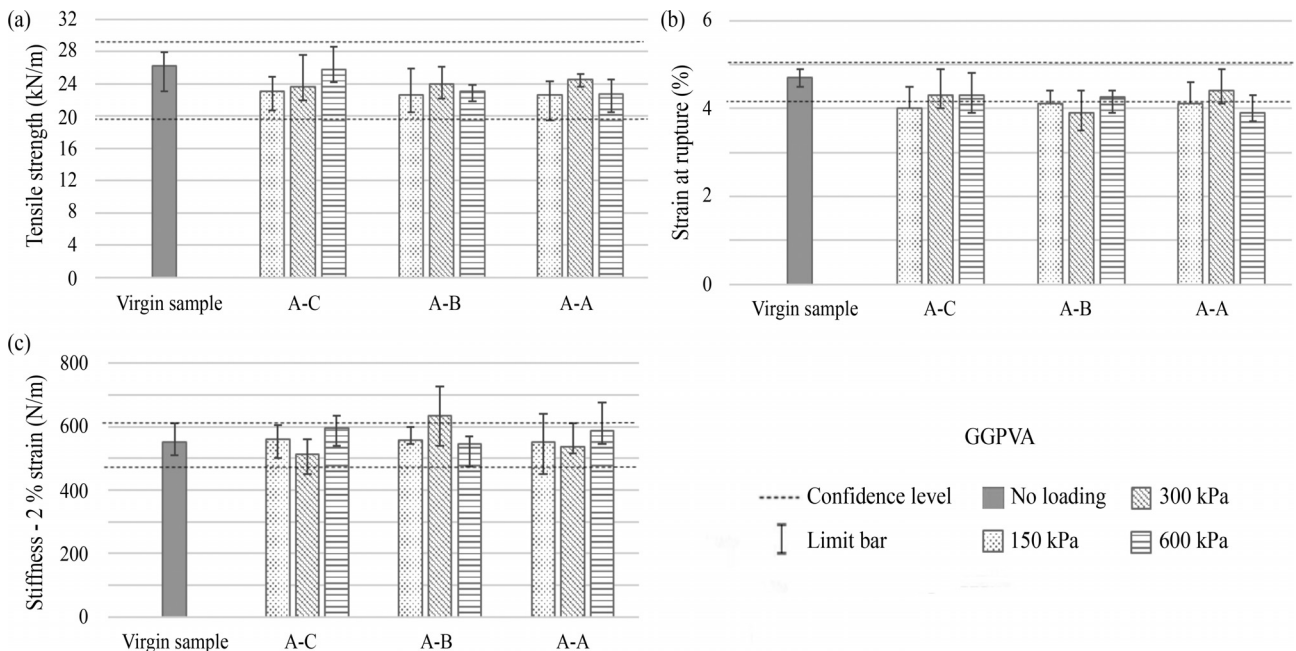
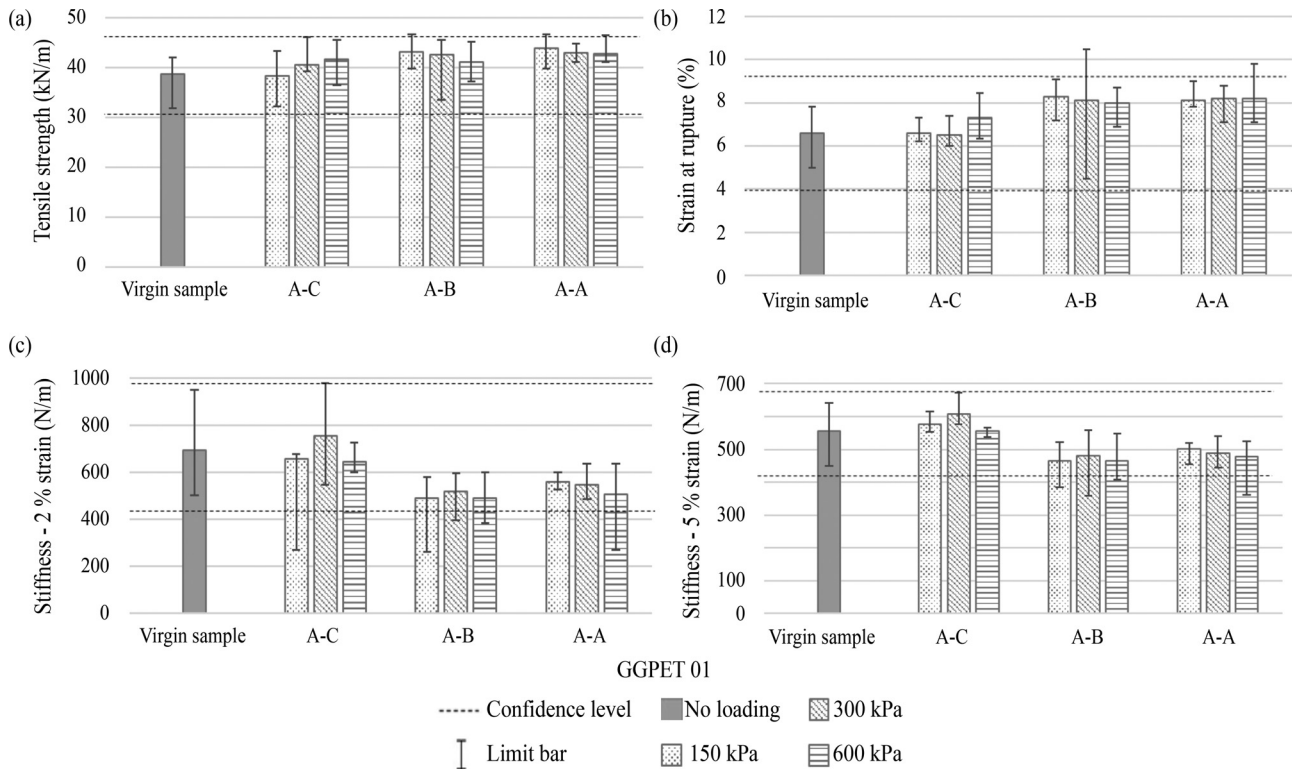


Figure 12 - GGPVA: a) Tensile strength; b) Rupture Strain; c) Stiffness - 2 % Strain.



**Figure 13** - GGPET 01: a) Tensile strength; b) Rupture Strain; c) Stiffness - 2 % Strain; and d) Stiffness - 5 % Strain.

tensile strength ( $\bar{T}_{ult}$ ) values outside the calculated limits (Fig. 14a). However, the Aggregate B sample (300 kPa) stands out due to the greater variation of the deformation at rupture ( $\epsilon_{rup}$ ) (Fig. 14b).

Aggregate C caused the higher reduction factor of average deformation at rupture ( $\bar{\epsilon}_{rup}$ ) when GGPET 02 was submitted to the load of 150 kPa (Fig. 14b), which proves that the responses of this parameter were not affected in a direct relation to load - as well as GGPVA. Results revealed that Aggregate B caused an increase of  $\epsilon_{rup}$  for all applied loads (Fig. 14b), with the load of 600 kPa being the most expressive one. For Aggregate A, it is possible to observe that a load of 600 kPa caused a higher increase of  $\epsilon_{rup}$ , and this reduction was not directly related to load (Fig. 14b).

In general, the analyses of stiffness at 2 % ( $J_{2\%}$ ) showed that the virgin sample presented a high value of  $COV$  (33.4 %). Besides that, all tested geogrids presented values smaller than the virgin sample (Fig. 14c). The Aggregate C and Aggregate A showed values within the confidence level. Only Aggregate B presented a reduction of  $J_{2\%}$  for loads of 300 kPa and 600 kPa (Fig. 14c). For this aggregate, the results revealed an increase of the  $COV$  of damaged samples in comparison to the one of virgin ones (e.g. scenario of 300 kPa presented a  $COV = 98.4\%$ ).

Considering the mean values of stiffness at 5 % ( $J_{5\%}$ ) (Fig. 14d), for all loads, Aggregate A and Aggregate C did not cause any reduction beyond the limits. Aggregate B caused some reduction in the  $J_{5\%}$  proportional to the applied

load, with the largest reduction of this parameter being observed for the load of 600 kPa. Although Aggregate A and Aggregate C did not cause any reduction factor ( $J_{5\%}$ ) in tested samples, these aggregates did present average values lower than virgin samples. Thus, the results revealed that the fact of Aggregate B being the coarser material can be pointed out as the reason why the greatest damages were observed in geogrids when using this material.

### 3.3.3. Reduction factors due to loading process

The results showed that the reduction factor ( $RF$ ) presented diverse magnitudes for each parameter and scenario. Considering the different scenarios evaluated (aggregates vs. loads), it was noticed that all tested geogrids (PVA or PET), irrespective of their catalogue tensile strength (35 kN/m or 55 kN/m), did not present average ultimate tensile strength values ( $\bar{T}_{ult}$ ) outside the calculated limits (confidence intervals). For other parameters, only the cases with 35 kN/m geogrids (GGPVA and GGPET 02) presented values of  $RF$  other than 1.0. In terms of reduction factors related to deformation at failure ( $RF\epsilon_{rup}$ ), the PVA geogrid showed values ranging from 1.15 to 1.21 (Table 5), hence becoming the most sensitive geogrid to the loading process. Aggregate A - classified as a poorly graded gravel with sand - presented moderate damages; while Aggregate B - classified as poorly graded gravel - contributed to a higher occurrence of damages. Aggregate C - classified as

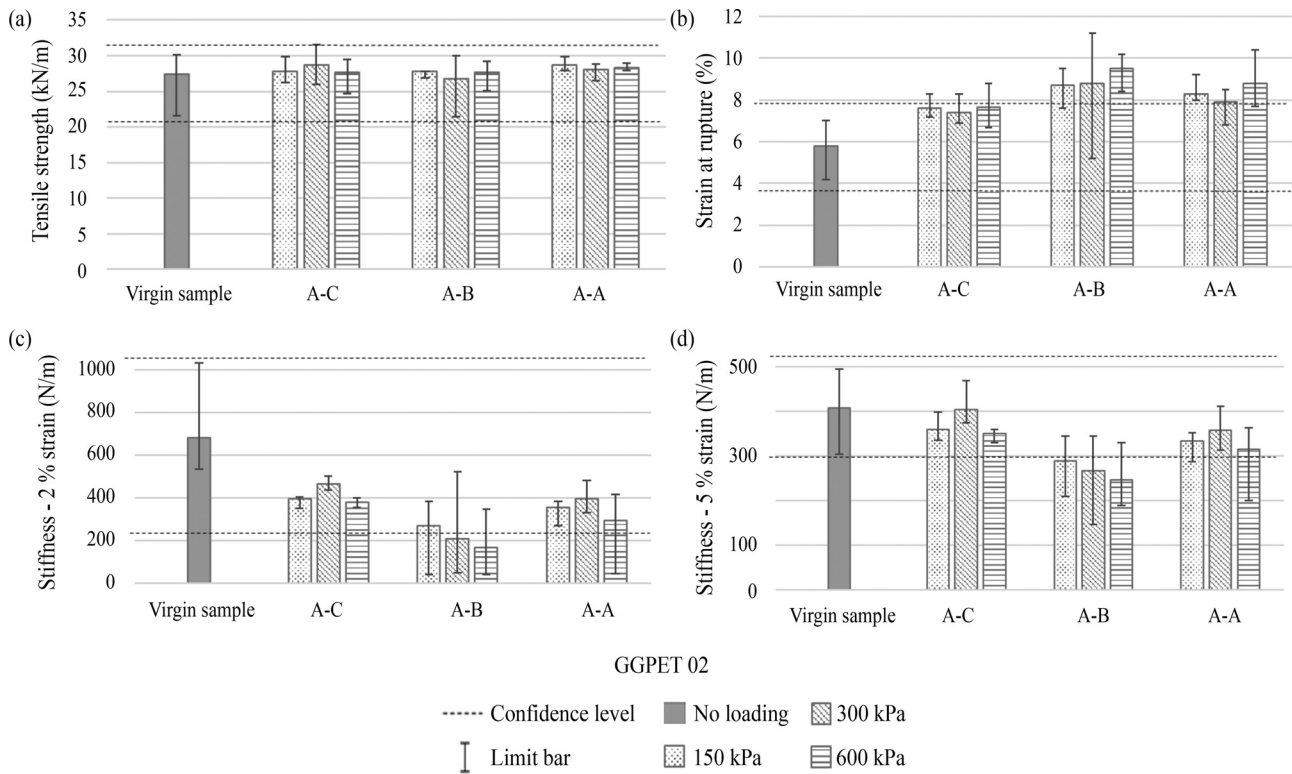


**Figure 14** - GGPET 02: a) Tensile strength; b) Rupture Strain; c) Stiffness - 2 % Strain; and d) Stiffness - 5 % Strain.

poorly graded silty gravel with sand - was the least aggressive material.

Concerning the reduction factors related to stiffness at 2 % ( $RF_{J_{2\%}}$ ), the PET geogrid (35 kN/m) presented values from 3.29 to 4.12 (Table 5), when tested with Aggregate B, for loads of 300 kPa and 400 kPa, respectively. However, as reported by Fleury *et al.* (2019), it is worth mentioning that the method of monitoring the strain during the tensile strength test (in only one longitudinal rib) may have been the reason for the wide range of secant tensile stiffness values obtained. Therefore, once virgin samples presented excessively broad confidence intervals, it is reasonable to have a high occurrence of reduction factors equal to 1.00. Moreover, whenever different values are observed, overstated magnitudes become evident. The results have also shown that the difficulty of obtaining reduction factors increases when concerning  $RF_{J_{2\%}}$ .

The values of reduction factor related to tensile stiffness at 5 % ( $RF_{J_{5\%}}$ ) varied from 1.41 to 1.66 for PET geogrid (35 kN/m) (Table 5), when tested with Aggregate B. Although the values of  $RF_{J_{5\%}}$  had shown a direct relation to load, one must bear in mind that this case was not observed in most of the scenarios investigated. Unlike what was perceived in the values of stiffness at 2 % ( $J_{2\%}$ ), those of stiffness at 5 % ( $J_{5\%}$ ) did not present a high variability (COV up to 16.6 %). Therefore,  $RF_{J_{5\%}}$  seems very reasonable.

Given that the majority of scenarios presenting values of  $RF$  greater than 1.00 were related to tests carried out with Aggregate B, it is possible to state that the characteristics of this material, correlated to i) the predominance of coarse particles (gravel,  $D_{85} = 18$  mm,  $D_{50} = 11$  mm,  $D_{10} = 6.5$  mm), ii) poorly graded grain size distribution ( $C_u = 1.85$ ), and iii) lower particle breakage occurrence, contributed to damage generation and its degree of severity. These characteristics create a condition with few points of contact between the aggregate (particles) and geogrid elements, causing a concentration of load and, as a consequence, more severe damages.

On the other hand, despite also presenting coarse particles (gravel with silt,  $D_{85} = 12$  mm,  $D_{50} = 7.5$  mm,  $D_{10} = 0.22$  mm), Aggregate C, due to the content of coarse, medium and fine sands (total amount around 26 %), the considerable value of coefficient of uniformity ( $C_u = 38.64$ ) and high particle breakage, was able to provide a condition of large particles surrounded by small ones, setting up better load transfer (large contact area) between its particles and the geogrids. This condition made Aggregate C (material produced from a mixture of three recycled materials) the least aggressive material, presenting only one scenario with  $RF$  greater than 1.0 (GGPAV, 150 kPa,  $RF_{\epsilon_{rup}} = 1.18$ ). Moreover, this aggregate is the cheapest material produced by the recycling plant. Table 5 summarizes all the reduction factors obtained by the tensile test.

**Table 5** - Reduction factors related to the investigated parameters.

| Aggregate | $RF_{\epsilon_{rup}}^a$ |                         | $RF_{J2\%}^b$           |            | $RF_{J5\%}^c$ |            |
|-----------|-------------------------|-------------------------|-------------------------|------------|---------------|------------|
|           | GGPVA                   | GGPET 02                | GGPVA                   | GGPET 02   | GGPVA         | GGPET 02   |
| A-C       | 1.18 (150)              | 1.00 (150)              | 1.00 (150)              | 1.00 (150) | -             | 1.00 (150) |
|           | 1.00 (300)              | 1.00 (300)              | 1.00 (300)              | 1.00 (300) | -             | 1.00 (300) |
|           | 1.00 (600)              | 1.00 (600)              | 1.00 (600)              | 1.00 (600) | -             | 1.00 (600) |
| A-B       | 1.15 (150)              | 0.67 <sup>d</sup> (150) | 1.00 (150)              | 1.00 (150) | -             | 1.41 (150) |
|           | 1.21 (300)              | 0.66 <sup>d</sup> (300) | 0.87 <sup>d</sup> (300) | 3.29 (300) | -             | 1.53 (300) |
|           | 1.00 (600)              | 0.61 <sup>d</sup> (600) | 1.00 (600)              | 4.12 (600) | -             | 1.66 (600) |
| A-A       | 1.15 (150)              | 0.70 <sup>d</sup> (150) | 1.00 (150)              | 1.00 (150) | -             | 1.00 (150) |
|           | 1.00 (300)              | 1.00 (300)              | 1.00 (300)              | 1.00 (300) | -             | 1.00 (300) |
|           | 1.21 (600)              | 0.66 <sup>d</sup> (600) | 1.00 (600)              | 1.00 (600) | -             | 1.00 (600) |

Note: <sup>a</sup>Reduction factor related to the strain at failure; <sup>b</sup>Reduction factor related to the secant tensile stiffness at 2 %; <sup>c</sup>Reduction factor related to the secant tensile stiffness at 5 %; <sup>d</sup>The adoption of reduction factor equal to 1.0 is recommended. Loads are presented between parentheses in kPa.

#### 4. Conclusions

This paper reported on mechanical damage caused to geogrids by recycled construction and demolition wastes (RCDW) with different grain size distributions. Laboratory tests were carried out to apply loads simulating the field condition to the composite (geogrid + RCDW). Tensile tests were performed on damaged geogrid specimens, and the RCDW grain size distribution was evaluated before and after the loading application. The main conclusions obtained are presented below.

- (1) The geotechnical characterization revealed that the RCDW presented non-plastic and non-liquid behavior. Besides, according to USCS, these materials presented grain size distributions from clean gravel to gravel with few fines. The mean value of dry unit weight was equal to 16.859 kN/m<sup>3</sup> and mean optimum water content was equal to 17.6 %, which showed that the content of ceramic materials is directly proportional to the optimum water content.
- (2) The grain size distribution curves of RCDW presented significant changes when subjected to different loading. No abrupt breakage of recycled aggregates subjected to loading was noticed, except for the removal of fines around the particles with loading. Thus, after application of the load, the material presented a smooth surface (less rough).
- (3) The analysis of grain roughness revealed that the particles larger than 9.5 mm were the ones most affected with the application of the load. The grain breakage can influence the mechanical and hydraulic properties of the materials.
- (4) The test simulating mechanical damage in geogrids revealed that: i) although the results presented some values of tensile strength outside the limits calculated based on virgin specimens, the mean values for all in-

vestigated scenarios were within the minimum and maximum limits; ii) the reduction factors related to the strain at rupture wound up being greater than those obtained for other analyzed parameters; iv) the GGPVA and GGPET 02 geogrids presented higher reduction factors related to strain at rupture and stiffness.

- (5) The damage caused by Aggregate B turned out to be more severe, given that this aggregate was the coarser one, presenting a poorly graded grain size distribution and revealing the lowest particle size variation (breakage) due to loading process. The aggregate mostly produced and sold by the recycling plant (Aggregate C), with the lowest selling price, was also the least aggressive material.
- (6) The values of RF calculated revealed the need for proper investigation when using RCDW as backfill material, which could enable them in the design phase. The authors believe the results presented may contribute to a better understanding of the processes involved in mechanical damage of polymeric reinforced elements, and to the goal of achieving positive economic, social and environmental benefits related to the use of recycled materials in geotechnical works.

#### Acknowledgments

The authors are indebted to the following institutions that supported the research activities reported in this paper in different ways: Federal University of Goiás (UFG), National Council for Scientific and Technological Development (CNPq), University of São Paulo (USP), and CAPES - Brazilian Ministry of Education. The authors also thank the manufacturer of geosynthetics and RNV - Waste Management, for providing information and materials presented in this paper.

## References

- ABNT (2016a). Gravel Grains Retained on the 4.8 mm Mesh Sieve - Determination of the Bulk Specific Gravity, of the Apparent Specific Gravity and of Water Absorption - NBR 6458:2016. The Brazilian Association of Technical Standards, Rio de Janeiro, RJ, Brazil, 10 p. (In Portuguese).
- ABNT (2016b). Soil - Granulometric Size Analysis - NBR 7181:2016. The Brazilian Association of Technical Standards, Rio de Janeiro, RJ, Brazil, 12 p. (In Portuguese).
- ABNT (2016c). Soil - Liquid Limit Determination - NBR 6459:2016. The Brazilian Association of Technical Standards, Rio de Janeiro, RJ, Brazil, 5 p. (In Portuguese).
- ABNT (2016d). Soil - Plasticity Limit Determination - NBR 7180:2016. The Brazilian Association of Technical Standards, Rio de Janeiro, RJ, Brazil, 3 p. (In Portuguese).
- ABNT (2016e). Soil - Compaction Test - NBR 7182:2016. The Brazilian Association of Technical Standards, Rio de Janeiro, RJ, Brazil, 1 p. (In Portuguese).
- Afshar, T.; Disfani, M.M.; Arulrajah, A.; Narsilio, G. A. & Eman, S. (2017). Impact of particle shape on breakage of recycled construction and demolition aggregates. *Powder Technology*, 308:1-12. <https://dx.doi.org/10.1016/j.powtec.2016.11.043>.
- Allen, T.M. & Bathurst, R.J. (1994). Characterization of geosynthetic load-strain behavior after installation damage. *Geosynthetic International*, 1(2):181-199. <https://doi.org/10.1680/gein.1.0008>.
- Allen, T.M. & Bathurst, R.J. (1996). Combined allowable strength reduction factor for geosynthetic creep and installation damage. *Geosynthetic International*, 3(3):407-439.
- Angulo, S.C.; Teixeira, C.E. & Castro, A.L. (2011). Construction and demolition waste: evaluation of quantification methods. *Engenharia Sanitária e Ambiental*, 16(3):299-306. <https://doi.org/10.1590/S1413-41522011000300013>.
- ASTM (2017). Standard Practice for Classification of Soils for Engineering Purposes (Unified Soil Classification System) - D2487-17e1. ASTM International, West Conshohocken, Pennsylvania, USA, 10 p.
- ASTM (2015). Standard Test Method for Determining Tensile Properties of Geogrids by the Single or Multi-Rib Tensile Method - D6637 / D6637M-15. ASTM International, West Conshohocken, Pennsylvania, USA, 6 p.
- Barbosa, K.R.M. (2017). Geogrid Degradation in Unpaved Roads Built with Recycled Construction and Demolition Wastes (RCDW). M.Sc. Thesis. Graduate Programme of Civil Engineering, University of Pernambuco, Recife, 122 p.
- Barbosa, F.A.S. & Santos, E.C.G. (2013). Geogrid mechanical damages due to recycled construction and demolition wastes. Proc. 14th International Waste Management and Landfill Symposium, Santa Margherita di Pula, Italy, v. 1, pp. 1-8. (CD-ROM)
- BSI (2007). Geosynthetics. Index test procedure for evaluation of mechanical damage under repeated loading. Damage Caused by Granular Material - EN ISO 10722:2007. British Standard Institution, London, United Kingdom, 12 p.
- BSI (2010). Code of Practice for Strengthened/Reinforced Soils and Other Fills - 8006-1. British Standard Institution, London, United Kingdom, 260 p.
- Cardoso, R.; Silva, R.V.; Brito, J. & Dhir, R. (2016). Use of recycled aggregates from construction and demolition waste in geotechnical applications: A literature review. *Waste Management*, 49:131-145. <https://doi.org/10.1016/j.wasman.2015.12.021>.
- Esin, T. & Cosgun, N. (2007). A study conducted to reduce construction waste generation in Turkey. *Building and Environment*, 42(4):1667-1674. <https://doi.org/10.1016/j.buildenv.2006.02.008>.
- Flury, M.P. (2018). Geogrid Strength after Mechanical Damages Caused by Recycled Construction and Demolition Wastes (RCDW). MSc. Thesis. Graduate Programme of Geotechnics, Structural and Civil Engineering, Federal University of Goiás, Goiânia, 160 p. (In Portuguese).
- Flury, M.P.; Santos, E.C.G.; Lins da Silva, J.; Palmeira, E.M. (2019). Geogrid installation damage caused by recycled construction and demolition waste. *Geosynthetics International*, 26(6):641-656. <https://doi.org/10.1680/jgein.19.00050>.
- Gonzalez-Torre, I.; Calzada-Perez, M.A.; Vega-Zamanillo, A. & Castro-Fresno, D. (2014). Damage evaluation during installation of geosynthetics used in asphalt pavements. *Geosynthetics International*, 21(6):377-386.
- Herrador, R.; Perez, P.; Garach L. & Ordonez J. (2012). Use of recycled construction and demolition waste aggregate for road course surfacing. *Journal of Transportation Engineering*, 138(2):182-190. DOI: 10.1061/(ASCE)TE.1943-5436.0000320.
- Huang, C.C. (2006). Laboratory simulation of installation damage of a geogrid. *Geosynthetics International*, 13(3):120-132.
- Huang, C.C. & Chiou, S.L. (2006). Investigation of installation damage of some geogrids using laboratory tests. *Geosynthetics International*, 13(1):23-35.
- Huang, C.C. & Wang, Z.N. (2007). Installation damage of geogrids: influence of load intensity. *Geosynthetics International*, 14(2):65-75.
- Jones, C.J.F.P. (1994). Economic construction of reinforced soil structures. Proc. International Symposium on Recent Case Histories of Permanent Geosynthetic-

- Reinforced Soil Retaining Walls, Tokyo. Balkema, Kalamazoo, pp. 103-106.
- Kartam, N.; Al-Mutairi, N.; Al-Ghusain, I. & Al-Humoud, J. (2004). Environmental management of construction and demolition waste in Kuwait. *Waste Management*, 24(10):1049-1059. <https://doi.org/10.1016/j.wasman.2004.06.003>.
- Leite, F.C.; Motta, R.S.; Vasconcelos, K.L. & Bernucci, L. (2011). Laboratory evaluation of recycled construction and demolition waste for pavements. *Construction and Building Materials*, 25(6):2972-2979. <https://doi.org/10.1016/j.conbuildmat.2010.11.105>.
- Mascarenha, M.M.A.; Cordão Neto, M.P.; Matos, T.H.C.; Chagas, J.V.R. & Rezende, L.R. (2018). Effects of the addition of dihydrate phosphogypsum on the characterization and mechanical behavior of lateritic clay. *Soils and Rocks*, 41(2):157-170. <https://doi.org/10.28927/SR.412157>.
- Ossa A.; Garcíá J.L. & Botero E. (2016). Use of recycled construction and demolition waste (CDW) aggregates: A sustainable alternative for pavement construction industry. *Journal of Cleaner Production*, 135:379-386. <https://doi.org/10.1016/j.jclepro.2016.06.088>.
- Paula, A.M.; Pinho-Lopes, M. & Lopes, M.L. (2004). Damage during installation laboratory test. Influence of the type of granular material. Proc. 3<sup>rd</sup> European Geosynthetics Conference, EUROGEO, Munich, Germany, pp. 603-606.
- Pinho-Lopes, M. & Lopes, M.L. (2014). Tensile properties of geosynthetics after installation damage. *Environmental Geotechnics*, 1(3):161-178.
- Rosete, A.; Lopes, P.M.; Pinho-Lopes, M. & Lopes, M.L. (2013). Tensile and hydraulic properties of geosynthetics after mechanical damage and abrasion laboratory tests. *Geosynthetics International*, 20(5):358-374.
- Santos E.C.G. (2007). Application of Recycled Construction and Demolition Waste (RCDW) in Reinforced Soil Structures. M.Sc. Thesis. Department of Geotechnics, University of São Paulo, São Carlos, 168 p. (In Portuguese).
- Santos, E.C.G. (2011). Experimental Evaluation of Reinforced Walls Built with Recycled Construction and Demolition Waste (RCDW) and Fine Soil. Ph.D. Thesis, Department of Civil and Environmental Engineering, University of Brasília, Brasília, 216 p. (In Portuguese).
- Santos, E.C.G.; Bueno, B.S. & Palmeira, E.M. (2012). Strength reduction of geosynthetics used in RSW built with RCDW as backfill material. Proc. 5<sup>th</sup> European Geosynthetics Congress, EUROGEO, Valencia, Spain, pp. 481-485.
- Santos E.C.G.; Palmeira E.M. & Bathurst, R.J. (2013). Behaviour of a geogrid reinforced wall built with recycled construction and demolition waste backfill on a collapsible foundation. *Geotextiles and Geomembranes*, 39(1):9-19. <https://doi.org/10.1016/j.geotexmem.2013.07.002>.
- Santos, E.C.G.; Palmeira E.M. & Bathurst, R.J. (2014). Performance of two geosynthetic reinforced walls with recycled construction waste backfill and constructed on collapsible ground. *Geosynthetic International*, 21(4):256-269. <https://doi.org/10.1680/gein.14.00013>.
- Santos, A.A.M. & Leite, M.B. (2018). Evaluation of recycled concrete with concrete coarse aggregate using ABCP mix design method modified. *Ambiente Construído*, 18(4):341-359. <http://dx.doi.org/10.1590/s1678-86212018000400309> (In Portuguese).
- Silva, R.V.; Brito, J. & Dhir, R.K. (2016). Availability and processing of recycled aggregates within the construction and demolition supply chain: A review. *Journal of Cleaner Production*, 143:598-614. <https://doi.org/10.1016/j.jclepro.2016.12.070>.
- Silva, M.V.; Rezende, L.R.; Mascarenha, M.M.A. & Oliveira, R.B. (2019). Phosphogypsum, tropical soil and cement mixtures for asphalt pavements under wet and dry environmental conditions. *Resources, Conservation & Recycling*, 144:123-136. <https://doi.org/10.1016/j.resconrec.2019.01.029>.
- Silvestre, G.R. (2019). Geogrid Strength Reduction due to Chemical Damages Caused by Recycled Construction and Demolition Wastes. M.Sc. Thesis. Graduate Programme of Geotechnics, Structural and Civil Engineering, University of Goiás, Goiânia, 146 p. (In Portuguese).
- Tam, V.W.Y. (2008). Economic comparison of concrete recycling: a case study approach. *Resource, Conservation and Recycling*, 52(5):821-828. <https://doi.org/10.1016/j.resconrec.2007.12.001>.
- Yoo, H.; Jeon, H.Y. & Chang, Y.C. (2009). Evaluation of engineering properties of geogrids for soil retaining walls. *Textile Research Journal*, 80(2):184-192.
- Wu H.; Zuo J.; Zillante G.; Wang J. & Yuan H. (2019). Status quo and future directions of construction and demolition waste research: A critical review. *Journal of Cleaner Production*, 240:1-13. <https://doi.org/10.1016/j.jclepro.2019.118163>.

## List of Symbols and Abbreviations

- ABNT: Brazilian Association of Technical Standards  
 ASTM: American Society for Testing and Materials  
 A-A: aggregate A ( $9.5 \text{ mm} > d > 4.8 \text{ mm}$ )  
 A-B: aggregate B ( $19 \text{ mm} > d > 9.5 \text{ mm}$ )  
 A-C: aggregate C ( $d < 9.5 \text{ mm}$ )  
 CDW: Construction and Demolition Waste  
 CL: confidence level (dimensionless)  
 $C_u$ : soil coefficient of uniformity ( $C_u = D_{60}/D_{10}$ )  
 d: diameter of the particle (m)  
 $D_{10}$ : diameter of the particle for which 10 % of soil in mass is smaller (than that diameter)

|  |  |
|--|--|
| $D_{50}$ : diameter of the particle for which 50 % of soil in mass is smaller (than that diameter) | $M_A$ : mass per unit area ( $\text{g/m}^2$ )  |
| $D_{85}$ : diameter of the particle for which 85 % of soil in mass is smaller (than that diameter) | RCDW: Recycled Construction and Demolition Waste                                       |
| EECA-UFG: School of Civil and Environmental Engineering of the Federal University of Goiás         | $RF$ : global reduction factor   |
| EESC-USP: School of Engineering of São Carlos, University of São Paulo                             | $RF_{CR}$ : creep reduction factor   |
| $F_0$ : tensile strength of virgin samples   | $RF_D$ : durability reduction factor   |
| GRS: Geosynthetic Reinforced Soil  | $RF_{ID}$ : installation damage reduction factor                                       |
| $G_s$ : specific gravity ( $\text{g/cm}^3$ )   | $RF_{MD}$ : mechanical damage reduction factor   |
| GGPVA: polyvinyl alcohol geogrid   | $T_{al}$ : allowable tensile strength  |
| GGPET 01: polyester geogrid with resistance of 55 kN/m   | $T_{ult}$ : ultimate tensile strength  |
| GGPET 02: polyester geogrid with resistance of 35 kN/m   | $\bar{T}_{ult}$ : ultimate tensile strength mean value                                 |
| $J_{sec}$ : secant tensile stiffness   | $T_{ult,v}$ : ultimate tensile strength mean value of virgin (undamaged) samples       |
| $J_{2\%}$ : secant tensile stiffness at 2 % strain (N/m)   | $T_{ult,d}$ : ultimate tensile strength mean value of damaged samples                  |
| $\bar{J}_{2\%}$ : secant tensile stiffness at 2 % strain mean value (N/m)                          | $w_{op}$ : optimum water content (%)   |
| $J_{5\%}$ : secant tensile stiffness at 5 % strain (N/m)   | USCS: Unified Soil Classification System   |
| $\bar{J}_{5\%}$ : secant tensile stiffness at 5 % strain mean value (N/m)                          | $\varepsilon_{rup}$ : strain or elongation at rupture mean value (dimensionless)       |
|  | $\bar{\varepsilon}_{rup}$ : strain or elongation at rupture mean value (dimensionless) |

# Numerical Investigations on Seismic Bearing Capacity of Interfering Strip Footings

R. Boufarh, D. Saadi, M.S. Laouar

**Abstract.** The interaction between footings placed at close proximity affects the ultimate bearing capacity, settlement, and tilt of adjacent footings, especially under seismic loading. This paper reports the numerical finite element analysis to investigate the interference effect on the seismic bearing capacity of closely spaced rigid strip footings for a wide range of footing spacings, friction angles and horizontal acceleration factor. The results are presented in terms of seismic efficiency factors, and their variation was computed with respect to the change in the spacing ratio between the two footings. The results revealed that the increase in the earthquake acceleration leads to a reduction in efficiency gains owing to the failure zone of footings interfere altering the performance of the footings.

**Keywords:** bearing capacity, numerical analysis, seismic interference factors, strip footings.

## 1. Introduction

In the earliest phases of the development of Geotechnical Engineering, several researchers have exhaustively studied the bearing capacity and settlement of isolated shallow foundations in static condition (*e.g.*, Bolton & Lau (1993); Casagrande (1966); Hansen (1970); Meyerhof (1963); Prandtl (1920); Schmertmann *et al.* (1978); Terzaghi (1943); Vesic (1973)) and the history behind it is long. Whereas, not taking into consideration the seismic forces may be one of the major reasons for soil liquefaction, slope failure and infrastructure collapse. After earthquake motions such as Michoacán (Mexico City, 1985), Kobe (Japan, 1995), and the Bhuj (India, 2001), failure and excessive settlements of foundations of buildings have been noticed. Thus, the design of geotechnical structures in seismic areas needs particular consideration compared to the static case.

In the presence of true seismic forces, a rigorous theoretical method for estimating the bearing capacity of the foundations is difficult to perform. In the literature, several researchers have followed a simple approach by incorporating pseudo-static seismic forces to study the reduction in the bearing capacity of an isolated strip footing. In this field, the available theoretical researches are mostly based on (1) the limit-equilibrium method (Budhu & Al-Karni (1993); Choudhury & Rao (2005); Jahani *et al.* (2019); Kumar & Kumar (2003); Pain *et al.* (2016); Richards *et al.* (1993); Saha & Ghosh (2015); Sarma & Chen (1995); Sarma & Iossifelis (1990)); (2) the upper-bound theorem of limit analysis (Dormieux & Pecker (1995); Ghosh (2008); Paolucci & Pecker (1997); Soubra (1999)); (3) the lower-

bound theorem of limit analysis (Chakraborty & Mahesh (2016); Kumar & Chakraborty (2013)); and (4) the method of stress characteristics (Cascone & Casablanca (2016); Keshavarz & Nemati (2017); Kumar & Mohan Rao (2002), (2003)). In addition, there exist limited experimental and numerical studies related to the estimation of the seismic bearing capacity of an isolated strip footing (Huang (2019); Knappett *et al.* (2006); Luo *et al.* (2019); Pane *et al.* (2016); Shafiee & Jahanandish (2010); Zeng & Steedma (1998)).

However, in practice, the foundations encountered are rarely isolated, and they are placed in close proximity to each other, such as railway sleepers and foundations near the property lines, the interference of the stress zones beneath the footings affects the bearing capacity and settlement of the soil and hence, in certain instances can lead to major damage to the buildings from both the strength and serviceability points of view, especially in seismic conditions. Stuart (1962) was the first author to study the bearing capacity and the corresponding failure mechanism of two interfering footings. Later, based on his study, many researchers have investigated the interference effect on the ultimate bearing capacity of two closely spaced strip footings (Das & Larbi-Cherif (1983); Ghosh & Sharma (2010); Kumar & Bhattacharya (2010); Kumar & Bhoi (2008); Kumar & Ghosh (2007); Kumar & Kouzer (2008); Lee & Eun (2009)).

Soil is defined as a complex multi-phase material, its stress, strain and strength being represented by pressure dependency with coupling between shear and volumetric behavior. With these complications, and to facilitate the solution of difficult Geotechnical problems, finite element

---

Rafik Boufarh, D.Sc., Associate Professor, Department of Civil Engineering, Faculty of Sciences and Technology, Larbi Tebessi University, Tebessa, Algeria. e-mail: rafik.boufarh@univ-tebessa.dz or rafikboufarh@gmail.com.

Djamel Saadi, D.Sc., Assistant Professor, Department of Civil Engineering, Faculty of Sciences and Technology, Larbi Tebessi University, Tebessa, Algeria. email: djamel.saadigtp@yahoo.fr.

Mohamed Salah Laouar, D.Sc., Full Professor, Department of Civil Engineering, Faculty of Sciences and Technology, Larbi Tebessi University, Tebessa, Algeria. email: c\_laouar@yahoo.fr.

Submitted on March 23, 2020; Final Acceptance on April 30, 2020; Discussion open until September 30, 2020.

DOI: 10.28927/SR.432247

methods have recently been widely used in many Geotechnical issues using sophisticated and advanced software, as well as powerful computers.

In recent years, several researchers employed numerical methods to determine the interference effect on the bearing capacity of neighboring footings in static conditions. Mabrouki *et al.* (2010) used the finite difference code FLAC to calculate the bearing capacity of two nearby strip footings, subjected to centered vertical loads with smooth and rough interfaces. The interference between the footings was investigated for several soil types, to determine the effects of cohesion, surcharge, and soil weight. The obtained results of efficiency factors were in good agreement with the solutions presented by Hazell (2004). Using model tests and characteristics method, Hazell (2004) studied the interference between two surface rough and smooth strip footings on dense and loose sand; the solutions of the characteristics method showed similar trends to the experimental model on dense sand. Ekbote & Nainegali (2019) studied the bearing capacity of two interfering strip footings embedded in cohesionless soil. The finite element software ABAQUS was used to evaluate the interference effect on the ultimate bearing capacity and the settlement of the foundations on homogeneous reinforced and unreinforced soil. The efficiency factors were presented for all terms of the bearing capacity equation. It was noted that for embedded interfering footings on reinforced soil medium, the reinforcement configurations have a significant impact effect on bearing capacity ratio. Acharyya & Dey (2017) carried out an investigation of the bearing capacity of square footings resting on sloping ground and the effects of the governing parameters (angle of internal friction of soil, setback distance, steepness of the slope, footing width and depth of embedment of the footing). It was noticed that a setback distance equal to three times the footing width is sufficient for the foundation to act as a footing resting on horizontal ground. Shokoohi *et al.* (2019) applied the finite element and the limiting equilibrium methods to investigate the bearing capacity of two neighboring shallow strip foundations on sand. The results of bearing capacity ratio indicated that both methods are in good agreement with available data in the literature. Using PLAXIS 3D, Acharyya *et al.* (2020) carried out a series of finite element analyses to investigate the bearing capacity of a square footing placed on the crest of a slope. An optimal 7-10-1 artificial neural network (ANN) architecture was also developed for direct prediction of bearing capacity. It was observed that the shear strength parameters of the soil, the footing width, the embedment depth, and the slope inclination have a significant influence on the bearing capacity value.

In light of the above-mentioned works, the determination of the ultimate bearing capacity of neighboring strip footings under seismic condition hardly received any attention. Therefore, this investigation examines the effect of different (geotechnical, geometrical) parameters on the

seismic ultimate bearing capacity of interfering strip footings, with the aid of 3-D finite element (FE) simulations using PLAXIS 3D V 2013. Moreover, the numerical model provides a description of the failure mechanism involved in the process of loading and failure of the footing.

## 2. Background and Problem Definition

For a shallow strip foundation, subjected to a centered vertical load, the static bearing capacity or ultimate load that a footing can sustain is usually calculated by superposition, where the contributions from soil cohesion  $c$ , soil unit weight  $\gamma$  and surcharge loading  $q$  are added together. Each contribution can be expressed as a bearing-capacity factor  $N_i$  to give the total capacity (Terzaghi (1943)):

$$q_u = 0.5\gamma BN_\gamma + qN_q + cN_c \quad (1)$$

where, the bearing capacity factors depend on the frictional parameter  $\phi$  of the soil.

For studying the seismic bearing capacity of foundations in seismic areas, there are several approaches in theoretical studies: pseudo-static, pseudo-dynamic and full dynamic analysis. For the pseudo-static approach, the horizontal and vertical accelerations are applied to the structure at the center of gravity or the base level, and the problem is reduced to a static case of bearing capacity with inclined eccentric loads. In most of these solutions, the inertia of the soil mass is not included. In the pseudo dynamic approach, the failure surface developed during dynamic condition is assumed to be similar to the one under static loading and the equation of motion is derived from the dynamic equilibrium conditions. In this context, the effect of the earthquake on the supporting soil is included in the equilibrium equations. Also, the distribution of earthquake acceleration is included. The full dynamic approach is based on time-history analysis using numerical methods.

In this study, the pseudo-static approach is adopted. The vertical downward static load applied by the structure to the footing is

$$W = mg \quad (2)$$

where  $W$  = weight (vertical load),  $m$  = Total mass applied by the structure,  $g$  = acceleration due to gravity ( $9.81 \text{ m/s}^2$ ).

Moreover, another vertical load at the base of the footing results from the presence of vertical seismic acceleration. Therefore, depending on the direction of the vertical seismic acceleration, it can be stated clearly that the structure will apply a total vertical downward load of magnitude:

$$W = (1 \pm k_v) mg \quad (3)$$

where  $k_v$  = vertical seismic coefficient.

Due to the horizontal seismic acceleration, the structure will apply a total horizontal load of magnitude

$$H = k_h mg \quad (4)$$

where  $H$  = horizontal load and  $k_h$  = horizontal seismic coefficient.

In a similar way, it can be written that the magnitude of vertical downward and horizontal body forces per unit volume will be equal to  $(1 \pm k_v) \gamma$  and  $k_h \gamma$ , respectively.

Only the horizontal seismic coefficient ( $k_h$ ) is accounted for in the present study and the seismic forces are considered as horizontal loads applied to the foundation, the surcharge and the underlying soil. The horizontal load is obtained by multiplying the horizontal seismic coefficient ( $k_h$ ) by foundation load ( $P$ ), surcharge ( $q$ ), and soil weight ( $W$ ).

For seismic bearing capacity and pseudo-static method, the seismic bearing capacity factors  $N_{cE}$ ,  $N_{qE}$ , and  $N_{\gamma E}$  substitute  $N_c$ ,  $N_q$ , and  $N_\gamma$  in Eq. 1. According to the available research, these factors are dependent on the soil friction angle and the seismic coefficient.

$$q_u = 0.5\gamma B N_{\gamma E} + q N_{qE} + c N_{cE} \quad (5)$$

In the case of two identical footings, Stuart (1962) took into account the interference effect on the ultimate bearing capacity of neighboring strip footings, with factors  $\xi_\gamma$ ,  $\xi_c$ , and  $\xi_q$  being employed to modify Terzaghi's superposition Eq. 1. The limit load is expressed in terms of bearing capacity factors and efficiency factors as follows:

$$q_u = 0.5\gamma B N_{\gamma} \xi_\gamma + q N_q \xi_q + c N_c \xi_c \quad (6)$$

The problem studied considers a footing of width  $B$  in interference with another identical footing, at a distance measured from axis to axis as shown in Fig. 1.

The magnitude of the seismic ultimate bearing pressure  $q_u$  is thus represented by the following expression:

$$q_{uE} = 0.5\gamma B N_{\gamma E} \xi_{\gamma,c,q} + q N_{qE} \xi_{qE} + c N_{cE} \xi_{cE} \quad (7)$$

where  $\xi_{(\gamma,c,q)E}$  are the seismic efficiency factors.

The three seismic efficiency factors in Eq. 7 can be calculated independently. They are defined as the ratio between the seismic bearing capacity of a single footing in presence of the other footings  $q_{uE(int)}$  and the seismic bearing capacity of an isolated footing having similar dimension  $q_{uE(iso)}$

$$\xi_{(\gamma,c,q)E} = \frac{q_{uE(int)}}{q_{uE(iso)}} \quad (8)$$

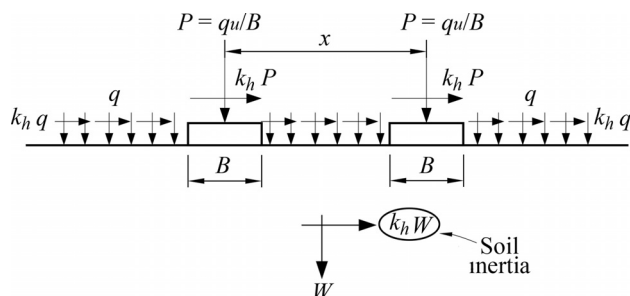


Figure 1 - Schematic diagram of the problem.

In order to estimate  $\xi_{cE}$ , a study was carried out in the case where the footings are acting on a weightless, cohesive-frictional soil with no surcharge; similarly, the factor  $\xi_{qE}$  is calculated by considering a weightless and cohesionless soil. For the  $\xi_{\gamma E}$  factor, PLAXIS is able to carry out pseudo-static analysis by applying horizontal acceleration to the soil weight. In order to compute  $\xi_{\gamma E}$ , the surcharge ( $q$ ) was kept equal to zero. A small value of  $c$  was chosen to prevent numerical instabilities. The calculations were performed in two separate phases. In the first phase the pseudo-static analysis was performed and in the second phase, the external inclined stresses were applied to the foundation. Additionally, to calculate the combined efficiency factor  $\xi_{\gamma c q}$  the soil is assumed to have non-zero values for the three parameters: cohesion  $c$ , friction angle  $\phi$  and density  $\gamma$ , and there is uniform surcharge pressure  $q$ .

### 3. Numerical Modeling and Analysis

In order to investigate the limit load for two closely spaced strip foundations in various conditions, nonlinear finite element analyses were performed to determine the seismic response as well as the settlement behavior of footings due to the application of horizontal loads. In the following, the problem definition and the finite element model are discussed. A numerical analysis using (Plaxis 3D-V 2013) software has been employed to separately characterize the load-settlement relationships of model strip footings. The computer program used in this study incorporates a fully automatic mesh-generation procedure, in which the geometry is divided into elements. Five different mesh densities are available in Plaxis, ranging from very coarse to very fine. In order to obtain the most suitable mesh for the present study, preliminary computations using the five available levels of global mesh coarseness were conducted. Since there is not too much difference in the results for different mesh configurations, it was decided to use the coarse mesh with refinement around the footing in all the analyses. The soil mechanical behavior is modeled using an elastic-perfectly plastic constitutive model following the Mohr-Coulomb failure criterion. The elastic parameters  $E = 2 \times 10^4$  kPa and  $\nu = 0.3$  were assumed. The values of  $c = 10$  kPa,  $q = 10$  kPa, and  $\gamma = 16$  kN/m<sup>3</sup> were considered in order to compute the bearing capacity factors. The friction angle  $\phi$  is varied from 20° to 40° in 5° increments, thus encompassing a wide range of soil types. It is assumed that the soil is completely dry and obeys the associated flow rule. The concrete footings were modeled using plate elements with linear elastic behavior. The normal stiffness and flexural rigidity of concrete foundations were considered as  $5 \times 10^6$  kN/m and  $9 \times 10^3$  kNm<sup>2</sup>/m, respectively. Several trial analyses were performed to choose an appropriate size for the soil domain. Finally, the generated mesh has dimensions of  $6B$  (width),  $40B$  (length) and  $20B$  (depth), while

that of the footing was 2.0 m width,  $x$  represents the axis to axis spacing between the footings.

The size of the finite element model is large enough to keep the boundary conditions at the bottom and the right and left sides from restricting the soil movement due to the footing load, so that the failure zones are freely developed without any interference from the boundary. The layout of mesh geometry is illustrated in Fig. 2.

“Standard fixity” has been applied on the numerical model, horizontal fixity was given to the vertical edges of the model. In the bottom edge of the model, both vertical and horizontal fixity were applied as the base of the model is assumed to be non-yielding.

The loading of rigid strip footing is modeled by imposing uniform inclined stresses at the surface nodes below the footing base. The inclination of imposed stresses is equal to the horizontal seismic coefficient ( $k_h$ ). The loading process is continued incrementally until (a) soil relative stiffness reaches zero and (b) the nodal out of balance forces get solved. The term “nodal out of balance forces” refers to the difference between the external loads and the forces that are in equilibrium with the current stresses. The stress vertical component that satisfies the above two conditions is the ultimate bearing capacity of the footing. After several attempts not reported for the sake of brevity, the best results, in terms of solution stability and convergence, were obtained. The finite element analyses are performed for  $0 \leq k_h \leq 0.6$ . The seismic efficiency factors were computed based on the superposition principle.

## 4. Results and Discussion

### 4.1. Seismic bearing capacity factors for an isolated strip footing

A preliminary simulation of the seismic bearing capacity of the system has been performed in order to check the validity and the degree of approximation of the numeri-

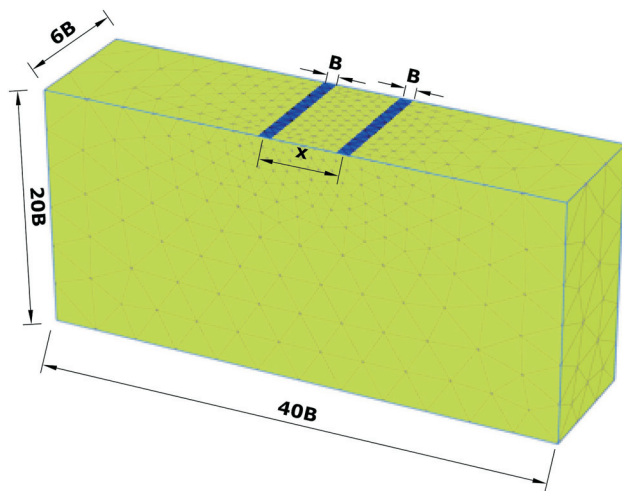


**Figure 2** - Finite element mesh and geometry of the problem (Not to scale).

cal procedure, by comparing the seismic bearing capacity factors obtained by the present numerical study with those obtained by other studies for  $\phi = 30^\circ$ , as shown in Figs. 3(a-c).

As seen in Figs. 3a and 3b, the values of  $N_{cE}$  and  $N_{qE}$  established from the present analyses are in good agreement with those reported by Kumar & Mohan Rao (2002); Pane *et al.* (2016); Shafiee & Jahanandish (2010); Soubra (1999). Results are slightly higher than other solutions, which may be due to the difference in the method of analy-

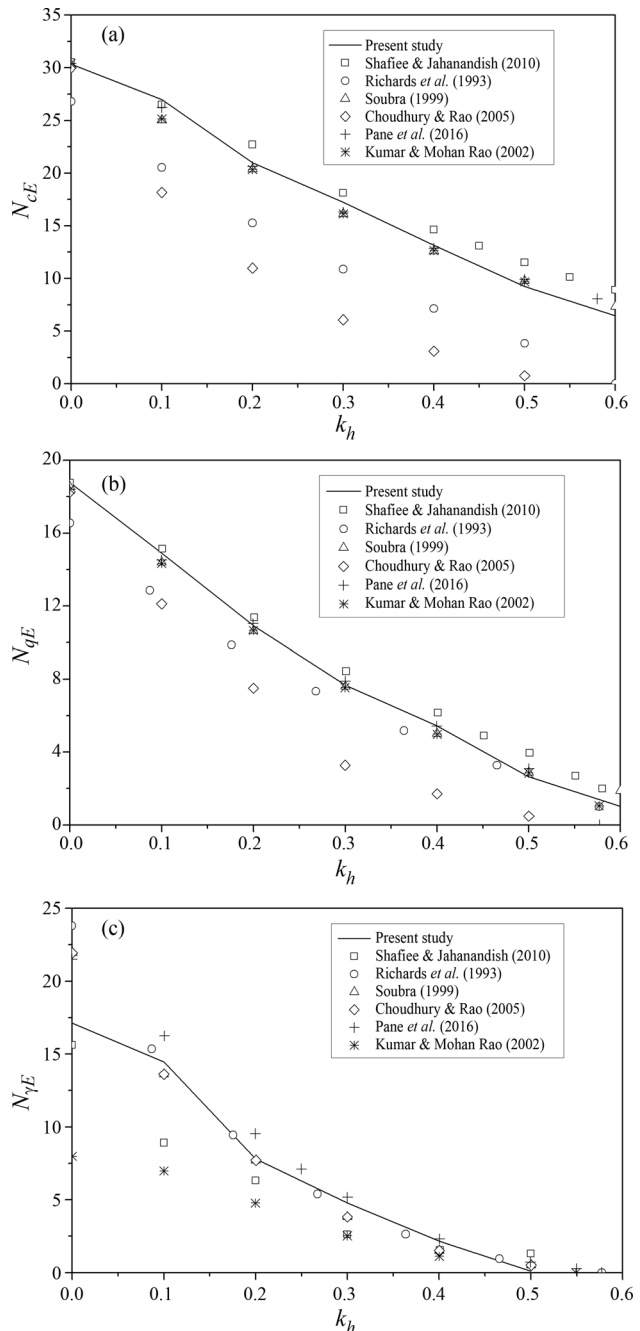


**Figure 3** - Comparison of (a)  $N_{cE}$ , (b)  $N_{qE}$  and (c)  $N_{\gamma E}$  of the present study with some of the available solutions in the literature.

sis. According to Fig. 3c, it is worth noting that, despite of the variation in the calculated bearing capacity factors, all of the solutions for  $N_{\gamma E}$  are almost coincident. Based on this evidence, and on the consequent confidence in the adopted numerical procedure, the model was further used to simulate the interference effect of two strip footings under seismic loading conditions.

## 4.2. Seismic efficiency factors

In the case of dry cohesionless soils, Richards *et al.* (1993) found out that the phenomenon of shear fluidization (*i.e.*, the material's plastic flow at a finite effective stress) may occur when  $k_h$  is greater than  $\tan(\varphi)$ . In this case, soil acts like a viscous flow. Therefore, the maximum plausible value for  $k_h$  is set to  $\tan(\varphi)$  for calculations of  $\xi_{qE}$ , and  $\xi_{\gamma E}$  for friction angles  $20^\circ$  to  $30^\circ$ . For  $\varphi = 35^\circ, 40^\circ$ , the maximum value of  $k_h$  is 0.6. Taking into account the above-mentioned, a large number of numerical analyses were conducted for a wide range of seismic coefficient  $k_h$  to estimate the values of seismic efficiency factors such as  $\xi_{cE}$ ,  $\xi_{qE}$ , and  $\xi_{\gamma E}$ . The effect of horizontal seismic coefficient  $k_h$  on the bearing capacity of strip footings for various spacing ( $x/B$ ) and friction angles ( $\varphi$ ) are presented in Figs. 4-6.

Figures 4 and 5 show the variation of efficiency factors  $\xi_{cE}$  and  $\xi_{qE}$ , respectively. It can be observed that, for a spacing of  $x = 1B$  there is no improvement in bearing capacity. If the distance between the footings is increased, for all values of horizontal seismic coefficient  $k_h$  the efficiency factor increases until a peak for spacing between  $1.5B$  and  $2.3B$ , followed by a progressive reduction to the value of 1 (value for widely spaced footings). Furthermore, for a given spacing between footings, the efficiency factor increases markedly with the increase in the friction angle.

The peak is found to be higher for smaller values of  $k_h$  and spacing less than about  $2.3B$ . For  $\varphi = 40^\circ$  with  $k_h = 0$ , the maximum computed efficiency factor was approximately 1.5. Similarly, for  $\varphi = 40^\circ$  with  $k_h = 0.6$ , the maximum values for  $\xi_{cE}$  and  $\xi_{qE}$  were found to be approximately 1.4 and 1.42, respectively. It should be noted that the increase in  $k_h$  leads to a reduction in efficiency gains as a result of the interaction between the foundations. For  $k_h = 0$  and spacing ratio greater than  $3B, 4B, 5B, 6B$  and  $7B$ , no interference effect was observed for friction angles  $\varphi = 20^\circ, 25^\circ, 30^\circ, 35^\circ$  and  $40^\circ$  respectively. This distance reduced with increases in the  $k_h$  value.

Figure 6 illustrates the variation of seismic efficiency factor  $\xi_{\gamma E}$  vs. spacing ratios  $x/B$  and  $k_h$  (for  $20^\circ \leq \varphi \leq 40^\circ$ ). As seen, for all values of  $k_h$  the values of  $\xi_{\gamma E}$  are gradually reduced with an increase in  $x/B$  for friction angles less than  $25^\circ$ . However, one can note a peak for the frictional angles  $25^\circ, 30^\circ, 35^\circ$  and  $40^\circ$ . It can be also noted that, on an average, the peak of  $\xi_{\gamma E}$  decreases by 10 % for increasing of the horizontal seismic coefficient  $k_h$ .

## 4.3. Combined efficiency factor ( $\xi_{\gamma c q}$ )

Figure 7 illustrates the effect of variation of the horizontal seismic coefficient  $k_h$  and angle of internal friction ( $\varphi$ ) on the combined efficiency factor  $\xi_{\gamma c q}$ . To calculate the combined efficiency factor  $\xi_{\gamma c q}$  the soil is assumed to have cohesion  $c$ , friction angle  $\varphi$  and density  $\gamma$ , and there is uniform surcharge pressure  $q$ .

It can be noticed that the results obtained for the combined efficiency factor  $\xi_{\gamma c q}$  are lower than those obtained for  $\xi_{\gamma}$  and they have the same overall pattern. It can be observed also that for any friction angle, the increase in  $k_h$  resulted in the decrease of the gain in efficiency, the effect being more prominent at higher values of  $\varphi$ . Concerning the distance  $x/B$  at which no interference effect occurs, as shown in Fig. 7,  $x/B$  decreases by  $1B$  for increasing in horizontal seismic coefficient  $k_h$  up to 0.6. The reason can be attributed to the extension and the depth of the shear zone being less than when the footing was under the static loading condition.

## 4.4. Failure mechanisms

The extent of the plastic zones for  $\varphi = 40^\circ, c = 10$  kPa,  $q = 10$  kPa and  $k_h = 0$  at different  $x/B$  ratios is shown in Fig. 8.

As seen, the shear zone is symmetrical about the center of the footings and similar to the failure mechanism proposed by Stuart (1962). Based in the geometry of the rupture surface in the soil mass assumed by Terzaghi (1943), Stuart (1962) suggested a failure mechanism for two closely spaced footings and some correction factors for the influence of the distance between the footings.

Figures 8 (a, b) show the failure patterns when the distance between the two footings is very small or zero, the behavior is analogous to that of a single footing of width  $2B + x$ . This behavior is referred to as the so-called "blocking effect". Based on this phenomenon, the soil between the footings behaves as a combined system and moves down as a single unit by loading application. If the spacing of the foundations is further increased, Figs. 8 (c, d) show the appearance of overlapping passive zones situated between the two footings. In this case the load capacity is influenced by the interference effect. From Fig. 8d, it can be seen that there is no overlap of failure surfaces at greater spacing. Also, the interference effect does not exist and the bearing capacity of each foundation is independent to the other.

Figures 9(a-e) indicate the failure patterns for the same case ( $\varphi = 40^\circ, c = 10$  kPa,  $q = 10$  kPa) with  $k_h = 0.60$ . It is clear that the failure pattern became non-symmetrical in the presence of earthquake acceleration; whereas the spreading of the plastic zone was more in the direction of horizontal pseudo-static body forces, and it increased with increases in the  $k_h$  values. As seen from Figs. 9, the extension and the depth of the shear zone was less than for the footing under the static loading condition. For the spacing between footings above  $5B$ , the shear zone is similar to the

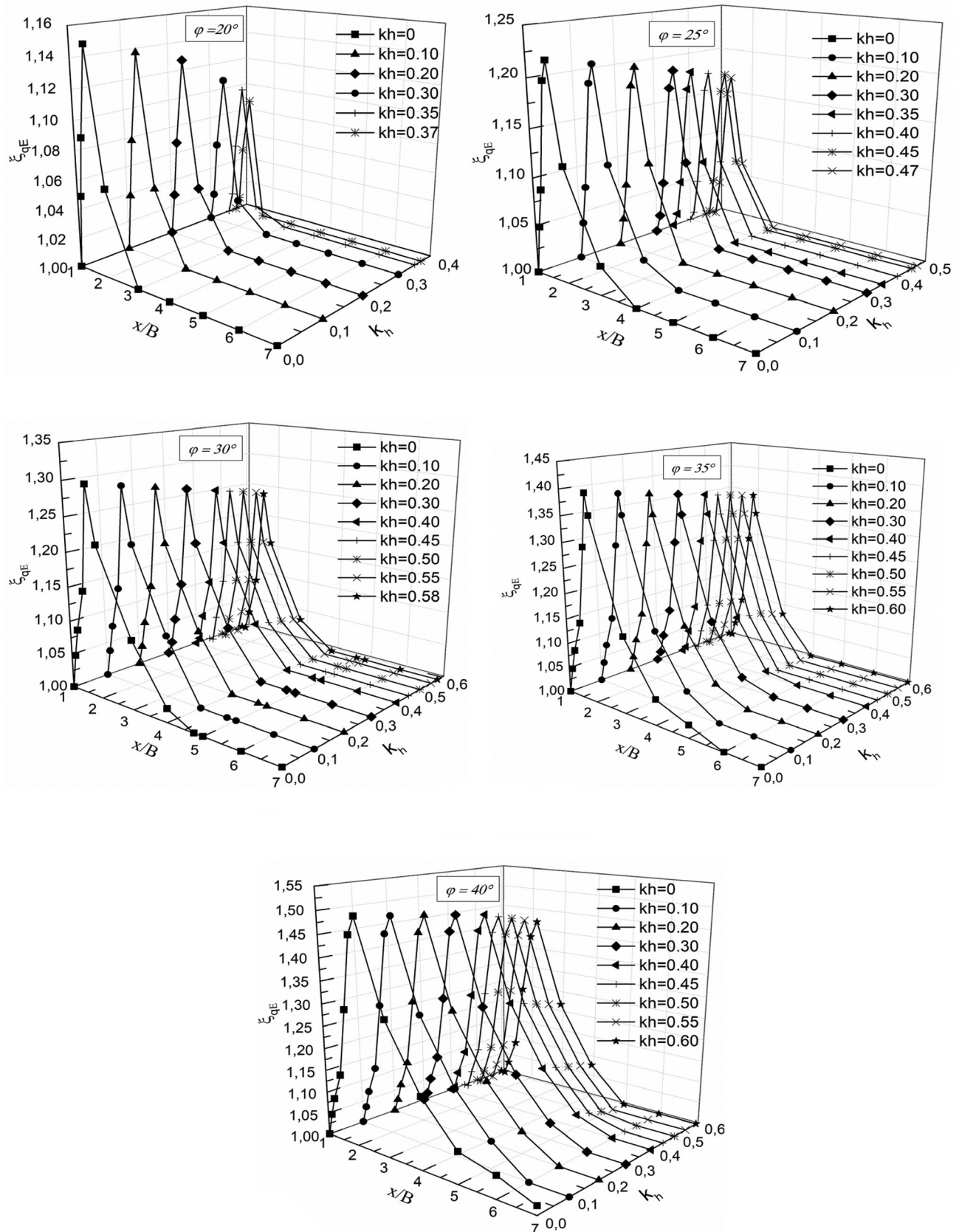


**Figure 4** -Variation of efficiency factors  $\xi_{qE}$  with  $x/B$  and horizontal seismic coefficient  $k_h$  for various values of angle of internal friction  $\varphi$ .

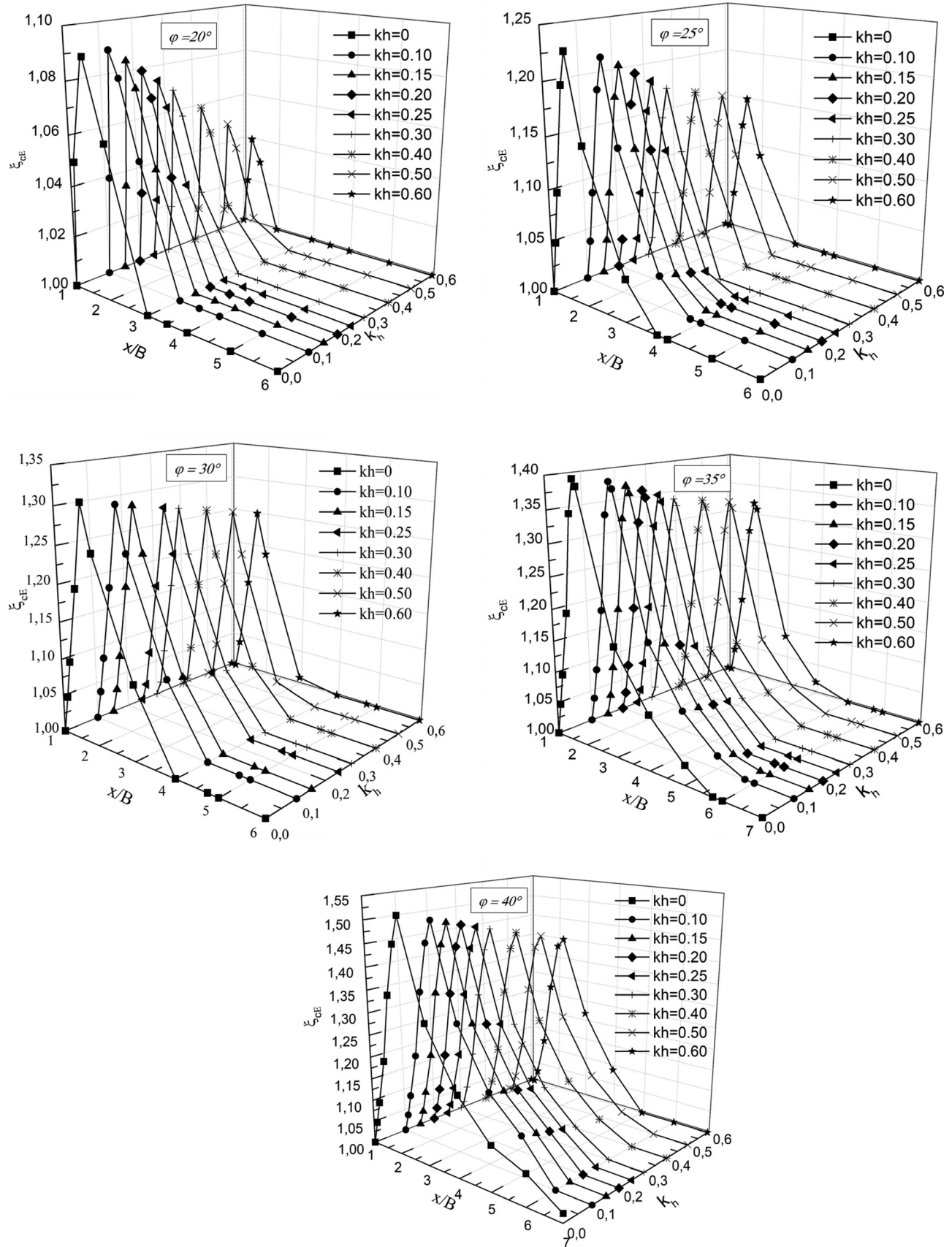


Figure 5 - Variation of efficiency factors  $\xi_{cE}$  with  $x/B$  and horizontal seismic coefficient  $k_h$  for various values of angle of internal friction  $\phi$ .

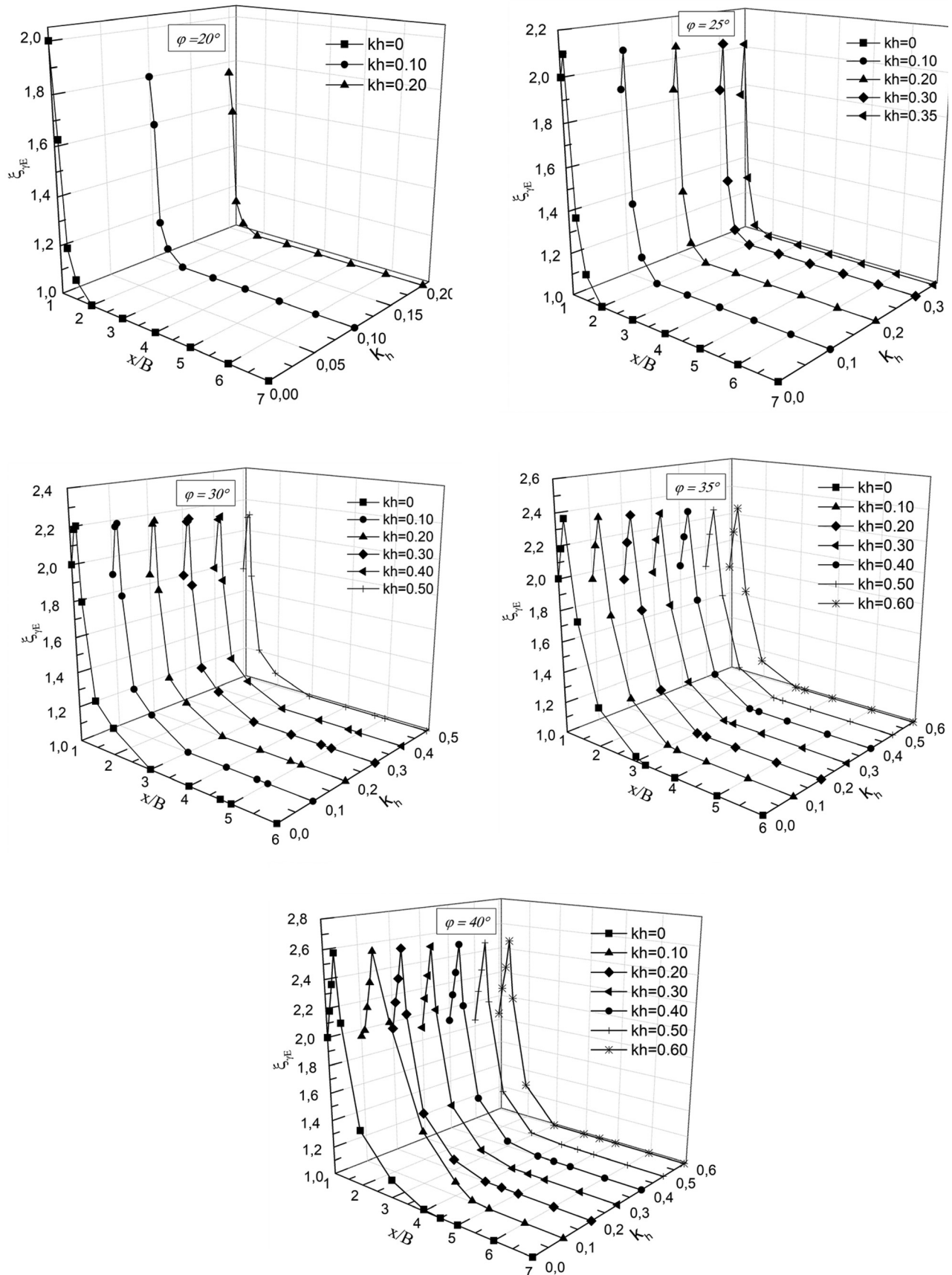


Figure 6 - Variation of efficiency factors  $\xi_{\gamma/E}$  with  $x/B$  and horizontal seismic coefficient  $k_h$  for various values of angle of internal friction  $\varphi$ .

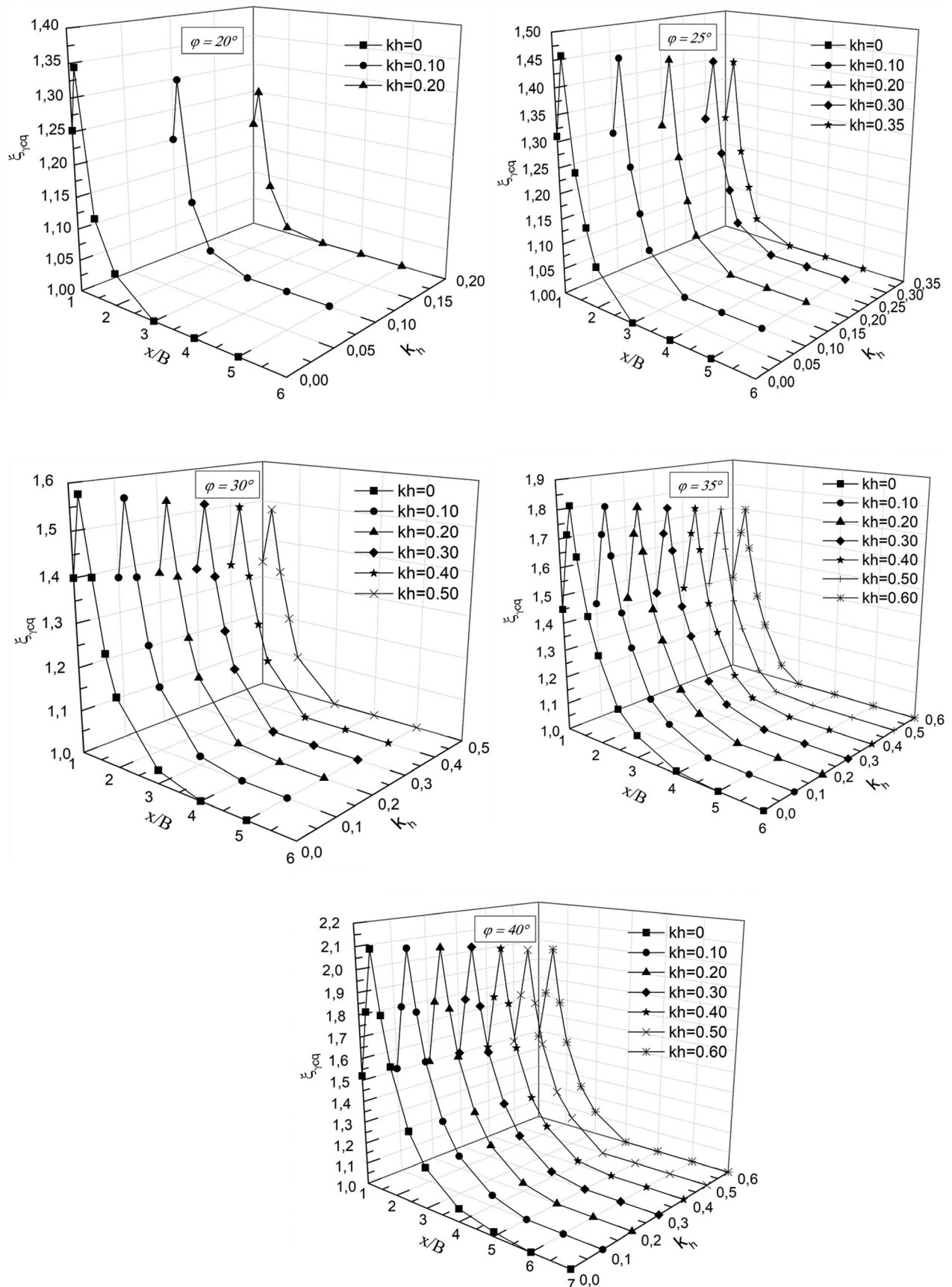
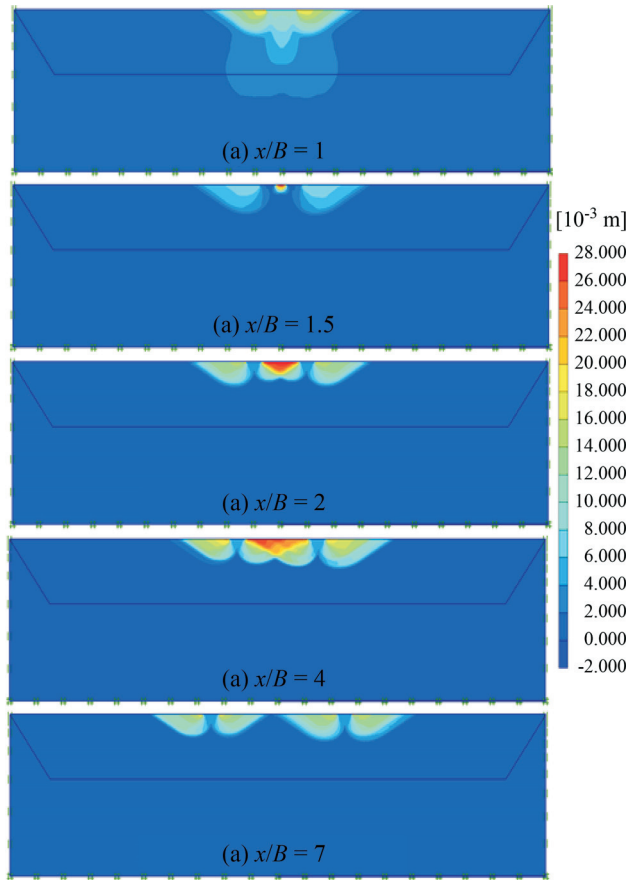
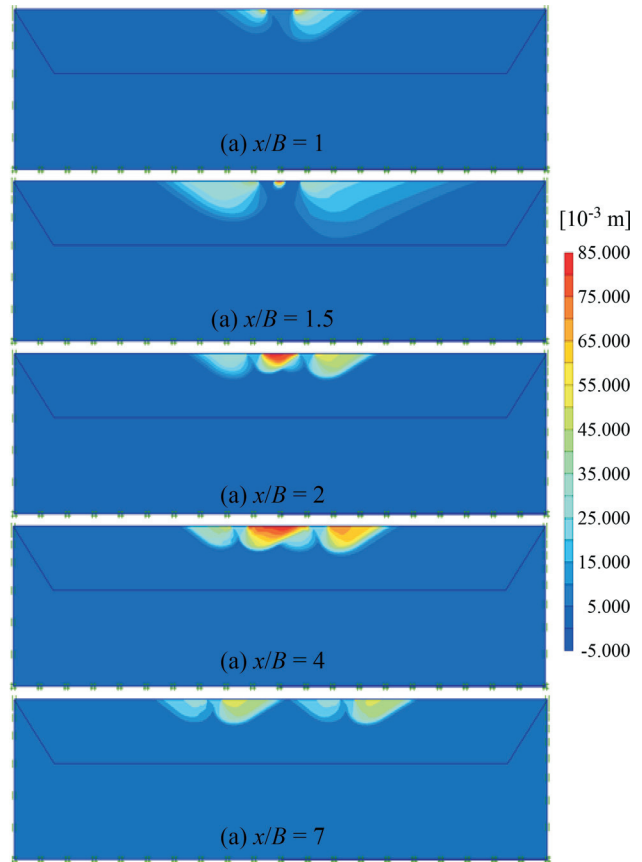


Figure 7 - Variation of efficiency factors  $\xi_{\gamma cq}$  with  $x/B$  and horizontal seismic coefficient  $k_h$  for various values of angle of internal friction  $\phi$ .



**Figure 8** - Total incremental displacement for interfering strip footings under the static loading condition at various spacings ( $x/B$ ).



**Figure 9** - Total incremental displacement for interfering strip footings under the seismic loading condition at various spacings ( $x/B$ ).

failure mechanism found by Kumar & Mohan Rao (2002) and Cascone & Casablanca (2016) in the analysis of an isolated strip footing. In addition, the settlement is smaller for larger spacings.

**4.5. Superposition error**

For the reason that the soil behaves nonlinearly specially under seismic action, the principle of superposition to compute the bearing capacity is not sufficiently accurate. For an isolated strip footing, Davis & Booker (1971) found that the error is on the safe side by applying the previous assumption, While for two interfering footings, Mabrouki *et al.* (2010) concluded that the error is always on the safe side; it underestimates the bearing capacity. To illustrate the superposition effect on the bearing capacity of two interfering footings, direct calculations of bearing capacity were executed for  $k_h = 0$  and  $k_h = 0.3$  ( $\varphi = 35^\circ$ ). Using Terzaghi's assumption, the bearing capacity  $q_u$  is calculated and compared in Fig. 10 with the results when  $c$ ,  $\gamma$ , and  $q$  are accounted for simultaneously.

As illustrated in Fig. 10, the range of error induced by applying the superposition principle is always on the safe side and the error percentage for seismic loading is greater than for the static case. Also, it is seen that the results for su-

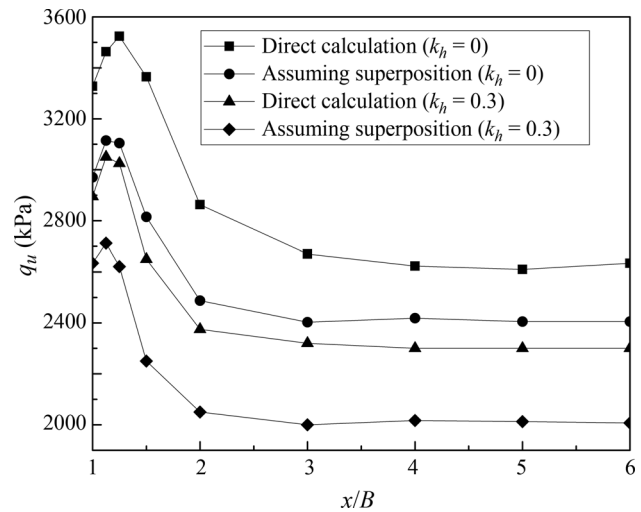


**Figure 10** - Effect of superposition and the direct computations on static/seismic bearing capacity.

perposition principle in case of  $k_h = 0$  are very close to the direct calculation results in the case of  $k_h = 0.3$ . In other words, using superposition assumption to estimate bearing capacity for interfering footing in the seismic case is more conservative than in the static case.

#### 4.6. Effect of soil inertia

For the case of an isolated strip footing, the effect of soil inertia on the seismic bearing capacity has been the subject of research by several authors such as Sarma & Iossifelis (1990), Dormieux & Pecker (1995), and Shafiee & Jahanandish (2010). All these studies observed that the load inclination is the principal reason of reduction in bearing capacity, and hence the soil inertia forces can be neglected. In this paper, to study the effect of soil inertia on the seismic bearing capacity of two interfering footings, all computations were carried out in two general cases including/neglecting soil inertia. Figure 11 illustrates the variation of the seismic efficiency factor  $\xi_{\gamma/E}$  with  $x = B$  in the case of horizontal seismic coefficient  $k_h = 0.3$  and for friction angles  $\varphi = 30^\circ$  and  $40^\circ$ . It was seen before that only the  $\xi_{\gamma/E}$  factor depends on the soil inertia.

In the case of two interfering footings, the soil inertia effects are found to be even less important than in the previous case of isolated strip foundations. This is shown in Fig. 11, where the results show a moderate reduction of the seismic efficiency factors  $\xi_{\gamma/E}$  with  $x/B$ , that becomes less important when interference effects are taken into account. This effect is not large and can be accommodated within the static safety factor.

#### 5. Discussion

This study does not examine the effects of vertical pseudo-static earthquake body forces on the magnitude of the foundation bearing capacity. Because the vertical body (gravitational) forces have already been incorporated in the problem, it is possible to integrate the impact of the vertical component of the earthquake acceleration simply by using the soil's revised unit weight ( $\gamma_r$ ). If  $\pm k_v g$  is the magnitude of vertical seismic acceleration, then the value of  $\gamma_r = \gamma(1 \pm k_v)$  should be used in place of  $\gamma$  to account for the presence

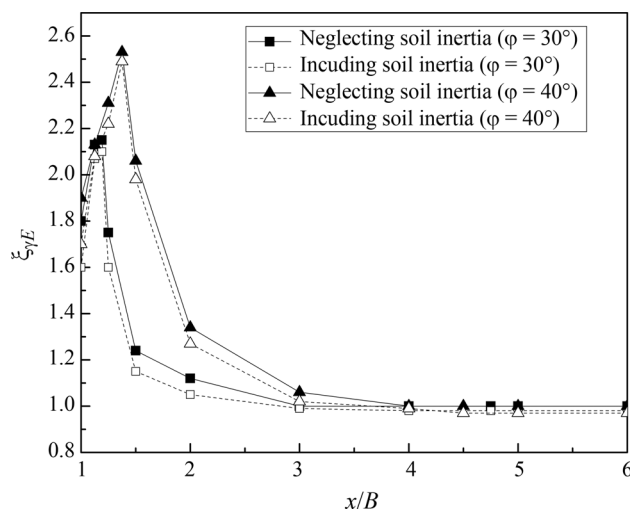


**Figure 11** - Effect of soil inertia on the seismic efficiency factor  $\xi_{\gamma/E}$  for horizontal acceleration factor  $k_h = 0.3$  and for  $\varphi = 30^\circ$  and  $40^\circ$ .

of  $k_v$ . Finally, the magnitude of the total bearing capacity in the presence of both the horizontal and vertical pseudo-static seismic forces can be calculated. It should be mentioned that for incorporating the effect of the vertical pseudo-static earthquake body forces on the bearing capacity factors for strip footings on a slope, Kumar & Rao (2003a) also recommended a similar formulation.

#### 6. Conclusions

In this study, various numerical analyses using PLAXIS 3D V 2013 were conducted to determine the interference effect on seismic bearing capacity of two footings for a wide range of spacings between the footings, friction angles and seismic coefficients. The pseudo-static approach has been adopted in the analyses. Based on the obtained results, the following important conclusions can be stated:

- The seismic bearing capacity factors obtained by the present numerical study are in good agreement with those obtained by other studies.
- For all values of the horizontal seismic coefficient, the seismic efficiency factors increase until a peak, followed by a gradual decrease to a constant value of one (value for widely spaced footings). The peak also decreases with increasing of  $k_h$  intensity which is at a spacing distance less than about  $2.3B$ . Moreover, the efficiency factor increases significantly with an increase in the friction angle. The above behaviours are the same in the case of static loads, but with relatively low values.
- Under seismic loading, the increase in the earthquake acceleration leads to a reduction in efficiency gains owing to the interaction between the foundations and the deformation of the shear zone.
- For all friction angles, it has been seen that the spacing required for interference to become extinct decreases with an increase in the earthquake acceleration value.
- The range of error induced by applying the superposition principle is always on the safe side and the error percentage for seismic loading is greater than for the static case.
- In the case of two interfering footings, the soil inertia effects are found to be even less important than in the previous case of isolated strip foundations. This effect is not large and can be accommodated within the static safety factor.

#### References

- Acharyya, R. & Dey, A. (2017). Finite element investigation of the bearing capacity of square footings resting on sloping ground. *INAE Letters*, 2(3):97-105. <https://doi.org/10.1007/s41403-017-0028-6>
- Acharyya, R.; Dey, A. & Kumar, B. (2020). Finite element and ANN-based prediction of bearing capacity of square footing resting on the crest of c- $\phi$  soil slope. *International Journal of Geotechnical Engineering*, 14(2):176-187. <https://doi.org/10.1080/19386362.2018.1435022>

- Bolton, M.D. & Lau, C. (1993). Vertical bearing capacity factors for circular and strip footings on Mohr-Coulomb soil. *Canadian Geotechnical Journal*, 30(6):1024-1033. <https://doi.org/10.1139/t93-099>
- Budhu, M. & Al-Karni, A. (1993). Seismic bearing capacity of soils. *Geotechnique*, 43(1):181-187. <https://doi.org/10.1680/geot.1993.43.1.181>
- Casagrande, L. (1966). Subsoils and foundation design in Richmond. *Journal of Soil Mechanics & Foundations Div*, 92(5):109-126.
- Cascone, E. & Casablanca, O. (2016). Static and seismic bearing capacity of shallow strip footings. *Soil Dynamics and Earthquake Engineering*, 84(1):204-223. <https://doi.org/10.1016/j.soildyn.2016.02.010>
- Chakraborty, D. & Mahesh, Y. (2016). Seismic bearing capacity factors for strip footings on an embankment by using lower-bound limit analysis. *International Journal of Geomechanics*, 16(3):1-11. [https://doi.org/10.1061/\(ASCE\)GM.1943-5622.0000553](https://doi.org/10.1061/(ASCE)GM.1943-5622.0000553)
- Choudhury, D. & Rao, K.S.S. (2005). Seismic bearing capacity of shallow strip footings. *Geotechnical & Geological Engineering*, 23(4):403-418. <https://doi.org/10.1007/s10706-004-9519-9>
- Das, B.M. & Larbi-Cherif, S. (1983). Bearing capacity of two closely-spaced shallow foundations on sand. *Soils and Foundations*, 23(1):1-7. <https://doi.org/10.3208/sandf1972.23.1>
- Davis, E. & Booker, J. (1971). The bearing capacity of strip footing from the standpoint of plasticity theory. *Proc. 1st Conf. in geomechanics, New Zealand, Australian*, pp. 276-282.
- Dormieux, L. & Pecker, A. (1995). Seismic bearing capacity of foundation on cohesionless soil. *Journal of Geotechnical Engineering*, 121(3):300-303. [https://doi.org/10.1061/\(ASCE\)0733-9410\(1995\)121:3\(300\)](https://doi.org/10.1061/(ASCE)0733-9410(1995)121:3(300))
- Ekbote, A.G. & Nainegali, L. (2019). Interference of two closely spaced strip footings embedded in cohesionless fibre-reinforced foundation soil bed. *Proc. 8th International Conference on Case Histories in Geotechnical Engineering, Philadelphia, Pennsylvania*, pp. 454-464. <https://doi.org/10.1061/9780784482094.041>
- Ghosh, P. (2008). Upper bound solutions of bearing capacity of strip footing by pseudo-dynamic approach. *Acta Geotechnica*, 3(2):115-123. <https://doi.org/10.1007/s11440-008-0058-z>
- Ghosh, P. & Sharma, A. (2010). Interference effect of two nearby strip footings on layered soil: theory of elasticity approach. *Acta Geotechnica*, 5(3):189-198. <https://doi.org/10.1007/s11440-010-0123-2>
- Hansen, J.B. (1970). A revised and extended formula for bearing capacity. *Danish Geotechnical Institute Bull*, 28(1):5-11.
- Hazell, E. (2004). Interaction of Closely Spaced Strip Footings. Final year project report. Department of Engineering Science, University of Oxford.
- Huang, C.-C. (2019). Experimental verification of seismic bearing capacity of near-slope footings using shaking table tests. *Journal of Earthquake Engineering*, 1-30. <https://doi.org/10.1080/13632469.2019.1665148>
- Jahani, M.; Oulapour, M. & Haghghi, A. (2019). Evaluation of the seismic bearing capacity of shallow foundations located on the two-layered clayey soils. *Iranian Journal of Science and Technology, Transactions of Civil Engineering*, 43(1):49-57. <https://doi.org/10.1007/s40996-018-0122-3>
- Keshavarz, A. & Nemati, M. (2017). Seismic bearing capacity of strip footings on fiber reinforced soils by the stress characteristics method. *Journal of Engineering Geology*, 10(3):3667-3688.
- Knappett, J.; Haigh, S.K. & Madabhushi, S.G. (2006). Mechanisms of failure for shallow foundations under earthquake loading. *Soil Dynamics and Earthquake Engineering*, 26(2-4):91-102. <https://doi.org/10.1016/j.soildyn.2004.11.021>
- Kumar, J. & Bhattacharya, P. (2010). Bearing capacity of interfering multiple strip footings by using lower bound finite elements limit analysis. *Computers and Geotechnics*, 37(5):731-736. <https://doi.org/10.1016/j.compgeo.2010.05.002>
- Kumar, J. & Bhoi, M.K. (2008). Interference of multiple strip footings on sand using small scale model tests. *Geotechnical and Geological Engineering*, 26(4):469-477. <https://doi.org/10.1007/s10706-008-9175-6>
- Kumar, J. & Chakraborty, D. (2013). Seismic bearing capacity of foundations on cohesionless slopes. *Journal of Geotechnical and Geoenvironmental Engineering*, 139(11):1986-1993. [https://doi.org/10.1061/\(ASCE\)GT.1943-5606.0000909](https://doi.org/10.1061/(ASCE)GT.1943-5606.0000909)
- Kumar, J. & Ghosh, P. (2007). Upper bound limit analysis for finding interference effect of two nearby strip footings on sand. *Geotechnical and Geological Engineering*, 25(5):499-507. <https://doi.org/10.1007/s10706-007-9124-9>
- Kumar, J. & Kouzer, K. (2008). Bearing capacity of two interfering footings. *International Journal for Numerical and Analytical Methods in Geomechanics*, 32(3):251-264. <https://doi.org/10.1002/nag.625>
- Kumar, J. & Kumar, N. (2003). Seismic bearing capacity of rough footings on slopes using limit equilibrium. *Geotechnique*, 53(3):363-369. <https://doi.org/10.1680/geot.2003.53.3.363>
- Kumar, J. & Mohan Rao, V. (2002). Seismic bearing capacity factors for spread foundations. *Geotechnique*, 52(2):79-88. <https://doi.org/10.1680/geot.2002.52.2.79>
- Kumar, J. & Mohan Rao, V. (2003). Seismic bearing capacity of foundations on slopes. *Geotechnique*, 53(3):347-361. <https://doi.org/10.1680/geot.2003.53.3.347>
- Lee, J. & Eun, J. (2009). Estimation of bearing capacity for multiple footings in sand. *Computers and Geotechnics*,

- 36(6):1000-1008.  
<https://doi.org/10.1016/j.compgeo.2009.03.009>
- Luo, W.; Zhao, M.; Xiao, Y.; Zhang, R. & Peng, W. (2019). Seismic bearing capacity of strip footings on cohesive soil slopes by using adaptive finite element limit analysis. *Advances in Civil Engineering*, 2019(1):1-16. <https://doi.org/10.1155/2019/4548202>
- Mabrouki, A.; Benmeddour, D.; Frank, R. & Mellas, M. (2010). Numerical study of the bearing capacity for two interfering strip footings on sands. *Computers and Geotechnics*, 37(4):431-439. <https://doi.org/10.1016/j.compgeo.2009.12.007>
- Meyerhof, G.G. (1963). Some recent research on the bearing capacity of foundations. *Canadian Geotechnical Journal*, 1(1):16-26. <https://doi.org/10.1139/t63-003>
- Pain, A.; Choudhury, D. & Bhattacharyya, S. (2016). The Seismic Bearing Capacity Factor for Surface Strip Footings. *Geo-Chicago*, Chicago, Illinois, pp. 197-206. <https://doi.org/10.1061/9780784480120.021>
- Pane, V.; Vecchiotti, A. & Cecconi, M. (2016). A numerical study on the seismic bearing capacity of shallow foundations. *Bulletin of Earthquake Engineering*, 14(11):2931-2958. <https://doi.org/10.1007/s10518-016-9937-0>
- Paolucci, R. & Pecker, A. (1997). Seismic bearing capacity of shallow strip foundations on dry soils. *Soils and Foundations*, 37(3):95-105. [https://doi.org/10.3208/sandf.37.3\\_95](https://doi.org/10.3208/sandf.37.3_95)
- Prandtl, L. (1920). Über die härte plastischer körper. *Nachrichten von der Gesellschaft der Wissenschaften zu Göttingen, Mathematisch-Physikalische Klasse*, 1920(1):74-85.
- Richards, J.; Elms, D. & Budhu, M. (1993). Seismic bearing capacity and settlements of foundations. *Journal of Geotechnical Engineering*, 119(4):662-674. [https://doi.org/10.1061/\(ASCE\)0733-9410\(1993\)119:4\(662\)](https://doi.org/10.1061/(ASCE)0733-9410(1993)119:4(662))
- Saha, A. & Ghosh, S. (2015). Pseudo-dynamic analysis for bearing capacity of foundation resting on c- $\Phi$  soil. *International Journal of Geotechnical Engineering*, 9(4):379-387. <https://doi.org/10.1179/1939787914Y.0000000081>
- Sarma, S. & Chen, Y. (1995). Seismic bearing capacity of shallow strip footings near sloping ground. *Proc. 5th Conference on European Seismic Design Practice, SECED*, Balkema, Rotterdam, pp.505-512.
- Sarma, S. & Iossifelis, I. (1990). Seismic bearing capacity factors of shallow strip footings. *Geotechnique*, 40(2):265-273. <https://doi.org/10.1680/geot.1990.40.2.265>
- Schmertmann, J.H.; Hartman, J.P. & Brown, P.R. (1978). Improved strain influence factor diagrams. *Journal of Geotechnical and Geoenvironmental Engineering*, 104(8):1131-1135.
- Shafiee, A.H. & Jahanandish, M. (2010). Seismic bearing capacity factors for strip footings. *Proc 5th National Congress on Civil Engineering*, Mashhad, Iran, pp.1-8.
- Shokoohi, M.; Veiskarami, M. & Hataf, N. (2019). A numerical and analytical study on the bearing capacity of two neighboring shallow strip foundations on sand. *Iranian Journal of Science and Technology, Transactions of Civil Engineering*, 43(1):591-602. <https://doi.org/10.1007/s40996-018-0189-x>
- Soubra, A.H. (1999). Upper-bound solutions for bearing capacity of foundations. *Journal of Geotechnical and Geoenvironmental Engineering*, 125(1):59-68. [https://doi.org/10.1061/\(ASCE\)1090-0241\(1999\)125:1\(59\)](https://doi.org/10.1061/(ASCE)1090-0241(1999)125:1(59))
- Stuart, J. (1962). Interference between foundations, with special reference to surface footings in sand. *Geotechnique*, 12(1):15-22. <https://doi.org/10.1680/geot.1962.12.1.15>
- Terzaghi, K. (1943). *Theoretical Soil Mechanics*. John Wiley & Sons, New York.
- Vesic, A.S. (1973). Analysis of ultimate loads of shallow foundations. *Journal of Soil Mechanics & Foundations Div ASCE*, 99(1):45-73.
- Zeng, X. & Steedma, R. (1998). Bearing capacity failure of shallow foundations in earthquakes. *Geotechnique*, 48(2):235-256. <https://doi.org/10.1680/geot.1998.48.2.235>



## ***Technical Notes***

***Soils and Rocks***  
**v. 43, n. 2**



# Drained and Undrained Behavior of an Aeolian Sand from Natal, Brazil

P.L. Souza Junior, O.F. Santos Junior, T.B. Fontoura, O. Freitas Neto

**Abstract.** The behavior of sands subjected to diverse loading conditions has been the object of many studies in recent decades. Constitutive models that are able to simulate the behavior of sands have been developed based on critical state theory. Researchers have shown that the defining parameters of the critical state line (CSL) can be obtained by performing drained and undrained tests on samples with different initial densities. This work aims to verify the drained and undrained behavior of aeolian sand from Natal, Brazil, based on critical state soil mechanics. Drained and undrained tests were performed on samples with initial void ratios equal to 0.7 and 0.8, which correspond to loose and medium-dense relative densities, respectively. Samples with both void ratios were subjected to confining stresses equal to 50, 100, 200 and 300 kPa. The results show that the critical state line can be defined from the drained and undrained tests performed on samples with loose and medium-dense initial relative densities. The parameters from the critical state theory were obtained using projections on the planes  $p' - q$  and  $\ln p' - v$ . The critical state friction angle is equal to  $31.5^\circ$ , and it is compatible with clean and uniformly graded sands with angular to subangular features and composed mostly of quartz. The obtained  $M$ ,  $\Gamma$  and  $\lambda$  values are equal to 1.26, 1.863 and 0.03, respectively. The obtained parameters will be used in analyses and numerical simulations of the geotechnical structures built on aeolian dune deposits from the city of Natal, Brazil.

**Keywords:** critical friction angle, critical state, dune sand, loose sand, steady state, triaxial test.

## 1. Introduction

Critical state theory has been the basis for the formulation of constitutive models capable of predicting the behavior of soils subjected to many loading conditions. The critical state is defined as the state eventually reached by the soil during shearing when strength variations and volume variations (in drained cases) or pore-pressure variations (in undrained cases) cease.

The critical state theory was based on tests performed on normal and overconsolidated clays. The mathematical formulations and the parameters from the theory were obtained from the projection of the critical state line plotted on  $q - p'$  and  $v - p'$  planes. It has been found that this model could also be used on sands. Understanding which elements affect the critical state line in sand is the subject of many studies (Sladen & Handford, 1987; Chu and Lo, 1993; Riemer & Seed, 1997; Murthy *et al.*, 2007; Li *et al.*, 2013).

Test results have become essential to the formulation and refinement of constitutive models for sands. The latest research explores the effects of fines content, initial fabric, and grain size distribution on the behavior of the critical state lines and their projections (Li & Dafalias, 2012; Gao *et al.*, 2013; Rahman & Lo, 2014; Wei & Yang, 2019; Woo

*et al.*, 2017; Yang & Luo, 2018). The initial state and drained conditions were not found to affect the positioning of the critical state line (Been *et al.*, 1991; Verdugo & Ishihara, 1996).

Sands from different regions around the world have been studied and continue to be studied under the critical state soil mechanics framework. Some urban areas from the city of Natal were positioned upon dunes, which are aeolian coastal deposits, consisting of unconsolidated or partially consolidated materials, and mostly made of quartz that is fine to medium in size.

Understanding the geotechnical behavior of these materials and obtaining their critical state parameters is required to perform numerical analyses of the geotechnical structures built on the dune fields from the city of Natal, Brazil, in addition to providing data that can be used in the calibration or refinement of constitutive models of sands with similar features. Furthermore, available research on aeolian sands is still scarce.

The present work aims to investigate the behavior of aeolian sand from the city of Natal, the capital of the State of Rio Grande do Norte in Brazil. Drained and undrained triaxial tests were performed on loose and medium-dense specimens.

---

Paulo Leite de Souza Junior, M.Sc., Graduate Student, Programa de Pós-Graduação em Engenharia Civil, Universidade Federal do Rio Grande do Norte, RN, Brazil. e-mail: pauloleitesjunior@yahoo.com.br.

Olavo Francisco dos Santos Junior, D.Sc., Full Professor, Programa de Pós-Graduação em Engenharia Civil, Universidade Federal do Rio Grande do Norte, Natal, RN, Brazil. e-mail: olavo.santos@ufrn.edu.br.

Tahyara Barbalho Fontoura, M.Sc., Assistant Professor, Instituto Federal do Rio Grande do Norte. São Paulo do Potengi, RN, Brazil. e-mail: tahyara.barbalho@ifrn.edu.br. Osvaldo de Freitas Neto, D.Sc., Associate Professor, Programa de Pós-Graduação em Engenharia Civil, Universidade Federal do Rio Grande do Norte, Natal, RN, Brazil. e-mail: osvaldocivil@ufrn.edu.br.

Submitted on June 5, 2019; Final Acceptance on March 11, 2020; Discussion open until September 30, 2020.

DOI: 10.28927/SR.432263

## 2. Materials and Methods

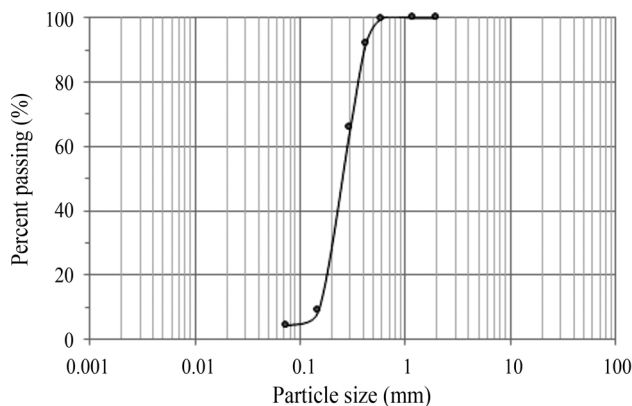
The data discussed in the present work were obtained from triaxial tests performed on sand collected in the main campus of the Federal University of Rio Grande do Norte.

Figure 1 shows the grain size distribution of the soil obtained by sieving. Grading is uniform, and approximately 70 % of the grains are considered to be medium sand.

The soil was classified as poorly graded sand (SP) according to the Unified Soil Classification System, with a fines content below 5 %. The soil grains were angular to subangular. The physical parameters of the Natal dune sand were obtained by Fontoura (2015) and are presented in Table 1.

Specimens were prepared by tamping moist sand in four layers into a metallic split mold 100 mm in height and 50 mm in diameter. The soil water content was 6 %. The specimens were compacted to reach two conditions: (1) the maximum void ratio, corresponding to the loosest density state; and (2) a relative density of 47 %, corresponding to a medium-dense state. Each specimen was tested under effective confining stresses of 50, 100, 200 and 300 kPa in both drained and undrained conditions, totaling 16 tests.

The removal of the metallic mold after the preparation of the specimens was the main difficulty in the study of sand, especially in the softest state. The tests performed by Fontoura (2015) showed that a moisture content of 6 % was sufficient to give the soil an “apparent cohesion” sufficient for modeling and demolding the specimens. Nevertheless, cases of specimen disaggregation occurred during demolding, requiring the specimen assembly procedure to be repeated in the triaxial chamber. Specimens were subjected to percolation, and increases in back pressure were applied to ensure saturation. Back pressure stages were applied at



**Figure 1** - Grain size distribution of the Natal dune sand.

**Table 1** - Physical parameters of the Natal dune sand.

| $D_{50}$ (mm) | $D_{10}$ (mm) | $C_u$ | $e_{min}$ | $e_{max}$ | $G_s$ |
|---------------|---------------|-------|-----------|-----------|-------|
| 0.25          | 0.15          | 1.86  | 0.590     | 0.800     | 2.660 |

50 kPa intervals until the B parameter reached 0.95 or higher. This value was usually reached after the application of 6 stages, corresponding to a total back pressure equal to 300 kPa.

After saturation, the specimens were isotropically consolidated until the desired confining stress was reached. During consolidation, the volume changes caused by increases in the confining pressure were measured. The void ratio was calculated from the sample size, the sand mass inserted into the mold and the water content used in the sample preparation (6 %). The void ratio after consolidation was calculated taking into account the sample volume variation that occurred at the time of consolidation. The initial (after molding) and final (after consolidation) void ratios are presented in Table 4.

Deformation was controlled during shearing, with a constant axial displacement rate equal to 0.20 mm/min in undrained tests and 0.06 mm/min in drained tests. These rates were obtained based on the ASTM standard. The strain rate is a function of the consolidation time. For the Natal sand, consolidation is virtually instantaneous with the application of stress. This would result in a very high strain rate. The values chosen were much lower than those indicated in the calculations. Thus, the equalization of pore pressures in the undrained tests and the inhibition of pore pressures in the drained tests were ensured.

## 3. Results and Discussion

### 3.1. Stress-strain curves

The results from drained tests with loose and medium-dense sand specimens are shown in Figs. 2 and 3, respectively.

In tests on the loose sand (Fig. 2), the deviatoric stress increases with strain and reaches a maximum value after 15 % of axial deformation. After that, the deviatoric stress remains constant. This is also evident in the  $q'/p'$  vs. axial strain curves. Regarding volumetric behavior, compressive volumetric strains were observed for all confining stresses. It is believed that volumetric compression tends to reach a constant value in all cases after reaching a strain equal to 20 %. The curves representing  $q - p'$  ratios against strain virtually overlap and reach a constant value at the end of the tests.

In tests with medium-dense specimens (Fig. 3), deviatoric stress reaches a maximum value after small strains and stays constant until the end of testing. Regarding volumetric behavior, tests with initial confining stress equal to 50 kPa and 100 kPa exhibit an initial compression followed by a volumetric expansion until the end of testing. Volume changes in the test with confining pressure equal to 200 kPa behave like those in the previous conditions but are less significant, and its curve is closer to the axis of zero volume variation. The curve related to the 300 kPa confining pressure shows compression at the beginning of testing, which

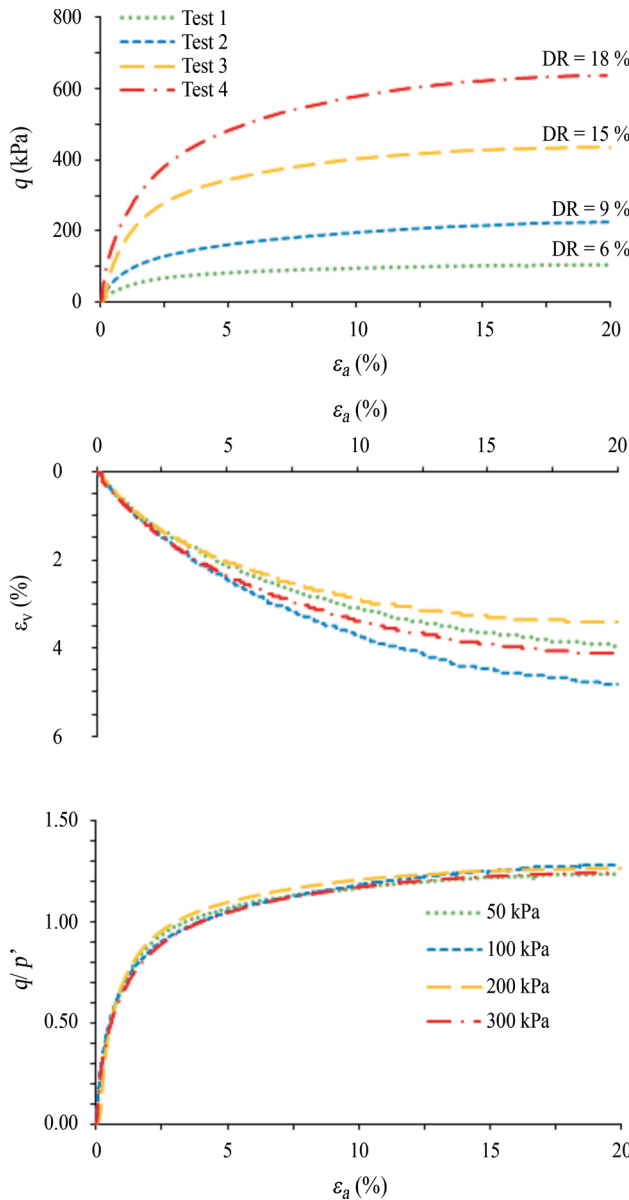


Figure 2 - Drained tests on loose sand.

is kept constant with strain. A slight expansion trend can be observed near the end of testing. Curves showing  $q - p'$  ratios seemingly reach a constant value at the end of the test.

Figures 4 and 5 show the undrained behavior of loose and medium-dense specimens.

Loose sand specimens under undrained conditions exhibit a deviatoric peak stress under small strains (Fig. 4). After the peak, a small decrease in strength occurs. This behavior can be observed for all confining stresses. Pore pressure changes are positive in all tests. The pore pressure increases as the confining stress increases. Curves with the ratio between stresses ( $q'/p'$ ) overlap and reach similar values at the end of testing. The maximum value of  $q'/p'$  reached in undrained tests was 1.20. These values are lower than those obtained in drained tests (1.28).

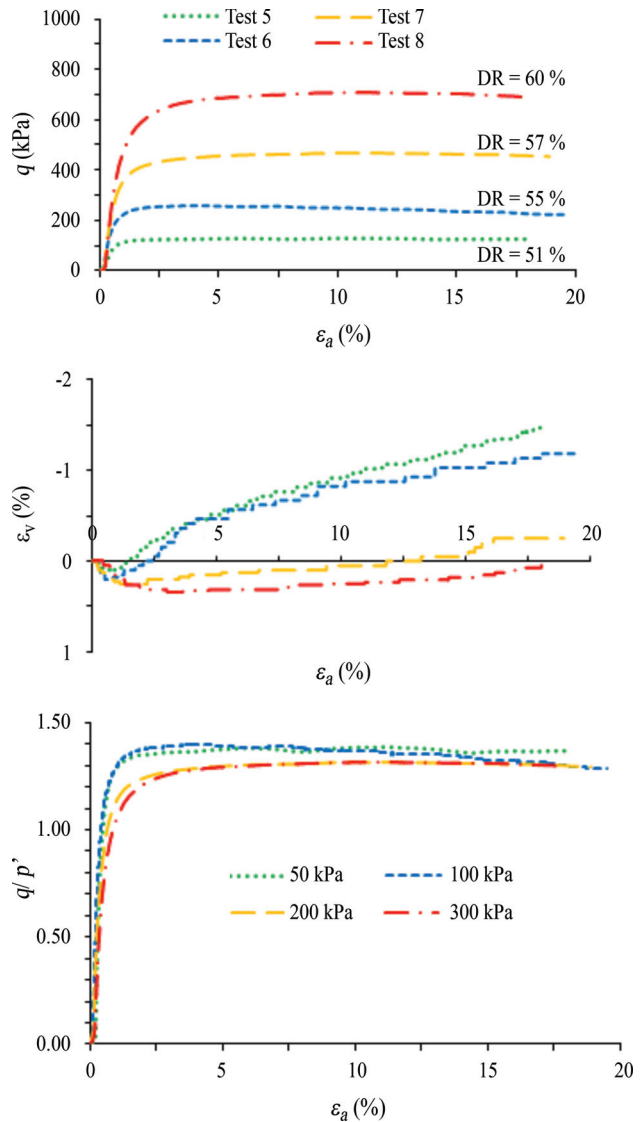


Figure 3 - Drained tests on medium-dense sand.

In tests with medium-dense sand, hardening behavior occurs during all initial confining stresses. The strength continues to increase even after the axial strain reaches 20%. Porewater pressure changes are positive at small axial strains and start decreasing and becoming negative at the end of the tests. All curves representing  $q/p'$  ratios virtually overlap, reaching a maximum value at small strains and staying constant until the end of the test.

### 3.2. Critical state line

Figure 6 shows the projections from the CSL in the  $q - p'$  plane using the final points obtained from the tests. The value of  $M$  is equal to 1.26, which corresponds to a critical state friction angle equal to  $31.5^\circ$ .

A literature review shows a recurrent discussion on the similarity between the critical state and steady state, as well as the uniqueness of the critical state line (or steady

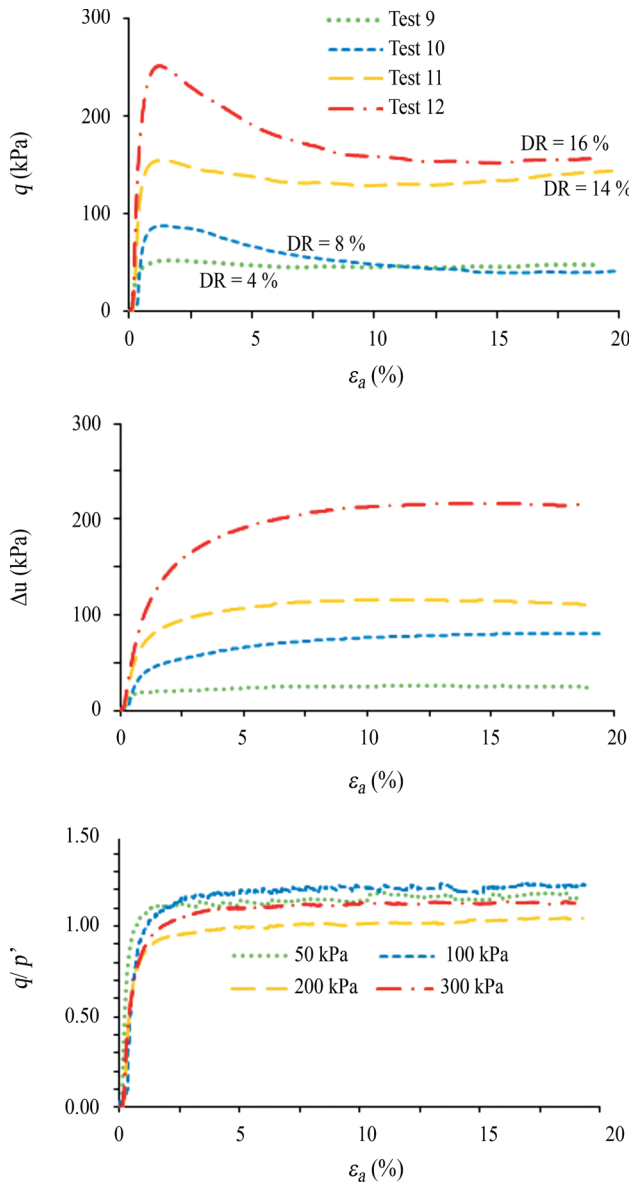


**Figure 4** - Undrained tests on loose sand.

state line). In this paper, it is assumed that the critical state and steady state are equivalent and that there is a single critical state line, since research has shown evidence that supports this idea (Mooney *et al.*, 1988; Been *et al.*, 1991; Kang *et al.*, 2019).

Figure 7 shows the curves obtained in the  $v - p'$  plane. Only one of the undrained tests in loose sand was used in this plot. The data from the other tests appear scattered when plotted on these planes, possibly because volume changes during the saturation process could not be reliably measured.

After analyzing the data from the drained and undrained tests with aeolian sand from Natal under different initial density conditions, the parameters from the critical state theory were obtained and are shown in Table 2.

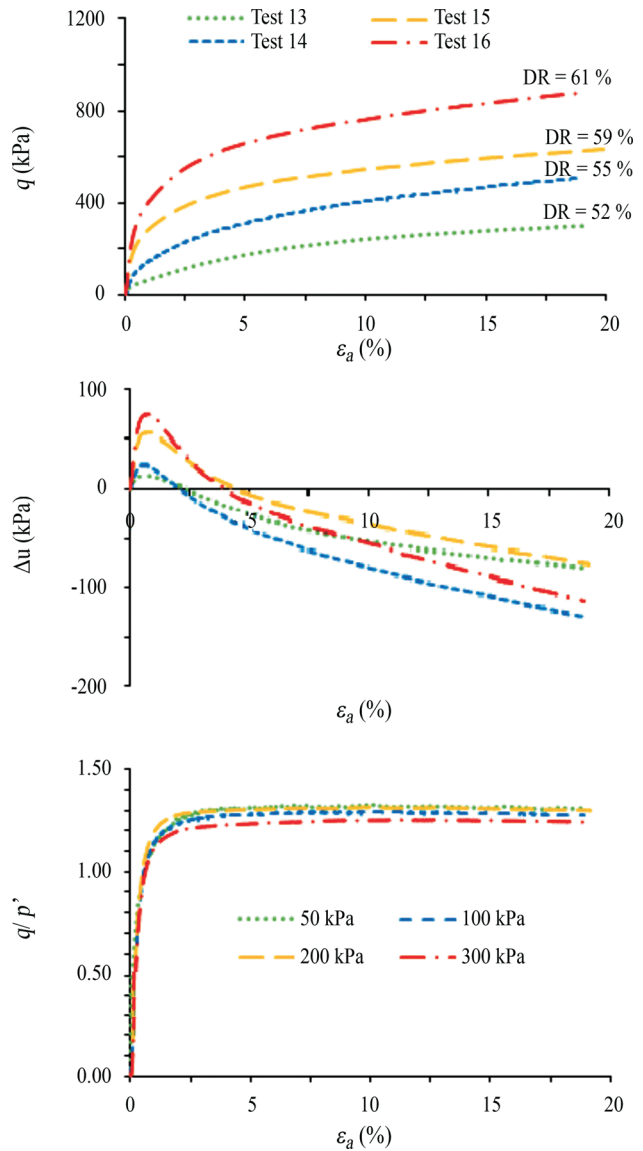


**Figure 5** - Undrained tests on medium-dense sand.

### 3.3. Critical state parameters of aeolian sand from Natal, Brazil

The results are compatible with those presented in the literature related to clean, uniformly graded quartz sands, as shown in Table 3.

All sands shown in Table 3 are characterized by grains with angular to subangular shapes. The Ottawa sand is the exception because it is composed of rounded grains, which may help explain its lower critical state angle value when compared to the critical state angle values of the other samples.

### 3.4. Stress paths

Figure 8 shows the stress paths from the tests with loose and medium-dense sands plotted on  $p - q'$  diagrams. The stress paths from the undrained tests in loose speci-

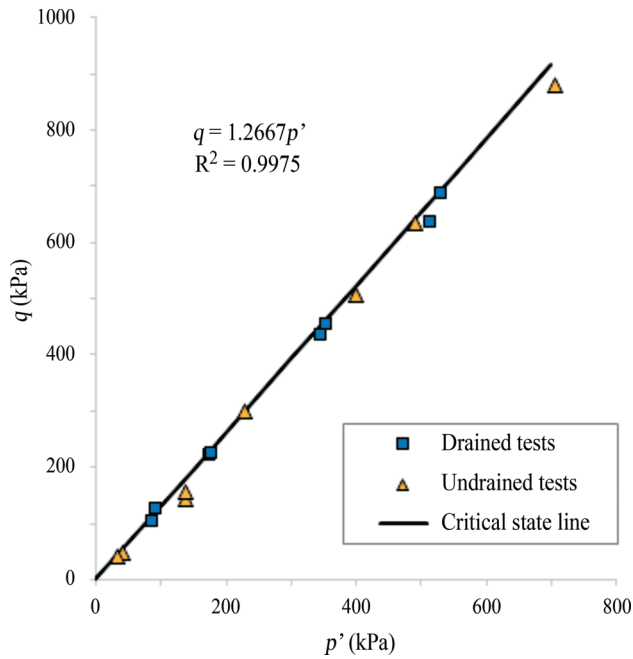


Figure 6 - Critical state line in the  $q - p'$  plane.

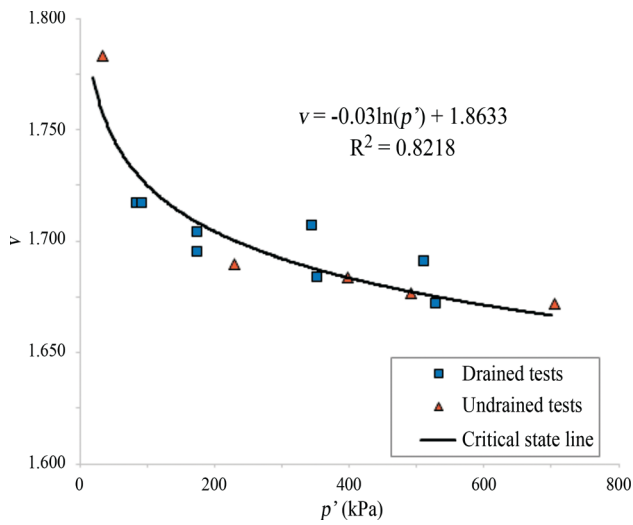


Figure 7 - Critical state line in the  $v - p'$  plane.

Table 2 - Critical state parameters of the Natal dune sand.

| M    | $\phi_{cs}$ (°) | $\Gamma$ | $\lambda$ |
|------|-----------------|----------|-----------|
| 1.26 | 31.5            | 1.863    | 0.03      |

Table 3 - Critical state parameters of the sands.

| Sand    | M    | $\phi_{cs}$ (°) | $\Gamma^*$ | $\lambda$ | Reference                        |
|---------|------|-----------------|------------|-----------|----------------------------------|
| Toyoura | 1.28 | 31.8            | 0.934      | 0.019     | (Verdugo & Ishihara, 1996)       |
| Ottawa  | 1.20 | 30.2            | 0.780      | 0.081     | (Murthy <i>et al.</i> , 2007)    |
| Coimbra | 1.29 | 32.0            | 0.976      | 0.04      | (Abreu, 2012)                    |
| Hostun  | 1.26 | 31.5            | 1.00**     | 0.07      | (Azeiteiro <i>et al.</i> , 2017) |

Note: \*Obtained in the  $e - p'$  plane. \*\* Adopted as being equal to  $e_{max}$ .

Table 4 - State parameters of all tests.

| Test | Drainage condition | Confining pressure | $e_0$ | $e_c$ | $\psi$ |
|------|--------------------|--------------------|-------|-------|--------|
| 1    | Drained            | 50                 | 0.8   | 0.788 | 0.042  |
| 2    |                    | 100                | 0.8   | 0.782 | 0.057  |
| 3    |                    | 200                | 0.8   | 0.768 | 0.064  |
| 4    |                    | 300                | 0.8   | 0.763 | 0.071  |
| 5    | Drained            | 50                 | 0.7   | 0.692 | -0.054 |
| 6    |                    | 100                | 0.7   | 0.684 | -0.041 |
| 7    |                    | 200                | 0.7   | 0.680 | -0.024 |
| 8    |                    | 300                | 0.7   | 0.673 | -0.019 |
| 9    | Undrained          | 50                 | 0.8   | 0.791 | 0.045  |
| 10   |                    | 100                | 0.8   | 0.783 | 0.058  |
| 11   |                    | 200                | 0.8   | 0.771 | 0.067  |
| 12   |                    | 300                | 0.8   | 0.766 | 0.074  |
| 13   | Undrained          | 50                 | 0.7   | 0.690 | -0.056 |
| 14   |                    | 100                | 0.7   | 0.684 | -0.041 |
| 15   |                    | 200                | 0.7   | 0.677 | -0.027 |
| 16   |                    | 300                | 0.7   | 0.672 | -0.020 |

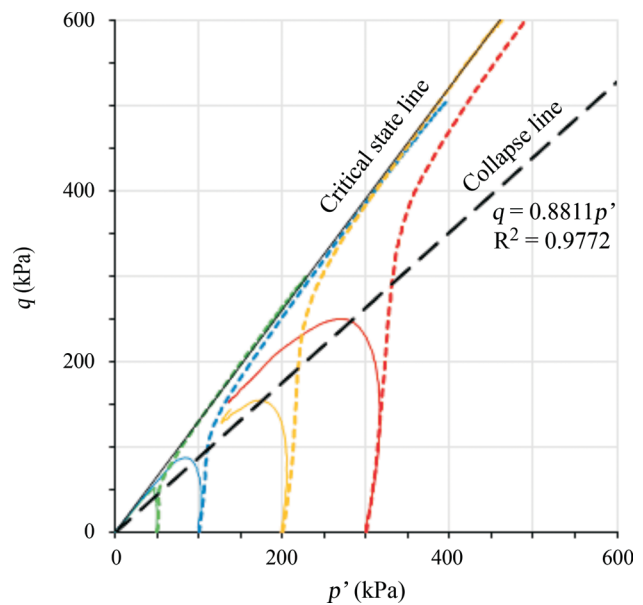
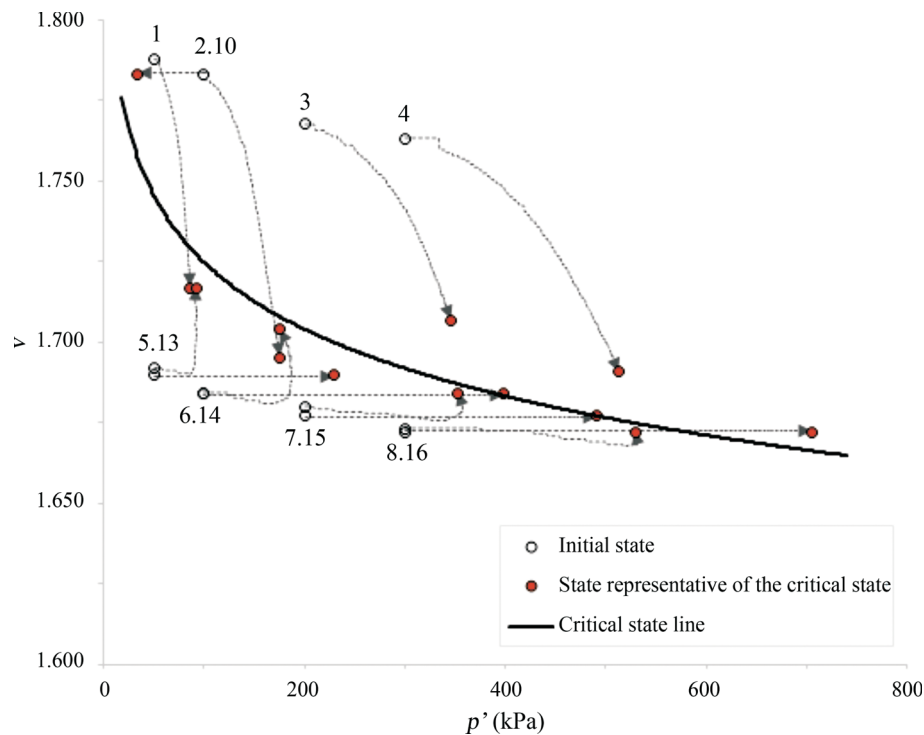


Figure 8 - Undrained stress paths for shear plotted on  $q - p'$  diagrams for loose and medium dense sand.



**Figure 9** - Drained and undrained paths in the  $v - p'$  plane.

mens are located to the left of the paths from the drained tests because positive porewater pressure was generated during shearing. This behavior is associated with the liquefaction phenomenon during static loading. A single liquefaction (or collapse) line is also presented in Fig. 8.

In the drained tests, the compressive behavior of loose sands can be observed in all confining stresses. The paths from medium dense sands exhibit dilation and compression behaviors. Paths from tests with confining pressures equal to 200 kPa and 300 kPa show compressive behavior, with slight dilation at the end of the test, and are presented as near horizontal lines. This finding suggests that shearing occurred in a state that was close to the critical state, as implied by the stress-strain and volume-strain plots.

In the undrained tests using medium-dense samples, the paths move to the right until they reach the critical state line. This behavior is typical of points located below the critical state line, under which negative porewater pressure occurs. In loose specimens, initial points are located above the critical state line; positive porewater pressures appear during shearing, producing a decrease in the effective average stress and causing the paths to move to the left toward the critical state line.

The paths from tests using confining pressure equal to 300 kPa show a peculiar behavior. In drained tests, only compressive behavior was observed. It was expected that its undrained counterpart would exhibit positive backpressure changes, which did not occur. Despite this behavior, it is possible to observe in Fig. 9 that the undrained path

would necessarily move toward the critical state line; therefore, the undrained path would have to exhibit negative porewater pressure, as actually observed in the tests.

Both paths overlap during the beginning of the tests and tend to diverge at the end of the tests. This dilation trend in the drained test is associated with the difficulties in representing the actual behavior of sands due to the high level of deformation in the specimens.

#### 4. Conclusions

The drained and undrained behavior of the aeolian sand from Natal, Brazil, has been studied through triaxial tests using different confining stresses and void ratios. The test results were analyzed in the critical state framework.

Specimens with an initial void ratio equal to 0.8 were located above the critical state line and exhibited compressive behavior; moreover, medium-dense specimens showed either dilation or compression, depending on the confining stress.

Specimens prepared with medium-dense sand and subjected to a confining stress equal to 300 kPa only exhibited compressive behavior.

The critical state line was defined from drained and undrained tests with loose and medium-dense specimens for an average confining stress level of almost 700 kPa.

Stress paths from the drained and undrained tests on loose and medium-dense specimens apparently converged to the critical state line, which validates the results presented.

The critical state theory parameters were obtained from projections on  $p'$  -  $q$  and  $v$  -  $\ln p'$  diagrams. The results obtained for aeolian sand are compatible with the values found in the literature when compared to sands of alluvial and marine origin with similar physical properties.

The critical state friction angle is equal to  $31.5^\circ$ , and it is compatible with clean, uniformly graded sands with angular to subangular shapes that are composed mostly of quartz.

The results from this research can be used as a reliable source of data for the calibration of constitutive models based on critical state theory; in addition, they can be used for numerical analyses involving the mechanical behavior of the aeolian Natal sand, including its susceptibility to liquefaction.

## Acknowledgments

The authors acknowledge the Coordination for the Improvement of Higher Education (CAPES) and the National Council for Scientific and Technological Development (CNPq) for their financial support.

## References

- Abreu, E.J.A. (2012). Study of Liquefaction Conditions of Coimbra Sand in Static and Cyclic Triaxial. Master Thesis, Department of Civil Engineering, University of Porto, Porto, 119 p. (In Portuguese).
- Azeiteiro, R.J.N.; Coelho, P.A.L.; Taborda, D.M.G. & Grazina, J.C.D. (2017). Critical state-based interpretation of the monotonic behavior of Hostun sand. *Journal of Geotechnical and Geoenvironmental Engineering*, 143(5):040170041-0401700414. [https://doi.org/10.1061/\(ASCE\)GT.1943-5606.0001659](https://doi.org/10.1061/(ASCE)GT.1943-5606.0001659)
- Been, K.; Jefferies, M.G. & Hachey, J. (1991). The critical state of sands. *Géotechnique*, 41(3):365-381. <https://doi.org/10.1680/geot.1991.41.3.365>
- Chu, J.; & Lo, S.C.R. (1993). On the measurement of critical state parameter of dense granular soils. *Geotechnical Testing Journal*, 16(1):27-35. [https://doi.org/10.1061/\(ASCE\)1090-0241\(2006\)132:5\(591\)](https://doi.org/10.1061/(ASCE)1090-0241(2006)132:5(591))
- Fontoura, T.B. (2015). Stress-Strain Behavior and Shear Strength of Artificially Cemented Dune Sand. Master Thesis, Postgraduate Program in Civil Engineering, Federal University of Rio Grande do Norte, Natal, 168 p. (In Portuguese).
- Gao, Z.; Zhao, J.; Li, X.S. & Dafalias, Y.F. (2013). A critical state sand plasticity model accounting for fabric evolution. *International Journal for Numerical and Analytical Methods in Geomechanics*, 38(4):370-390. <https://doi.org/10.1002/nag.2211>
- Kang, X.; Xia, Z.; Chen, R.; Ge, L. & Liu, X. (2019). The critical state and steady state of sand: A literature review. *Marine Georesources & Geotechnology*, 37(9):1105-1118. <https://doi.org/10.1080/1064119X.2018.1534294>
- Li, X.S. & Dafalias, Y.F. (2012). Anisotropic critical state theory: Role of fabric. *Journal of Engineering Mechanics*, 138(3):263-275. [https://doi.org/10.1061/\(ASCE\)EM.1943-7889.0000324](https://doi.org/10.1061/(ASCE)EM.1943-7889.0000324)
- Li, G.; Ovalle, C.; Dano, C. & Hicher, P.Y. (2013). Influence of Grain Size Distribution on Critical State of Granular Materials. *Springer Series in Geomechanics and Geoengineering*, Berlin, pp. 207-210. [https://doi.org/10.1007/978-3-642-32814-5\\_25](https://doi.org/10.1007/978-3-642-32814-5_25)
- Mooney, M.A.; Finno, R.j. & Viggiani, M.G. (1988). A unique critical state for sand? *Journal of Geotechnical and Geoenvironmental Engineering*, 124(11):1100-1108. [https://doi.org/10.1061/\(ASCE\)1090-0241\(2000\)126:1\(97\)](https://doi.org/10.1061/(ASCE)1090-0241(2000)126:1(97))
- Murthy, T.G.; Loukidis, D.; Carraro, J.A.H.; Prezzi, M. & Salgado, R. (2007). Undrained monotonic response of clean and silty sands. *Géotechnique*, 57(3):273-288. <https://doi.org/10.1680/geot.2007.57.3.273>
- Rahman, M.M. & Lo, S. R. (2014). Undrained behavior of sand-fines mixtures and their state parameter. *Journal of Geotechnical and Geoenvironmental Engineering*, 140(7):040140361-0401403612. [https://doi.org/10.1061/\(ASCE\)GT.1943-5606.0001115](https://doi.org/10.1061/(ASCE)GT.1943-5606.0001115)
- Riemer, M.F. & Seed, R.B. (1997). Factors affecting apparent position of steady-state line. *Journal of Geotechnical and Geoenvironmental Engineering*, 123(3):281-288. [https://doi.org/10.1061/\(ASCE\)1090-0241\(1997\)123:3\(281\)](https://doi.org/10.1061/(ASCE)1090-0241(1997)123:3(281))
- Sladen, J.A. & Handford, G. (1987). A potential systematic error in laboratory testing of very loose sands. *Canadian Geotechnical Journal*, 24(1987):462-466. <https://doi.org/10.1139/t87-058>
- Verdugo, R. & Ishihara, K. (1996). The steady state of sandy soils. *Soils and Foundations*, 36(2):81-91. [https://doi.org/10.3208/sandf.36.2\\_81](https://doi.org/10.3208/sandf.36.2_81)
- Wei, X. & Yang, J. (2019). A critical state constitutive model for clean and silty sand. *Acta Geotechnica*, 14(2):1-17. <https://doi.org/10.1007/s11440-018-0675-0>
- Woo, S.I.; Seo, H. & Kim, J. (2017). Critical-state-based Mohr-Coulomb plasticity model for sands. *Computers and Geotechnics*, 92(1):179-185. <https://doi.org/10.1016/j.compgeo.2017.08.001>
- Yang, J. & Luo, X.D. (2018). The critical state friction angle of granular materials: Does it depend on grading? *Acta Geotechnica*, 13(3):535-547. <https://doi.org/10.1007/s11440-017-0581-x>

## List of Symbols

- $p'$ : mean effective stress  
 $q$ : deviatoric stress  
 $v$ : specific volume

$D_{50}$ : mean grain size

$D_{10}$ : effective grain size

$DR$ : relative density

$C_u$ : uniformity coefficient

$e_{\min}$ : minimum void ratio

$e_{\max}$ : maximum void ratio

$e_0$ : void ratio at molding

$e_c$ : void ratio after consolidation

$G_s$ : specific gravity

$\psi$ : state parameter

$M$ : slope of critical state line on  $q - p'$  plane

$\Gamma, \lambda$ : fitting parameters for the critical state line equation

$\phi_{cs}$ : friction angle at critical state

$\varepsilon_a$ : axial strain

$\varepsilon_v$ : volumetric strain

$\Delta u$ : pore water pressure variation

# Effects of Hydraulic Gradient Variation on the Structure and Strength of a Compacted Tropical Soil

W.G. Silva, H.N. Pitanga, T.O. Silva, S.L.S. Dias Neto, D.C. Lima, T.P. Trindade

**Abstract.** Tropical soils have been extensively studied to evaluate the technical feasibility of their application in hydraulic earthworks such as compacted clay barriers in landfills. In these earthworks, the water flow in the porous medium generates percolation forces that can promote structural changes in the soil, with possible deleterious repercussions on its mechanical and hydraulic properties. In this context and considering the geotechnical peculiarities of tropical soils, this research aimed to characterize the influence of the hydraulic gradient used in column percolation tests on the structure of a compacted tropical soil and, therefore, on its shear strength. Compacted test specimens were subjected to water percolation tests and then to direct shear tests. Thin sections were removed from the compacted layers for micromorphological analysis. The results showed that, statistically, at 5 % probability level, no significant variation in the overall mean shear strength and in the micromorphological features was found as a function of the applied hydraulic gradients. In general, the non-statistically significant change in soil structure also justifies the lack of significant variability on shear strength. The research highlights the importance of micromorphological analysis supported by statistics in understanding the structural aspects of compacted soils responsible for their engineering behaviors.

**Keywords:** compacted tropical soil, hydraulic gradient, micromorphological analysis, shear strength, statistical analysis.

## 1. Introduction

Brazilian standard NBR 8419 (ABNT, 1996) defines landfill as a method of final disposal of solid waste in the soil, which must operate using engineering principles in such a way as to confine the solid waste in the smallest possible volume without causing damage or threats to health, safety, and the environment. As a result of this definition and in order to classify a solid waste disposal site as a landfill, Vertematti (2015) pointed out that it must have waterproofing devices at both the base and the top, intermediate layers for coverage, subsurface drainage, internal drainage of gases and leachate, and surface water drainage.

The present research focused mainly on studying engineering properties of hydraulic barriers for the composition of landfill bases, which have been the object of numerous studies aimed at characterizing their most relevant properties, considering the appropriate use and their good functional performance in such geoenvironmental works (Daniel & Wu, 1993; Benson *et al.*, 1994).

Tropical soils have been extensively studied to evaluate the technical feasibility of their application in such constructions, mainly considering the geotechnical peculiarities of these materials compared to the soils of temperate regions. According to Wesley (1990) and Benatti *et al.* (2013), residual soils can be misleadingly evaluated as

problematic soils just because some of their behavioral aspects do not conform to those of typical sedimentary soils considered suitable for engineering purposes.

Considering the potential of tropical soils to be applied in hydraulic barriers of landfills, there are the examples of studies by Ola (1980), Galvão *et al.* (2004), Taha & Kabir (2005), Osinubi & Nwaiwu (2006), Frempong & Yanful (2008), Bello (2011), and Kundiri *et al.* (2016). In general, the primary concern of those studies is the influence of the following variables on the strength, rigidity, and permeability properties of these compacted soils destined for landfills: degree of saturation, moisture and compaction energy, soil structure, chemical composition, mineralogical composition, drying shrinkage potential, clay content and chemical stabilization.

From Classical Soil Mechanics, based on sedimentary soils formed in temperate regions, it is known that the velocity of percolation of a liquid in the soil can promote structural changes in the soil, with possible repercussions on its mechanical and hydraulic properties (Fox, 1996; Kaoser *et al.*, 2006; Ke & Takahashi, 2012, 2014; Al-Taie *et al.*, 2014).

Based on geotechnical peculiarities of the tropical soils, there is interest in evaluating the possible influence of the percolation rate used in column percolation tests on soil

---

Weiner Gustavo Silva, M.Sc., Assistant Professor, Centro de Ciências Exatas e Tecnológicas, Universidade Federal do Recôncavo da Bahia, Cruz das Almas, BA, Brazil. e-mail: weiner.ufrb@gmail.com.

Heraldo Nunes Pitanga, Ph.D., Associate Professor, Departamento de Engenharia Civil, Universidade Federal de Viçosa, Viçosa, MG, Brazil. e-mail: heraldo.pitanga@ufv.br.

Taciano Oliveira da Silva, D.Sc., Associate Professor, Departamento de Engenharia Civil, Universidade Federal de Viçosa, Viçosa, MG, Brazil. e-mail: taciano.silva@ufv.br.

Sérgio Leandro Scher Dias Neto, M.Sc., Departamento de Engenharia Civil, Universidade Federal de Viçosa, Viçosa, MG, Brazil. e-mail: sergio.scher.7@gmail.com.

Dario Cardoso de Lima, Ph.D., Full Professor, Departamento de Engenharia Civil, Universidade Federal de Viçosa, Viçosa, MG, Brazil. e-mail: dclima@ufv.br.

Tiago Pinto da Trindade, D.Sc., Process Coordinator, Companhia de Saneamento Ambiental do Distrito Federal, DF, Brazil. e-mail: tptrindade@gmail.com.

Submitted on August 7, 2019; Final Acceptance on May 26, 2020; Discussion open until September 30, 2020.

DOI: 10.28927/SR.432271

structure and, consequently, on soil engineering properties. Additionally, contributions from microscopic studies directed to the characterization of compacted tropical soils are welcome.

Studies on microscopic soil characterization have been carried out since the 1950s, gaining emphasis in the last three or four decades, and, over this time, techniques have been developed or improved to better characterize the structure and behavior of these materials. Among the methods applied to study the arrangement between individual particles and particle and pore clusters in natural or compacted soils, emphasis is given on the application of techniques of optical microscopy, electron microscopy, X-ray diffraction, mercury porosimetry and, more recently, computerized tomography (Mitchell & Soga, 2005; Romero & Simms, 2008).

In soil morphology studies, the use of the optical petrographic microscope is quite common. In optical microscopy, features such as fractured surfaces, silt-size particles or larger particles, aggregates of clay particles, preferential orientation of particles, homogeneity, pore size and distribution, and shearing zones can be observed (Bullock & Murphy, 1980).

According to Crispim *et al.* (2011), these studies mainly recognized three elements in the micromorphological description of soils: plasma, of colloidal size (about  $10^6$  to  $10^9$  m), representing the material that can be moved by mechanical actions or by the action of water in the soil; and skeleton, formed by grains larger than colloidal; and pores, corresponding to the voids present in the soil. In the micromorphological study, from the analysis of fine sections, the soil constituents are recognized, observing the size, shape, arrangement, and orientation of the aggregates and the voids that separate them, as well as the relative distribution of the plasma in relation to the skeleton grains (Fitzpatrick, 1993). Stoops (2003) presents other more detailed and in-depth aspects of the morphological and microstructural characterization of soils. For Brazilian tropical soils, there are studies by Schaefer (2001), Viana *et al.* (2004), Trindade (2006), and Crispim *et al.* (2011).

In this framework and considering the geotechnical peculiarities of tropical soils, the objective of the present study was to evaluate the influence of the hydraulic gradient variation on the structure of a compacted tropical residual soil and, consequently, on its mechanical properties, represented by the shear strength. Simultaneously, the research aimed to highlight the importance of micromorphological analysis supported by statistics in understanding the structural aspects of compacted soils responsible for their engineering behaviors.

## 2. Material

A soil classified geotechnically as gneiss mature residual and, pedologically, as Red-Yellow Latosol (RYL) with great expressiveness in the Brazilian territory, and es-

pecially in the Zona da Mata Norte of Minas Gerais, in the southeastern region of Brazil, was used throughout the study. Disturbed samples were collected in a borrow pit, located in the city of Viçosa, in the state of Minas Gerais, Brazil, at coordinates  $20^{\circ}45'35''$  S;  $42^{\circ}52'28''$  W.

The pH values of the soil, measured in water [pH  $H_2O$  (1:2.5) = 6.1] and in a solution of KCl 1 mol/L [pH KCl (1:2.5) = 5.96], allow to characterize it as slightly acidic. The cation exchange capacity is relatively low (CEC = 2.09 cmol<sub>c</sub>/kg) and compatible with the mineralogy of its clay fraction, which is predominantly composed of kaolinite and iron and aluminum oxides. Regarding the percentage base saturation (V %), the soil presented a value of 52.6 %. According to Brady and Weil (1999), soils from tropical and wet regions, in which silicate clays predominate, are acidic when V % is lower than 80 %. Therefore, the V % value is in line with the pH value determined and with the clay minerals present in the studied soil.

A specific study was directed to the qualitative and semiquantitative determination of the presence of chemical elements in the soil using the microanalysis technique. The energy-dispersive X-ray spectroscopy (EDS) spectrum presented in Fig. 1 shows that the soil is basically constituted by Al, Si, and Fe. The high amount of Fe found in the soil, a Red-Yellow Latosol, may be associated with the presence of goethite and the significant amounts of Al and Si probably related to the minerals kaolinite and quartz. The mineralogical analysis of soil samples allowed for the identification of the presence of quartz in the sand fraction (Fig. 2a), and of kaolinite, quartz, goethite, gibbsite, portlandite, and rankinite in the clay fraction (Fig. 2b).

The microstructure was characterized by an analysis of the secondary electron images obtained in Scanning Electron Microscope (SEM). Samples from soil compacted at the optimum conditions ( $w_{opt}$  and  $\gamma_{dmax}$ ) of the standard Proctor test were analyzed. It was observed (Fig. 3) that the volume of soil analyzed was composed predominantly of plasma (compared to the skeleton) that formed a continuous phase and, in some cases, was presented in the form of spherical micro-aggregates joined together. These micro-

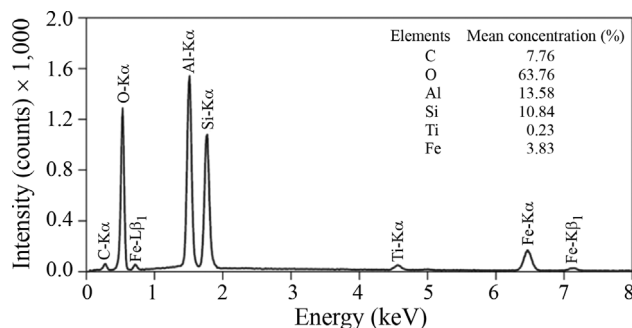


**Figure 1** - EDS (Energy-dispersive X-ray spectroscopy) spectrum and mean concentration of chemical elements determined for the studied soil.

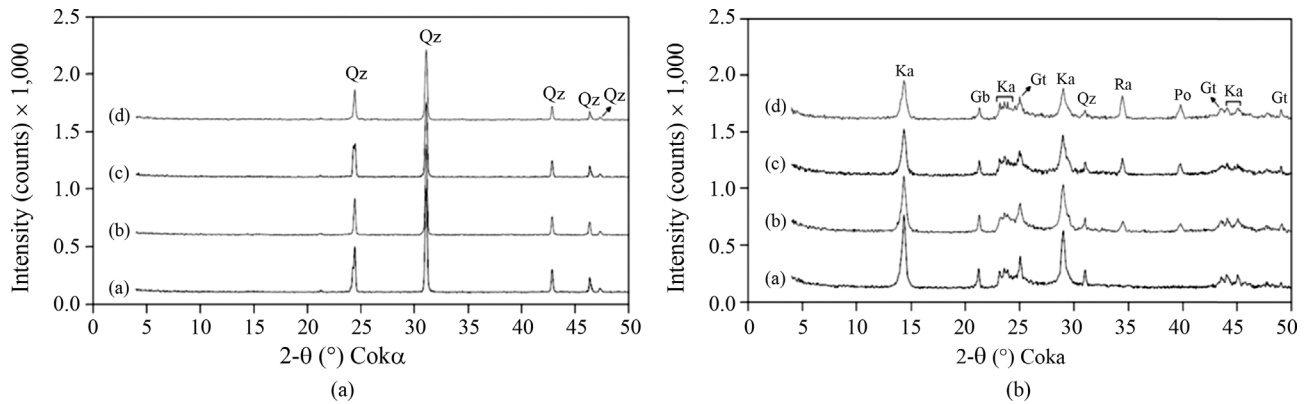


**Figure 2** - Data from XRD (X-ray diffraction) analyses performed on soil samples: (a) XRD patterns of  $\geq 53 \mu\text{m}$  fraction of soil: Qz = quartz [ $\text{SiO}_2$ ]; (b) XRD patterns of  $< 53 \mu\text{m}$  fraction of soil: Gb = gibbsite [ $\text{Al}(\text{OH})_3$ ], Gt = goethite [ $\alpha\text{-FeO}(\text{OH})$ ], Ka = kaolinite [ $\text{Al}_2\text{Si}_2\text{O}_5(\text{OH})_4$ ], Po = portlandite [ $\text{Ca}(\text{OH})_2$ ], Qz = quartz [ $\text{SiO}_2$ ] and Ra = rankinite [ $\text{Ca}_3\text{Si}_2\text{O}_7$ ].

aggregates were formed by small-size particles, randomly placed, formed by aggregations of kaolinite and gibbsite minerals wrapped and cemented by iron oxyhydroxides responsible for the stability of their arrangement.

### 3. Methods

The compaction tests were carried out with the standard Proctor effort ( $600 \text{ kN}\cdot\text{m}/\text{m}^3$ ), according to ABNT (2016), with limits for acceptance of soil samples related to the maximum dry unit weight of  $\pm 0.30 \text{ kN}/\text{m}^3$  and the optimum water content of  $\pm 0.5 \%$ . The soil samples were compacted dynamically into PVC cylinders in three layers, 12 cm high and 10 cm in diameter, so that after molding they could be used directly in the column percolation equipment, where they were subjected to upward percolation of deaerated and deionized water, in a room maintained at a constant temperature of  $21 \text{ }^\circ\text{C} \pm 1 \text{ }^\circ\text{C}$ , according to the guidelines in (ABNT, 2000) and (ABNT, 1995a).

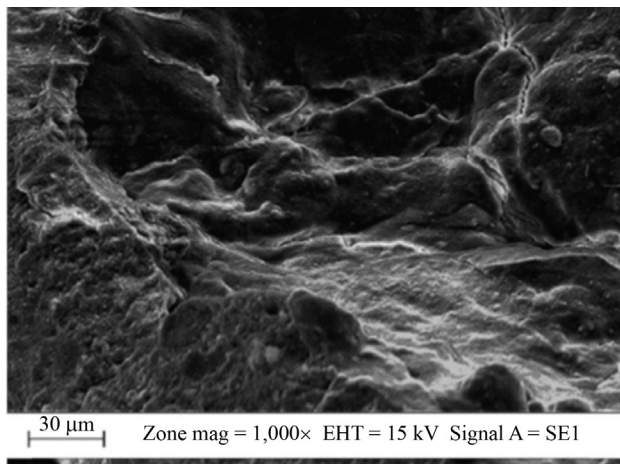


**Figure 3** - Samples compacted at the standard Proctor effort images obtained by secondary electron signals produced in Scanning Electron Microscope (SEM).

In column percolation, hydraulic gradients (HG) of 15, 66, 85, and 140 were applied until reaching constant flow in a set of four compacted cylindrical specimens for each HG. After column percolation test, for each hydraulic gradient, specimens were molded for direct shear test (three specimens) and micromorphological analysis (one specimen). Figure 4 shows a schematic sketch of extraction of soil samples for molding  $6 \text{ cm} \times 6 \text{ cm} \times 2.5 \text{ cm}$  specimens for direct shear test (ASTM, 2011).

After inundation with deaerated and deionized water for a period of two hours, aiming to eliminate the influence of the suction variable in the analysis, each soil specimen was consolidated and tested in the direct shear apparatus at the vertical stress of 100 kPa and the horizontal displacement velocity of  $0.15 \text{ mm}/\text{min}$ . to determine the mean shear strength of each specimen layer (three determinations were used to calculate the mean shear strength).

In the micromorphological analysis, the fourth specimen subjected to column percolation under constant hydraulic gradient was used to extract two thin sections, respectively, from the top and bottom compacted layers (Figs. 5a and 5b). From these thin sections, microscopic images were obtained to analyze the pattern and microstructural composition of the compacted material. A similar procedure was applied to a compacted soil test specimen not subjected to water percolation (hydraulic gradient

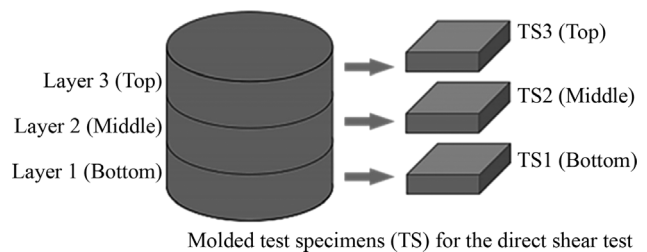


**Figure 4** - Schematic sketch of soil samples extraction of each specimen already tested in the column percolation test.

HG = 0), which served as a reference for structural comparison purposes. The protocol for preparation of the thin sections was adopted according to Crispim *et al.* (2011).

The photomicrographs obtained under an optical microscope were edited using Paint.NET image editing software (Brewster, 2014). Quantitative measurements of pores, plasma and grains were performed using ImageJ software (Schneider *et al.*, 2012). In the analysis of the images, the micromorphological features were separated into three groups (Fig.5c), namely: quartz grains and opaque minerals, here called quartz grains (Grains Qz), corresponding to the soil skeleton; slits and vesicles, corresponding to the soil pores; and plasma. For the top and bottom thin sections, the mean percentages of the identified features were obtained from five microscope images.

A Complete Randomized Design (CRD) was used in the statistical analysis of the direct shear tests and micromorphological study data encompassing analysis of variance (ANOVA) at 5 % probability, as follows:

- (1) Results of the direct shear tests: differences between the means of the shear strength of each layer of the test specimens for each hydraulic gradient; differences between the means of the shear strength of each layer of the test specimens for all hydraulic gradients; and differences between the general means of shear strength determined for each hydraulic gradient; and
- (2) Results of the micromorphological study: differences between the means of the micromorphological features of the top and bottom layers of the test specimen for the same hydraulic gradient; and differences between the means of the micromorphological features of each layer group for all hydraulic gradients.

Whenever significant differences were found, the means were compared by Tukey’s test, at 5 % probability.

## 4. Results and Discussion

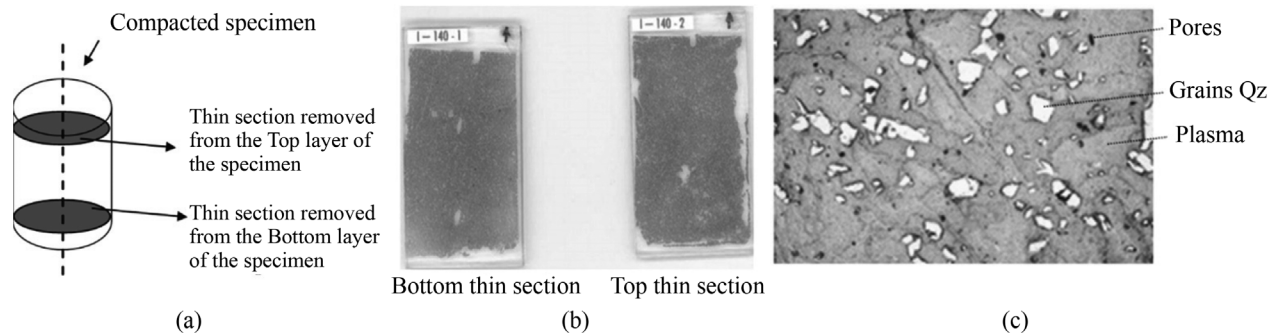
### 4.1. Geotechnical parameters of test specimens

Table 1 lists the results of the soil geotechnical characterization, including Atterberg limits [liquid limit (LL), plastic limit (PL)] and plasticity index (PI), specific gravity of soil solids ( $\gamma_s$ ), particle-size distribution according to the scale adopted by ABNT (1995b), and optimum compaction parameters from the standard Proctor compaction procedure.

Table 2 presents the results of the post-molding mean geotechnical parameters of twelve test specimens subjected to the column percolation tests. The respective standard deviation values attest to the relative uniformity of the specimens prepared for the tests. The magnitude of their mean degree of saturation (DS) indicates that, before the column

**Table 2** - Post-molding mean geotechnical parameters of all specimens used in the column percolation tests.

| Geotechnical parameters of the test specimens | Mean   | Standard deviation |
|---|--------|--------------------|
| Water content (%)                             | 31.35  | 0.365              |
| Dry unit weight (kN/m <sup>3</sup> )          | 14.05  | 0.061              |
| Void ratio                                    | 0.941  | 0.009              |
| Porosity (%)                                  | 48.47  | 0.224              |
| Degree of compaction (%)                      | 103.03 | 0.477              |
| Degree of saturation (%)                      | 92.83  | 1.146              |



**Figure 5** - Micromorphological analysis: (a) schematic diagram indicating the region of removal of the thin soil sections; (b) sections to be analyzed; (c) micromorphological aspects of soil subjected to quantification in ImageJ software.

**Table 1** - Results of the geotechnical characterization of the RYL soil sample.

| Atterberg limits and plasticity index |        |        | $\gamma_s$ (kN.m <sup>-3</sup> ) | Particle size distribution |          |          | $W_{opt}$ (%) | $\gamma_{dmax}$ (kN.m <sup>-3</sup> ) |
|---------------------------------------|--------|--------|----------------------------------|----------------------------|----------|----------|---------------|---------------------------------------|
| LL (%)                                | PL (%) | PI (%) |                                  | Sand (%)                   | Silt (%) | Clay (%) |               |                                       |
| 82                                    | 46     | 36     | 27.27                            | 23                         | 10       | 67       | 31.37         | 13.54                                 |

Note: PI (%) = LL (%) - PL (%).

percolation tests, they were physically close to the saturated condition (DS = 100 %), which was probably reached during the tests, when the constancy condition of the water flow was reached.

#### 4.2. Direct shear tests

Figure 6 presents the overall mean of all shear strength measurements obtained and the means per layer of the specimens for each hydraulic gradient.

From the geotechnical point of view, based on the results in Fig. 6, there is an upward trend for the mean shear strength from the bottom layer to the top layer of the test specimens, although of small magnitude, with values of the order of 6 kPa for the hydraulic gradient 15, and 7 kPa for the hydraulic gradient 66. However, for the hydraulic gradients 85 and 140, an opposite behavior is observed, noticing a decrease in the shear strength from the bottom to the top, of the order of 6 kPa and 13 kPa, respectively. Thus, there are two distinct responses in the mean shear strength values of the layers, respectively, for the hydraulic gradient sets 15-66 and 85-140. In addition, based on data from Figs. 6b and 6c, and for practical geotechnical engineering purposes:

- (1) There is a slight superiority, of the order from 8 kPa to 9 kPa, in the overall mean of the shear strength related to the hydraulic gradient 15 in comparison to the others, and there is no difference between the results obtained for the gradients 66, 85 and 140; and
- (2) There is significant variation in the means of shear strength of the top layer of the tested specimens between the hydraulic gradients 15 and 140, which is of the order of + 20 kPa; however, based on the results concerning the middle and the bottom of the specimens, there are minor variations between the referred hydraulic gradients, respectively, of the order of + 11 kPa and + 0.6 kPa.

On the other hand, at the 5 % probability level, the results of the statistical analyses evidence that:

- (1) There is no significant difference in the means of shear strength determined in the top, middle and bottom

layers of the tested specimens for each hydraulic gradient analyzed;

- (2) There is no significant variation in the means of the shear strength of each layer considering all hydraulic gradients tested; and
- (3) There is no significant contrast in the overall means of the shear strength of the tested specimens for the same hydraulic gradient.

#### 4.3. Micromorphological analysis

From Fig. 7, optical microscopy images show the relative distribution between skeleton and plasma, classified as porphyric according to Stoops (2003), with the distribution of larger particles in a soil matrix of much smaller particles.

From the micromorphological analysis, there is an almost complete loss of the packing pores in the compacted material, forming a structure with unconnected voids in the shape of stars, densified at the edges. Loss of most of the medium and large porosity occurs, forming an unconnected network of cracks and voids along the planes of intergranular adjustments, composing a new network of voids that do not favor infiltrability. Also, the structure resulting from the compaction of the smaller soil particles is composed predominantly of plasma when compared to the other identifiable features (Grains Qz and soil pores).

Regarding all hydraulic gradients tested and considering the bottom and top positions of the specimens tested, Figs. 8 and 9 show, respectively, the mean percentages of the areas of features Grains Qz, pores, and plasma together, and the same percentages for each of these features separately.

The data show that, regardless of the hydraulic gradient adopted in the column percolation tests, there were no relevant percentage changes, at the base and at the top of the test specimens, for the quartz grains, porosity and plasma, compared to the structure of the non-percolated specimens. This experimental evidence applies when comparing such structural aspects at the base and top for the same hydraulic gradient, or when considering all the hydraulic gra-

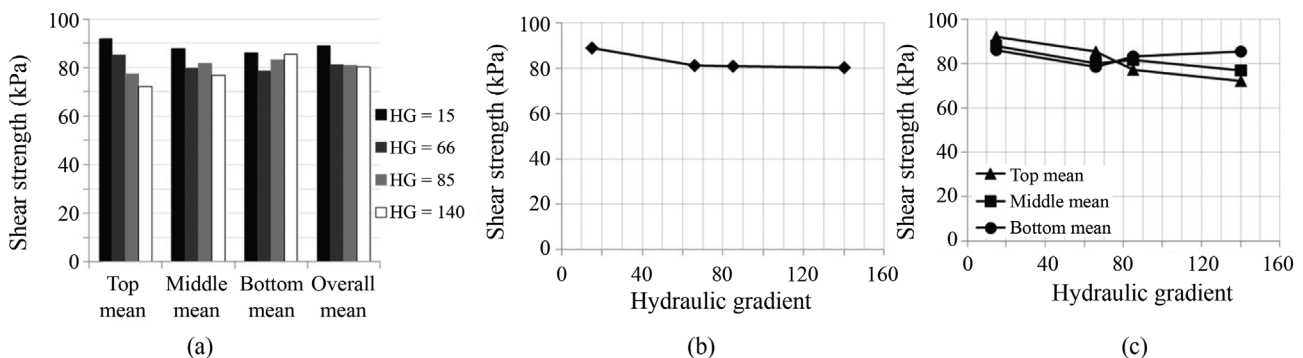


**Figure 6** - Results of the shear strength tests: (a) comparison between the overall mean and the means per layer considering the hydraulic gradients analyzed; (b) overall mean shear strength; (c) mean shear strength per layer.

dients considered in the study. Although there is a tendency of differentiation between the base and the top for the porosity (Figs. 9c and 9d), it is verified that this distinction oc-

curs in a percentage range that is effectively restricted and of low magnitude (minimum of 0.59 %, maximum of 1.68 %).

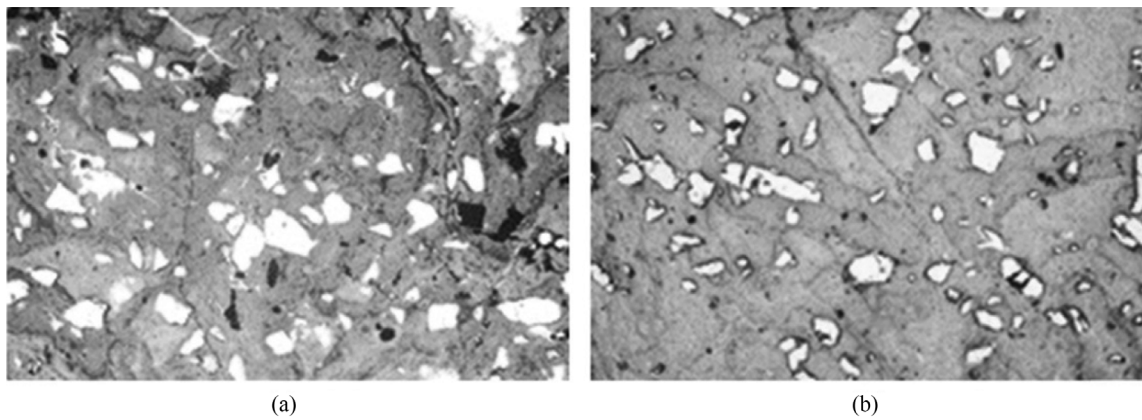


**Figure 7** - Samples of optical microscopy images of thin sections of the soil tested specimens: (a) top thin section; (b) bottom thin section.

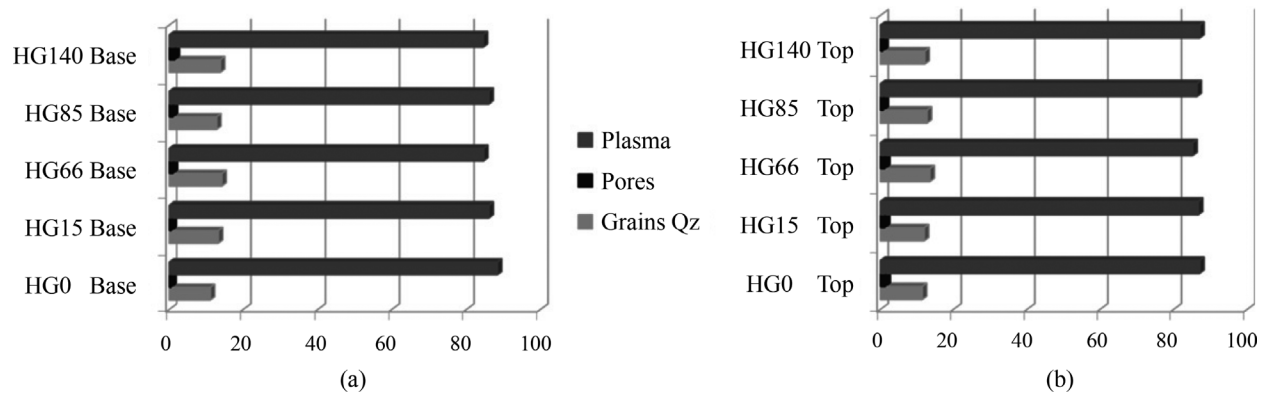


**Figure 8** - Joint graphical representation of the mean percentages of the areas of features Grains Qz, pores and plasma on the bottom and top positions of specimens, for all hydraulic gradients: (a) at the bottom of the specimens; (b) at the top of the specimens.

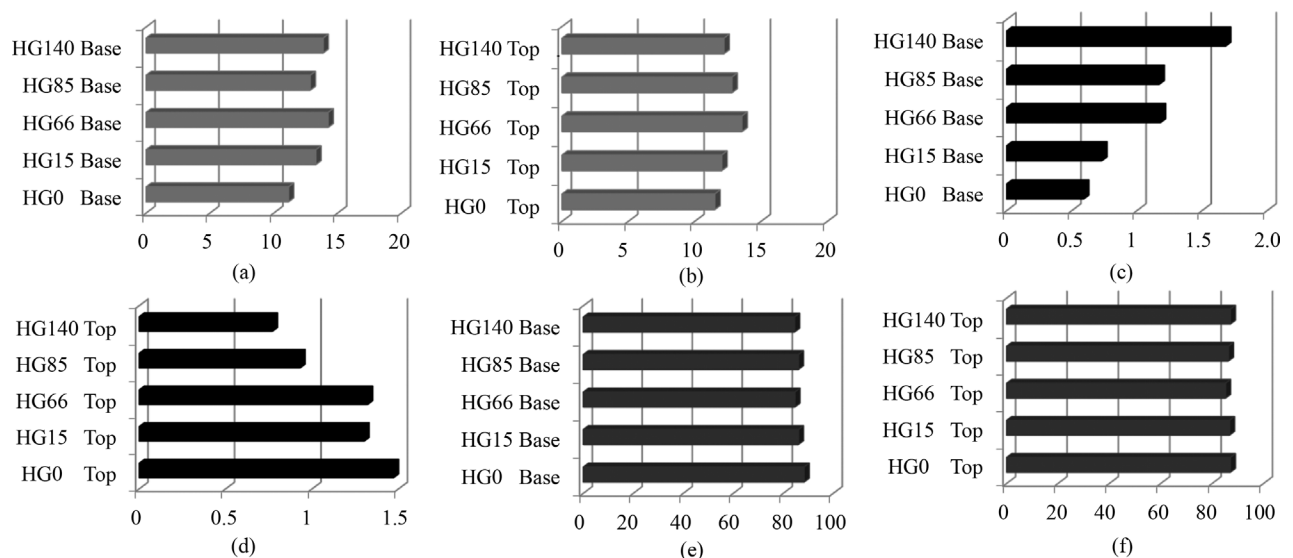


**Figure 9** - Separate graphic representations of the mean percentages of features Qz Grains, pores and plasma on the bottom and top positions of specimens, for all hydraulic gradients: (a) Qz Grains at the bottom (b) and the top; (c) Pores at the bottom and (d) the top; (e) Plasma at the bottom (e) and the top (f).

## 5. Conclusions

Based on the results obtained, for the particularities of the present study and the soil in the compacted state, it is concluded that: (1) under the geotechnical perspective, it is possible that there is a slight downward trend in the general mean of the shear strength with the elevation in the hydraulic gradient; (2) there is no significant variation in the shear strength means determined in the top, middle and bottom layers of the specimens, regarding the results of the direct shear tests, for each hydraulic gradient analyzed, no significant variation was observed between the shear strength means of each layer, considering all hydraulic gradients, and there was no significant difference between the overall shear strength means of the specimens with the variation in the hydraulic gradient; and (3) statistically, at the 5 % probability level, the results of the micromorphological analysis show that there is no significant variation in the micromorphological features of the porosity, quartz grains, and plasma as a function of the hydraulic gradient used in the tests. The soil structural stability under variations in the water percolation conditions suggests that the compacted tropical soil would offer good functional performance in hydraulic barriers or landfills. It is also assumed that the geotechnical peculiarities of the compacted soil are responsible for its structural stability. Special emphasis is given to micromorphological analysis supported by statistics in understanding the structural aspects of compacted soils responsible for their engineering behavior.

## Acknowledgments

The authors acknowledge the financial support by the Coordinating Agency for Advanced Training of Graduate Personnel (CAPES).

## References

- ABNT (1995a). Soil - Determination of the Coefficient of Permeability of Granular Soil by Constant-Head. Test Method. NBR 13292. Rio de Janeiro, Brazil, 8 p. (In Portuguese).
- ABNT (1995b). Rocks and Soils. Terminology. NBR 6502. Rio de Janeiro, Brazil, 18 p. (In Portuguese).
- ABNT (1996). Introduction of Projects for Sanitary Filling of Urban Solid Wastes. Procedure. NBR 8419. Rio de Janeiro, Brazil, 7 p. (In Portuguese).
- ABNT (2000). Soil - Determination of the Coefficient of Permeability of Clay Soils. NBR 14545. Rio de Janeiro, Brazil, 12 p. (In Portuguese).
- ABNT (2016). Soil - Compaction Test. NBR 7182. Rio de Janeiro, Brazil, 9 p. (In Portuguese).
- Al-Taie, L.; Pusch, R. & Knutsson, S. (2014). Hydraulic properties of smectite rich clay controlled by hydraulic gradients and filter types. *Applied Clay Science*, 87:73-80. DOI: 10.1016/j.clay.2013.11.027.
- ASTM (2011). Standard Test Method for Direct Shear Test of Soils under Consolidated Drained Conditions. D3080/D3080M-11. ASTM International, West Conshohocken, PA, USA, 9 p.
- Bello, A.A. (2011). Analysis of shear strength of compacted lateritic soils. *Pacific Journal of Science and Technology*, 12(1):425-433.
- Benson, C.H.; Zhai, H. & Wang, X. (1994). Estimating hydraulic conductivity of compacted clay liners. *Journal of Geotechnical Engineering*, 12(1):366-387. DOI: 10.1061/(ASCE)0733-9410(1994)120:2(366).
- Benatti, J.C.B.; Rodrigues, R.A. & Miguel, M.G. (2013). Aspects of mechanical behavior and modeling of a tropical unsaturated Soil. *Geotechnical and Geological Engineering*, 31(4):1569-1585. DOI: 10.1007/s10706-013-9682-y.
- Brewster, R. (2014). Paint.NET. Version 4.0. dotPDN LLC.
- Brady, N.C. & Weil, R.R. (1999). *The Nature and Property of Soils*. Prentice Hall, Upper Saddle River, 960 p.
- Bullock, P. & Murphy, C.P. (1980). Towards the quantification of soil structure. *Journal of Microscopy*, 120(3):317-328. DOI: 10.1111/j.1365-2818.1980.tb04151.x.
- Crispim, F.A.; Lima, D.C.; Schaefer, C.E.G.R.; Silva, C.H.C.; Carvalho, C.A.B.; Barbosa, P.S.A. & Brandão, E.H. (2011). The influence of laboratory compaction methods on soil structure: Mechanical and micromorphological analyses. *Soils and Rocks*, 34(1):91-98.
- Daniel, D.E. & Wu, Y.K. (1993). Compacted clay liners and covers for arid sites. *Journal of Geotechnical Engineering*, 199(2):223-237. DOI: 10.1061/(ASCE)0733-9410(1993)119:2(223).
- Fitzpatrick, E.A. (1993). *Soil Microscopy and Micromorphology*. John Wiley & Sons, New York, 304 p.
- Fox, P. (1996). Analysis of hydraulic gradient effects for laboratory hydraulic conductivity testing. *Geotechnical Testing Journal*, 19(2):181-190. DOI: 10.1520/GTJ10340J.
- Frempong, E.M. & Yanful, E.K. (2008). Interactions between three tropical soils and municipal solid waste landfill leachate. *Journal of Geotechnical and Geoenvironmental Engineering*, 134(3):379-396. DOI: 10.1061/(ASCE)1090-0241(2008)134:3(379).
- Galvão, T.C.B.; Elsharief, A. & Simões, G.F. (2004). Effects of hydrated lime on permeability and compressibility of two tropical residual soils. *Journal of Environmental Engineering*, 130(8):881-885. DOI: 10.1061/(ASCE)0733-9372(2004)130:8(881).
- Kaoser, S.; Barrington, S.; Elektorowicz, M. & Ayadat, T. (2006). The influence of hydraulic gradient and rate of erosion on hydraulic conductivity of sand-bentonite mixtures. *Soil and Sediment Contamination: An International Journal*, 15(5):481-496. DOI: 10.1080/15320380600847815.

- Ke, L. & Takahashi, A. (2012). Strength reduction of cohesionless soil due to internal erosion induced by one-dimensional upward seepage flow. *Soils and Foundations*, 52(4):698-711. DOI: 10.1016/j.sandf.2012.07.010.
- Ke, L. & Takahashi, A. (2014). Experimental investigations on suffusion characteristics and its mechanical consequences on saturated cohesionless soil. *Soils and Foundations*, 54(4):713-730. DOI: 10.1016/j.sandf.2014.06.024.
- Kundiri, A.M.; Muhammed, A.S. & Abah, G. (2016). Effect of compactive efforts on desiccation - Induced volumetric shrinkage strain of some compacted tropical soils. *Malaysian Journal of Civil Engineering*, 28(2):284-299.
- Mitchell, J.K. & Soga, K. (2005). *Fundamentals of Soil Behavior*. Wiley, Chichester, 577 p.
- Ola, S.A. (1980). Permeability of three compacted tropical soils. *Quarterly Journal of Engineering Geology and Hydrogeology*, 13(2):87-95. DOI: 10.1144/GSL.QJEG.1980.013.02.03.
- Osinubi, K.J. & Nwaiwu, C.M. (2006). Design of compacted lateritic soil liners and covers. *Journal of Geotechnical and Geoenvironmental Engineering*, 132(2):203-213. DOI: 10.1061/(ASCE)1090-0241(2006)132:2(203).
- Romero, E. & Simms, P.H. (2008). Microstructure investigation in unsaturated soils: A review with special attention to contribution of mercury intrusion porosimetry and environmental scanning electron microscopy. *Geotechnical and Geological Engineering*, 26(6):705-27. DOI: 10.1007/s10706-008-9204-5.
- Schaefer, C.E.R. (2001). Brazilian latosols and their B horizon microstructure as long-term biotic constructs. *Australian Journal of Soil Research*, 39(5):909-926. DOI: 10.1071/SR00093.
- Schneider, C.A.; Rasband, W.S. & Eliceiri, K.W. (2012). NIH Image to ImageJ: 25 years of image analysis. *Nature Methods*, 9(7):671-675. DOI: 10.1038/nmeth.2089.
- Stoops, G. (2003). *Guidelines for Analysis and Description of Soil and Regolith Thin Section*. Soil Science Society of America, Madison, 184 p.
- Taha, M.R. & Kabir, M.H. (2005). Tropical residual soil as compacted soil liners. *Environmental Geology*, 47(3):375-381. DOI: 10.1007/s00254-004-1160-7.
- Trindade, T.P. (2006). *Technological Characterization of Residual Soils Chemically Stabilized for Highway and Environmental Geotechnical Applications*. Ph.D Dissertation, Departamento de Engenharia Civil, Universidade Federal de Viçosa, Viçosa, 254 p. (In Portuguese).
- Viana, J.H.M.; Fernandes Filho, E.I. & Schaefer, C.E.G.R. (2004). Effects of wetting and drying cycles on the reorganization of the microgranular structure of latosols. *Revista Brasileira de Ciência do Solo*, 28(1):1-19 (In Portuguese). DOI: 10.1590/S0100-06832004000100002.
- Vertematti, J.C. (2015). *Brazilian Manual of Geosynthetics*. Edgard Blucher, São Paulo, 576 p. (In Portuguese).
- Wesley, L.D. (1990). Influence of structure and composition on residual soils. *Journal of Geotechnical Engineering*, 116(4):589-603. DOI: 10.1061/(ASCE)0733-9410(1990)116:4(589).

# Physicochemical Modifications in Geomaterials and Their Leachates Extracted from Acidic Attack

S.T. Ferrazzo, R.S. Tímbola, L. Bragagnolo, E. Prestes, E.P. Korf, P.D.M. Prietto, G.D.L.P. Vargas

**Abstract.** Exposure of geomaterials to acid leachates may cause chemical species desorption, mineral dissolution, and metal leaching. This study seeks to understand the changes in the physicochemical composition of liquid extracts resulting from the exposure of four different geomaterials (uniform fine sand, basalt residual soil, kaolin, and bentonite) to a blank solution (distilled water) and sulfuric acid solutions at the concentrations of 0.01, and 1.00 mol/L. It was also investigated the relationship between alterations in both chemical and mineralogical constitutions of geomaterials. The elemental composition of the geomaterials was determined by X-ray fluorescence. In the liquid extracts, Na, Mg, Al, K, Ca, Fe, and Mn concentrations were obtained by inductively coupled plasma atomic emission spectrometry, as well as pH and electrical conductivity were evaluated. pH and electrical conductivity data showed that bentonite had buffering capacity until 0.01 mol/L concentration and higher ion dissolution with increasing acid concentration. Acidic attack by the 1.00 mol/L solution resulted in the solubilization of the constituent metals, corresponding to reductions in elemental composition and alterations in geomaterials mineralogy.

**Keywords:** clayey, metal solubilization, mineralogy, silty and sandy soils, sulfuric acid.

## 1. Introduction

Anthropogenic processes may cause modification in soil behavior due to contamination by acidic solutions, which, under extreme conditions ( $\text{pH} < 1$ ), result in significant volumetric variations and structural changes in soils (Chavali *et al.*, 2018). Considered chemically aggressive, acidic leachates from industrial and mining solid wastes constitute a considerable source of environmental impact, causing changes in soil structure, as increased hydraulic conductivity and reduced reactive power. Acidic pH solutions increase the mobility of dissolved contaminants, which have the main destination at soil and water resources (Agbenyeku *et al.*, 2016; Candeias *et al.*, 2014; González-Fernández *et al.*, 2018; Grande *et al.*, 2018; Hueckel *et al.*, 1997; Knop *et al.*, 2008; Pecorini *et al.*, 2017).

Usually, geomaterials are used in waste containment liner systems, as mixtures of clayey soils and cement, with or without bentonite added, to improve hydraulic and reactive properties of contention barrier (Ghadr & Assadi-Langroudi, 2018; Gueddouda *et al.*, 2016; Hassanlourad *et al.*, 2016; Mao *et al.*, 2018; Miguel *et al.*, 2017; Morandini & Leite, 2015; Verástegui-Flores & Di Emidio, 2014; Wang

*et al.*, 2018, 2016). It has been recognized that high plasticity clayey soils are likely to lose structure when in contact with leachates containing multispecies contaminants, thus reducing their impermeability potential (Amadi, 2011). Therefore, for the efficient performance of liner systems, properties of the geomaterials must not be compromised over time by the exposure to acidic leachates (such as mining drainage). Therefore, the study of the interaction between clay soil constituents and high acidity solutions, focusing on changes in chemical and mineralogical composition, is fundamental for the correct management, as well as the treatment of contaminated soils (Agbenyeku *et al.*, 2016).

Several studies in the literature reporting the effects of exposure of geotechnical materials to chemically aggressive solutions (Agbenyeku *et al.*, 2016; Chavali *et al.*, 2017, 2018; Hamdi & Srasra, 2013; Li *et al.*, 2013; Liu *et al.*, 2015; Miguel *et al.*, 2017; Sucha *et al.*, 2002; Verástegui-Flores & Di Emidio, 2014), indicate, in general, that contact with acidic waters causes soil pH reduction, metal dissolution, chemical species desorption (Agbenyeku *et al.*, 2016; Miguel *et al.*, 2017), and cation exchange reactions

---

Suellen Tonatto Ferrazzo, M.Sc., Programa de Pós-Graduação em Ciência e Tecnologia Ambiental, Universidade Federal da Fronteira Sul, Erechim, RS, Brazil. e-mail suellenferrazzo@hotmail.com.

Rafael de Souza Tímbola, D.Sc. Student, Programa de Pós-Graduação em Engenharia Civil e Ambiental, Universidade de Passo Fundo, Passo Fundo, RS, Brazil. e-mail rafaeltimbola@hotmail.com

Lucimara Bragagnolo, M.Sc. Student, Programa de Pós-Graduação em Ciência e Tecnologia Ambiental, Universidade Federal da Fronteira Sul, Erechim, RS, Brazil. e-mail lucimarabragagnolo@hotmail.com.

Elvis Prestes, Student, Curso de Engenharia Ambiental e Sanitária, Universidade Federal da Fronteira Sul, Erechim, RS, Brasil. e-mail prestes.elvis@gmail.com.

Eduardo Pavan Korf, D.Sc., Associate Professor, Programa de Pós-Graduação em Ciência e Tecnologia Ambiental, Universidade Federal da Fronteira Sul, Erechim, RS, Brazil. e-mail eduardo.korf@uffs.edu.br.

Pedro Domingos Marques Prietto, D.Sc., Assistant Professor, Programa de Pós-Graduação em Engenharia Civil e Ambiental, Universidade de Passo Fundo, Passo Fundo, RS, Brazil. e-mail pdmp@upf.br.

Gean Delise Leal Pasquali Vargas, D.Sc. Associate Professor, Programa de Pós-Graduação em Ciência e Tecnologia Ambiental, Universidade Federal da Fronteira Sul, Erechim, RS, Brazil. e-mail geandelise@uffs.edu.br.

Submitted on November 7, 2019; Final Acceptance on April 17, 2020; Discussion open until September 30, 2020.

DOI: 10.28927/SR.432279

with partial mineral dissolution (Chavali *et al.*, 2018), in addition to changes in hydraulic conductivity in clayey soils (Hamdi & Srasra, 2013; Li *et al.*, 2013; Liu *et al.*, 2015) and modifications in their mechanical properties (Hassanlourad *et al.*, 2016). However, Chavali *et al.* (2018) highlight that most of these studies evaluate soil contamination by inorganic acidic solutions with pH under natural conditions ( $3 < \text{pH} < 6$ ). However, this pH range covers natural pH values in some Brazilian soils, such as Cerrado soils (pH 3.75-4.85) (Leite *et al.*, 2006; Leite *et al.*, 2018) and basalt residual soil (pH 5.5) (Korf *et al.*, 2020).

Thus, further studies are needed to evaluate changes in soils in contact with more aggressive acidic solutions at pH below 1, such as those from mine drainage storage ponds, where water evaporation causes the increase in hydrogen ion concentration (Liu *et al.*, 2013). These wastewaters contain sulfuric acid molecules generated by the oxidation of sulfide minerals in the presence of oxygen and water. A decrease in pH increases the solubility of soil and rock constituents (Knop *et al.*, 2008). Also, it may occur acidic contamination of soils not only by sulfuric acid from spills or leaks (Chavali *et al.*, 2018) but also by acid mine drainage (AMD) from mining in coal plants (Liu *et al.*, 2013) and mining of metallic sulfide ores (Blowes *et al.*, 2014; Luo *et al.*, 2020).

Therefore, this study seeks to shed light on the alterations in geotechnical materials as they are exposed to different concentrations of sulfuric acid with pH lower than 1, by investigating the changes in the physicochemical composition of the liquid extract resulting from the exposure of four geomaterials to sulfuric acid solutions, as well as the changes in the elemental composition and its relationship with the mineralogy of each geomaterial tested. A better understanding of the alterations in geomaterials as a result of the acid attack may be helpful in designing and modeling of compacted barriers, as well as predicting the response of foundation soils.

## 2. Methodology

### 2.1. Materials

In this study, the following geomaterials were used: Osorio Fine Sand (OFS), Basalt Residual Soil (BRS), Kaolin (KAO), and sodium Bentonite (BEN). The sand was collected in a natural deposit in the municipality of Osorio, in the Rio Grande do Sul state, in southern Brazil, and it is considered uniform fine sand (ABNT, 1995; ASTM, 1993). The Basalt residual soil was collected at the Experimental Geotechnical Field of the Technology Center (CETEC) of the University of Passo Fundo (UPF), in the Rio Grande do Sul state, Brazil. It is characterized as a Humic Dystrophic Red Latosol (Streck *et al.*, 2008), with high clay content, classified as low plasticity clay (ASTM, 1993). The Kaolin was purchased from a mineral products supplier located in the municipality of Pântano Grande, in the state of Rio

Grande do Sul, Brazil. This material is commercially known as “pink kaolin” and is classified as a low plasticity inorganic silt (ASTM, 1993). Sodium bentonite of white color was obtained from a supplier located in the municipality of Soledade, in the state of Paraíba, in northeast Brazil, and is classified as a high plasticity inorganic clay (ASTM, 1993). Sulfuric acid used in the experiments was grade P.A., Merck brand with purity 95-97 % and density  $1.84 \text{ g.cm}^{-3}$ .

### 2.2. Methods

The preparation of the geomaterials testing samples followed the standard NBR 6457 (ABNT, 2016). The acidic attack on the geomaterials was simulated by a batch testing adapted from ASTM D4646 - 03 (ASTM, 2008). In these tests, the following variables were considered: sulfuric acid concentration at 0.00 mol/L (pH of distilled water equal to  $7 \pm 2$ ), 0.01 mol/L (pH 2) and 1.00 mol/L (pH 0), and four geomaterials (OFS, BRS, KAO and BEN), resulting in 12 experimental treatments. The batch tests procedures were as follow:

- a) Insertion of samples of each material into a 2000 mL Erlenmeyer flask at a soil-solution ratio of 1:20;
- b) Horizontal continuous shaking at 215 rotations per minute for 24 h at  $22 \pm 5 \text{ }^\circ\text{C}$ ;
- c) Decantation and centrifugation of samples to separate solid and liquid phases. The supernatant centrifugation process was performed in a centrifuge under 3000 rpm for 10 min (USEPA, 1996). Subsequently, the liquid extract was filtered through a  $0.45 \text{ }\mu\text{m}$  nitrocellulose membrane;
- d) Drying of the resulting solid material, in porcelain capsules, in an oven at a temperature of 40 to  $50 \text{ }^\circ\text{C}$ , until constancy of mass. After, each sample was macerated in porcelain crucibles until a powdery material was obtained and placed in properly sealed and identified plastic bags.

Liquid extracts were physical-chemically characterized through the determination of pH and electrical conductivity. pH was determined by pH meter, model HI 2221 Hanna brand, glass body Ag/AgCl electrode with ceramic junction, diameter 9.5 mm, pH range 0 to 13 and temperature  $20\text{-}40 \text{ }^\circ\text{C}$ . Electrical conductivity was determined by microprocessor conductivity meter, model DM-32 Digimed brand with conductivity cell/sensor DMC-010M (range  $0.001 \text{ }\mu\text{S.cm}^{-1}$  to  $2 \text{ S.cm}^{-1}$  and resolution  $0.001/0.01/0.1/1$ ). Also, Na, Mg, Al, K, Ca, Fe, and Mn concentrations were determined for the experimental treatments corresponding to the extremes of the acidic range concentration (0.00 mol/L and 1.00 mol/L) by inductively coupled plasma atomic emission spectrometry (Shimadzu-branded ICP-AES). The pattern solution used to running at ICP-AES was multi element standard XXI for ICP Certipur Merck brand (30 elements in diluted nitric acid- $\text{HNO}_3$ ).

The chemical compositions of the geomaterials, before and after the acidic attack, were determined by X-ray fluorescence spectrometry (XRF), in a pressed sample, with the STD-1 calibration, allowing for the non-standard analysis of the chemical elements comprised between fluoride and uranium in a Bruker S8 Tiger spectrometer.

The mineralogical constitutions were determined by X-ray diffraction (XRD), by the powder method, in a Bruker X-ray diffractometer, model D8 Endeavor, with a position-sensitive detector. The identification of the crystalline phases was obtained by comparing the sample diffractogram with the International Center for Diffraction Data (ICDD) PDF2 database using the X'Pert High Score software.

### 3. Results and Discussion

Figure 1 shows the pH and electrical conductivity results of the liquid extracts for the four tested geomaterials. The pH results of the OFS, BRS, and KAO remained close to the initial pH of the acidic solutions to which they were exposed. BEN presented pH above neutrality, especially the sample submitted to the 0.01 mol/L solution (pH 2), due to the acid buffering power associated with the high cation exchange capacity of this soil (Nessa *et al.*, 2007). BEN also presented the highest pH value (0.41) amongst the geomaterials tested at 1.00 mol/L concentration (pH 0). Similar results were observed by Liu *et al.* (2013), who

evaluated that acidic leachate from three sodium bentonites had pH ~ 2 at lower concentrations (0.015 mol/L to 0.25 mol/L), and pH ~ 0 at higher concentrations (0.5 mol/L and 1mol/L).

The results indicate that bentonite has a higher acid neutralization capacity at 0.01 mol/L solution (pH 2). This condition may contribute to the attenuation of contaminants from acidic leachate. According to Yong *et al.* (1990), smectite soil (*e.g.* bentonite) shows significant resistance to pH changes due to its high cation-exchange capacity (CEC). The H<sup>+</sup> adsorption from smectite-contamination leachate occurs mainly by cation exchange, and when exchange sites are unavailable, the pH decreases rapidly. On the other hand, kaolinite soil does not show considerable resistance to pH changes (Yong *et al.*, 1990), which was observed in BRS and KAO samples.

In general, all geomaterials presented a positive correlation between electrical conductivity and concentration of sulfuric acid, which indicates a higher concentration of dissolved ions in the liquid extracts at 1.00 mol/L. The results of metals concentration by ICP-AES (Table 1) and the XRF (Table 2) indicate the solubilization of the chemical constituents of geomaterials. For the OFS, the significant electrical conductivity measured in the liquid extract of the sample at 1.00 mol/L, is probably due to the presence of hydrogen ions (H<sup>+</sup>) in the solution, which did not bind to the active sites of the soil minerals, since quartz has low reactivity to sulfuric acid.

Table 1 shows the metals concentrations in the liquid extract resulting from the geomaterials tested at the extreme values of the concentration range (0.00 mol/L and 1.00 mol/L). These results are consistent with the chemical constitution of the samples (Table 2), demonstrating that exposure to the 1.00 mol/L solution of sulfuric acid caused loss by solubilization of the constituent metals of the geomaterials, mostly aluminum (Al), iron (Fe), calcium (Ca), and magnesium (Mg), in addition to sodium (Na) for the bentonite liquid extract. Knop *et al.* (2008) reported that these metals are commonly mobilized in rocks or soils due to the leaching of sulfuric acid present in acidic mining drainage.

The expressive concentrations of Fe in the liquid extracts were an expected result since this metal is highly soluble in acidic environments. This feature was observed mainly for the BRS, which has significant Fe content in its natural composition (see Table 2). For the specimen SRB at 1.00 mol/L, it was observed a Fe concentration of 458 mg/L, confirming the loss of hematite identified by the XRD analysis (Table 3). According to Sunil *et al.* (2006), Fe leaching from a lateritic soil reduces the bonds between soil particles, resulting in alterations in their mechanical and physical properties, such as reduced compressive strength and maximum dry density and increased optimal moisture content. Also, a high concentration of aluminum was detected in the liquid extracts, corroborating the idea

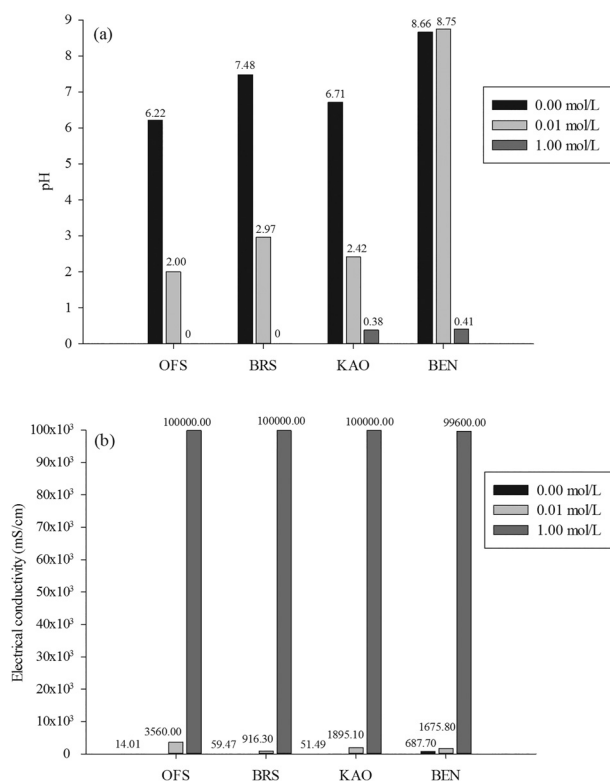


**Figure 1** - pH (a) and electrical conductivity (b) of the liquid extract of the geomaterials tested.

**Table 1** - Metal concentration of liquid geomaterials extract (mg/L).

| Specimen       | Na             | Mg     | Al             | K              | Ca             | Fe     | Mn             |
|----------------|----------------|--------|----------------|----------------|----------------|--------|----------------|
| OFS 0.00 mol/L | - <sup>1</sup> | 0.21   | 2.31           | - <sup>1</sup> | - <sup>1</sup> | 0.85   | - <sup>1</sup> |
| OFS 1.00 mol/L | - <sup>1</sup> | 1.79   | 10.03          | 1.06           | 2.16           | 6.94   | 0.16           |
| BRS 0.00 mol/L | - <sup>1</sup> | 0.85   | - <sup>1</sup> | - <sup>1</sup> | 1.69           | 0.06   | 0.24           |
| BRS 1.00 mol/L | - <sup>1</sup> | 4.27   | 418.12         | 1.99           | 8.39           | 458.12 | 3.00           |
| KAO 0.00 mol/L | - <sup>1</sup> | 0.49   | 7.34           | 1.47           | 0.04           | 1.14   | - <sup>1</sup> |
| KAO 1.00 mol/L | - <sup>1</sup> | 12.93  | 205.98         | 8.56           | 14.10          | 9.57   | 1.91           |
| BEN 0.00 mol/L | 161.98         | 11.27  | 96.32          | 2.64           | 5.27           | 38.00  | 0.05           |
| BEN 1.00 mol/L | 332.97         | 132.99 | 136.32         | 8.63           | 282.50         | 46.33  | 0.86           |

<sup>1</sup>: Below detection limit.

**Table 2** - Elemental chemical composition of solid extracts of geomaterials (mg/kg).

| Specimen       | Na   | Mg   | Al     | P   | Si     | S     | K     | Ca    | Ti   | Fe    | Mn  | Zr  | Ba  |
|----------------|------|------|--------|-----|--------|-------|-------|-------|------|-------|-----|-----|-----|
| OFS Pure       | 900  | 400  | 11600  | -   | 435200 | 100   | 7100  | 500   | 900  | 2800  | -   | -   | -   |
| OFS 0.00 mol/L | 900  | 300  | 9900   | -   | 445500 | -     | 6000  | 400   | 700  | 2100  | -   | -   | -   |
| OFS 1.00 mol/L | -    | -    | 5800   | -   | 401600 | 11300 | 5100  | -     | 500  | 2000  | -   | -   | -   |
| BRS Pure       | -    | 2100 | 128100 | 500 | 216900 | 300   | 3400  | 200   | 9800 | 74800 | 300 | 500 | -   |
| BRS 0.00 mol/L | -    | 1700 | 109600 | 400 | 232300 | 300   | -     | 300   | 9400 | 73400 | 300 | -   | -   |
| BRS 1.00 mol/L | -    | 600  | 37500  | -   | 94000  | 63700 | -     | 200   | 3800 | 27000 | -   | 200 | -   |
| KAO Pure       | -    | 900  | 189500 | 100 | 221600 | 300   | 7000  | 800   | 900  | 8200  | 100 | -   | 500 |
| KAO 0.00 mol/L | -    | 500  | 191600 | -   | 216900 | -     | 8900  | 900   | 1300 | 11600 | -   | -   | -   |
| KAO 1.00 mol/L | -    | 500  | 128600 | -   | 143500 | 31800 | 5600  | 700   | 600  | 6200  | -   | -   | -   |
| BEN Pure       | 5900 | 5900 | 166200 | 200 | 217400 | 100   | 10300 | 8400  | 2200 | 18300 | 100 | 100 | 400 |
| BEN 0.00 mol/L | 2400 | 5100 | 130200 | -   | 247300 | -     | 24100 | 17800 | 1600 | 15700 | -   | 200 | 600 |
| BEN 1.00 mol/L | 900  | 3200 | 102700 | -   | 162200 | 35600 | 7300  | 1600  | 1500 | 12900 | -   | 100 | 400 |

that at very low pH values (less than 4.5), this metal is solubilized in the forms of  $Al^{+3}$  and  $AlO_2^-$  (Miguel *et al.*, 2017).

Spagnoli *et al.* (2012) reported that, in a solution with pH close to 3,  $Al^{+3}$  dissolution acts as a coagulant agent in kaolinite, increasing shear strength. According to the authors, the occurrence of clay mineral dissolution in acidic environments is a function of protonation reactions of the hydroxide ( $OH^-$ ) and oxide ( $O^{2-}$ ) termination sites, which weaken the bonds that support the aluminum and, consequently, displace it from the structure to the liquid phase as  $Al^{3+}$ . In the study of Bakhshipour *et al.* (2016), it was found that the reduction of aluminum and iron contents of a residual soil by acidic leaching increased Atterberg limits and optimum moisture content and reduced shear strength and maximum dry density.

For the BEN sample, the acidic attack resulted in an increase of sodium, calcium, and magnesium in the liquid extract. The desorption of these bentonite elements is supported by the results of the XRF analysis (Table 2). This

feature was probably due to the bentonite high cation exchange capacity (Asof *et al.*, 2017; Caglar *et al.*, 2013; Koch, 2002). According to Liu *et al.* (2013), the concentrations of sodium and calcium in leachates of sodium bentonite reflect hydrogen ion exchanges. The authors reported that around 90 % and 50 % of Na and Ca, respectively, were displaced by  $H^+$ .

Considering the application of bentonite in waste containment liner systems and degraded areas exposed to acid contaminants, the loss of cations from bentonite, as observed in this study, points out to potential changes in expansion capacity, plasticity, microstructure, and permeability (Bouazza *et al.*, 2006; Egloffstein, 2001; Koch, 2002; Mazzieri *et al.*, 2017; Ruhl & Daniel, 1997; Shackelford *et al.*, 2000). Chavali *et al.* (2018) reported that contamination of sodium bentonite by sulfuric acid caused a reduction in the expansion of this clay, where equilibrium expandabilities of 67 % and 50 % were measured at 1 mol/L and 4 mol/L concentrations, respectively. According to the authors, these changes in bentonite are due to the cation ex-

change process, in which sodium ions are replaced by hydrogen ions, whose ionic radius (0.012 Å) is smaller than that of sodium (1.02 Å), resulting thus in smaller expansion. Liu *et al.* (2013), for three sodium bentonites, found that the contact with sulfuric acid solutions (0.015 mol/L to 1 mol/L) caused the displacement of cation ions by hydrogen ions, resulting in a reduction of Atterberg limits and expandability index, which might compromise the hydraulic performance of these geomaterials when applied in waterproofing systems.

The elemental characterization presented in Table 2 is consistent with the metal concentrations found in the liquid extracts, for all geomaterials exposed at 1.00 mol/L, demonstrating expressive reductions of Fe, Al, Mg, Ca, and Na in sodium bentonite.

Table 3 shows the mineralogical compositions of the geomaterials samples. In line with the results of the FRX (Table 2) and ICP-AES (Table 1), a significant reduction of iron occurred for all four geomaterials exposed to the most acidic solution, especially for the BRS, likely due to the acidic attack to the iron oxides adsorbed on the surface of soil particles, evidenced by the loss of hematite ( $\text{Fe}_2\text{O}_3$ ) and

the formation of coquimbite ( $\text{Fe}_2(\text{SO}_4)_3 \cdot 9\text{H}_2\text{O}$ ) and pyrophyllite ( $\text{Al}_2\text{Si}_4(\text{OH})$ ) in the sample exposed to the 1.00 mol/L solution. For the other geomaterials exposed to the most acidic solution, there was also a significant reduction in the Al content, as well as in the other constituent elements (Table 2), which was corroborated by the loss of albite ( $\text{Na}(\text{AlSi}_3\text{O}_8)$ ) and the formation of gibbsite ( $\text{Al}(\text{OH})_3$ ) in the OFS; the loss of anatase ( $\text{TiO}_2$ ) in the BRS; the loss of calcite ( $\text{CaCO}_3$ ) and hydrobiotite ( $\text{KMgAlSi}_2\text{O}_7 \cdot \text{H}_2\text{O}$ ) in the BEN; and the formation of alunogen ( $\text{Al}_2(\text{SO}_4)_3 \cdot 17\text{H}_2\text{O}$ ) in the BRS, KAO, and BEN. The hydrate sulfate alunogen present in the samples is explained by the increased sulfur content. Similarly, there was a correspondence between anatase loss in the SRB and calcite loss in the BEN, with a significant reduction in Ti and Ca contents for both geomaterials (Table 2).

The OFS showed lesser chemical reactivity in contact with sulfuric acid compared to the other geomaterials, which is plausible since this soil is mostly composed of quartz. From the works of MacCarthy *et al.* (2014) and Brady & Walther (1989), it may be inferred that the acid concentrations, pH values and temperature conditions used in the present study promoted the dissolution of amorphous silica and that the presence of Fe, Al, Mg, Si, and Na influenced the adsorption rate or the attack of  $\text{H}^+$  ions to the active sites of quartz particles.

In general, the exposure of the geomaterials to the 1.00 mol/L solution resulted in liquid extracts with higher metal concentrations. These results correspond to the elementary and mineralogical variations of the geomaterials. In this regard, it is important to note that in acidic environments, mineral structure dissolution, cation leaching, anion adsorption, changes in the clay particles edge charges and the diffuse double layer, and the formation of sulfate minerals are able to affect the engineering behavior of soils (Bakhshipour *et al.*, 2016; Chavali *et al.*, 2018). In the present study, the expressive concentration of several metals found in the liquid extracts, especially for the BEN exposed to the 1.00 mol/L solution, correspond to liquids with higher concentrations of multivalent cations. These cations (such as  $\text{Ca}^{+2}$  and  $\text{Mg}^{+2}$ ) tend to shrink the diffuse double layer in clay particles, causing soil flocculation, macropore formation and consequently increased hydraulic conductivity (Amadi, 2011; Mitchell, 1993; Ruhl & Daniel, 1997).

Spagnoli *et al.* (2012) report that kaolinite has no forces in the double layer because the surface charge is considered neutral. According to Bakhshipour *et al.* (2016), in residual soils consisting mainly of illite, kaolinite, and goethite, acidic contamination does not provoke changes in the diffuse double layer sufficient to promote variations in properties such as Atterberg limits, hydraulic conductivity, and compaction characteristics. In contrast, in smectite clay minerals, both faces have oxide ( $\text{O}^{2-}$ ) terminations, and the edges have hydroxide ( $\text{OH}^-$ ) and  $\text{O}^{2-}$  terminations. In smectites, the diffuse double layer governs the mechanical prop-

**Table 3** - Mineral composition of geomaterials samples.

| OFS Pure     | OFS 0.00 mol/L | OFS 1.00 mol/L |
|--------------|----------------|----------------|
| Quartz       | Quartz         | Quartz         |
| Microcline   | Microcline     | Microcline     |
| Albite       | Albite         | Gibbsite       |
| BRS Pure     | BRS 0.00 mol/L | BRS 1.00 mol/L |
| Quartz       | Quartz         | Quartz         |
| Hematite     | Hematite       | Alunogen       |
| Kaolinite    | Kaolinite      | Coquimbite     |
| Anatase      | Anatase        | Kaolinite      |
| -            | -              | Pyrophyllite   |
| -            | -              | Microcline     |
| KAO Pure     | KAO 0.00 mol/L | KAO 1.00 mol/L |
| Quartz       | Quartz         | Quartz         |
| Kaolinite    | Kaolinite      | Kaolinite      |
| Microcline   | Microcline     | Microcline     |
| Muscovite    | Muscovite      | Muscovite      |
| -            | -              | Alunogen       |
| BEN Pure     | BEN 0.00 mol/L | BEN 1.00 mol/L |
| Quartz       | Quartz         | Quartz         |
| Kaolinite    | Kaolinite      | Kaolinite      |
| Microcline   | Microcline     | Microcline     |
| Muscovite    | Muscovite      | Muscovite      |
| Calcite      | Calcite        | Alunogen       |
| Hydrobiotite | Hydrobiotite   | -              |

erties, since oscillations in the pH increase the concentration of ions in the double layer. At low pH values, the increase in  $H^+$  concentration causes the reduction of the double layer (Spagnoli *et al.*, 2012).

The available literature suggests that the effects of inorganic acids on different types of geomaterial might include dissolution of minerals, leaching of metals such as iron and aluminum, and high loss of cations, which in turn influence properties such as Atterberg limits, expandability, maximum dry density, optimal moisture content, mechanical strength, and permeability.

#### 4. Conclusions

In this study, the physical-chemical composition of the liquid extracts and the elemental compositions of four geomaterials exposed to sulfuric acid solutions were evaluated and related to changes in their mineralogical constitution. The following experimental findings were achieved:

- The pH values showed that only the bentonite liquid extract reached a pH above neutrality after exposure to the 0.01 mol/L  $H_2SO_4$  solution. Under higher acid concentration, the liquid extracts remained at pH did not present a buffer capacity for that level of acid concentration with values close to the initial value (pH ~ 0);
- The electrical conductivity results showed a positive correlation with the increase of acid concentration, indicating a higher concentration of dissolved ions in the liquid extracts of geomaterials submitted to the 1.00 mol/L  $H_2SO_4$  solution;
- Exposure to the 1.00 mol/L solution of  $H_2SO_4$  resulted in the solubilization of metals, mainly in basalt residual soil and bentonite. The concentrations of metals in the liquid extracts matched the reduction of the geomaterial constituent elements, as well as the alterations in the mineralogical composition, with loss and formation of minerals.

In conclusion, when considering the potential application of the geomaterials studied to constitute impermeable barriers, one should pay attention to the solubilization of metals and loss of minerals in extreme acidity conditions and the associated susceptibility to structural changes and consequent modification in the mechanical properties and hydraulic performance of waterproofing systems.

#### Acknowledgments

This study was financed in part by the Coordenação de Aperfeiçoamento de Pessoal de Nível Superior (CAPES), Brazil - Finance Code 001. The authors are also grateful for the financial support of Fundação de Amparo à Pesquisa do Estado do Rio Grande do Sul (FAPERGS) (Grant 16/2551-0000205-3, Note 08/2014 - First Project Programs) and CNPq (Grants 486506/2013-4, 312756/2017-8, 438328/2018-3).

#### References

- ABNT (2016). Amostras de Solo: Preparação para Ensaios de Compactação e Caracterização - NBR 6457. ABNT, Rio de Janeiro, Brazil, 12 p.
- ABNT (1995). Rochas e Solos - NBR 6502. ABNT, Rio de Janeiro, Brazil, 18 p.
- Agbenyeku, E.E.; Muzenda, E. & Msibi, M.I. (2016). Chemical alterations in three clayey soils from percolation and interaction with acid mine drainage (AMD). *South African Journal of Chemical Engineering*, 21:28-36. <https://doi.org/10.1016/j.sajce.2016.04.003>.
- Amadi, A.A. (2011). Hydraulic conductivity tests for evaluating compatibility of lateritic soil-fly ash mixtures with municipal waste leachate. *Geotechnical and Geological Engineering*, 29(3):259-265. <https://doi.org/10.1007/s10706-010-9358-9>.
- Asof, M.; Rachman, S.A.; Nurmawi, W.A. & Ramayanti, C. (2017). Recovery of  $H_2SO_4$  from spent acid waste using bentonite adsorbent. *Proc. MATEC Web of Conferences*, v. 101, pp. 02007. <https://doi.org/10.1051/mateconf/201710102007>
- ASTM (1993). Standard Practice for Classification of Soils for Engineering Purposes (Unified Soil Classification System) - D2487-06. ASTM International, West Conshohocken, Pennsylvania, USA, 12 p.
- ASTM (2008). Standard Test Method for 24-h Batch-Type Measurement of Contaminant Sorption by Soils and Sediments - D4646-03. ASTM International, West Conshohocken, Pennsylvania, USA, 4 p.
- Bakhshpour, Z.; Asadi, A.; Huat, B.B.K.; Sridharan, A. & Kawasaki, S. (2016). Effect of acid rain on geotechnical properties of residual soils. *Soils and Foundations*, 56(6):1008-1020. <https://doi.org/10.1016/j.sandf.2016.11.006>.
- Blowes, D.W.; Ptacek, C.J.; Jambor, J.L.; Weisener, C.G.; Paktunc, D.; Gould, W.D. & Johnson, D.B. (2014) *The geochemistry of acid mine drainage*. D.W. Blowes, C.J. Ptacek, J.L. Jambor, and C.G. Weisener (eds), *Treatise on Geochemistry*, Elsevier, Oxford, pp. 131-190. <https://doi.org/10.1016/B978-0-08-095975-7.00905-0>.
- Bouazza, A.; Vangpaisal, T. & Jefferis, S. (2006). Effect of wet-dry cycles and cation exchange on gas permeability of geosynthetic clay liners. *Journal of Geotechnical and Geoenvironmental Engineering*, 132(8):1011-1018. [https://doi.org/10.1061/\(ASCE\)1090-0241\(2006\)132:8\(1011\)](https://doi.org/10.1061/(ASCE)1090-0241(2006)132:8(1011)).
- Brady, P.V. & Walther, J.V. (1989). Controls on silicate dissolution rates in neutral and basic pH solutions at 25 °C. *Geochimica et Cosmochimica Acta*, 53(11):2823-2830. [https://doi.org/10.1016/0016-7037\(89\)90160-9](https://doi.org/10.1016/0016-7037(89)90160-9).
- Caglar, B.; Afsin, B.; Koksai, E.; Tabak, A. & Eren, E. (2013). Characterization of unye bentonite after treat-

- ment with sulfuric acid. *Quimica Nova*, 36(7):955-959. <https://doi.org/10.1590/S0100-40422013000700006>.
- Candeias, C.; Freire, P.; Ferreira, E.; Ferreira, A.; Rita, A. & Paulo, J. (2014). Acid mine drainage from the Panasqueira mine and its influence on Zêzere river (Central Portugal). *Journal of African Earth Sciences*, 99:705-712. <https://doi.org/10.1016/j.jafrearsci.2013.10.006>.
- Chavali, R.V.P.; Reddy, P.H.P.; Murthy, R.V. & Sivapullaiah, P.V. (2018). Swelling characteristics of soils subjected to acid contamination. *Soils and Foundations*, 58(1):110-121. <https://doi.org/10.1016/j.sandf.2017.11.005>.
- Chavali, R.V.P.; Vindula, S.K.; Reddy, P.H.P.; Babu, A. & Pillai, R.J. (2017). Swelling behavior of kaolinitic clays contaminated with alkali solutions: A micro-level study. *Applied Clay Science*, 135:575-582. <https://doi.org/10.1016/j.clay.2016.10.045>.
- Egloffstein, T.A. (2001). Natural bentonites - Influence of the ion exchange and partial desiccation on permeability and self-healing capacity of bentonites used in GCLs. *Geotextiles and Geomembranes*, 19(7):427-444. [https://doi.org/10.1016/S0266-1144\(01\)00017-6](https://doi.org/10.1016/S0266-1144(01)00017-6).
- Ghadr, S. & Assadi-Langroudi, A. (2018). Structure-based hydro-mechanical properties of sand-bentonite composites. *Engineering Geology*, 235:53-63. <https://doi.org/10.1016/j.enggeo.2018.02.002>.
- González-Fernández, B.; Rodríguez-Valdés, E.; Boente, C.; Menéndez-Casares, E.; Fernández-Braña, A. & Gallego, J.R. (2018). Long-term ongoing impact of arsenic contamination on the environmental compartments of a former mining-metallurgy area. *Science of the Total Environment*, 610-611:820-830. <https://doi.org/10.1016/j.scitotenv.2017.08.135>.
- Grande, J.A.; Santisteban, M.; de la Torre, M.L.; Dávila, J.M. & Pérez-Ostale, E. (2018). Map of impact by acid mine drainage in the river network of The Iberian Pyrite Belt (Sw Spain). *Chemosphere*, 199:269-277. <https://doi.org/10.1016/j.chemosphere.2018.02.047>.
- Gueddouda, M.K.; Goual, I.; Benabed, B.; Taibi, S. & Aboubekr, N. (2016). Hydraulic properties of dune sand-bentonite mixtures of insulation barriers for hazardous waste facilities. *Journal of Rock Mechanics and Geotechnical Engineering*, 8(4):541-550. <https://doi.org/10.1016/j.jrmge.2016.02.003>.
- Hamdi, N. & Srasra, E. (2013). Hydraulic conductivity study of compacted clay soils used as landfill liners for an acidic waste. *Waste Management*, 33(1):60-66. <https://doi.org/10.1016/j.wasman.2012.08.012>.
- Hassanlourad, M.; Khatami, M.H. & Ahmadi, M.M. (2016). Effects of sulphuric acid pollutant on the shear behaviour and strength of sandy soil and sand mixed with bentonite clay. *International Journal of Geotechnical Engineering*, 11(2):114-119. <https://doi.org/10.1080/19386362.2016.1193662>.
- Hueckel, T.; Kaczmarek, M. & Caramuscio, P. (1997). Theoretical assessment of fabric and permeability changes in clays affected by organic contaminants. *Canadian Geotechnical Journal*, 34(4):588-603. <https://doi.org/10.1139/t97-013>.
- Knop, A.; VanGulck, J.; Heineck, K.S. & Consoli, N.C. (2008). Compacted artificially cemented soil-acid leachate contaminant interactions: Breakthrough curves and transport parameters. *Journal of Hazardous Materials*, 155(1-2):269-276. <https://doi.org/10.1016/j.jhazmat.2007.11.056>.
- Koch, D. (2002). Bentonites as a basic material for technical base liners and site encapsulation cut-off walls. *Applied Clay Science*, 21:1-11. [https://doi.org/10.1016/S0169-1317\(01\)00087-4](https://doi.org/10.1016/S0169-1317(01)00087-4).
- Korf, E.P.; Prietto, P.D.M.; Silveira, A.A.; Ulsen, C.; Consoli, N.C. & Bragagnolo, L. (2020). Modifications in the chemical and mineralogical composition of compacted mature residual soil submitted to the percolation of acidic leachates. *Soils and Rocks*, 43(1):159-167. <https://doi.org/10.28927/SR.43100X>.
- Leite, G.L.D.; Veloso, R.V.S.; Zanoncio, J.C.; Fernandes, L.A. & Almeida, C.I.M. (2006). Phenology of *Caryocar brasiliense* in the Brazil cerrado region. *Forest Ecology and Management*, 236 (2-3):286-294. <https://doi.org/10.1016/j.foreco.2006.09.013>.
- Leite, M.V.M.; Bobul'ská, L.; Espíndola, S.P.; Campos, M.R.C.; Azevedo, L.C.B. & Ferreira, A.S. (2018). Modeling of soil phosphatase activity in land use ecosystems and topsoil layers in the Brazilian Cerrado. *Ecological*, 385:182-188. <https://doi.org/10.1016/j.ecolmodel.2018.07.022>.
- Li, J.; Xue, Q.; Wang, P. & Liu, L. (2013). Influence of leachate pollution on mechanical properties of compacted clay: A case study on behaviors and mechanisms. *Engineering Geology*, 167:128-133. <https://doi.org/10.1016/j.enggeo.2013.10.013>.
- Liu, Y.; Bouazza, A.; Gates, W.P. & Rowe, R.K. (2015). Hydraulic performance of geosynthetic clay liners to sulfuric acid solutions. *Geotextiles and Geomembranes*, 43(1):14-23. <https://doi.org/10.1016/j.geotexmem.2014.11.004>.
- Liu, Y.; Gates, W.P. & Bouazza, A. (2013). Acid induced degradation of the bentonite component used in geosynthetic clay liners. *Geotextiles and Geomembranes*, 36:71-80.
- Luo, C.; Routh, J.; Dario, M.; Sarkar, S.; Wei, L.; Luo, D. & Liu, Y. (2020). Distribution and mobilization of heavy metals at an acid mine drainage affected region in South China, a post-remediation study. *Science of the Total Environment*, 724:138122. <https://doi.org/10.1016/j.geotexmem.2012.10.011>.
- MacCarthy, J.; Nosrati, A.; Skinner, W. & Addai-Mensah, J. (2014). Dissolution and rheological behaviour of hematite and quartz particles in aqueous media at pH 1.

- Chemical Engineering Research and Design, 92(11):2509-2522.  
<https://doi.org/10.1016/j.cherd.2014.02.020>.
- Mao, X.; Xiong, L.; Hu, X.; Yan, Z.; Wang, L. & Xu, G. (2018). Remediation of ammonia-contaminated groundwater in landfill sites with electrochemical reactive barriers: A bench scale study. *Waste Management*, 78:69-78. <https://doi.org/10.1016/j.wasman.2018.05.015>.
- Mazzieri, F.; Di Emidio, G. & Pasqualini, E. (2017). Effect of wet-and-dry ageing in seawater on the swelling properties and hydraulic conductivity of two amended bentonites. *Applied Clay Science*, 142:40-51. <https://doi.org/10.1016/j.clay.2016.10.031>
- Miguel, M.G.; Barreto, R.P. & Pereira, S.Y. (2017). Study of a tropical soil in order to use it to retain aluminum, iron, manganese and fluoride from acid mine drainage. *Journal of Environmental Management*, 204:563-570. <https://doi.org/10.1016/j.jenvman.2017.09.024>.
- Mitchell, J.K. (1993). *Fundamentals of soil behavior*, 2nd ed. John Wiley & Sons, New York, 456 p.
- Morandini, T.L.C. & Leite, A.L. (2015). Characterization and hydraulic conductivity of tropical soils and bentonite mixtures for CCL purposes. *Engineering Geology*, 196:251-267. <https://doi.org/10.1016/j.enggeo.2015.07.011>
- Nessa, S.A.; Idemitsu, K.; Yamasaki, Y.; Inagaki, Y. & Arima, T. (2007). Measurement of pH of the compacted bentonite under the reducing condition. *Memoirs of the Faculty of Engineering*, 67(1):25-31.
- Pecorini, I.; Baldi, F.; Bacchi, D.; Carnevale, E.A. & Corti, A. (2017). Leaching behaviour of hazardous waste under the impact of different ambient conditions. *Waste Management*, 63:96-106. <https://doi.org/10.1016/j.wasman.2016.10.037>.
- Ruhl, J.L. & Daniel, D.E. (1997). Geosynthetic clay liners permeated with chemical solutions and leachates. *Journal of Geotechnical and Geoenvironmental Engineering*, 123(4):369-381. [https://doi.org/10.1061/\(ASCE\)1090-0241\(1997\)123:4\(369\)](https://doi.org/10.1061/(ASCE)1090-0241(1997)123:4(369)).
- Shackelford, C.D.; Benson, C.H.; Katsumi, T.; Edil, T.B. & Lin, L. (2000). Evaluating the hydraulic conductivity of GCLs permeated with non-standard liquids. *Geotextiles and Geomembranes*, 18(2-4):133-161. [https://doi.org/10.1016/S0266-1144\(99\)00024-2](https://doi.org/10.1016/S0266-1144(99)00024-2).
- Spagnoli, G.; Rubinos, D.; Stanjek, H.; Fernández-Steeger, T.; Feinendegen, M. & Azzam, R. (2012). Undrained shear strength of clays as modified by pH variations. *Bulletin of Engineering Geology and the Environment*, 71:135-148. <https://doi.org/10.1007/s10064-011-0372-9>.
- Streck, E.V.; Kampf, N.; Dalmolin, R.S.D.; Klamt, E.; Nascimento, P.C.; Giasson, E. & Pinto, L.F.S. (2008). *Solos do Rio Grande do Sul*, 2 ed. EMATER/RS-ASCAR, Porto Alegre, 222 p. [https://doi.org/10.1016/S0016-7061\(02\)00225-2](https://doi.org/10.1016/S0016-7061(02)00225-2).
- Sucha, V.; Dubiková, M.; Cambier, P.; Elsass, F. & Pernes, M. (2002). Effect of acid mine drainage on the mineralogy of a dystric cambisol. *Geoderma*, 110(3-4):151-167. [https://doi.org/10.1016/S0016-7061\(02\)00225-2](https://doi.org/10.1016/S0016-7061(02)00225-2).
- Sunil, B.M.; Nayak, S. & Surathkal, S. (2006). Effect of pH on the geotechnical properties of laterite. *Engineering Geology*, 85(1):197-203. <https://doi.org/10.1016/j.enggeo.2005.09.039>.
- USEPA (1996). *Acid digestion of sediments, sludges, and soils - Method 3050B*. USEPA, Washington, USA, 12 p.
- Verástegui-Flores, R.D. & Di Emidio, G. (2014). Impact of sulfate attack on mechanical properties and hydraulic conductivity of a cement-admixed clay. *Applied Clay Science*, 101:490-496. <https://doi.org/10.1016/j.clay.2014.09.012>.
- Wang, S.; Zhu, W.; Fei, K.; Xu, C. & Zhang, N. (2018). Study on non-darcian flow sand-clay mixtures. *Applied Clay Science*, 151:102-108. <https://doi.org/10.1016/j.clay.2017.10.028>.
- Wang, Y.; Chen, Y.; Xie, H.; Zhang, C. & Zhan, L. (2016). Lead adsorption and transport in loess-amended soil-bentonite. *Engineering Geology*, 215:69-80. <https://doi.org/10.1016/j.enggeo.2016.11.002>.
- Yong, R.N.; Warkentin, B.P.; Phadungchewit, Y. & Galvez, R. (1990). Buffer capacity and lead retention in some clay materials. *Water, Air, and Soil Pollution*, 53:53-67. <https://doi.org/10.1007/BF00154991>.

# Sample Quality Assessment: Comparison Between Brass Shelby Tubes and Reinforced PVC Tube Samplers

A.V. Abreu, M.S.S. Almeida

**Abstract.** Laboratory tests were conducted in soft clay deposits at the Macaé/RJ airport in order to obtain geotechnical parameters for a new runway design. The quality of soil samples, extracted with both brass tube (thin-walled) and reinforced PVC tube (thick-walled) soil samplers, was assessed. Both samplers were 700 mm long, with a 7 degree chamfered cutting edge and no internal clearance. Oedometer tests were conducted to compare the results of tests performed on the samples obtained using the two samplers. Based on classifications in the literature, both samplers provided very good to excellent samples in most of the cases. Moreover, given the lower cost and faster delivery of the PVC samplers, this option is shown to be a good alternative to the brass samplers.

**Keywords:** open tube soil sampler, sample disturbance, sample quality, sampling, soft clay.

## 1. Introduction

Laboratory tests are often used to obtain geotechnical parameters to be used in the design of geotechnical structures. Oedometer and triaxial tests require undisturbed samples to yield reliable soil parameters. However, sample quality continues to be an obstacle to obtaining good quality geotechnical parameters. The soil sampling process involves a number of steps described by Ladd & De Groot (2003) who provided a list of recommendations for minimizing sample disturbance.

Several types of sampling tools and methods are described in the literature (Hvorslev, 1949; Bertuol *et al.*, 2009; La Rochelle *et al.*, 1981; Lefebvre & Poulin, 1979; Tanaka *et al.*, 1996; Hight, 2001).

The Brazilian practice (ABNT, 1997) has relied on the use of thin-walled open tubes (Shelby tubes), fitted with a drive head with a suction ball valve to help secure the sample during extraction. In general, these open tubes are manufactured in brass or stainless steel, with a thin wall (typically 1.58 mm thick).

However, the cost of brass or steel samplers is also a factor that must be considered. Januzzi *et al.*, 2013 carried out soft clay sampling with a thick-walled PVC tube sampler and concluded that its use should be encouraged, provided the sample quality criteria could be met. Marques *et al.* (2017) conducted a site investigation using PVC tubes, with satisfactory results, where 60 % of the samples were classified as good to excellent according to the Coutinho (2007) sample quality evaluation criteria.

Although the ABNT (1997) recommends the use of brass or stainless steel tube samplers, three factors have arisen in Brazilian common practice to support the use of PVC tubes. These factors include: time, cost and handling.

PVC tubes can be acquired more quickly than brass or stainless steel tubes, they are significantly less expensive than metal tubes, and they are easier to handle during sample extrusion.

This paper deals with the analysis of tube samplers made of different materials in order to compare the novel use of thick-walled PVC tube samplers and the impact of their use on the geotechnical parameters of the samples.

Lunne & Long (2006) presented a broad discussion of the detailed physical characteristics of the core sampling tubes, such as: diameter, wall thickness (or area ratio), cutting edge angle, inside clearance, inside friction, and outside friction. Extensive literature exists on these topics. Regarding the physical characteristics of the core sampling tubes the following studies are of particular importance: Hvorslev (1949), Kallstenius (1963), Lefebvre & Poulin (1979), La Rochelle *et al.* (1981), Andresen (1981), Hight *et al.* (1992), Lunne *et al.* (1997), Lunne *et al.* (1998), Lunne *et al.* (2006), Lunne (2009), Tanaka & Tanaka (1999), Di Buò *et al.* (2019). Furthermore, Karlsson *et al.* (2016) and Lim *et al.* (2019) reported that a little more care in sample handling and testing can result in large cost savings as a result of more reliable model parameters.

The aim of this article is to assess and compare the quality of soil samples extracted using two different soil sampling tubes, a brass (thin-walled) tube sampler and a PVC (thick-walled) sampler. Undisturbed soil samples were needed to determine geotechnical parameters for a civil engineering project at the Macaé airport in Brazil. Each tube sampler was used to extract three samples from an 8 m deep soft clay deposit. The sample quality was assessed according to parameters proposed by Lunne *et al.* (1997) and Coutinho (2007).

---

André do Valle Abreu, M.Sc. Student, Universidade Federal do Rio de Janeiro, COPPE, Rio de Janeiro, RJ, Brazil. e-mail: andre@iqsengenharia.com.br.

Márcio de Souza Soares de Almeida, Ph.D., Professor, Universidade Federal do Rio de Janeiro, COPPE, Rio de Janeiro, RJ, Brazil. e-mail: almeida@coc.ufrj.br.

Submitted on January 6, 2020; Final Acceptance on May 20, 2020; Discussion open until September 30, 2020.

DOI: 10.28927/SR.432287

## 2. Sample Quality Evaluation

The classification of sample quality proposed by Lunne *et al.* (1997) is based on the ratio of  $\Delta e/e_{v0}$ , where  $\Delta e$  is equal to  $e_0 - e_{v0}$ , *i.e.*, the difference between the void ratio  $e_0$  at the start of the oedometer consolidation test and the void ratio  $e_{v0}$  at the *in situ* vertical effective stress. Coutinho (2007) used the same ratio,  $\Delta e/e_{v0}$ , but suggested different limits, taking into consideration the fact that Brazilian soft clays are, in general, softer and more plastic than the Scandinavian clays used in the Lunne *et al.* (1997)'s study. Table 1 shows the criteria for classification of sample quality, including the ranges and limits of the overconsolidation ratios (OCR) used for each approach.

## 3. Brass and Reinforced PVC Soil Sampler Tubes

The PVC tube sampler was manufactured according to the recommendations of De Groot *et al.* (2005), with a 7° cutting edge (ABNT (1997) recommends an angle range between 5° and 10°, no internal clearance (Fig. 1), a 100 mm diameter, a 700 mm length and a wall thickness of 2.50 mm. The geometric and material characteristics of the tube samplers used in this study are presented in Table 2.

The cost of obtaining undisturbed soil samples is an important factor to be considered with respect to the overall sampling process, particularly in the Brazilian context. The prices for brass Shelby tube samplers used in three different projects are listed in Table 3. The table shows that the cost of soil sampling using reinforced PVC samplers varies between 47 % to 68 % relative to the cost of sampling with brass samplers. The main reason for this is the fact that the cost of the brass and PVC tubes are, respectively about 50 % and 10 % of the overall sampling cost, thus the PVC tube sampler is much cheaper than the brass sampler. It should be also noted that the time needed to manufacture and deliver brass tubes is usually about one month, whereas reinforced PVC tubes can easily be found, cut and put through the lathe.

**Table 1** - Criteria used to evaluate sample quality.

| $\Delta e/e_0$ (Lunne <i>et al.</i> , 1997) |                        |              |           |           |
|---|------------------------|--------------|-----------|-----------|
| OCR   | Very good to excellent | Good to fair | Poor      | Very poor |
| 1-2   | < 0.04                 | 0.04-0.07    | 0.07-0.14 | > 0.14    |
| 2-4   | < 0.03                 | 0.03-0.05    | 0.05-0.10 | > 0.10    |
| $\Delta e/e_0$ (Coutinho, 2007)             |                        |              |           |           |
| OCR   | Very good to excellent | Good to fair | Poor      | Very poor |
| 1-2.5                                       | < 0.05                 | 0.05-0.08    | 0.08-0.14 | > 0.14    |

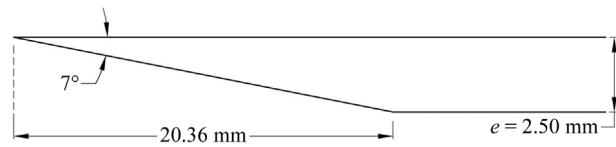


**Figure 1** - Detail of the PVC sampler cutting edge.

**Table 2** - Characteristics of the tube samplers used.

|   | Reinforced PVC <sup>1</sup> | Brass |
|---|-----------------------------|-------|
| Nominal diameter (mm)                             | 100                         | 100   |
| Wall thickness (mm)                               | 2.5                         | 1.58  |
| Rigidity modulus (GPa)                            | 3.2                         | 40    |
| Absolute roughness <sup>2</sup> - $\epsilon$ (mm) | 0.003                       | 0.007 |

<sup>1</sup>Commercial Ref. Amanco.

<sup>2</sup>Lencastre, 1996.

## 4. The Test Site

The area studied, shown in Fig. 2, is near the Macaé river, which flows into the Atlantic 2.5 km downstream from the city of Macaé.

The Macaé soft clay deposit was formed about 5000 years ago from sediments originating from the erosion of the surrounding mountains carried by tributary rivers, as

**Table 3** - Cost comparison - Extraction with PVC vs Brass 100 mm diameter soil tube samplers.

| Project   | Year | Location        | Material       | Cost of soil sample plus tube sampler-USD <sup>4</sup> /m |
|---|------|-----------------|----------------|---|
| Porto Alegre Airport - Cargo Apron <sup>1</sup> | 2014 | Porto Alegre/RS | Brass          | 316.18  |
| PCTEG <sup>2</sup>                              | 2015 | Guaratiba/RJ    | Brass          | 460.83  |
| Macaé Airport <sup>3</sup>                      | 2019 | Macaé/RJ        | Reinforced PVC | 215.38  |

<sup>1</sup>Public Bid Process 011/ADSU/SBPA/2012.

<sup>2</sup>Public Bid Process 02/2014 - 1ª RM.

<sup>3</sup>Private Bid Process.

<sup>4</sup>Currency exchange rate USD/BRL = 5.58.

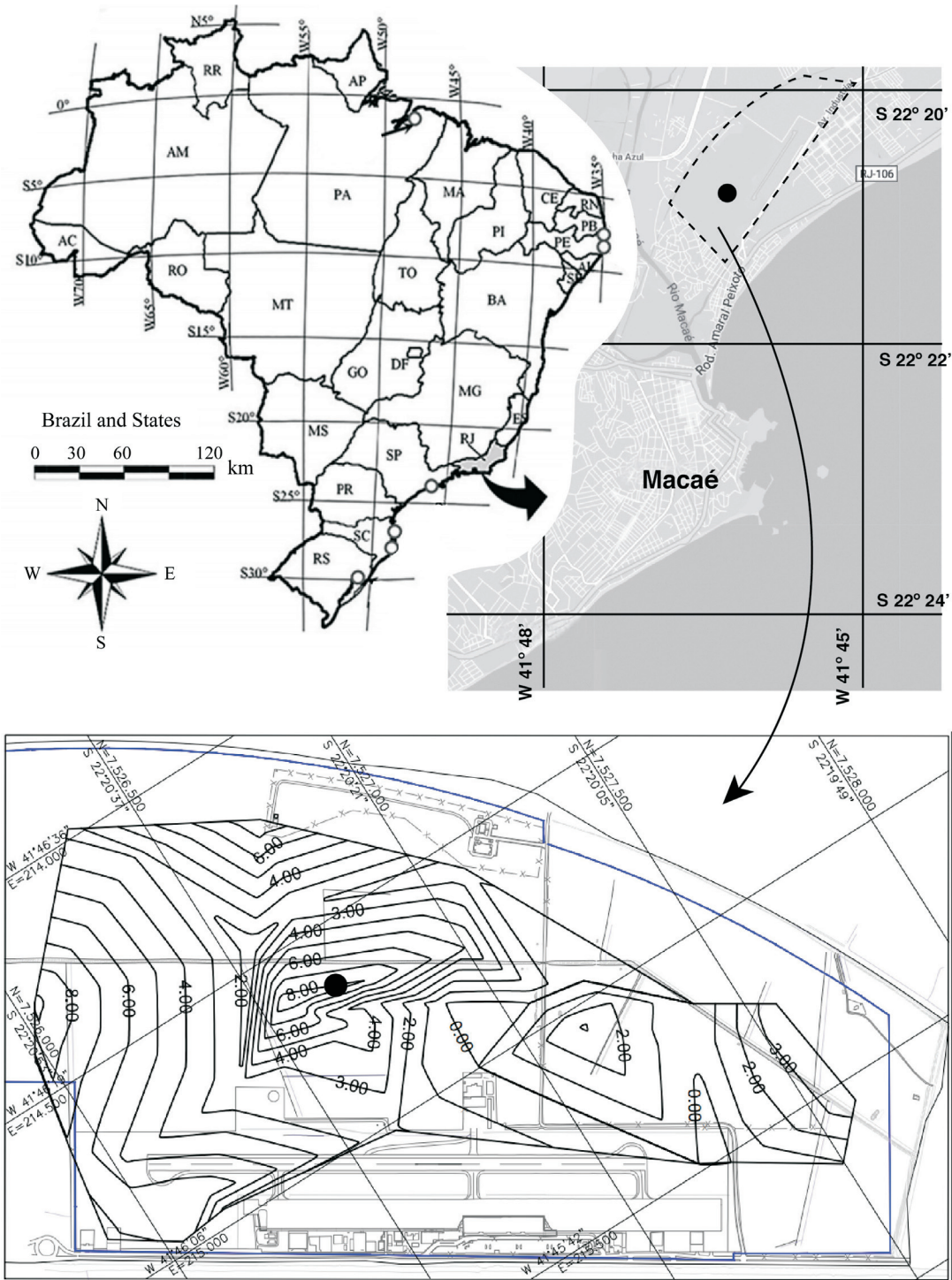


**Figure 2** - Curves of equal thickness for the Macaé Airport soft soil deposit.

well as from marine sediments deposited by sea regression (Martin *et al.*, 1984). Mineralogical tests performed on samples collected at the site showed that the clay fraction is composed primarily of kaolinite, although illite and/or smectite can also be found in smaller proportions. The organic matter content of this soil deposit, determined by the Embrapa Method (Embrapa, 1997), is around 6%. There-

fore, this clay can be classified as slightly organic (Mitchell & Coutinho, 1991).

The black hatched circle shown in Fig. 2, the deepest point of the soft soil at the airport site, represents the location studied in this article.

Figure 3 summarizes the main characteristics of the Macaé soft soil deposit based on the site investigation car-

ried out. The eight-meter thick very soft clay layer ( $N_{SPT} < 2$ ) overlies the fine to coarse sand layer. The water table at the site is just below ground surface and is influenced by sea level. Natural unit weight ( $\gamma_n$ ) varies from 11.5 to 14.5 kN/m<sup>3</sup> (Fig. 3a). The Macaé clay is very plastic and the plasticity index ( $I_p$ ) varies from 78 % to 85 %, measured without previous drying (Fig. 3b), with water content ( $w_n$ ) being slightly superior to the liquid limit ( $w_L$ ). Figure 3(c) shows that specific gravity ( $G_s$ ) is nearly constant and equal to 2.61, although at 7.0 and 8.0 m depth  $G_s$  is lower (about 2.10) due to organic matter. The *in situ* void ratio ( $e_0$ ), varies from 2.2 to 5.0 between one meter to eight meters depth, although from the surface to one-meter depth,  $e_0$  increases from 0.5 to 4.0 (Fig. 3d). Lower values of  $e_0$  near the surface (< 1.0 m depth) are due to a higher sand content and water level fluctuation. The Macaé site soil composition is a clayey silt with an average of 30 % clay, 60 % silt and 10 % sand, as shown in Fig. 3e.

When compared with other soft soil deposits in the state of Rio de Janeiro, Brazil, it is important to mention that the clay content of the studied deposit at the Macaé Airport is lower than other studied areas, such as Sarapuí (Almeida & Marques, 2003; Almeida *et al.*, 2008), and Barra da Tijuca (Baroni & Almeida, 2017 and Baroni & Almeida, 2012). In these other areas, the average clay content is 69 % for Sarapuí (Almeida & Marques, 2003), 70 % for the Juturnaiba deposit (Coutinho & Lacerda, 1987), and the Barra da Tijuca clay composition varies from 23 % to 80 % (Baroni & Almeida, 2012). Moreover, Póvoa *et al.* (2018) found a clay composition of 65 % for soft soil deposits about 5 km distant from this studied site at Macaé Airport.

For all of these sites, the water content is in the range 80-150 %, and close to the liquid limit. Nevertheless, the site in the present study has a lower clay content (an average of 30 % whereas other sites in Rio de Janeiro have, at least, 65 %), while other geotechnical parameters such as natural unit weight, water content, plasticity index and void

**Table 4** - Tests performed on the Macaé clay.

| Investigation        | Test types   |
|----------------------|--|
| <i>In situ</i> tests | SPT, CPTu (*), Vane tests (**)                                       |
| Laboratory tests     | Oedometer tests (see next section); triaxial tests (UU, CIU and CAU) |

(\*) COPPE/UFRJ equipment measuring  $u_1$  and  $u_2$ .

(\*\*) COPPE/UFRJ vane borer equipment.

ratio are consistent with the parameters found in the Sarapuí and Juturnaiba deposits for instance.

The site investigation for the Macaé clay included laboratory and *in situ* tests as summarized in Table 4.

The results of this site investigation are presented and a summary of the main findings of the triaxial, vane and piezocone tests is presented in Table 5.

### 5. Oedometer Consolidation Tests Results

Soil samples extracted from the site were transported to the laboratory according to local practice (Aguiar, 2008), which involved the sample being carried in a wooden box filled with damp saw dust to avoid disturbance and also to prevent water content loss. Once in the laboratory, the samples were handled according to recommendations in the literature (Ladd & De Groot, 2003).

**Table 5** - Summary of triaxial and vane test results.

| Parameter                       | Value / Range |
|---------------------------------|---------------|
| Peak friction angle $\phi'$ (°) | 38.3          |
| Cohesion $c'$ (kPa)             | 1.10          |
| Undrained strength $S_u$ (kPa)  | 10.6-18.0     |
| Average clay sensitivity $S_t$  | 4             |
| Piezocone cone factor $N_{kt}$  | 10            |
| Pore pressure ratio $B_q$       | 0.33          |

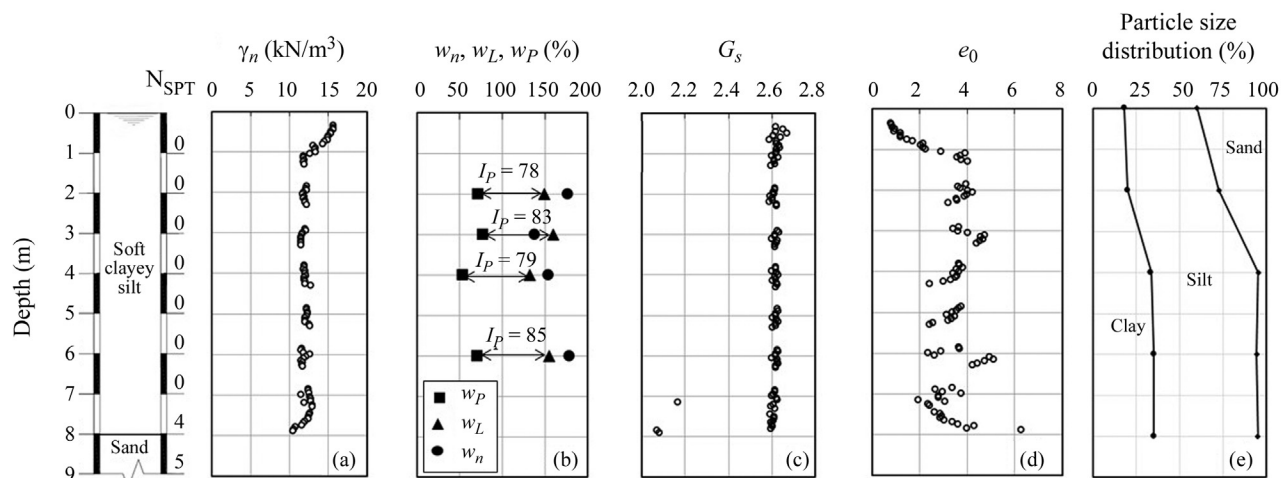


**Figure 3** - Characteristics of Macaé soft soil deposit.

The reinforced PVC tube sampler was used to extract three samples from the deposit, at depths of 2.5 m, 4.0 m and 6.0 m. Three additional samples (2.0 m distant from PVC borehole) were then extracted using the brass tube sampler at the same depths. Incremental loading 24 h oedometer tests were conducted on all samples using the same loading test sequence to enable comparison.

In total, eleven samples were extracted, however four of these showed atypical water content values and were, therefore, rejected at the beginning of the tests. One sample was classified as poor based on the Lunne *et al.* (1997) cri-

teria and was also rejected. Hence, six (three for each tube sampler type) out of eleven samples were analyzed in greater detail. The vertical effective stress *vs.* void ratio curves for each of these six tests are shown in Fig. 4, Fig. 5 and Fig. 6, respectively for samples at 2.5 m, 4.0 m and 6.0 m of depth from the borehole SP 16. These figures show the complete curve ( $\log \sigma'_v$  *vs.*  $e$ ) on the left, and on the right, the preconsolidation stress region in greater detail, with a modified scale to better visualize the preconsolidation stress values, calculated using the Pacheco Silva method.

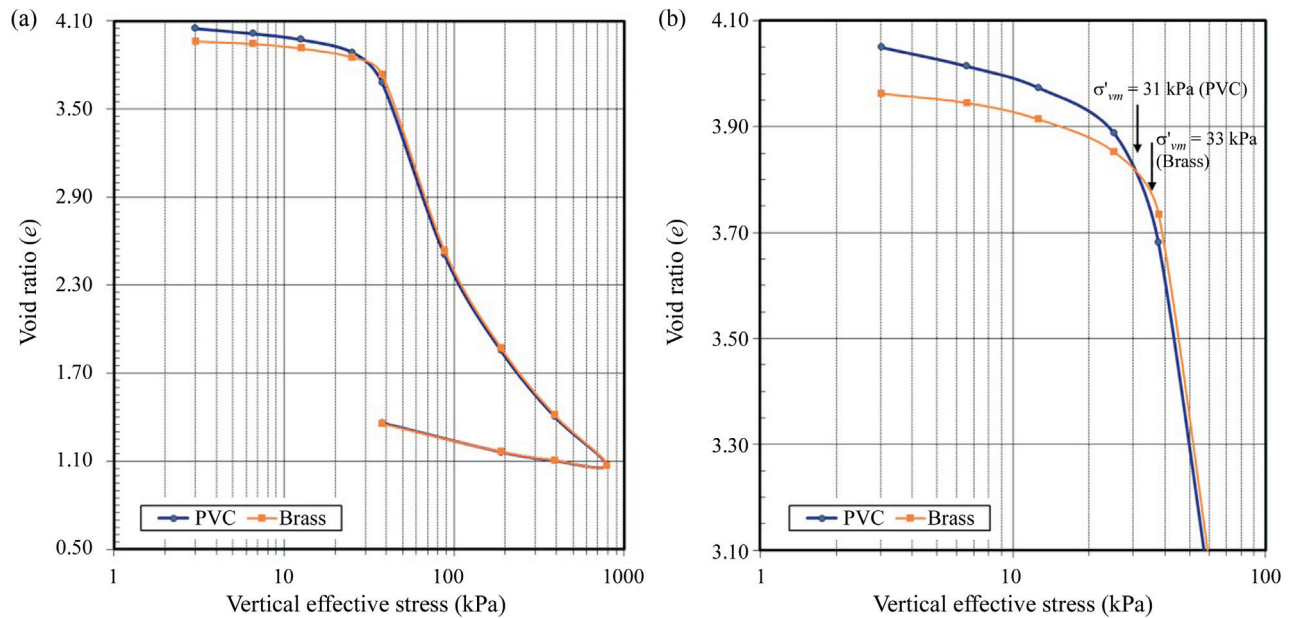


**Figure 4** - (a)  $\log(\sigma'_v)$  *vs.*  $e$  curve at SP 16 - 2.5 m ; (b) Detail at Preconsolidation Stress region.

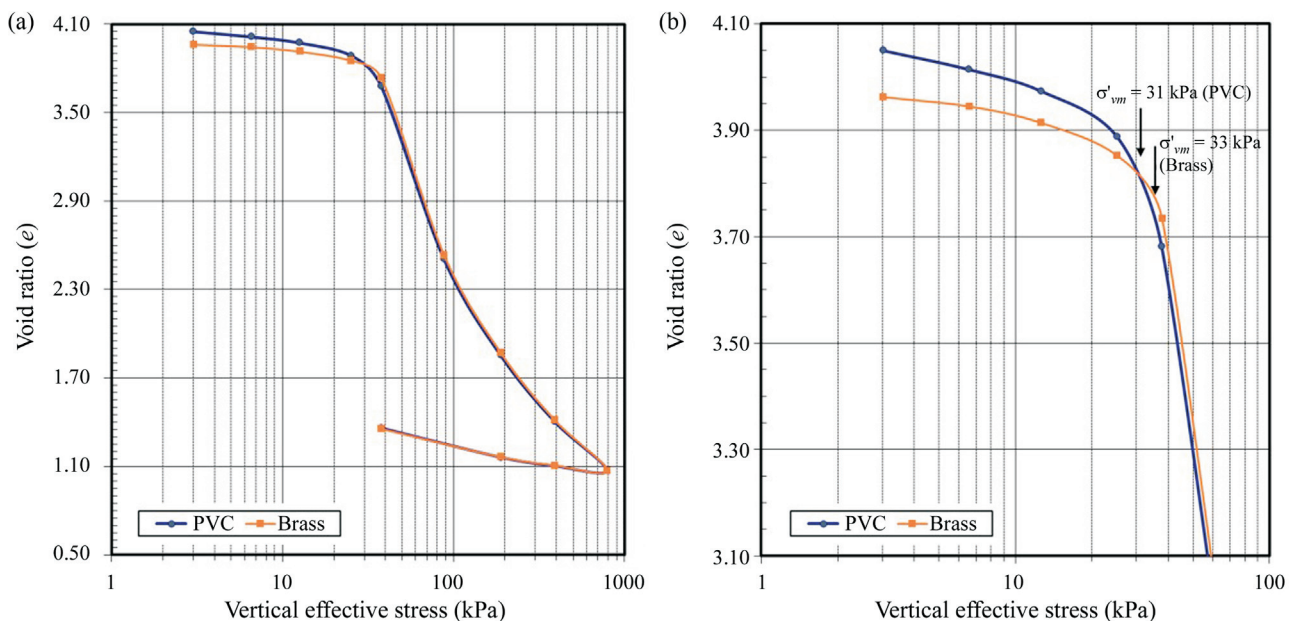


**Figure 5** - (a)  $\log(\sigma'_v)$  *vs.*  $e$  curve at SP 16 - 4 m ; (b) Detail at Preconsolidation Stress region.

A summary of the six oedometer tests is presented in Table 6.

An overall summary, with average values of the compressibility and consolidation data for the Macaé clay, is shown in Table 7.

### 6. Summary and Discussion

The last two columns of Table 6 present the sample quality according the criteria proposed by Lunne *et al.* (1997) and Coutinho (2007), for the six samples analyzed. The sampling process *in situ* was conducted quite carefully, which is not common in engineering practice. The study also closely followed the recommendations found in the lit-

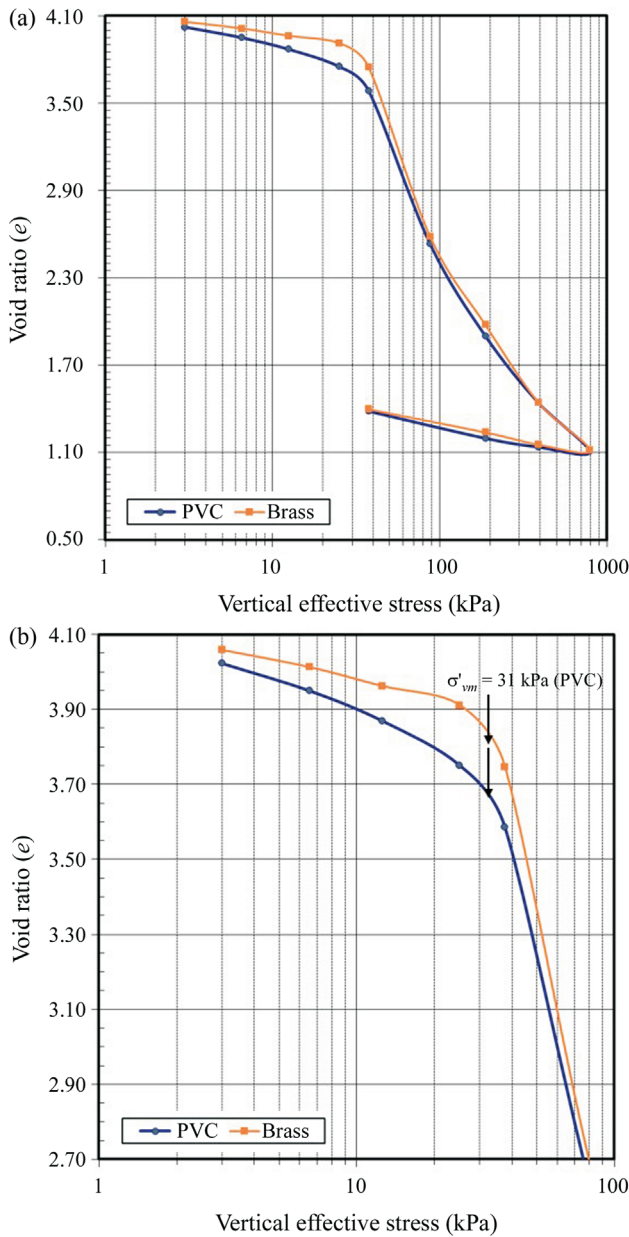


**Figure 6** - (a)  $\log(\sigma'_v)$  vs.  $e$  curve at SP 16 - 6 m ; (b) Detail at Preconsolidation Stress region.

**Table 6** - Summary of the oedometer test results.

| Sample        | Sample tube material | z (m) | $w_n$ (%) | $e_0$ | $e_{s0}$ | OCR  | $C_c^1$ | $C_s^2$ | Quality        |                        |                        |
|---------------|----------------------|-------|-----------|-------|----------|------|---------|---------|----------------|------------------------|------------------------|
|               |                      |       |           |       |          |      |         |         | $\Delta e/e_0$ | Coutinho (2007)        |                        |
| SP 16 - 2.5 m | Brass                | 2.5   | 153.97    | 3.96  | 3.92     | 3.69 | 1.99    | 0.19    | 0.011          | very good to excellent | OCR > 2.5              |
|               | PVC                  | 2.5   | 153.49    | 4.05  | 3.98     | 3.52 | 1.99    | 0.19    | 0.015          | very good to excellent | OCR > 2.5              |
| SP 16 - 4 m   | Brass                | 4.0   | 153.39    | 4.06  | 3.94     | 2.34 | 1.81    | 0.25    | 0.027          | very good to excellent | very good to excellent |
|               | PVC                  | 4.0   | 149.89    | 4.02  | 3.82     | 2.27 | 1.95    | 0.19    | 0.048          | good to fair           | very good to excellent |
| SP 16 - 6 m   | Brass                | 6.0   | 144.49    | 3.93  | 3.79     | 1.89 | 2.14    | 0.16    | 0.033          | very good to excellent | very good to excellent |
|               | PVC                  | 6.0   | 146.48    | 3.97  | 3.84     | 1.96 | 2.29    | 0.16    | 0.031          | very good to excellent | very good to excellent |

<sup>1</sup> $C_c$  = compression index.

<sup>2</sup> $C_s$  = swelling index.

**Table 7** - Summary of the compressibility and consolidation parameters for the Macaé Clay.

| Parameter   | Average value        |
|---|----------------------|
| Compression ratio: $CR = C_c / (1 + e_0)$   | 0.39                 |
| $C_s / C_c$   | 0.10                 |
| Coefficient of vertical consolidation ( $c_v$ ) at normal consolidation condition ( $m^2/s$ ) | $3.2 \times 10^{-8}$ |

erature (Ladd & De Groot, 2003; De Groot *et al.*, 2005; Aguiar, 2008), which may explain the good values of  $\Delta e/e_0$  found in here. The use of samplers with a 7° cutting edge (within the 5° to 10° range indicated by ABNT (1997)), as well as no internal clearance also facilitated insertion of both tube samplers.

Overall, the values of  $\Delta e/e_0$  for the PVC tubes samples are on average 36 % higher than  $\Delta e/e_0$  values for reinforced brass tube at the same depth. Although higher  $\Delta e/e_0$  values were observed in the PVC samples relative to brass samples, this was found to be relatively insignificant, as it did not change the sample quality classifications based on Lunne *et al.* (1997) and Coutinho (2007).

These findings are consistent with other recent campaigns conducted in Brazil. Jannuzzi *et al.* (2013) reported excellent and good to fair quality samples at the Sarapuí II deposit in four out of six PVC tube samples, therefore, 67 %, according to Lunne *et al.* (1997). Marques *et al.* (2017) used PVC tube samplers at Guaratiba/RJ and reported a lower percentage for excellent and good to fair quality samples (3 out of 6 samples; 50 %). In the present study, 55 % of the original eleven samples were considered excellent and good-to-fair quality according to Lunne *et al.* (1997) or Coutinho (2007). However, it is important to mention that atypical water content values presented a major problem in four of those samples and they were therefore excluded from the analysis. Essentially, only one of the original samples was considered poor according to the criteria. Table 8 compares the brass and reinforced PVC tube samplers showing their advantages and disadvantages. The greater stiffness of the brass tubes seems to explain the smaller  $\Delta e/e_0$  ratio compared with values from samples extracted with the PVC tubes. The greater stiffness reduces the strain on the tubes resulting in smaller sample disturbance. However, this is not sufficient reason for rejecting the use of PVC tubes as they have important advantages over the brass tube sampler, in terms of cost, time and handling.

## 7. Conclusion

The quality of samples extracted *in situ* is a fundamental factor in obtaining accurate geotechnical parameters. In this study, the use of reinforced PVC tube soil samplers (700 mm long, with a 7 degree chamfered cutting edge and no internal clearance) for extracting undisturbed soil samples was shown to be feasible, with advantages in

**Table 8** - Comparison between brass and reinforced PVC tube samplers.

| Tube type      | Advantages   | Disadvantages                         |
|----------------|--|---------------------------------------|
| Brass          | Traditionally used; greater stiffness  | greater cost, greater roughness index |
| Reinforced PVC | Lower cost, shorter delivery time, lower roughness index, easier to cut and trim | Smaller stiffness                     |

terms of cost, time and handling. Oedometer tests were conducted to compare the results of tests performed on the samples obtained using the brass and PVC samplers. Indeed, based on the sample quality criteria of both Lunne *et al.* (1997) and Coutinho (2007), most of the samples were assessed to be in the “very good to excellent” range.

Although the wall of the PVC tube soil sampler is thicker than the brass tubes, yielding a lower rigidity module, good results were achieved due to: i) the absence of internal clearance on the sampler; ii) the lower absolute roughness of the PVC compared to the brass tube; and iii) the use of careful and patient sample handling and trimming in the extraction process.

Despite the limited number of samples in this study, the results are still encouraging and are consistent with the findings of Jannuzzi *et al.* (2013) and Marques *et al.* (2017). In this context, the findings indicate that the use of PVC samplers enable cost and operational time savings when compared with brass tubes, without compromising sample quality.

## References

- ABNT (1997). Assessment of Undisturbed Low Consistency Solid Samples from Boreholes - Procedure - NBR 9820. Rio de Janeiro, Brazil, 5 p. (in Portuguese).
- Aguiar, V.N. (2008). Consolidation Characteristics from Santos Port Channel Clay at Barnabé Island Region. M.Sc. Dissertation, COPPE, Federal University of Rio de Janeiro, Rio de Janeiro, Brasil, 223 p. (in Portuguese).
- Almeida, M.S.S. & Marques, M.E.S. (2003). The behaviour of Sarapuí soft clay. Tan, T.S.; Phoon, K.K.; Hight, D.W. & Leroueil, S. (eds), Characterisation and Engineering Properties of Natural Soils. Balkema, Rotterdam, v. 1, pp. 477-504.
- Almeida, M.S.S.; Futai, M.M.; Lacerda, W.A. & Marques, M.E.S. (2008). Laboratory Behaviour of Rio de Janeiro Soft Clays - Part 1. Soils & Rocks, 31(2):69-75.
- Andresen, A. (1981). Exploration, sampling and in-situ testing of soft clay. Soft clay engineering. Brand, E.W. & Brenner, R.P. (eds) Developments in Geotechnical Engineering, v. 20. Elsevier, Amsterdam, pp. 245-308.
- Baroni, M. & Almeida, M.S.S. (2012). In situ and laboratory parameters of extremely soft organic clay deposits. Proc. 4th International Conference on Geotechnical and Geophysical Site Characterization (ISC'4), Porto de Galinhas, Pernambuco, Brazil, v. 2, pp. 1611-1619.

- Baroni, M. & Almeida, M.S.S. (2017). Compressibility and stress history of very soft organic clays. *Proc. ICE - Geotechnical Engineering*, v. 170, p. 148-160.
- Bertuol, F.; Bressani, L.A. & Bica, A.V.D. (2009). Development of sampler for low consistency soils. *Proc.V Seminário de Engenharia Geotécnica do Rio Grande do Sul (GEORS)*, Pelotas (in Portuguese).
- Coutinho, R.Q. (2007). Characterization and Engineering Properties of Recife Soft Clays - Brazil. The 2<sup>nd</sup> International Workshop on Characterization and Engineering Properties of Natural Soils. Tan, T.S.; Phoon, K.K.; Hight, D.W. & Leroueil, S. (eds), Singapore, v. 3, pp. 2049-2100.
- Coutinho, R.Q. & Lacerda, W.A. (1987). Characterization - Consolidation of Juturnaíba organic clay. *Proc. International Symposium on Geotechnical Engineering of Soft Soil, Mexico*, v.1, pp. 17-24.
- De Groot, D.J.; Poiriermelissa, S.E. & Landon, M. (2005). Sample disturbance - Soft clay. *Studia Geotechnica et Mechanica*, 27(3-4):91-105.
- Di Buò, B.; Selänpää, J.; Länsivaara, T.T. & D'Ignazio, M. (2019). Evaluation of sample quality from different sampling methods in Finnish soft sensitive clays. *Canadian Geotechnical Journal*, 56(8):1154-1168.
- EMBRAPA (1997). *Manual for Soil Analysis Methods*. Centro Nacional de Pesquisa de Solos, Rio de Janeiro, Brazil, pp. 85-87 (in Portuguese).
- Hight, D.W. (2001). Sampling effects in soft clays: an update on Ladd and Lambe (1963). *ASCE, Symposium on Soil Behaviour and Soft Ground Construction*. ASCE Geotechnical Special Publication, v. 119, pp. 86-121.
- Hight, D.W.; Boese, R.; Butcher, A.P.; Clayton, C.R.I. & Smith, P.R. (1992). Disturbance of Bothkennar clay prior to laboratory testing. *Géotechnique*, 42(2):99-217.
- Hvorslev, M.J. (1949). *Subsurface Exploration and Sampling of Soils for Civil Engineering Purposes*. Waterways Experiment Station, Vicksburg, USA.
- Januzzi, G.M.F.; Danziger, F.A.B. & Martins, I.S.M. (2013). Surprising soil behaviour in soil sampling. *Soils and Rocks*, 36(3):265-274.
- Kallstenius, T. (1963). Studies on clay samples taken with standard piston sampler. *Proc. Royal Swedish Geol. Inst.*, v. 21, pp. 210.
- Karlsson, M.; Emdal, A. & Dijkstra, J. (2016). Consequences of sample disturbance when predicting long-term settlements in soft clay. *Canadian Geotechnical Journal*, 53(12):1965-1977.
- La Rochelle, P.; Sarrailh, J.; Tavenas, F.; Roy, M. & Leroueil, S. (1981). Causes of sampling disturbance and design of a new sampler for sensitive soils. *Canadian Geotechnical Journal*, 18(1):52-66.
- Ladd, C.C. & De Groot, D.J. (2003). Recommended practice for soft ground site characterization. *Proc. 12th Panamerican Conference on Soil Mechanics and Geotechnical Engineering*, Cambridge, v. 1, pp. 3-57.
- Lencastre, A. (1996). *General Hydraulics*. Author Edition, Lisbon, 651 p. (in Portuguese).
- Lefebvre, G. & Poulin, C. (1979). A new method of sampling in sensitive clay. *Canadian Geotechnical Journal*, 16(1):226-233.
- Lim, G.T.; Pineda, J.; Boukpeti, N.; Carraro, J.A.H. & Fourie, A. (2019). Effects of sampling disturbance in geotechnical design. *Canadian Geotechnical Journal*, 56(2):275-289.
- Lunne, T. (2009). Soil design parameters in soft clay and importance of sample disturbance (Information). *Soil Mechanics and Foundation Engineering*, 46(6):232-235.
- Lunne, T. & Long, M. (2006) Review of long seabed samplers and criteria for new sampler design. *Marine Geology*, 226(1-2):145-165.
- Lunne, T.; Berre, T.; Andersen, K.; Strandvik, S. & Sjørusen, M. (2006). Effects of sample disturbance and consolidation procedures on measured shear strength of soft marine Norwegian clays. *Canadian Geotechnical Journal*, 43(7):726-750.
- Lunne, T.; Berre, T. & Strandvik, S. (1998). Sample disturbance effects in deep water soil investigations. *Offshore Site Investigation and Foundation Behaviour*. New Frontiers. In Society for Underwater Technology (SUT) Conference London, pp. 199- 220.
- Lunne, T.; Berre, T. & Strandvik, S. (1997). Sample disturbance effects in soft low plastic Norwegian clay. *Proc. of the Conference on Recent Developments in Soil and Pavement Mechanics*, Rio de Janeiro, Brazil, pp. 81-102.
- Marques, M.E.S.; Berbert, L.A.; Abreu, A.V. & Slongo, G.R. (2017). Sample quality on compressible soils. *Revista Fundações*, 76:54-64.
- Martin, L.; Suguio, K.; Flexor, J.M.; Dominguez, J.M.L. & Azevedo, A.E.G. (1984). Evolution of Coastal Quaternary Formation at Paraíba do Sul (RJ) river: Influence of Sea Level Fluctuations. *Proc. of the 23<sup>rd</sup> Brazilian Conference on Geology*, Rio de Janeiro. v.1 pp. 84-97. (in Portuguese).
- Mitchell, J.K. & Coutinho, R.Q. (1991). Occurrence, geotechnical properties, and special problems of some soils of America. *Special Report for the Ninth Panamerican Conference on Soil Mechanics and Foundation Engineering*, Viña del Mar, Chile, v. 4, pp. 1651-1741.
- Póvoa, L.M.M.; Nascimento P.N.C & Maia P.C.A. (2018). Laboratory parameters of a soft soil deposit in Macaé, Brazil. *Soils & Rocks*, 41(1):3-16.
- Tanaka, H. & Tanaka, M. (1999). Key factors governing sample quality. Tsuchida, N. (ed), *Characterization of Soft Marine Clays*. Balkema, Rotterdam, pp. 57-81.
- Tanaka, H.; Sharma, P.; Tsushida, T., & Tanaka, M. (1996). Comparative study on sample quality using several types of samplers. *Japan, Soils and Foundations*, 36(2):57-67.

## **Case Study**

**Soils and Rocks**  
**v. 43, n. 2**



# Influence of Weathering and Correlations Between Wave Propagation Velocity and Durability with Physical and Mechanical Parameters in Phyllites

T.R.R. Carvalho, M.F. Leão, E.A.G. Marques

**Abstract.** Ultrasonic longitudinal wave velocity ( $V_p$ ) and durability are characteristics largely determined in geotechnical evaluations. These properties are useful in the analysis of weathered rocks because they usually have good relationships with physical and mechanical properties of rocks. Additionally, the tests to obtain these parameters are easy to perform. However, few studies have been performed specifically on low degree metamorphic rocks. The purpose of this study is to evaluate the influence of weathering on these parameters, as to propose correlations between  $V_p$  and some mechanical and physical parameters. This study was carried out using phyllites from three weathering profiles located along the highway BR-356, Minas Gerais, Brazil. The results reveal a clear influence of weathering on  $V_p$  and durability mainly due to increased porosity. However, as the variation of this parameter is heterogeneous, the relationship between  $V_p$ , durability, and weathering is not uniform, although they present general trends. The behavior shown by porosity reflects the complex role of chemical weathering on fractures. The non-uniform pattern of  $V_p$  and durability throughout the weathering classes is also a consequence of the heterogeneity and anisotropy intrinsic to these phyllites. The empirical relationships established exhibit good correlation coefficients.

**Keywords:** correlations, durability, Minas Gerais, phyllite, wave propagation velocity, weathering.

## 1. Introduction

Ultrasonic wave propagation test is non-destructive, easy to apply, and thus has been increasingly employed in the characterization of rocks for engineering purposes, including the determination of effects of weathering on rocky materials.

Several researchers have studied the relationship between ultrasonic longitudinal wave propagation velocity ( $V_p$ ) and rock properties, finding an intimate relationship between them (Gardner *et al.*, 1974; Gaviglio, 1989; Souza *et al.*, 2005; Çobanoğlu & Çelik, 2008; Sharma *et al.*, 2011; Nefeslioglu, 2013; Jamshidi *et al.*, 2016; Wen *et al.*, 2018; Kanji & Leão, 2020). Although many attempts have been performed to correlate  $V_p$  with physical and mechanical rock properties, few studies have focused on low and medium degree metamorphic rocks (Sharma & Singh, 2008; Sarkar *et al.*, 2012; Khandelwal, 2013).

Ultrasonic longitudinal wave propagation velocity ( $V_p$ ) in rocks is influenced by many factors such as lithology, density, porosity, grain size and shape, anisotropy, confinement pressure, weathering, bedding, joint characteristics (fill material, water, direction, dip, among others) (Kahraman, 2001).

Weathering is known to lead to rapid changes in the properties of rock materials. Alterations of a particular rock type and their rate of occurrence (alterability) are often described by a durability parameter (Crosta, 1998) known as the durability index ( $I_d$ ) and obtained through slake durability test.

The slake durability test is used to evaluate the resistance to rock alteration as a function of the disintegration resulting from a standard wetting and drying cycle (Franklin & Chandra, 1972). Durability is a characteristic largely affected by mineralogy, texture, porosity, and water content and is strongly related to the history of alteration after its formation (Koncagül & Santi, 1999; Cetin *et al.*, 2000; Dhakal *et al.*, 2002; Yilmaz & Karacan, 2005; Gupta & Ahmed, 2007; Ioanna *et al.*, 2009).

In this sense, this study shows the effects of weathering on  $V_p$  and durability, as well as the correlation between these properties and physical and mechanical parameters in phyllites from the region of Minas Gerais, Brazil.

Phyllites were collected in road slopes located in the state of Minas Gerais, Brazil. These slopes are inserted in the geological context of the Iron Quadrangle, an important mineral province of Brazil, consisting of five main lithostratigraphic units (Alkmim & Marshak, 1998): crystalline

---

Tatiane Robaina Rangel de Carvalho, Ph.D. Student, Departamento de Engenharia Civil, Universidade Federal de Viçosa, Viçosa, MG, Brazil. e-mail: tatianerrcarvalho@gmail.com.

Marcio Fernandes Leão, D.Sc., Senior Research, Departamento de Engenharia Civil, Universidade Federal de Viçosa, Viçosa, MG, Brazil. e-mail: marciotriton@hotmail.com.

Eduardo Antonio Gomes Marques, D.Sc., Full Professor, Departamento de Engenharia Civil, Universidade Federal de Viçosa, Viçosa, MG, Brazil. e-mail: eagmarques1965@gmail.com.

Submitted on March 31, 2020; Final Acceptance on April 22, 2020; Discussion open until September 30, 2020.

DOI: 10.28927/SR.432297

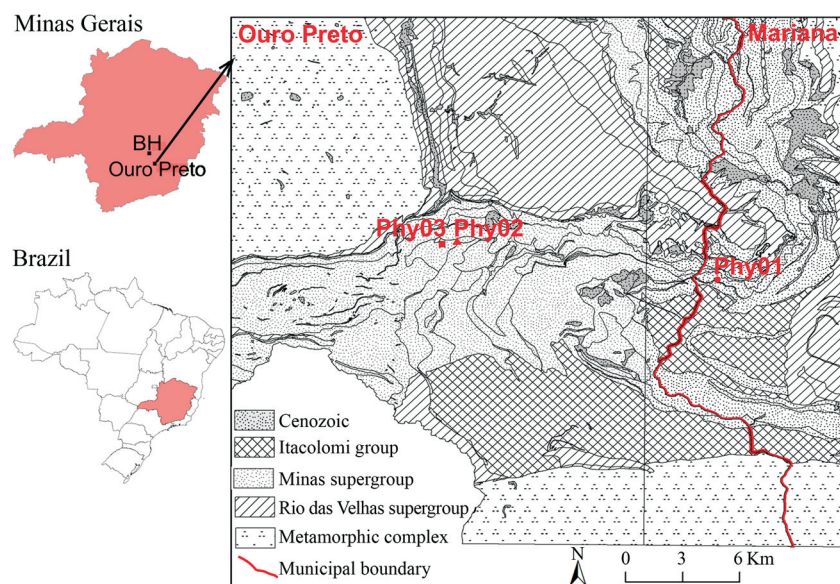


**Figure 1** - Geological map with the location of the studied weathering profiles, located in the contiguous cities of Mariana (Phy01) and Ouro Preto (Phy02 and Phy03) (adapted from da Silva *et al.*, 2005; Romano *et al.*, 2017). Ouro Preto is approximately 100 km from the capital of the State of Minas Gerais (Belo Horizonte, BH), Brazil.

basement, metamorphic complexes of Archean age; Rio das Velhas Supergroup, consisting of an Archean volcano-sedimentary sequence (greenstone belt); Minas Supergroup, formed by Proterozoic, metamorphosed, and folded sediments; post-Minas intrusions; Itacolomi Group, consisting of Proterozoic clastic metasediments. As shown in Fig. 1, the studied phyllites belong to the Minas Supergroup.

## 2. Methodology

Phyllite samples at different degrees of weathering were taken from three road slopes located along BR-356 in the state of Minas Gerais, Brazil (Table 1). The degrees of weathering were identified in each profile from the classification proposed by the International Society of Rock Mechanics (ISRM, 2015).

These samples were taken for laboratory tests to obtain physical indices, wave propagation velocity, point load strength index, durability, and mineralogical analysis. It is part of the scope of this paper to present and discuss  $V_p$  and durability data for materials at different levels of weathering, as well as correlate the properties  $V_p$  and durability,  $V_p$  and physical indices, and  $V_p$  and the point load strength ( $Is_{(50)}$ ). Tests were performed according to the suggestions of ISRM (2007).

Listed next are the number of samples used for each weathering class contemplated in this study: 13 from phyllite W1/W2, 19 from phyllite W2, 20 from phyllite W2/W3, 38 from phyllite W3, 23 from phyllite W3/W4, 19 from phyllite W4.

Least-squares regression analyses were applied between  $V_p$  and durability,  $V_p$  and physical indices, and  $V_p$

and  $Is_{(50)}$  to verify the possible relationships between these properties. The best-fit line and the correlation coefficients were determined. Different relationships (linear, exponential, logarithmic, and power) were tested in order to obtain the highest correlation coefficient values.

**Table 1** - Degrees of weathering of phyllites sampled for laboratory tests. The classification was carried out according to ISRM (2015) guidelines.

| Weathering profiles | Class   | Term  |
|---------------------|---|-------|
| Phy01               | Slightly weathered rock                         | W2    |
|                     | Moderately weathered rock                       | W3    |
|                     | Highly weathered rock                           | W4    |
| Phy02               | Sound to slightly weathered rock                | W1/W2 |
|                     | Slightly weathered rock                         | W2    |
|                     | Slightly weathered to moderately weathered rock | W2/W3 |
|                     | Moderately weathered rock                       | W3    |
| Phy03               | Moderately weathered to highly weathered rock   | W3/W4 |
|                     | Moderately weathered rock                       | W3*   |
|                     | Highly weathered rock                           | W4    |

\*In the Phy03 profile, three distinct collection points of the moderately altered phyllite (W3) were chosen to evaluate the influence of possible textural and mineralogical differences.

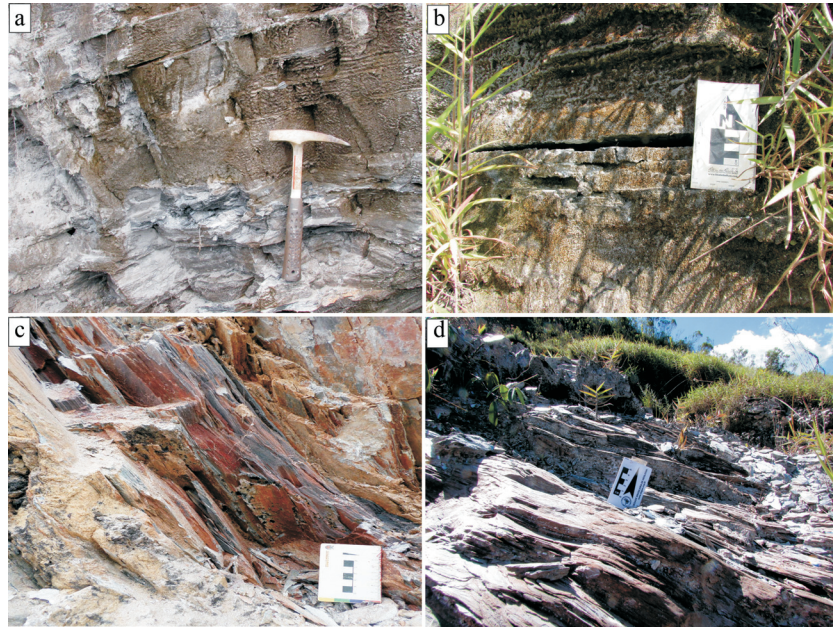


**Figure 2** - Outcrops of phyllite W3 (a) and W4 (b) from profile Phy01, W3/W4 from profile Phy02 (c), and W3 from profile Phy03 (d), highlighting discontinuities parallel to foliation resulting from exposure of these rocks to weathering.

### 3. Results and Discussions

#### 3.1. Main characteristics of the studied phyllites

The studied phyllites are composed of muscovite, quartz, opaque minerals and chlorite. The main products of weathering on primary minerals are iron oxide/hydroxide and kaolinite. Foliation is penetrative, millimeter-spaced, formed by the alternation of thin micaceous bands, quartz-micaceous bands, and quartz veins. There are also veins consisting of chlorite and opaque minerals, parallel to metamorphic foliation.

One of the main effects of the exposure of these rocks to atmosphere conditions is the formation of fractures parallel to the metamorphic foliation, which intensifies with the advancement of weathering (Fig. 2). There is also increased openness of these discontinuities that become more degraded in the most altered members. This striking characteristic observed in the studied profiles is also noticeable in the petrographic slide due to the presence of micro-fractures, especially transgranular and intragranular (Fig. 3). As physical weathering is processed, creating preferential spaces for water to enter the rock, opaque minerals are dissolved and iron oxides are precipitated. These results are in agreement with studies carried out in phyllites under tropical (Leão *et al.*, 2017) and subtropical (Marques *et al.*, 2017; Marques *et al.*, 2020; Robert & Hack, 2020) climates. Figures 4, 5, and 6 show the main implications of weathering on the matrix of this rock.

#### 3.2. Physical indices

Dry and saturated apparent specific gravity, apparent porosity, and apparent water absorption capacity are shown

in Table 2. Physical parameters are clearly influenced by weathering processes. However, the variation of these parameters is not homogeneous in soil-rock transition materials (W3, W3/W4, and W4). It is mainly due to the increased number of micro-fractures and the widening of pre-existing discontinuities parallel to metamorphic foliation. This increase in porosity with the advancement of weathering is also accompanied by higher precipitation of iron oxide/hydroxide rich solutions, as previously discussed. These characteristics occur most sharply from phyllite W3. Sousa *et al.* (2005) observed that, unlike what happened in intact or slightly altered granites, the porosity variation was not homogeneous in a very altered granite. This is due, according to the authors, to the action of weathering on micro-fractures, making their performance increasingly complex and reflecting on the physical characteristics of the rock.

#### 3.3. Durability

The lowest obtained durability index corresponds to phyllite W3 from profile Phy01 (Table 3). It can be explained by the reduced internal cohesion of its matrix, which was also pointed out by Leão *et al.* (2017) in altered sericite phyllites from the same site. These phyllites are characterized by levels of mafic and siliceous minerals that fill foliation (Fig. 4). Leão (2017) performed durability studies on phyllites located in profile Phy01 and obtained nonlinear behavior of  $I_{d2}$  values among phyllites with different degrees of weathering. The author attributed this behavior to the presence of cemented levels, whose origin would not be the result of the weathering action. These levels are unevenly distributed throughout the profile, causing heterogeneities in the rock. Thus, the conclusion reached

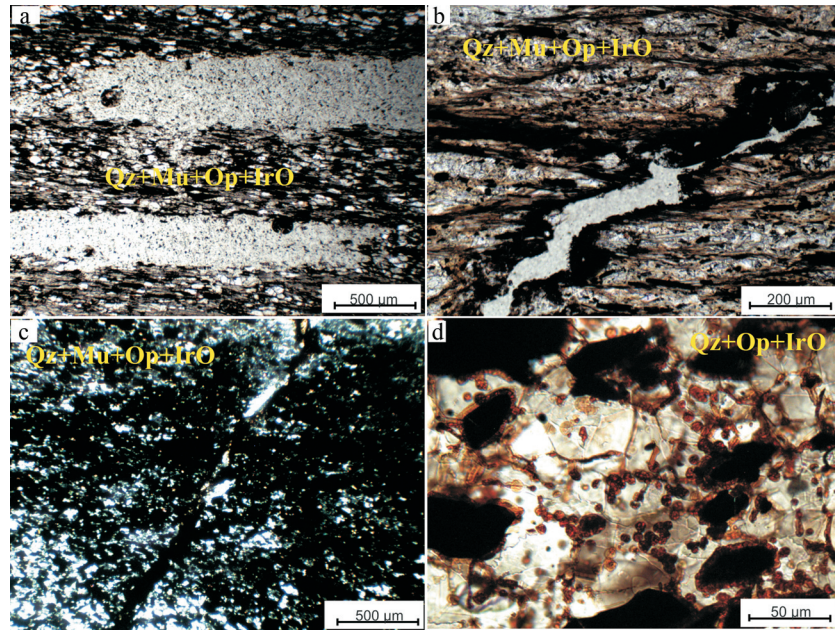


**Figure 3** - Textural and mineralogical aspects of phyllites in petrographic slides. Slides are from samples collected from profile Phy03. The abbreviation means: *IrO* iron oxides/hydroxides; *Mu* muscovite; *Op* Opaque; *Qz* quartz. In (a) there is a fracture parallel to metamorphic foliation (phyllite W3). In (b and c) there is a transgranular fracture and precipitation of iron oxides/hydroxides due to the weathering of opaque (phyllite W3 and W4, respectively). In (d) there is a precipitation of iron oxides/hydroxides in the matrix and intragranular fractures of quartz grains (phyllite W3).

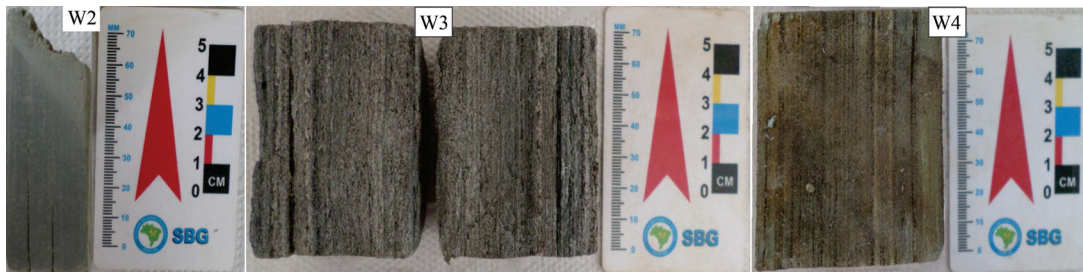


**Figure 4** - Aspects of the phyllite matrix at different degrees of weathering of profile Phy01. Scale in centimeters (cm). SBG - Brazilian Geological Society.

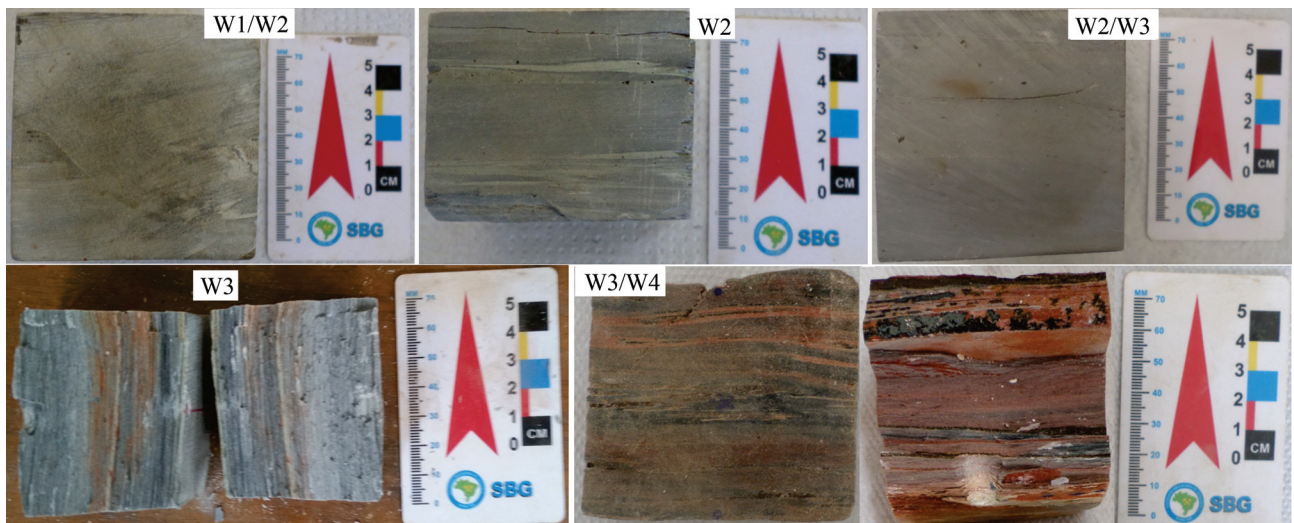


**Figure 5** - Aspects of the phyllite matrix at different degrees of weathering of profile Phy02. Scale in centimeters (cm). SBG - Brazilian Geological Society.

by this author is in agreement with the results from the present study, as these same levels were also identified in this research, which would explain the increase in durability found in phyllite W4 in relation to W3 from profile Phy01.

In profile Phy02,  $I_{d2}$  values obtained for slightly altered phyllites (W1/W2, W2, and W2/W3) are above 90 %.

Similar values were found by Ramamurthy *et al.* (1993) (97.56 % for intact micaceous phyllites), Andrade & Saraiya (2010) (90.7 to 98.9 % for phyllites W1 and W2), Marques *et al.* (2010) (durability values higher than 95 % for gneisses W1 and W2), and Silva & Lana (2012) (90.36 to 91.56 % for sericite phyllites W2).

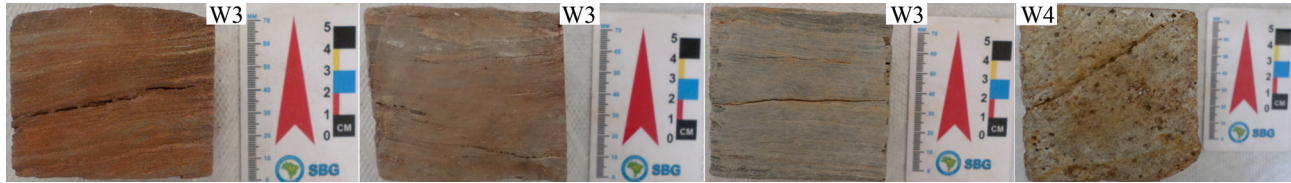


**Figure 6** - Aspects of the matrix of weathered phyllites of profile Phy03. Samples of phyllite W3 were collected from three different points of the profile, demonstrating the heterogeneity of the rock. Scale in centimeters (cm). SBG - Brazilian Geological Society.

**Table 2** - Mean (M) and standard deviation (SD) of values of dry ( $\rho_{dry}$ ) and saturated ( $\rho_{sat}$ ) apparent specific gravity, apparent porosity ( $\eta$ ), and apparent water absorption (*abs*) for different classes of phyllite weathering of the three weathering profiles.

|       | Class | $\rho_{dry}$ (g/cm <sup>3</sup> ) | SD (g/cm <sup>3</sup> ) | $\rho_{sat}$ (g/cm <sup>3</sup> ) | SD (g/cm <sup>3</sup> ) | $\eta$ (%) | SD (%) | <i>abs</i> (%) | SD (%) |
|-------|-------|-----------------------------------|-------------------------|-----------------------------------|-------------------------|------------|--------|----------------|--------|
| Phy01 | W2    | 2.79                              | 0.03                    | 2.85                              | 0.03                    | 6.06       | 0.25   | 2.18           | 0.11   |
|       | W3    | 2.38                              | ND*                     | 2.53                              | ND                      | 14.29      | ND     | 6.00           | ND     |
|       | W4    | 1.95                              | ND                      | 2.09                              | ND                      | 14.07      | ND     | 7.23           | ND     |
| Phy02 | W1/W2 | 2.8                               | 0.01                    | 2.84                              | 0.01                    | 4.17       | 0.19   | 1.49           | 0.07   |
|       | W2    | 2.72                              | 0.02                    | 2.78                              | 0.02                    | 6.14       | 0.43   | 2.26           | 0.17   |
|       | W2/W3 | 2.75                              | 0.05                    | 2.83                              | 0.04                    | 8.57       | 0.29   | 3.12           | 0.16   |
|       | W3    | 2.44                              | 0.03                    | 2.59                              | 0.03                    | 14.89      | 0.52   | 6.09           | 0.29   |
|       | W3/W4 | 2.14                              | 0.14                    | 2.36                              | 0.10                    | 22.00      | 4.11   | 10.35          | 2.59   |
| Phy03 | W3    | 2.38                              | 0.03                    | 2.54                              | 0.01                    | 15.76      | 1.60   | 6.63           | 0.75   |
|       | W3    | 2.30                              | 0.06                    | 2.48                              | 0.04                    | 17.99      | 1.76   | 7.84           | 0.98   |
|       | W3    | 2.40                              | 0.09                    | 2.55                              | 0.07                    | 15.12      | 2.26   | 6.32           | 1.18   |
|       | W4    | 2.37                              | 0.07                    | 2.54                              | 0.05                    | 16.20      | 2.17   | 6.84           | 1.11   |

\*ND Not determined.

**Table 3** - Durability index ( $I_{d1}$  and  $I_{d2}$ ) and wave propagation velocity ( $Vp$ ) of phyllites at different states of alteration of the three weathering profiles.

| Weathering profiles | Class | $I_{d1}$ (%) | $I_{d2}$ (%) | $Vp$ perpendicular direction (m/s) | $Vp$ parallel direction (m/s) |
|---------------------|-------|--------------|--------------|------------------------------------|-------------------------------|
| Phy01               | W2    | 88.19        | 76.76        | 445.14                             | 4795.00                       |
|                     | W3    | 8.19         | 1.66         | 126.00                             | 3474.25                       |
|                     | W4    | 11.67        | 7.44         | ND*                                | ND                            |
| Phy02               | W1/W2 | 98.18        | 96.82        | 2040.10                            | 5382.42                       |
|                     | W2    | 97.32        | 95.52        | 969.71                             | 4601.33                       |
|                     | W2/W3 | 95.18        | 91.75        | 1011.42                            | 4716.65                       |
|                     | W3    | 95.49        | 91.81        | 742.00                             | 4243.79                       |
|                     | W3/W4 | 76.47        | 60.34        | 501.92                             | 4415.32                       |
| Phy 3               | W3    | 61.34        | 44.08        | 394.67                             | 4011.83                       |
|                     | W3    | 85.51        | 73.83        | 366.00                             | 3802.14                       |
|                     | W3    | 71.94        | 55.05        | 523.43                             | 3830.78                       |
|                     | W4    | 75.56        | 65.65        | 945.78                             | 3588.21                       |

\*ND Not determined.

The durability obtained from phyllites W3 is quite variable. Except for phyllite W3 from profile Phy01, which has a very low internal cohesion (a characteristic of this profile),  $I_{d2}$  ranged from 91.81 (profile Phy02) to 44.08 % (profile Phy03). High variations in moderately weathered phyllites were also reported by Andrade & Saraiva (2010) (between 59.6 and 98.2 %) and Silva & Lana (2012) (between 86.18 and 54.32 %).

The variation in durability found for phyllites W3 may be related to the following changes imposed by weathering, which increase significantly in this degree of alteration: increase in pore volume and significant presence of altered opaque minerals, *i.e.*, which had their crystalline form modified (Fig. 3d). Similarly to the present study, Dhakal *et al.* (2002) found a close relationship between durability and weathering in clastic rocks since it provided changes in pore volume and distribution and caused crystalline changes in smectites, which coincides with the results of the present study.

Graphs of Figs. 7 and 8 compare the average values of  $I_{d2}$  and porosity and  $I_{d2}$  and amount of oxides, respectively, in the different weathering classes, being possible to observe the influence of these factors on durability. The increased porosity, associated with permeability, provides a larger surface area of the rock available for contact with water (specific surface), which acts to decrease durability, by weakening chemical bonds, changing properties of mineral constituents and causing instability along weakness planes due to pore water pressure (Koncagül & Santi, 1999).

Figures 9 and 10 show, respectively,  $I_{d2}$  values with weathering progression and phyllite samples after being subjected to two wetting and drying cycles. As can be observed, although  $I_{d2}$  does not uniformly follow the evolution of the alteration, there is a general trend to reduce this parameter with weathering.

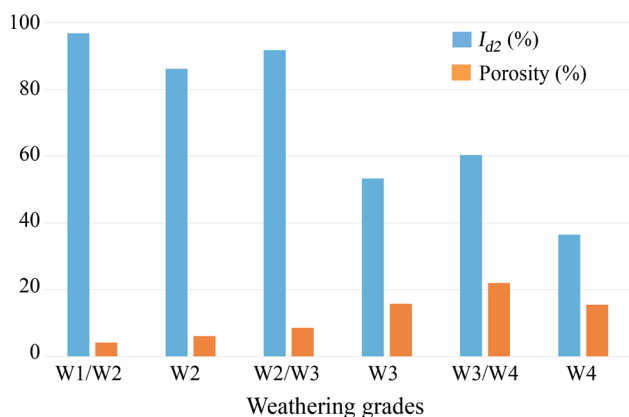


**Figure 7** - Mean values of  $I_{d2}$  and porosity of each weathering class. A more significant reduction in durability is observed as there is a more significant increase in porosity from the moderately altered phyllite (W3).

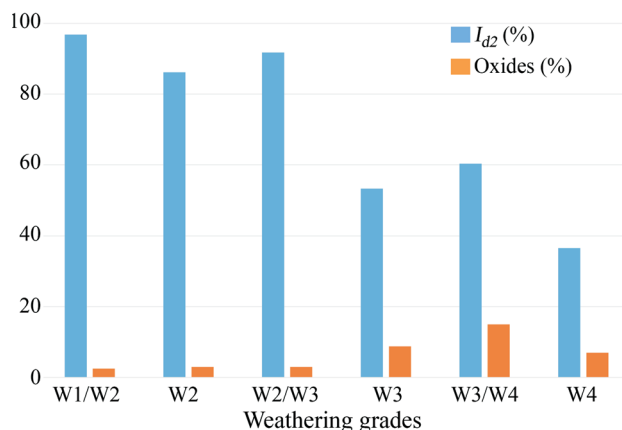


**Figure 8** - Mean values of  $I_{d2}$  and oxide concentration of each weathering class. There is a more marked decrease in durability while a more significant increase in oxide precipitation from the moderately weathered phyllite (W3). Elevated oxide concentration indicates a higher alteration in opaque minerals.

The variability found in durability between phyllites of the same alteration class is also attributed to the heterogeneity of the rock, including the same profile. It happened, for instance, in phyllites W3 collected at distinct points in profile Phy03 (Fig. 2). Depending on profile position, the rock may contain more or less opaque and hence, oxide content, as well as variations in quartz content. Thus, durability is influenced not only by secondary processes derived from weathering but also by the heterogeneity itself intrinsic to the mineralogical composition variation of these phyllites.

### 3.4. Wave propagation velocity

Some samples showed no detection of  $Vp$  signal measured perpendicularly to foliation, while in others (the majority), the intensity signal detected during tests was very low, rarely 100 %. The attenuation of  $Vp$  in the perpendicular direction is caused by the presence of fractures parallel to foliation that make the rock discontinuous, affecting it significantly. There are often reports in the literature of dif-

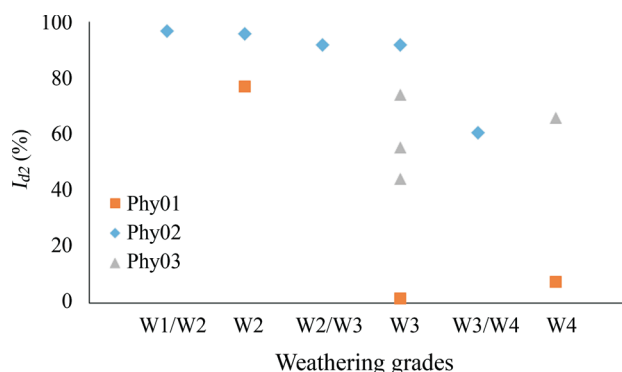


**Figure 9** - Relationship between  $I_{d2}$  and different degrees of alteration of phyllite samples collected in three distinct weathering profiles (Phy01, Phy02, and Phy03).

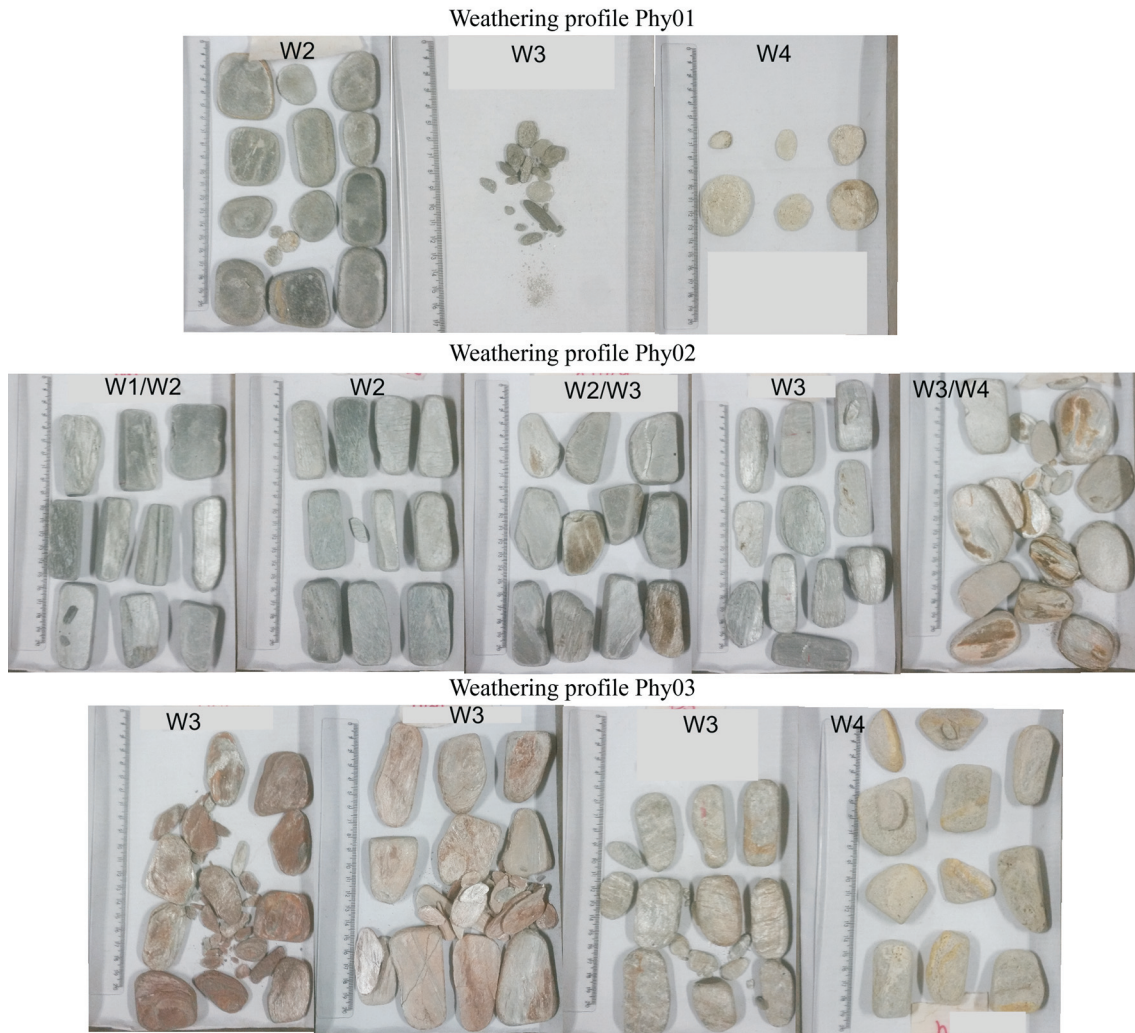


**Figure 10** - Results of samples of altered phyllites after two wetting and drying cycles.

ferences in  $V_p$  in the direction perpendicular and parallel to foliation in rocks with anisotropic properties (Ramamurthy *et al.*, 1993; Marques *et al.*, 2010; Kurtulus *et al.*, 2012; Nikrouz *et al.*, 2016). Jensen & Elming (2013) reported as potential causes of seismic anisotropy the micro-fissures, joints, faults, macroscopic foliation, stratification, and weathering. These authors found anisotropy in  $V_p$  in metarolites with microfoliation, obtaining the highest values in the direction parallel to it.

The values of  $V_p$  obtained in the parallel direction for slightly altered phyllites (W1/W2, W2, and W2/W3) are in the range of 4601.33-5382.42 (m/s), being compatible with the results of phyllites with similar mineralogical composition considered intact or little altered by other researchers (Ramamurthy *et al.*, 1993; Andrade & Saraiva, 2010).

As shown in Fig. 11, moderately to very altered phyllites (W3, W3/W4, and W4) transmit the ultrasonic waves with less efficiency.  $V_p$  is sensitive to the state of alteration of the studied rocks, showing a general trend of reduction as weathering increases.

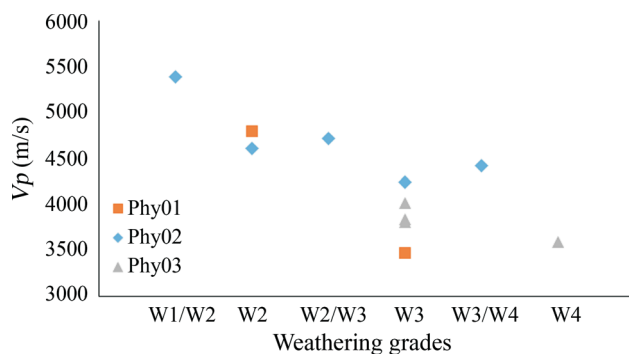


**Figure 11** - Relationship between the velocity of ultrasonic wave propagation measured parallel to foliation and the degree of alteration of phyllite samples collected in three weathering profiles (Phy01, Phy02, and Phy03).

### 3.5. Correlations

#### 3.5.1. Correlation between $I_{d1}$ and $I_{d2}$ with $Vp$

The values of  $Vp$  measured in the direction perpendicular to foliation were not considered, due to the low intensity signal detected during tests.

Figure 12 shows the correlations between  $I_{d1}$  and  $Vp$  and  $I_{d2}$  and  $Vp$ . In Figs. 12a and 12b, correlations were performed between the mean values of each alteration class, while in Figs. 12c and 12d, the individual values were used, obtaining a much lower correlation coefficient. The dispersed values shown in Figs. 12c and 12d are the result of the influence of weathering and anisotropy of the studied phyllites.

Based on the obtained results, the use of mean values was adequate to correlate durability and wave propagation velocity. Khandelwal (2013) obtained a good correlation between  $Vp$  and  $I_{d1}$  for different rock types, including shales, for  $Vp$  values in the range from 1682 to 4657 m/s. Sharma & Singh (2008) also found a good correlation between these two parameters when evaluating seven different types of rock, including phyllites and shales.

#### 3.5.2. Correlation between $Vp$ and physical indices

Figure 13 shows that all the physical indices have a strong relationship with  $Vp$ , with a reduction in  $Vp$  as density decreases (increased porosity and water absorption). These results are in agreement with Gaviglio (1989), Tur-

grul & Zarif (1999), Yasar & Erdogan (2004), Kurtulus *et al.* (2010), Diamantis *et al.* (2011), Sarkar *et al.* (2012), Khandelwal (2013), and Azimian & Ajalloeian (2015), who studied the relationship between physical properties and  $Vp$  and obtained good correlations between these parameters.

#### 3.5.3 Correlations between $Vp$ and $Is$

Graphs in Fig. 14 show the relationship between  $Vp$  and  $Is_{(50)}$ . As expected, the lower the  $Is_{(50)}$  is, the lower the  $Vp$ . There is a good relationship between  $Vp$  and  $Is_{(50)}$  measured perpendicular to foliation, with a correlation coefficient of 0.7779 (Table 4), while the correlation coefficient between  $Vp$  and  $Is_{(50)}$  measured parallel to foliation is lower ( $R^2 = 0.6139$ ), unlike expected. Thus, despite showing influence on  $Vp$  and  $Is_{(50)}$ , metamorphic foliation is not sufficient to explain the good relationship obtained between these properties.

On the other hand, porosity is closely related to  $Vp$  (Fig. 13) and influences the resistance of weathered rocks (Marques *et al.*, 2010; Andrade & Saraiva, 2010; Leão *et al.*, 2017) since the presence of pores makes the rock less continuous, decreasing  $Vp$  and increasing the fragility of the matrix when subjected to compression (Sousa *et al.*, 2005). Thus, the increased porosity due to weathering processes may play a preponderant role in the variation of these properties ( $Vp$  and  $Is_{(50)}$ ) in the studied phyllites.

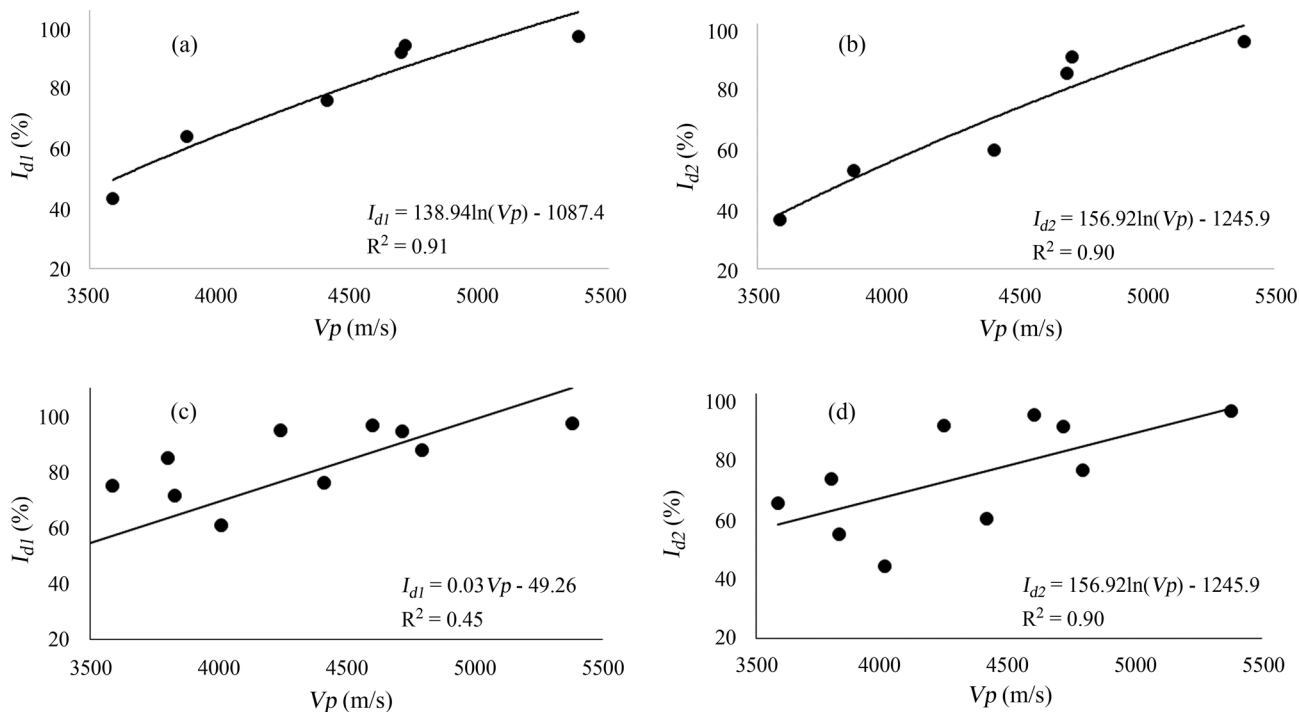


**Figure 12** - Correlations between  $I_{d1}$  and  $Vp$  (parallel to foliation) and  $I_{d2}$  and  $Vp$  (parallel to foliation). In (a) and (b), correlation between the mean values of each alteration class. In (c) and (d), correlation between the values obtained from all weathering grades of the three studied profiles.

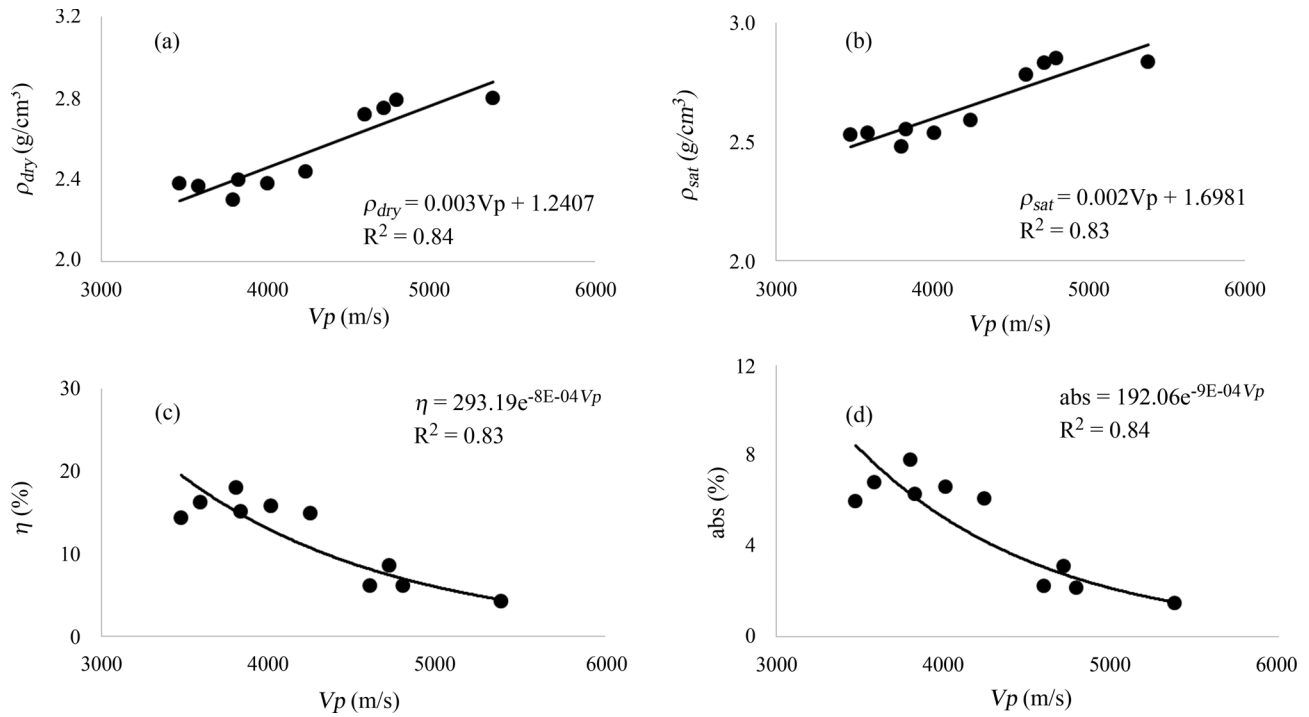


**Figure 13** - Correlations between  $V_p$  (parallel to foliation) and physical indices: dry (a) and saturated apparent specific gravity (b), porosity (c), and water absorption capacity (d).

**Table 4** - Equations correlating  $V_p$  (parallel to foliation) and  $I_{s(50)}$  in different types of rock.

| Equations                          | Correlation coefficient | References                    | Rock                        |
|------------------------------------|-------------------------|-------------------------------|-----------------------------|
| $I_{s(50)} = 6.67\ln(V_p) - 51.9$  | 0.93                    | Jamshidi <i>et al.</i> (2016) | Travertine                  |
| $I_{s(50)} = 0.0018(V_p) - 1.9906$ | 0.95                    | Kurtulus <i>et al.</i> (2010) | Andesites                   |
| $I_{s(50)} = 0.0042(V_p) - 14.602$ | 0.90                    | Kurtulus <i>et al.</i> (2012) | Serpentine ultrabasic rocks |
| $V_p = -16.784I_{s(50)} + 6078.9$  | 0.55                    | Jensen & Elming (2013)        | Meta-riolites               |
| $V_p = 859.02I_{s(50)}^a + 3475.2$ | 0.78                    | Present study                 | Phyllite                    |
| $V_p = 3155.9I_{s(50)}^b + 3574.1$ | 0.61                    | Present study                 | Phyllite                    |

$I_{s(50)}^a$  Direction of loading perpendicular to foliation.

$I_{s(50)}^b$  Direction of loading parallel to foliation.

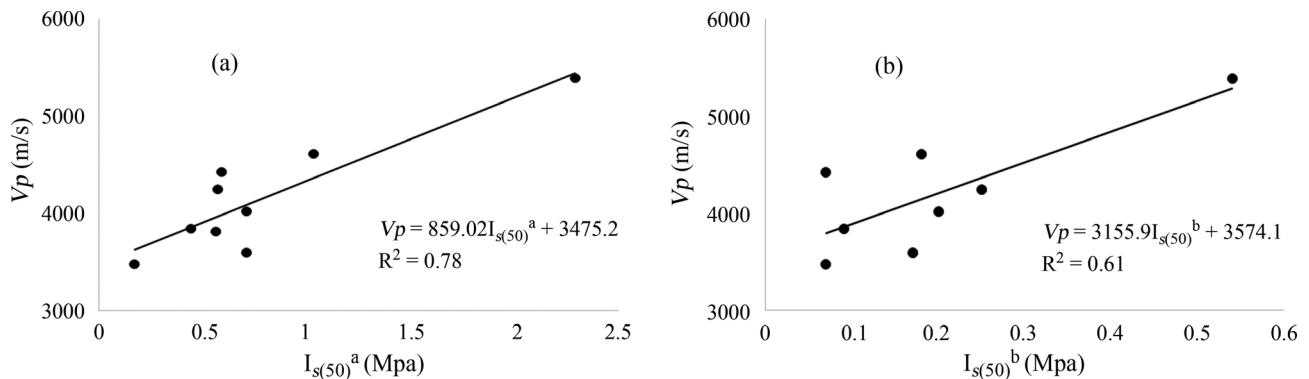


**Figure 14** - Relationship between  $V_p$  (parallel to foliation) and  $I_{s(50)}$  perpendicular to foliation ( $I_{s(50)}^a$ ) and parallel to foliation ( $I_{s(50)}^b$ ).

## 4. Conclusions

The slake durability test performed in the studied phyllites showed that weathering has a clear influence on this geotechnical property, affecting the texture and mineralogical composition of these rocks. As expected, the progressive increase in porosity and mineral alteration due to weathering was accompanied by a reduction in durability, but the intensity in which this process occurs was established.

$V_p$  decrease with weathering is closely related to variation of physical indices, as proved by the significant correlation coefficients found. Intact rock strength and  $V_p$  are influenced by metamorphic foliation. Also, the very good correlation found between  $V_p$  and  $I_{s(50)}$  may be influenced by the effects of weathering, which cause a higher increase in porosity when compared to the anisotropy intrinsic to phyllites resulting from mineral alignment.

$V_p$  and durability, although presenting general trends, do not evolve uniformly with the weathering progression since porosity, the main physical parameter that influences strength has heterogeneous behavior. This behavior attributed to porosity is probably associated with physical weathering, due to the increase in spacing of pre-existing discontinuities and formation of a micro-fracture network. Therefore, the action of weathering on fractures and micro-fractures makes their effects increasingly complex, reflecting on the physical characteristics of the rock.

In addition to the influence of secondary weathering processes on the variability of physical and mechanical parameters, there is also the mineralogical heterogeneity intrinsic to these phyllites, observed between samples with the same degree of alteration in the same profile, but taken from different points. Both heterogeneity and anisotropy are also revealed in the correlation established between  $V_p$  and  $I_{d1}$  and  $V_p$  and  $I_{d2}$  when all values for each sample from all three slopes are incorporated. The use of mean values of each alteration class improves the correlation between these properties and allows concluding that the evaluated physical parameters should be used prudently in geotechnical projects, being important that they are associated with a field control, contemplating descriptions of the rocky massif (including discontinuity characteristics), petrographic and micropetrographic analyses, as well as other types of physical and mechanical tests.

Good correlations were found for  $V_p$  and slake durability index, for  $V_p$  and all physical indices, and for  $V_p$  and point load strength measured perpendicular to foliation.

Finally, the authors suggest that similar studies, with the same tests/analyses, should be performed on similar rock types (and also with other lithotypes) from other regions from Brazil.

## Acknowledgments

Authors thank Fundação de Amparo à Pesquisa do Estado de Minas Gerais (FAPEMIG) (Process APQ-

01143-16) for granting funding and Universidade Federal de Viçosa -Brazil, for funding and providing laboratory support for the laboratory tests.

## References

- Alkmim, F.F. & Marshak, S. (1998). Transamazonian orogeny in the southern São Francisco Craton region, Minas Gerais, Brazil: Evidence for paleoproterozoic collision and collapse in the Quadrilátero Ferrífero. *Precambrian Research*, 90(1-2):29-58. DOI 10.1016/S0301-9268(98)00032-1
- Andrade, P.S. & Saraiva, A.A. (2010). Physical and mechanical characterization of phyllites and metagreywackes in central Portugal. *Bull. Eng. Geol. Env.*, 69(2):207-214. DOI 10.1007/s10064-009-0251-9
- Azimian, A. & Ajalloeian, R. (2015). Empirical correlation of physical and mechanical properties of marly rocks with P-wave velocity. *Arab. J. Geosci.*, 8:2069-2079. DOI 10.1007/s12517-013-1235-4
- Cetin, H.; Laman, M. & Ertune, A. (2000). Settlement and slaking problems in the world's fourth largest rock-fill dam, the Ataturk Dam in Turkey. *Eng. Geol.*, 56(3-4):225-242. DOI 10.1016/S0013-7952(99)00049-6
- Çobanoğlu, I. & Çelik, S.B. (2008). Estimation of uniaxial compressive strength from point load strength, Schmidt hardness and P-wave velocity. *Bull. Eng. Geol. Env.*, 67:491-498. DOI 10.1007/s10064-008-0158-x
- Crosta, G. (1998). Slake durability Vs ultrasonic treatment for rock durability determinations. *Int. J. Rock. Mech. Min. Sci.*, 35(6):815-824
- Dhokal, G.; Yoneda, T.; Kato, M. & Kaneko, K. (2002). Slake durability and mineralogical properties of some pyroclastic and sedimentary rocks. *Eng. Geol.*, 65(1):31-45 DOI 10.1016/S0013-7952(01)00101-6
- Diamantis, K.; Bellas, S.; Migiros, G. & Gartzos, E. (2011). Correlating wave velocities with physical, mechanical properties and petrographic characteristics of peridotites from the Central Greece. *Geotech. Geol. Eng.*, 29:1049-1062. DOI 10.1007/s10706-011-9436-7
- Franklin, J.A. & Chandra, R. (1972). The slake durability test. *Int. J. Rock. Mech. Min. Sci.*, 9(3):325-341. DOI 10.1016/0148-9062(72)90001-0
- Gardner, G.H.F.; Gardner, L.W. & Gregory, A.R. (1974). Formation velocity and density: the diagnostic basis for stratigraphy. *Geophysics*, 39(6):770-780. DOI 10.1190/1.1440465
- Gaviglio, P. (1989). Longitudinal wave propagation in a limestone: the relationship between velocity and density. *Rock Mech. Rock Eng.*, 22:299-306. DOI 10.1007/BF01262285
- Gupta, V. & Ahmed, I. (2007). The effect of pH of water and mineralogical properties on the slake durability (degradability) of different rocks from the Lesser Hima-

- laya, India. *Eng. Geol.*, 95(3-4):79-87. DOI 10.1016/j.enggeo.2007.09.004
- ISRM (2007). *The Complete ISRM Suggested Methods for Rock Characterization, Testing and Monitoring: 1974-2006*. ISRM, Springer, Cham, 628 p.
- ISRM (2015). *The IRSM Suggested Methods for Rock Characterization, Testing and Monitoring: 2007-2014*. ISRM, Springer, Cham, 293 p.
- Jamshidi, A.; Nikudel, M.R.; Khamsehchiyan, M.; Sahamieh, R.Z. & Abdi, Y. (2016). A correlation between P-wave velocity and Schmidt hardness with mechanical properties of travertine building stones. *Arab. J. Geosci.*, 9:568. DOI 10.1007/s12517-016-2542-3
- Jensen, M.B. & Elming, S.Å. (2013). Magnetic, seismic and mechanical properties of porphyritic meta-rhyolites - The effect of microscopic foliation on rock strength and P-wave velocity in drill cores. *Eng. Geol.*, 157(8):93-102. DOI 10.1016/j.enggeo.2013.01.008
- Kahraman, S. (2001). A correlation between P-wave velocity, number of joints and Schmidt hammer rebound number. *Int. J. Rock Mech. Min. Sci.*, 38:729-733. DOI 10.1016/S1365-1609(01)00034-X
- Kanji, M. & Leão, M. F. (2020). Correlation of soft rock properties. Kanji, M.; He, M. & Sousa, L.R. (eds), *Soft Rock Mechanics and Engineering*. Springer, Switzerland, pp. 407-423. DOI 10.1007/978-3-030-29477-9
- Khandelwal, M. (2013). Correlating P-wave velocity with the physico-mechanical properties of different rocks. *Pure Appl. Geophys.*, 170:507-514. DOI 10.1007/s00024-012-0556-7
- Koncagül, E.C. & Santi, P.M. (1999). Predicting the unconfined compressive strength of the Breathitt shale using slake durability, shore hardness and rock structural properties. *Int. J. Rock Mech. Min. Sci.*, 36(2):139-153. DOI 10.1016/S0148-9062(98)00174-0
- Kurtulus, C.; Bozkurt, A. & Endes, H. (2012). Physical and mechanical properties of serpentinized ultrabasic rocks in NW Turkey. *Pure Appl. Geophys.*, 169:1205-1215. DOI 10.1007/s00024-011-0394-z
- Kurtulus, C.; Serkan Irmak, T. & Sertçelik, I. (2010). Physical and mechanical properties of Gokceada: Imbros (NE Aegean Sea) Island andesites. *Bull. Eng. Geol. Environ.*, 69:321-324. DOI 10.1007/s10064-010-0270-6
- Leão, M.F.; Barroso, E.V.; Polivanovi, H.; Marques, E.A.G. & Vargas Jr, E.A. (2017). Weathering of metapelites from the Quadrilátero Ferrífero mineral province, southeastern Brazil. *Bull. Eng. Geol. Env.*, 78(1):19-33. DOI 10.1007/s10064-017-1036-1
- Leão, M.F. (2017). *Geomechanical Behavior of Weathering Front in Filito of the Quadrilátero Ferrífero Region*. Ph.D. Thesis, Department of Geology, Federal University of Rio de Janeiro, Rio de Janeiro, 186 p. (in Portuguese)
- Ioanna, I.; Dimitrios, R.; Theodora, P. & Paris, T. (2009). Geotechnical and mineralogical properties of weak rocks from Central Greece. *Cent. Eur. J. Geosci.*, 1:431-442. DOI 10.2478/v10085-009-0029-0
- Marques, E.A.G.; Barroso, E.V.; Menezes Filho, A.P. & Vargas JR, E.A. (2010). Weathering zones on metamorphic rocks from Rio de Janeiro - Physical, mineralogical and geomechanical characterization. *Eng. Geol.*, 111(1-4):1-18. DOI 10.1016/j.enggeo.2009.11.001
- Marques, E.A.G.; Williams, D.J.; Assis, I.R. & Leão, M.F. (2017). Effects of weathering on characteristics of rocks in a subtropical climate: weathering morphology, in situ, laboratory and mineralogical characterization. *Environ. Earth Sci.*, 76:602. DOI 10.1007/s12665-017-6936-7
- Marques, E.A.G.; Vargas Jr., E.A. & Leão, M.F. (2020). Weathering of rocks in Brazil. Kanji, M.; He, M. & Sousa, L.R. (eds), *Soft Rock Mechanics and Engineering*. Springer, Switzerland, pp. 251-291.
- Nefeslioglu, H.A. (2013). Evaluation of geo-mechanical properties of very weak and weak rock materials by using non-destructive techniques: Ultrasonic pulse velocity measurements and reflectance spectroscopy. *Eng. Geol.*, 160:8-20. DOI 10.1016/j.enggeo.2013.03.023
- Nikrouz, R.; Moomivand, H. & Azad, R. (2016). Effect of foliation orientation on the P- and S-wave velocity anisotropies and dynamic elastic constants of the quartz-micaschists metamorphic rocks, Angouran mine, Iran. *Arab. J. Geosci.*, 9:1-9. DOI 10.1007/s12517-016-2699-9
- Ramamurthy, T.; Rao, G.V. & Singh, J. (1993). Engineering behavior of phyllites. *Eng. Geol.*, 33(3):209-225. DOI 10.1016/0013-7952(93)90059-L
- Robert, H. & Hack, G.H. (2020). Weathering, erosion, and susceptibility to weathering. Kanji, M.; He, M. & Sousa, L.R. (eds.), *Soft Rock Mechanics and Engineering*. Springer, Switzerland, pp. 291-335.
- Romano, A.W.; Rezende, L.F.S. & Macedo, B.O.P. (2017). *Ouro Preto Map, SF.23-X-A-III, scale 1:100.000: Triângulo Mineiro Project*. CODEMIG, Belo Horizonte (in Portuguese).
- Silva, W.G.; França, A.V.M. & Sampaio, J.L.D. (2005) *Mariana Map, SF.23-X-B-I-3 e SF.23-X-B-IV-1, scale 1:50.000: Geology project of the Quadrilátero Ferrífero - Integration and Cartographic Correction in GIS*. CODEMIG, Belo Horizonte (in Portuguese).
- Silva, C.H.C. & Lana, M.S. (2012). Influence of slake durability on geotechnical behavior of phyllites of Pau Branco Mine. *Rev. Esc. Minas.*, 65(3):413-418. DOI 10.1590/S0370-44672012000300019
- Sarkar, K.; Vishal, V. & Singh, T.N. (2012). An empirical correlation of index geo-mechanical parameters with the compressional wave velocity. *Geotech. Geol. Eng.*, 30(2):469-479. DOI 10.1007/s10706-011-9481-2
- Sharma, P.K.; Khandelwal, M. & Singh, T.N. (2011). A correlation between Schmidt hammer rebound numbers with impact strength index, slake durability index and

- P-wave velocity. *Int. J. Earth Sci.*, 100(1):189-195. DOI 10.1007/s00531-009-0506-5
- Sharma, P.K. & Singh, T.N. (2008). A correlation between P-wave velocity, impact strength index, slake durability index and uniaxial compressive strength. *Bull. Eng. Geol. Environ.*, 67:17-22. DOI 10.1007/s10064-007-0109-y
- Sousa, L.M.O.; Río, L.M.S.D.; Calleja, L.; Argandoña, V.G.R. & Rey, A.R. (2005). Influence of microfractures and porosity on the physico-mechanical properties and weathering of ornamental granites. *Eng. Geol.*, 77(1):153-168. DOI 10.1016/j.enggeo.2004.10.001
- Turgrul, A. & Zarif, I.H. (1999). Correlation of mineralogical and textural characteristics with engineering properties of selected granitic rocks from Turkey. *Eng. Geol.*, 51(4):303-317. DOI 10.1016/S0013-7952(98)00071-4
- Yasar, E. & Erdogan, Y. (2004). Correlating sound velocity with the density, compressive strength and Young's modulus of carbonate rocks. *Int. J. Rock Mech. Min. Sci.*, 41(5):871-875. DOI 10.1016/j.ijrmms.2004.01.012
- Yilmaz, I. & Karacan, E. (2005). Slaking durability and its effect on the doline formation in the gypsum. *Environ. Geol.*, 47:1010-1016. DOI 10.1007/s00254-005-1234-1
- Wen, L.; Luo, Z.; Yang, S.; Qin, Y. & Wang, W. (2018). Correlation of geo-mechanics parameters with uniaxial compressive strength and P-wave velocity on dolomitic limestone using a statistical method. *Geotech. Geol. Eng.*, 77(1-2):153-168. DOI 10.1016/j.enggeo.2004.10.001

# SOILS and ROCKS

An International Journal of Geotechnical and Geoenvironmental Engineering

## Publication of

**ABMS - Brazilian Association for Soil Mechanics and Geotechnical Engineering**

**SPG - Portuguese Geotechnical Society**

**Volume 43, N. 2, April-June 2020**

## Author index

|                   |          |                         |             |
|-------------------|----------|-------------------------|-------------|
| Abreu, A.V.       | 287      | Laouar, M.S.            | 247         |
| Almeida, M.C.F.   | 219      | Leão, M.F.              | 297         |
| Almeida, M.S.S.   | 287      | Lima, C.A.              | 57          |
| Arêdes, A.C.N.B.  | 85       | Lima, D.C.              | 271         |
| Assis, A.P.       | 171      | Liu, J.L.               | 43          |
| Assis, L.E.       | 57       | Lopes, Ma.B.            | 171         |
| Augusto Filho, O. | 71       | Luo, Y.S.               | 43          |
| Bicalho, K.V.     | 103      | Marques, E.A.G.         | 57, 85, 297 |
| Bobet, A.         | 123      | Melchior Filho, J.      | 11          |
| Bonan, V.H.F.     | 11       | Menezes, S.J.M.C.       | 57          |
| Borges, J.L.      | 199      | Messad, A.              | 181         |
| Borges, R.G.      | 219      | Miguel, G.D.            | 151         |
| Boufarh, R.       | 247      | Moura, A.S.             | 11          |
| Bragagnolo, L.    | 159, 279 | Moussai, B.             | 181         |
| Braun, A.B.       | 97       | Oliveira Filho, A.G.    | 103         |
| Bressani, L.A.    | 31       | Oliveira, A.H.C.        | 85          |
| Carvalho, T.R.R.  | 297      | Pitanga, H.N.           | 271         |
| Celestino, T.B.   | 123      | Prestes, E.             | 279         |
| Consoli, N.C.     | 159      | Prietto, P.D.M.         | 159, 279    |
| Craig, A.M.L.     | 71       | Roque, L.A.             | 57          |
| Cui, Y.X.         | 43       | Saadi, D.               | 247         |
| da Silva, J. Lins | 231      | Santos Junior, O.F.     | 263         |
| de Freitas, A.C.  | 3, 141   | Santos, E.C.G.          | 231         |
| Debbab, O.Y.      | 181      | Santos, R.M.            | 199         |
| Dias Neto, S.L.S. | 271      | Saraiva, A.             | 141         |
| Domiciano, M.L.   | 231      | Silva, A.C.             | 191         |
| Donato, M.        | 151      | Silva, T.O.             | 271         |
| Dong, J.G.        | 21       | Silva, W.G.             | 271         |
| dos Santos, L. F. | 3, 141   | Silveira, A.A.          | 159         |
| Favretto, J.      | 151      | Soares de Almeida, M.S. | 219         |
| Ferrazzo, S.T.    | 279      | Souza Junior, L.O.      | 219         |
| Ferreira, S.R.M.  | 191      | Souza Junior, P.L.      | 263         |
| Flores, J.A.      | 31       | Thomé, A.               | 97          |
| Floss, M.F.       | 151      | Tímbola, R.S.           | 279         |
| Fontoura, T.B.    | 263      | Totola, L.B.            | 103         |
| Freitas Neto, O.  | 263      | Trentin, A.W.S.         | 97          |
| Fucale, S.        | 191      | Trindade, T.P.          | 271         |
| Heidemann, M.     | 31       | Ulsen, C.               | 159         |
| Hisatugu, W.H.    | 103      | Vargas, G.D.L.P.        | 279         |
| Hou, T.S.         | 43       | Visentin, C.            | 97          |
| Korf, E.P.        | 159, 279 | Vitali, O.P.M.          | 123         |
|                   |          | Wei, G.F.               | 21          |

**BUILDING THE WORLD, BETTER**



**EPF**



## Engineering and Architectural Consultancy

Geology, Geotechnics, Supervision of Geotechnical Works  
Embankment Dams, Underground Works, Retaining Structures  
Special Foundations, Soil Improvement, Geomaterials



MEMBER OF

**TPF - CONSULTORES DE ENGENHARIA E ARQUITETURA, S.A.**  
[www.tpf.pt](http://www.tpf.pt)

**40**  
years



- > **Prospecção Geotécnica**  
*Site Investigation*
- > **Consultoria Geotécnica**  
*Geotechnical Consultancy*
- > **Obras Geotécnicas**  
*Ground Treatment-Construction Services*
- > **Controlo e Observação**  
*Field Instrumentation Services and Monitoring Services*
- > **Laboratório de Mecânica de Solos**  
*Soil and Rock Mechanics Laboratory*

Certificada ISO 9001 por



# Geocontrole



Parque Oriente, Bloco 4, EN10  
2699-501 Bobadela LRS  
Tel. 21 995 80 00  
Fax. 21 995 80 01  
e.mail: mail@geocontrole.pt  
www.geocontrole.pt

  
**Geocontrole**  
Geotecnia e Estruturas de Fundação SA



**COBA**

**GEOLOGY AND GEOTECHNICS**

Hydrogeology • Engineering Geology • Rock Mechanics • Soil Mechanics • Foundations and Retaining Structures • Underground Works • Embankments and Slope Stability  
Environmental Geotechnics • Geotechnical Mapping



- Water Resources Planning and Management
- Hydraulic Undertakings
- Electrical Power Generation and Transmission
- Water Supply Systems and Pluvial and Wastewater Systems
- Agriculture and Rural Development
- Road, Railway and Airway Infrastructures
- Environment
- Geotechnical Structures
- Cartography and Cadastre
- Safety Control and Work Rehabilitation
- Project Management and Construction Supervision



**PORTUGAL**

CENTER AND SOUTH REGION  
Av. 5 de Outubro, 323  
1649-011 LISBOA  
Tel.: (351) 210125000, (351) 217925000  
Fax: (351) 217970348  
E-mail: coba@coba.pt  
www.coba.pt

Av. Marquês de Tomar, 9, 6.  
1050-152 LISBOA  
Tel.: (351) 217925000  
Fax: (351) 213537492

**NORTH REGION**

Rua Mouzinho de Albuquerque, 744, 1.  
4450-203 MATOSINHOS  
Tel.: (351) 229380421  
Fax: (351) 229373648  
E-mail: engico@engico.pt

**ANGOLA**

Praceta Farinha Leitão, edifício nº 27, 27-A - 2º Dto  
Bairro do Maculusso, LUANDA  
Tel./Fax: (244) 222338 513  
Cell: (244) 923317541  
E-mail: coba-angola@netcabo.co.ao

**MOZAMBIQUE**

Pestana Rovuma Hotel. Centro de Escritórios.  
Rua da Sé nº114. Piso 3, MAPUTO  
Tel./Fax: (258) 21 328 813  
Cell: (258) 82 409 9605  
E-mail: coba.mz@tdm.co.mz

**ALGERIA**

09, Rue des Frères Hocine  
El Biar - 16606, ARGEL  
Tel.: (213) 21 922802  
Fax: (213) 21 922802  
E-mail: coba.alger@gmail.com

**BRAZIL**

**Rio de Janeiro**  
COBA Ltd. - Rua Bela 1128  
São Cristóvão  
20930-380 Rio de Janeiro RJ  
Tel.: (55 21) 351 50 101  
Fax: (55 21) 258 01 026

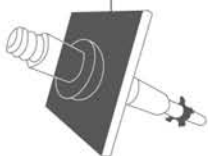
**Fortaleza**

Av. Senador Virgílio Távora 1701, Sala 403  
Aldeota - Fortaleza CEP 60170 - 251  
Tel.: (55 85) 3261 17 38  
Fax: (55 85) 3261 50 83  
E-mail: coba@esc-te.com.br

**UNITED ARAB EMIRATES**

Corniche Road - Corniche Tower - 5th Floor - 5B  
P. O. Box 38360 ABU DHABI  
Tel.: (971) 2 627 0088  
Fax: (971) 2 627 0087

Much more support  
to your business.



**Incotep - Anchoring Systems**

Incotep anchoring Systems is a division of Açotubo Group, which engaged in the development of Anchoring Systems, used in geotechnical and structural applications where high quality prestressing systems are designed to meet diverse needs.

**Know our solutions for your processes**

- Self Drilling Injection Hollow Bar
- Cold Rolled Thread Bars and Micropiles
- Hot Rolled Thread Bars
- Incotep Tie Rods (Port and Dike Construction)

- Umbrella Tubes Drilling System
- Pipes for Root Piles, among others

[www.incotep.com.br](http://www.incotep.com.br)  
+55 11 2413-2000

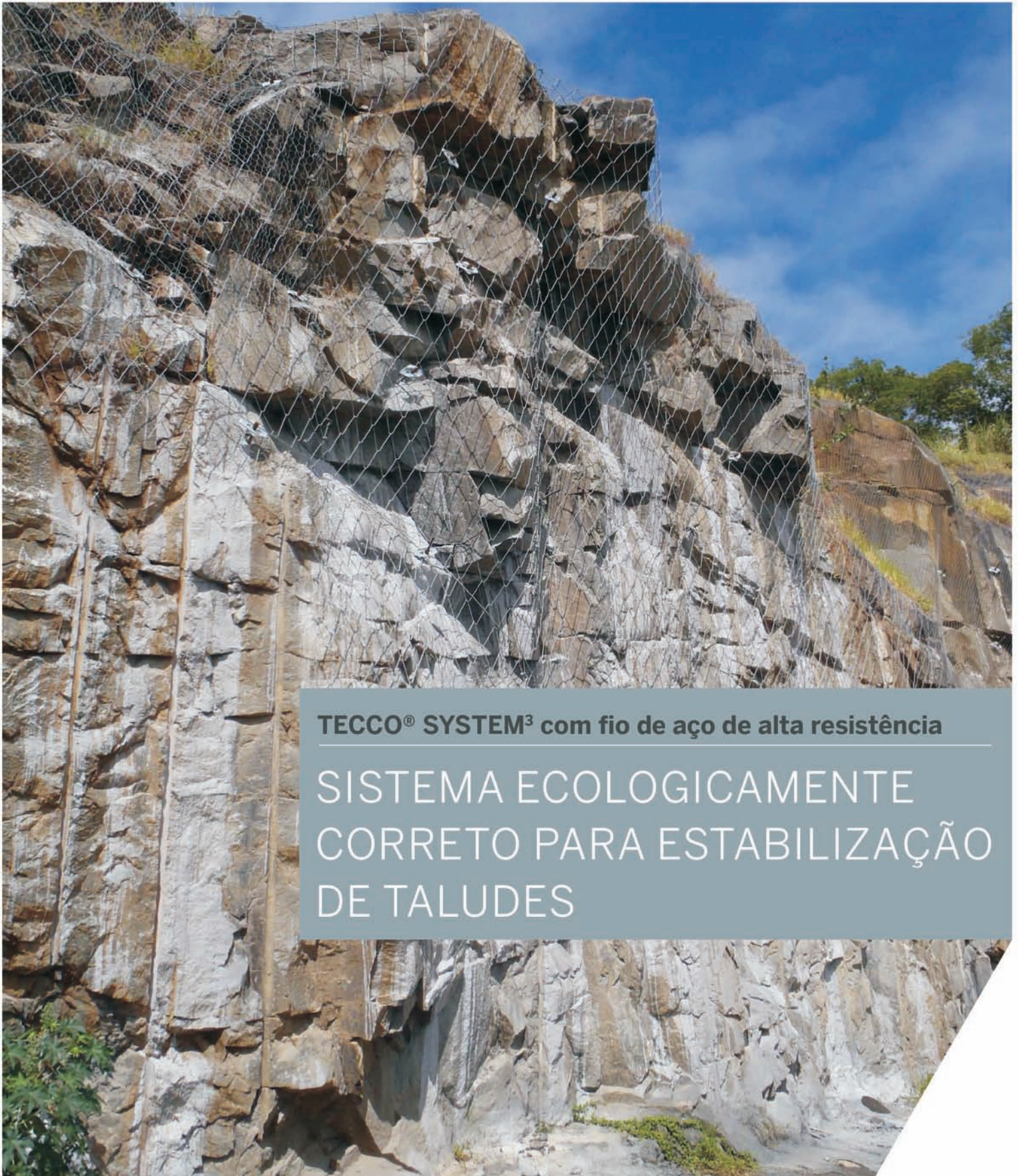
**INCOTEP**  
Sistemas de Ancoragem

A company Açotubo Group





Conheça mais:  
[www.geobrugg.com/pt/taludes](http://www.geobrugg.com/pt/taludes)



**TECCO® SYSTEM<sup>3</sup> com fio de aço de alta resistência**

SISTEMA ECOLOGICAMENTE  
CORRETO PARA ESTABILIZAÇÃO  
DE TALUDES

# Reliable solutions with **technology, quality,** and **innovation** for Civil Engineering proposes



## MACCAFERRI POLIMAC

New polymeric coating with high performance  
**PoliMac™**



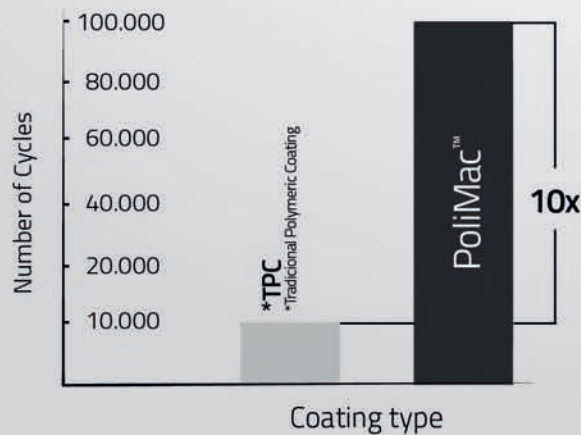
Long-life galvanising  
**GalMac® 4R**

Intermetallic coating

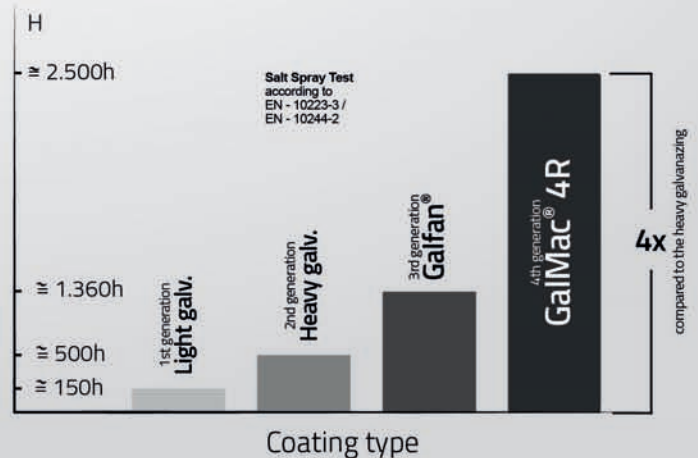
Steel wire LCC\*  
\*Low Carbon Content



The **PoliMac™** in controlled abrasion resistance tests, it showed its excellent performance by resisting up to 100,000 cycles in the standard tests **ABNT NBR 7577** and **EN 10223-3**; about **10x more** than the traditional coating.



The **GalMac® 4R** coating complies with the main national and international standards such as: **EN 10223-3: 2013, ASTM B860** and **NBR 8964**.



Follow us on our **social media**



/maccaferri



/maccaferriatriz



@Maccaferri\_BR



+MaccaferriWorld



/maccaferriworld



**MACCAFERRI**

[www.maccaferri.com/br](http://www.maccaferri.com/br)

# SPECIALISTS IN GEOTECHNICAL IN-SITU TESTS AND INSTRUMENTATION

## GEOTECHNICAL SERVICES (onshore and offshore)

### ■ IN-SITU TESTS

Seismic CPT  
Cone Penetration Testing Undrained-CPTu (cordless system)  
Vane Shear Testing (electrical apparatus)  
Pressuremeter Testing (Menard)  
Flat Dilatometer Test-DMT (Machetti)  
Standard Penetration Test-SPT-T

### ■ INSTRUMENTATION

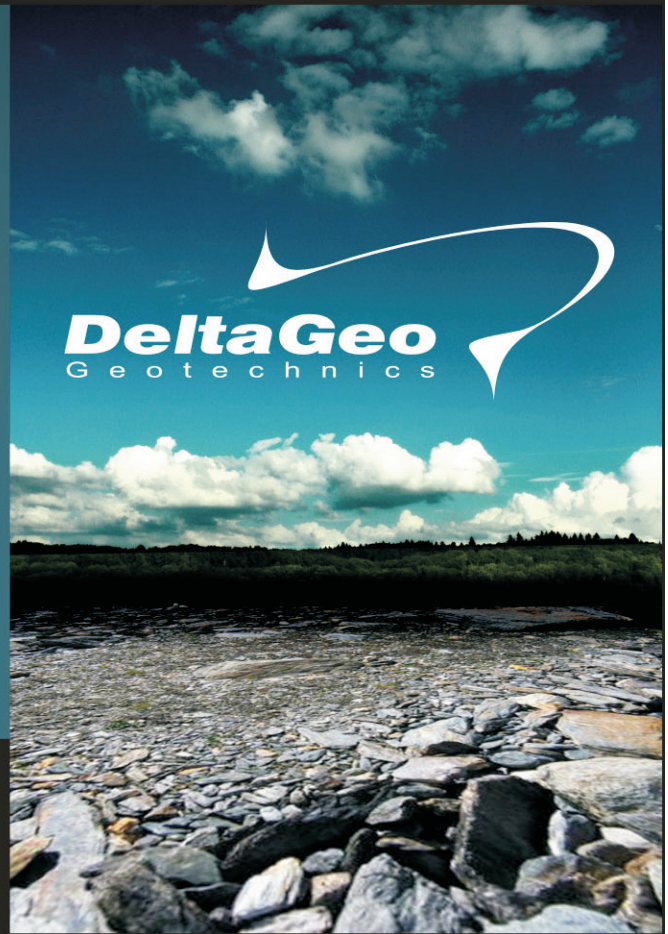
Instrumentation, installation and direct import  
Routine Monitoring  
Operation and Maintenance  
Engineering analyses  
Consultancy, design & geotechnical engineering services

### ■ SAMPLING

Soil sampling and monitoring  
Groundwater sampling and monitoring  
Field and laboratory testing

### ■ ENVIRONMENTAL

Environmental Services  
Soil and groundwater sampling and monitoring  
Field and laboratory testing

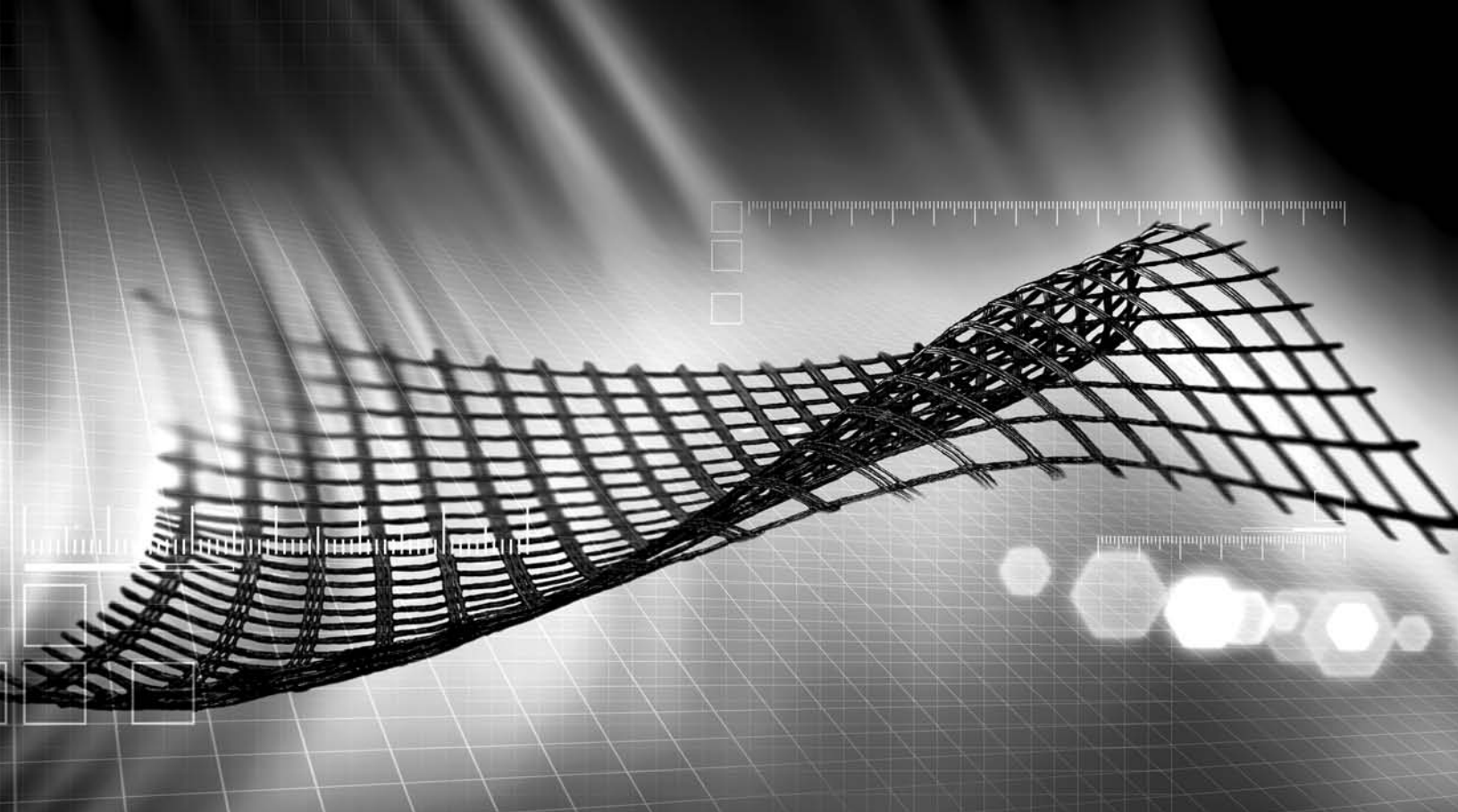


**0800 979 3436**

**São Paulo: +55 11 8133 6030**

**Minas Gerais: +55 31 8563 2520 / 8619 6469**

**[www.deltageo.com.br](http://www.deltageo.com.br) [deltageo@deltageo.com.br](mailto:deltageo@deltageo.com.br)**



# A strong, lasting connection.

With a history of over 150 years of pioneering in geosynthetics, we strive to create solutions for the most diverse engineering challenges.

Our business areas:



**Earthworks and  
Foundations**



**Environmental  
Engineering**



**Roads and Pavements**



**Hydraulic Engineering**

Talk to HUESKER Brasil:  
[www.HUESKER.com.br](http://www.HUESKER.com.br)  
[HUESKER@HUESKER.com.br](mailto:HUESKER@HUESKER.com.br)  
+55 (12) 3903 9300

Follow HUESKER Brasil in social media:



**# HUESKER**  
Ideen. Ingenieure. Innovationen.

# PIONEERING AND INNOVATION

SINCE 1921

 **TEIXEIRA DUARTE**  
ENGENHARIA E CONSTRUÇÕES, S.A.

PORT FACILITY CONSTRUCTION  
NACALA - MOZAMBIQUE

LICENCE NO. 24 - PUB.



Building a better world.  
[teixiraduarteconstruction.com](http://teixiraduarteconstruction.com)

# Instructions for Submission of Manuscripts

## Category of the Papers

Soils and Rocks is the international scientific journal edited by the Brazilian Association for Soil Mechanics and Geotechnical Engineering (ABMS) and the Portuguese Geotechnical Society (SPG). The aim of the journal is to publish (in English) original research and technical works on all geotechnical branches.

According to its content the accepted paper is classified in one of the following categories: Article paper, Technical Note, Case Study or Discussion. An article paper is an extensive and conclusive dissertation about a geotechnical topic. A paper is considered as a technical note if it gives a short description of ongoing studies, comprising partial results and/or particular aspects of the investigation. A case study is a report of unusual problems found during the design, construction or the performance of geotechnical projects. A case study is also considered as the report of an unusual solution given to an ordinary problem. The discussions about published papers, case studies and technical notes are made in the Discussions Section.

When submitting a manuscript for review, the authors should indicate the category of the manuscript, and is also understood that they:

- assume full responsibility for the contents and accuracy of the information in the paper;
- assure that the paper has not been previously published, and is not being submitted to any other periodical for publication.

## Manuscript Instructions

Manuscripts must be written in English. The text is to be typed in a word processor (preferably MS Word), **single column**, using ISO A4 page size, left, right, top, and bottom margins of 25 mm, Times New Roman 12 font, and line spacing of 1.5. All lines and pages should be numbered. The text should be written in the third person.

The first page of the manuscript must include the title of the paper followed by the names of the authors with the abbreviation of the most relevant academic title. The affiliation, address and e-mail must appear below each author's name. An abstract of 200 words follows after the author's names. A list with up to six keywords at the end of the abstract is required.

Although variations on the sequence and title of each section are possible, it is suggested that the text contains the following sections: Introduction, Material and Methods, Results, Discussions, Conclusions, Acknowledgements, References and List of Symbols. A brief description of each section is given next.

**Introduction:** This section should indicate the state of the art of the problem under evaluation, a description of the problem and the methods undertaken. The objective of the work should be clearly presented at the end of the section.

**Materials and Methods:** This section should include all information needed to the reproduction of the presented work by other researchers.

**Results:** In this section the data of the investigation should be presented in a clear and concise way. Figures and tables should not repeat the same information.

**Discussion:** The analyses of the results should be described in this section.

**Conclusions:** The content of this section should be based on the data and on the discussions presented.

**Acknowledgements:** If necessary, concise acknowledgements should be presented in this section.

**References:** References to other published sources must be made in the text by the last name(s) of the author(s), followed by the year of publication, similarly to one of the two possibilities below:

...while Silva & Pereira (1987) observed that resistance depended on soil density... or It was observed that resistance depended on soil density (Silva & Pereira, 1987).

In the case of three or more authors, the reduced format must be used, e.g.: Silva *et al.* (1982) or (Silva *et al.*, 1982). Two or more citations belonging to the same author(s) and published in the same year are to be distinguished with small letters, e.g.: (Silva, 1975a, b, c.). Standards must be cited in the text by the initials of the entity and the year of publication, e.g.: ABNT (1996), ASTM (2003).

Full references shall be listed alphabetically at the end of the text by the first author's last name. Several references belonging to the same author shall be cited chronologically. Some examples are listed next:

Papers: Bishop, A.W. & Blight, G.E. (1963). Some aspects of effective stress in saturated and unsaturated soils. *Geotechnique*, 13(2):177-197.

Books: Lambe, T.W. & Whitman, R.V. (1979). *Soil Mechanics*, SI Version. John Wiley & Sons, New York, 553 p.

Book with editors: Sharma, H.D.; Dukes, M.T. & Olsen, D.M. (1990). Field measurements of dynamic moduli and Poisson's ratios of refuse and underlying soils at a landfill site. Landva, A. & Knowles, G.D. (eds), *Geotechnics of Waste Fills - Theory and Practice*, American Society for Testing and Materials - STP 1070, Philadelphia, pp. 57-70.

Proceedings (printed matter or CD-ROM): Jamiolkowski, M.; Ladd, C.C.; Germaine, J.T. & Lancellotta, R. (1985). New developments in field and laboratory testing of soils. Proc. 11th Int. Conf. on Soil Mech. and Found. Engn., ISSMFE, San Francisco, v. 1, pp. 57-153. (specify if CD ROM).

Thesis and dissertations: Lee, K.L. (1965). *Triaxial Compressive Strength of Saturated Sands Under Seismic Loading Conditions*. PhD Dissertation, Department of Civil Engineering, University of California, Berkeley, 521 p.

Standards: ASTM (2003). *Standard Test Method for Particle Size Analysis of Soils - D 422-63*. ASTM International, West Conshohocken, Pennsylvania, USA, 8 p.

Internet references: *Soils and Rocks* available at <http://www.abms.com.br> and downloaded on August 6th 2003.

On line first publications must also bring the digital object identifier (DOI) at the end.

Figures shall be either computer generated or drawn with India ink on tracing paper. Computer generated figures must be accompanied by the corresponding digital file (.tif, .jpg, .pcx, etc.). All figures (graphs, line drawings, photographs, etc.) shall be numbered consecutively and have a caption consisting of the figure number and a brief title or description of the figure. This number should be used when referring to the figure in text. Photographs should be black and white, sharp, high contrasted and printed on glossy paper.

Tables shall be numbered consecutively in Arabic and have a caption consisting of the table number and a brief title. This number should be used when referring to the table in the text. Units should be indicated in the first line of the table, below the title of each column. Acronyms should be avoided. When applicable, the units should come right below the corresponding column heading. Additional comments can be placed as footnotes.

Equations shall appear isolated in a single line of the text. Numbers identifying equations must be flushed with the right margin. International System (SI) units must be used. The definitions of the symbols used in the

equations must appear in the List of Symbols. It is recommended that the symbols used are in accordance with Lexicon in 8 Languages, ISSMFE (1981) and the ISRM List of Symbols.

The text of the submitted manuscript (including figures, tables and references) intended to be published as an article paper or a case history should not contain more than 30 pages, formatted according to the instructions mentioned above. Technical notes and discussions should have no more than 15 and 8 pages, respectively. Longer manuscripts may be exceptionally accepted if the authors provide proper explanation for the need of the required extra space in a cover letter.

### **Discussion**

Discussions must be written in English. The first page of a discussion should contain:

The title of the paper under discussion;

Name of the author(s) of the discussion, followed by their position, affiliation, address and e-mail. The author(s) of the discussion should refer to himself (herself/themselves) as the reader(s) and to the author(s) of the paper as the author(s).

Figures, tables and equations should be numbered following the same sequence of the original paper. All instructions previously mentioned for the preparation of article papers, case studies and technical notes also apply to the preparation of discussions.

### **Editorial Review**

Each paper will be evaluated by reviewers selected by the editors according to the subject of the paper. The authors will be informed about the results of the review process. If the paper is accepted, the authors will be required to submit a version of the revised manuscript with the suggested modifications. If the manuscript is rejected for publication, the authors will be informed about the reasons for rejection. In any situation comprising modification of the original text, classification of the manuscript in a category different from that proposed by the authors, or rejection, the authors can reply presenting their reasons for disagreeing with the reviewer comments.

### **Submission**

The author(s) must upload a digital file of the manuscript to the Soils and Rocks website.

### **Follow Up**

The online management system will provide a password to the corresponding author, which will enable him/her to follow the reviewing process of the submitted manuscript at the Soils and Rocks website.

## Volume 43, N. 2, April-June 2020

## Table of Contents

## ARTICLES

- Application of Grouting Intensity Number in Spillway Foundation at Jirau HPP/RO*  
M.B. Lopes, A.P. Assis 171
- A Laboratory Study of the Collapse Behaviour of a Compacted Sabkha Soil*  
O.Y. Debbab, B. Moussai, A. Messad 181
- Hydromechanical Behavior of Soil with Tire Fibers*  
A.C. Silva, S. Fucale, S.R.M. Ferreira 191
- Bottom Reinforcement in Braced Excavations: Coupled Analysis and New Method for Basal-Heave Stability Study*  
J.L. Borges, R.M. Santos 199
- Relationship Between Shear Wave Velocity and Piezocone Penetration Tests on the Brazilian Continental Margin*  
R.G. Borges, L.O. Souza Junior, M.C.F. Almeida, M.S.S. Almeida 219
- Geogrid Mechanical Damage Caused by Recycled Construction and Demolition Waste (RCDW): Influence of Grain Size Distribution*  
M.L. Domiciano, E.C.G. Santos, J. Lins da Silva 231
- Numerical Investigations on Seismic Bearing Capacity of Interfering Strip Footings*  
R. Boufarh, D. Saadi, M.S. Laouar 247
- TECHNICAL NOTES
- Drained and Undrained Behavior of an Aeolian Sand from Natal, Brazil*  
P.L. Souza Junior, O.F. Santos Junior, T.B. Fontoura, O. Freitas Neto 263
- Effects of Hydraulic Gradient Variation on the Structure and Strength of a Compacted Tropical Soil*  
W.G. Silva, H.N. Pitanga, T.O. Silva, S.L.S. Dias Neto, D.C. Lima, T.P. Trindade 271
- Physicochemical Modifications in Geomaterials and Their Leachates Extracted from Acidic Attack*  
S.T. Ferrazzo, R.S. Tímbola, L. Bragagnolo, E. Prestes, E.P. Korf, P.D.M. Prietto, G.D.L.P. Vargas 279
- Sample Quality Assessment: Comparison Between Brass Shelby Tubes and Reinforced PVC Tube Samplers*  
A.V. Abreu, M.S.S. Almeida 287
- CASE STUDY
- Influence of Weathering and Correlations Between Wave Propagation Velocity and Durability with Physical and Mechanical Parameters in Phyllites*  
T.R.R. Carvalho, M.F. Leão, E.A.G. Marques 297